Department of Engineering
University of Leicester

The Effect of Heat Treatment on the Embrittlement of Dissimilar Welded Joints

by

Michael Francis Dodge

PhD Thesis

ABSTRACT

The Effect of Heat Treatment on the Embrittlement of Dissimilar Welded Joints

Michael F. Dodge

In oil and gas transportation systems, austenitic nickel alloy filler metals are deposited on low alloy steel forgings, to form dissimilar welded joints. An example is the joint between forged hubs and linepipes used in subsea operations. A buttering technique is used, allowing the steel forging to be post weld heat treated (PWHT) before an offshore closure weld is carried out. Many years of successful service has been achieved; however high profile failures have occurred within the fusion zone of the ferritic forging and nickel alloy buttering, due to hydrogen ingress.

To investigate the embrittlement mechanisms, a programme of microstructural characterisation, environmental performance testing, strain measurements, and fractography was conducted. Two forging materials were compared: i) F22, a 2.25wt% chromium, low alloy steel, and ii) 8630, a low alloy forging steel with a higher carbon content than the F22. The forgings were buttered with Alloy 625; an austenitic weld metal. The effect of PWHT on microstructure evolution and fracture resistance was studied by applying heat treatments to the as-welded specimens. Slow strain rate notched bend tests, within a simulated marine environment, were conducted to rank the resistance to fracture. Strain evolution during PWHT was measured using neutron diffraction.

Microstructural examination of the dissimilar welds clarified a tri-modal split in the mechanical properties between as-welded, heat treated, and 'over-aged' samples. Modelling of carbon diffusion across the fusion boundary revealed the extent of phase precipitation during PWHT. In the as-welded samples interfacial failure was dominant due to disbonding at the fusion boundary, whilst in 'over-aged' samples, failure occurred by linking cracks at M_7C_3 precipitates. A competitive failure mechanism was proposed: the optimal heat-treatment of dissimilar joints can be predicted by examining the competing mechanisms of heat-affected zone tempering, residual stress reduction, and diffusion-controlled precipitate formation.

For my family

ACKNOWLEDGEMENTS

I would like to express my great appreciation to Professor Hongbiao Dong for his supervision, encouragement and support throughout my time at University. Without your efforts and in-depth technical knowledge, my desire to further my interest in engineering and science would not have been engendered, thank you.

My thanks are extended to those at TWI, particularly Mike Gittos and Marcio Milititsky, whose scientific expertise comes second only to their hospitality and patience. Similarly, I would like to thank Kasra Sotoudeh, Roger Barnett, Hiroto Kitaguchi and Ashley Spencer for training me in the skills necessary to undertake my studies.

I would like to thank those within the Mechanics of Materials group at The University of Leicester. My undergraduate tutor, Professor Helen Atkinson, is thanked for pushing me to succeed since my first day of University. Likewise, Professor Sarah Hainsworth is thanked for her notable contributions to the current work, in terms of both structure and technical content. Graham Clarke is also thanked for his time and patience in training me on the fundamentals of the laboratory equipment.

I would like to thank Shu Yan Zhang, Joe Kelleher and Saurabh Kabra of ISIS, Rutherford Appleton Laboratory, for training me in the intricacies of ENGIN-X and for involving me in interesting projects throughout my postgraduate career.

Special thanks also go to my friends and fellow research students: Tristram Broadbent, Adam Brown, Yu Xie, Scott Simmonds, Lee Aucott, Mykhailo Melnykov, Nick Jarman, Duyao Zhang, Nishad Karim and Gary Nolan. Thanks for making me

laugh every day that I have been here - I will undoubtedly look back on the last few years with fond memories.

MintWeld partners, Olga Barrera and Alan Cocks of The University of Oxford, are thanked for their contributions. Our meetings together are always thought-provoking and never cease to further my passion for the subject. I would also like to thank Lars Höglund, for his invaluable help with the diffusion modelling.

Financially, this work was funded by TWI Ltd., the Engineering and Physical Sciences Research Council (EPSRC) and MintWeld, a European Commission Seventh Framework Programme (FP7) sponsored project (contract No: NMP3-SL-2009-229108). I feel privileged to have had the opportunity to work on this project, thanks.

PUBLICATIONS

M. F. Dodge, H. B. Dong, M. Milititsky, V. Marques and M. F. Gittos (2012) 'Environment-Induced Cracking in Weld Joints in Subsea Oil and Gas Systems: Part I ', *ASME 2012 31st International Conference on Ocean, Offshore and Arctic Engineering, Rio de Janeiro, Brazil. 3(1), pp. 305-312.*

M. F. Dodge, H. B. Dong, M. Milititsky, R. P. Barnett and M. F. Gittos (2013) 'Environment-Induced Cracking in Weld Joints in Subsea Oil and Gas Systems: Part II ', *ASME 2013 32nd International Conference on Ocean, Offshore and Arctic Engineering, Nantes, France 3(1).*

M. F. Dodge, H. B. Dong, M. F. Gittos, T. Mobberley (2014) 'Fusion Zone Microstructure Associated With Embrittlement Of Subsea Dissimilar Joints', *ASME 2014 34th International Conference on Ocean, Offshore and Arctic Engineering, San Francisco, California, USA.*

M. Tong, G. Duggan, J. Liu, Y. Xie, M. Dodge, L. Aucott, H. Dong, R. L. Davidchack, J. Dantzig et al. (2013) 'Multiscale, Multiphysics Numerical Modeling of Fusion Welding with Experimental Characterization and Validation', *JOM*, 65(1), pp. 99-106

M. F. Dodge, H. B. Dong, M. F. Gittos (2014) 'Effect of post-weld heat treatment on microstructure evolution in dissimilar joints for subsea oil and gas systems ', *Materials Research Innovations,* 18(S4), pp. S907-S913.

M.F.Dodge, M.F.Gittos, H.Dong, S.Y .Zhang, S.Kabra, J.F.Kelleher (2014) 'In-Situ Neutron Diffraction Measurement of Stress Redistribution in a Dissimilar Joint during Heat Treatment', (in process).

ACRONYMS

AIDE	Adsorption induced dislocation emission
BS	Backscatter
BCC	Body-centred cubic
BCT	Body-centred tetragonal
CP	Cathodic protection
CTOD	crack tip opening displacement
DF	Darkfield
ED	Electro-discharge (machining)
EBSD	Electron backscattering diffraction
EDX	Energy dispersive x-ray (spectroscopy)
FCC	Face-centred cubic
FEGSEM	Field emission gun scanning electron microscope
FDZ	Filler deficient zone
FIB	Focussed ion beam
GTA	Gas tungsten arc
GB	Grain boundary
GCHAZ	Grain coarsened heat-affected zone
H-S	Hashin-Shtrikman
HAZ	Heat-affected zone
HE	Hydrogen embrittlement
HEDE	Hydrogen enhanced decohesion
HELP	Hydrogen enhanced localised plasticity
HIC	Hydrogen induced cracking
HAC	Hydrogen-assisted cracking
LAS	Low alloy steel
MIG	Metal inert gas
NBD	Nanobeam Diffraction
NPI	Net peak intensity
OES	Optical emission spectroscopy
PM	Parent metal
PMZ	Partially-mixed zone
PWHT	Post weld heat treatment

ROV	remotely operated vehicle
SCE	Saturated calomel electrode
SEM	Scanning electron microscopy
STEM	Scanning transmission electron microscopy
S-G	Scheil-Gulliver
SE	Secondary electron
SENB	Single edge notched bend
SSR	Slow strain rate
S-L	Solid-liquid
SAVs	superabundant vacancies
TEM	Transmission electron microscopy
TIG	Tungsten inert gas

TABLE OF CONTENTS

CHAPTER 1. Introduction to Subsea Dissimilar Joints

There are a number of scenarios where the joining of two dissimilar metals provides engineering advantages. Within the petrochemicals and power generation industries, dissimilar welds take advantage of the unique mechanical properties of both alloys, theoretically resulting in a cost-effective component that doesn't compromise on service life. The application of dissimilar welds in these industries is extensive and ranges from simple overlaying of Cr-Mo alloy steel with Ni-based fillers in waterwall tubing in power boilers to the welding of austenitic stainless steels in power plants to improve high temperature creep and thermal-fatigue resistance [1].

The oil and gas industry routinely uses dissimilar welds, in part due to the corrosive nature of the environments in which the components lie, but also due to the multitude of parts that need to be connected where flanged connections are impracticable. Typical applications of a dissimilar weld include cladding of ferritic components to improve corrosion resistance or transition joints between flowlines, valves and manifolds, the latter of which is the principal focus of this work.

Within subsea architectures the manifold is a control component that plays a crucial role in joining of multiple wells to flowlines and risers. This allows for the mass transfer of water, gas and chemicals whilst minimising the number of fatigue susceptible risers. A schematic of a typical subsea oil and gas field is shown in

Figure 1-1. In-field flowlines (green) connect each cluster of well-heads. Water lines (blue) are used to pump water back into the reservoir. Gas injection flowlines (red) can act in a similar manner, recirculating gas flow back into the well in order to maintain oil pressure at the well head. Control umbilical cords (white) feed information such as pressure, temperature and flow rate back to the rig whilst also controlling various valves on the sea floor.

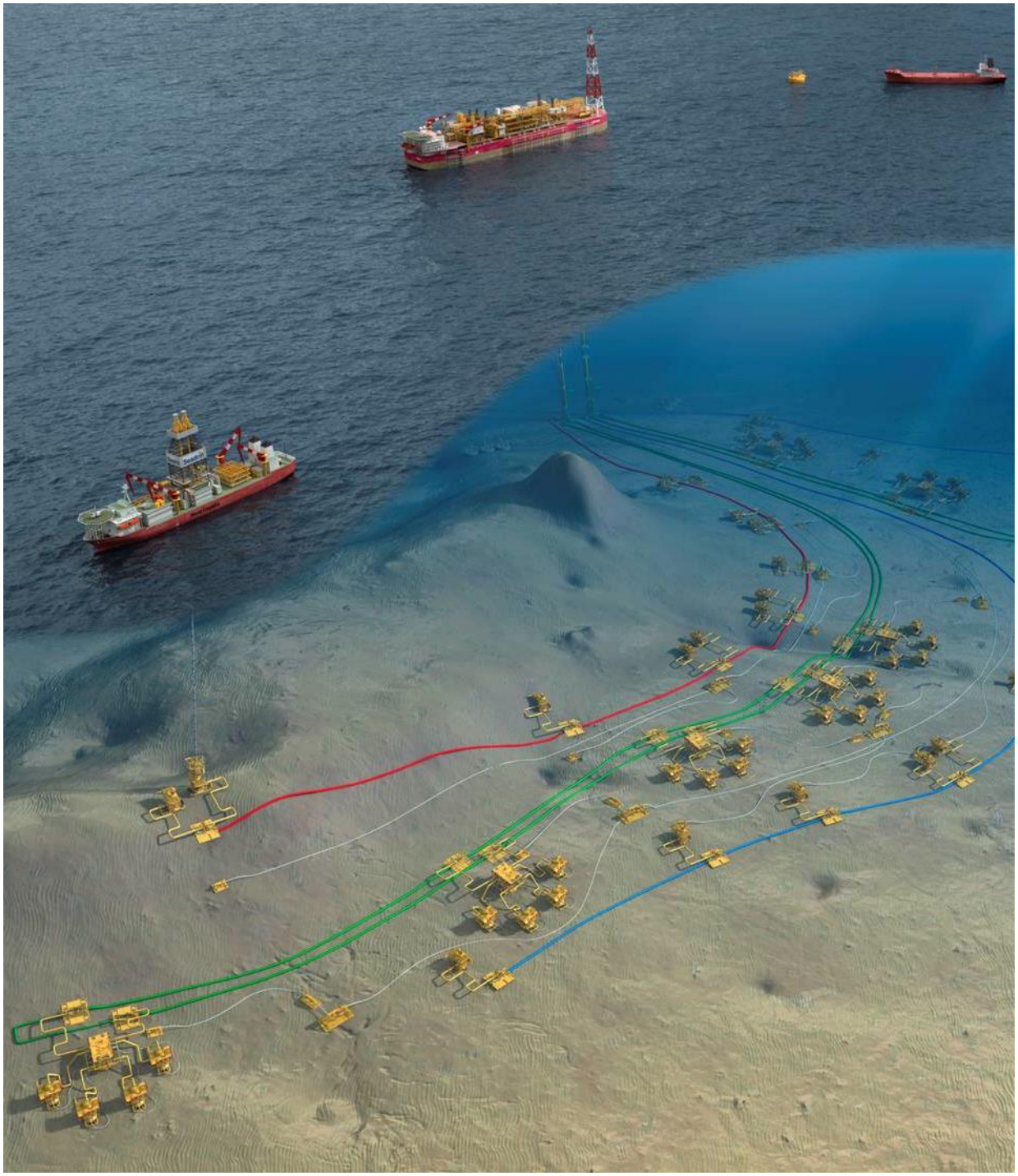

Figure 1-1 - Diagram of a typical subsea oil and gas field.[1]

The image also shows a number of manifolds, each connected to a group of surrounding 'Christmas trees'- well-capping components located above subterranean pipes. These are shown in greater detail in Figure 1-2.

[1] Images courtesy of Total E&P Nigeria

Figure 1-2 - Schematic of a subsea manifold surrounded by Christmas trees.

Whilst large components such as production jumpers and manifolds arrive offshore in a pre-assembled condition, shipping limitations require a certain amount of final assembly including the welding of linepipes to forged low alloy steel (LAS) manifold hubs. Simply welding the high hardenability hub to the leaner alloy steel pipeline could create brittle zones as well as a stress mismatch caused by the differences in coefficients of thermal expansion. As a result a two stage welding process is employed, together with an intermediate post weld heat treatment (PWHT). In the first stage, the LAS forging (e.g. AISI alloy 8630) is welded using nickel based filler metals (such as ERNiCrMo-3, 'Alloy 625') using a buttering preparation. PWHT of the forging is then carried out onshore in order to relax residual stress, temper martensite that has formed at the interface, and return ductility to the weld heat affected zone (HAZ). Following PWHT, the buttering is bevelled, enabling a closure weld to

be performed offshore to join the hub to the lower hardenability linepipe (e.g. X or F-65). The positioning of the bevel is such that the closure weld HAZ lies entirely within the heat treated austenitic layers, and thus no further PWHT is required.

As a means of corrosion prevention of the ferritic parts, structures of this type are subjected to cathodic protection (CP) using aluminium based sacrificial anodes mounted to the manifold frame. Whilst CP has proven successful as a means of preventing corrosion of the steel components, failures along the dissimilar metal interfaces have been observed [2], [3]. It is thought that the positioning of the sacrificial anodes too close to the dissimilar joints can create an over-potential, resulting in the evolution of hydrogen. Hydrogen that is absorbed by the metallic components readily diffuses through the structure where it may accumulate in plastically deformed regions and interfaces between different microstructures. The effect of hydrogen in metallic systems is well documented [4]–[6] it is known to reduce ductility, resulting in hydrogen embrittlement (HE) and premature failure of components.

In order to gain a deeper understanding of the above, the research presented herein took a multifaceted approach; that of characterisation, thermodynamic modelling and mechanical testing. Study is carried out on two specimen types: retrieved ex-service joints and those fabricated specifically for investigation of PWHT.

The joints retrieved from subsea service are 8630 low alloy steel, buttered with Alloy 625. Using microanalysis techniques, these are analysed in order to establish the properties typical of an industry standard joint.

The joints fabricated specifically for investigation of PWHT were provided in the as-welded condition and were the focus of characterisation, environmental performance testing and residual stress measurements by neutron diffraction. The three joints are as follows:

- 8630 (AISI 8630) -Alloy 625 (ERNiCrMo-3)
- F22 (ASTM A-182 F22)-Alloy 625 (ERNiCrMo-3)

- F22 (ASTM A-182 F22)- 309 (ER 309LSi)

Heat treated 8630-Alloy 625 dissimilar joints are known to be problematic subsea as shown by a number of in-service failures. As a result of this a greater emphasis is placed on this particular dissimilar metal weld. The specified compositions for the parent and weld metals are given below, note that all compositions stated in this thesis are expressed as weight percentages:

Table 1 – Specified nominal compositions (wt%) of the components of the three dissimilar weld combinations

	Parent metals		Weld metals	
	8630 (AISI 8630)	F22 (ASTM A-182)	309 (ER309LSi)	Alloy 625 (ERNiCrMo-3)
C	0.28-0.33	0.08-0.15	max 0.03	0.01-0.1
Mn	0.70-0.90	0.30-0.60	1-2.5	0.125-0.5
Ni	0.40-0.70	0.5 max	12-14	>58.0
Cr	0.40-0.60	2.0-2.50	23-25	20.0-23.0
Mo	0.15-0.25	0.90-1.10	max 0.75	8.0-10.0
Si	0.15-0.30	0.15-0.50	0.65-1.0	0.125-0.5
Nb	-	-	-	3.15-4.15
Fe	Bal.	Bal.	Bal.	5.0 max

CHAPTER 2. Processing, Microstructures and Embrittlement of Dissimilar Welded Joints

Dissimilar welding is considerably more complex than the welding of similar materials, and is characterised by large compositional gradients and microstructural changes across the fusion boundary. These localised variations result in interesting and varied chemical, physical and mechanical properties within the fusion zone. Problems experienced when joining dissimilar materials are not limited to those experienced in the unwelded materials; instead they may arise from any of the possible alloying combinations experienced when mixing the filler and parent metals. The primary considerations in the successful commissioning of a dissimilarly welded component include [7]:

i. General alloying problems
ii. Widely different melting points
iii. Differences in coefficients of thermal expansion
iv. Differences in thermal conductivity
v. Corrosion problems, such as galvanic corrosion, oxidation, hydrogen cracking, and sensitisation.

The above points are examined in regard to both the microstructures that arise immediately after welding, and during subsequent post weld heat treatment.

2.1 Microstructure of dissimilar welded joints

Fluid flow and solidification are important considerations in the discussion of fusion welding. Fluid flow affects the shape and solidification of the weld pool, and solidification affects the microstructure, properties and defects of the completed weld [8]. Within this subsection, the fusion zone of dissimilar welds is considered, beginning with the heat affected zone microstructure that forms after the passing of a welding torch. A review of the opposing

weld metal fluid flow and microstructure is then presented, followed by an assessment of compositional gradients that exist between the two sides.

2.1.1 **Microstructure in the HAZ of dissimilar joints**

The temperature field produced by travelling distributed heat sources across a metal surface can create complex microstructural morphology in the base metal heat affected zone (HAZ). The thermal cycle in arc welding consists of rapid heating (hundreds of degrees per second), followed by relatively fast cooling (of the order of tens to hundreds of degrees per second). Microstructural change in the HAZ is dependent on the heating and cooling rates, which in turn are determined by the welding heat-input; the thickness of the part being welded, geometry and interpass temperature are also important considerations [9]. Rosenthal first presented calculations for the heat distribution of a travelling heat source [10], using HAZ measurements to inform his theoretical calculations, forming the basis of subsequent studies of heat flow in welding [11]. Clearly, as microstructural changes in the HAZ are dependent on the welding thermal cycle, the morphology and size of the HAZ is consequent to the welding process used. The subsequent microstructural changes will directly affect not only the mechanical properties, such as strength of weldment, but also the corrosion resistance.

The HAZ can be divided into a number of sub-zones depending on the material being welded. These are illustrated in Figure 2-1 for the case of 0.3wt % carbon steel. The HAZ of a ferritic base metal may consist of microstructures indicated in Figure 2-1b, including a coarse grained HAZ, fine grained recrystallized zone, intercritical HAZ, partially transformed ‘spheroidised HAZ’ and the recrystallized or tempered HAZ.

The coarse grained region is present due to the elevated temperature beyond the austenitic transformation temperature. In this region the high temperature causes previously

ferritic grains to transform to austenite and coarsen, resulting in a region with larger grain size than further into the HAZ. In the same way, the fine grained HAZ undergoes a transformation, as it exists within the face-centred cubic austenite phase region, Figure 2-1c. However, the extent of coarsening within this region is reduced due to the shallower temperature profile experienced at this point in the parent metal.

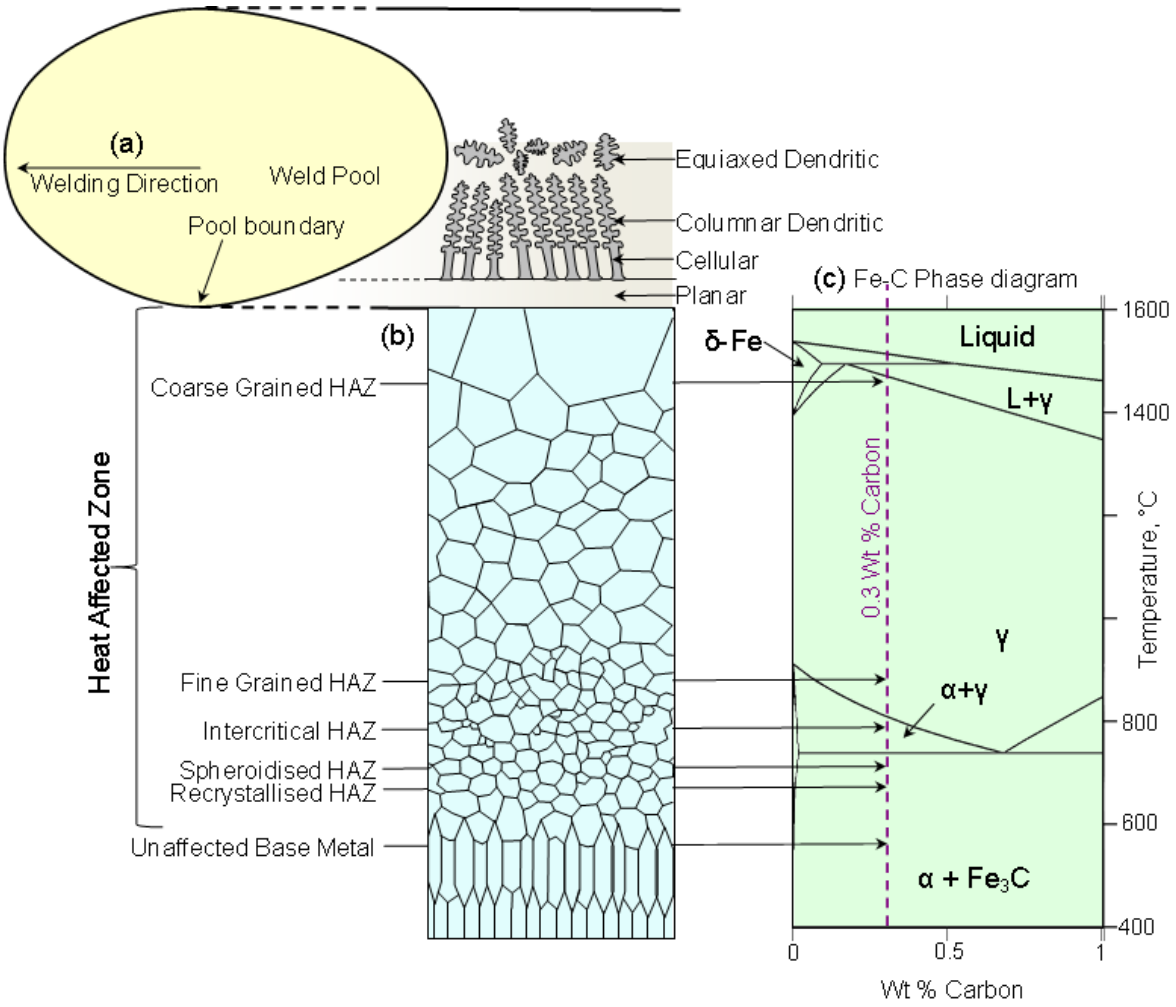

Figure 2-1 - Microstructure formation as a result of a passing welding torch. a) Weld pool showing different solidification modes; b) HAZ microstructure corresponding to c) the iron-carbon phase diagram calculated using Thermo-calc. Adapted from [12]–[15].

Each of the subzones corresponds to an altered microstructure, a result of the different thermal histories that each respective point has experienced. Importantly, this means the mechanical properties of each heat affected subzone will be different. Subzone width is

determined by the thermal cycle and on the pre-welding microstructure, from thermo-mechanical processing of the workpiece. For example, the recrystallization behaviour will be different in a material that has previously been annealed, compared to one which is cold worked. The extent of new grain growth is therefore dependent on the prior grain size and the presence of precipitates, the solubility of which changes with temperature. Similarly, it is important to consider HAZ regions that have experienced a temperature greater than the ferrite-austenite transformation temperature of 723°C (A_1), whereupon transformation to brittle martensite is possible during cooling. It is due to the formation of martensite that post weld heat treatment is applied - by reheating the base metal to below the A_1 temperature, the martensite is tempered, reducing the susceptibility to embrittlement.

In buttered joints (those of interest to hub forging applications), the HAZ is further complicated by the use of multiple welding passes. By using multiple passes, refinements in microstructure, reductions in residual stress and improvements in toughness are possible. An illustration of a cross section of a weld bead is shown in Figure 2-2a. The HAZ of the weld shows typical microstructures that are illustrated in Figure 2-1, including a coarse grained, fine grained and intercritical zone. With each subsequent weld pass, Figure 2-2b, the thermal cycle effectively grain refines (normalises) part of the previous weld metal, resulting in recrystallised coarse, and recrystallised fine grained zones. As a result, with each welding run, the heat input is decreased in order to reduce new grain growth. The annealing effect of subsequent passes extends the cooling time by acting as weld preheating, which also acts to reduce residual stress.

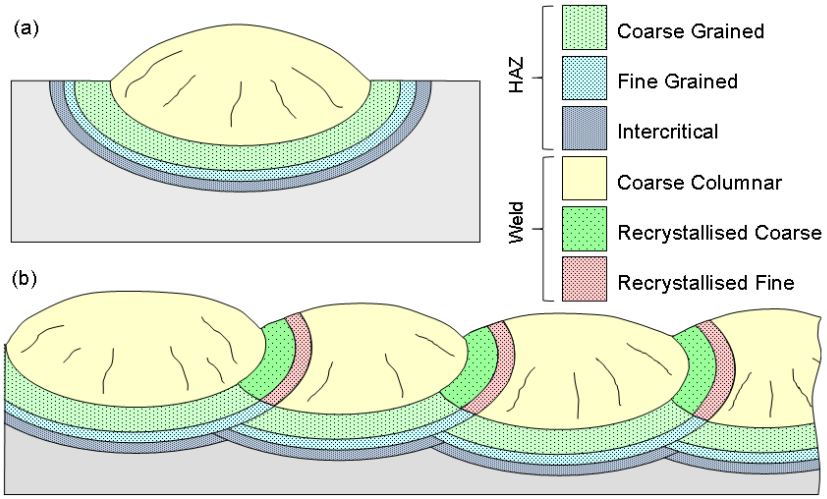

Figure 2-2 - Comparison of microstructures in a) a single bead; b) a multiple pass weld. Adapted from [16], [17].

With multiple passes, only a small amount of the HAZ is exposed to the highest peak temperatures during both weld passes, therefore, multi-pass welding acts as a method of mild heat-treatment. If a large number of weld beads are used, there is a greater fraction of reheated weld-metal, whereas fewer (larger) runs tends to increase the amount of recrystallized weld [15]. By increasing the volume of grain refined weld metal, a higher notch toughness is achieved, possibly as a result of the removal of segregation effects, such as columnar grain boundary carbides [18].

2.1.2 **Weld metal microstructure**

HAZ microstructures that form in the unmolten parent metal are presented in Figure 2-1, which also illustrates a number of typical dissimilar weld solidification morphologies. These morphologies may be explained with reference to solidification modes of transparent organic materials with similar behaviour to metals, such as those given in Figure 2-3. In the first instance, Figure 2-3b, a planar solid liquid (S-L) interface is observed, a common mode of solidification in pure metals without severe undercooling. In the second image, Figure 2-3c, the planar S-L interface has broken down into a cellular solidification front.

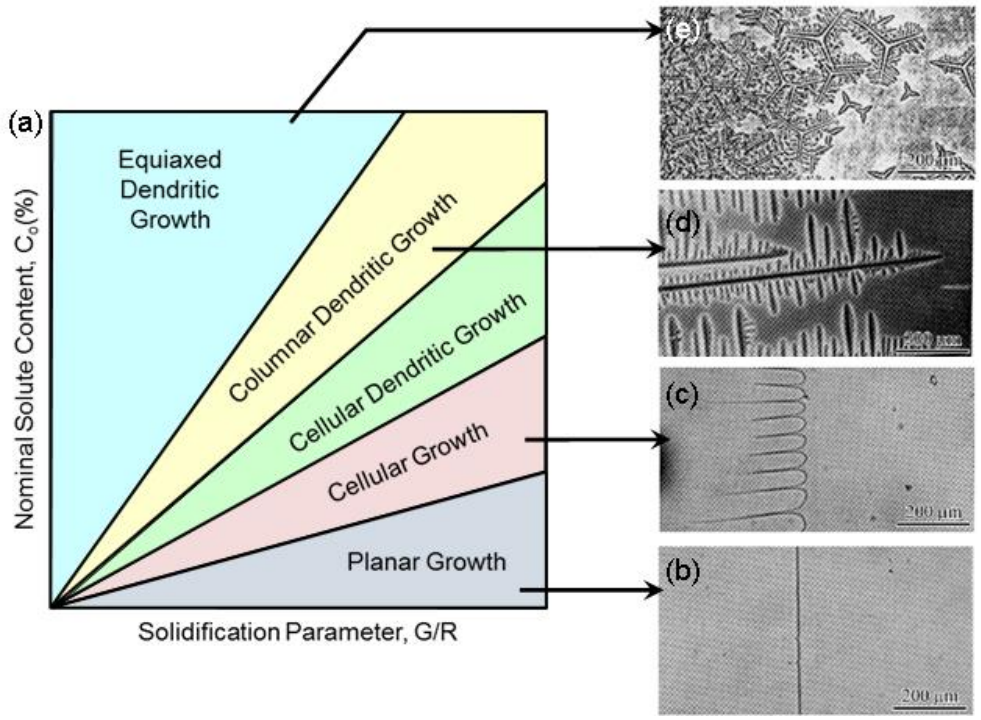

Figure 2-3 –Illustration of common solidification modes, a) factors controlling the growth mode during the solidification of liquid metals. Adapted from [19]; b) planar solidification of carbon tetrabromide [20]; c) cellular solidification of carbon tetrabromide with a small amount of impurity [20]; d) columnar dendritic solidification of carbon tetrabromide with several percent of impurity [20]; e) equiaxed dendritic solidification of cyclohexanol with impurity [21].

As the solidification boundary continues, the grains grow in a columnar fashion, followed by equiaxed dendritic growth, Figure 2-3d and e. Competitive growth between neighbouring columns of dendrites may result in relative size changes, but as a general rule, the weld metal grain size is determined by the grain size of the solid metal at the fusion boundary. Whilst the solidified weld metal has a primary grain structure, the individual grains have a substructure that results from microsegregation. Microsegregation substructure is determined by the form the solidification front takes, which in turn is influenced by the solute content of the liquid weld metal. Substructure is also determined by a solidification parameter that is equal to the temperature gradient, G (in the direction of solidification), divided by R, the rate of advance of the solidification front. These factors, and their influence

on the mode of solidification are illustrated in Figure 2-3a. As shown, for a fixed solute content, a decrease in the ratio of G/R is accompanied by a higher likelihood for dendritic solidification. For especially high solute contents, the possibility of planar and cellular growth is reduced.

A succinct review of the constitutional supercooling theory behind the breakdown of the stability of the planar front is given in [13], although a more complex theory also exists, that of interface stability by Mullins and Sekerka [22]–[24]. The constitutional supercooling theory was first described by Rutter and Chalmers [25] and described quantitatively by Tiller, Jackson, Rutter and Chalmers [26]. The Mullins-Sekerka interface stability theory considers the interface kinetic and heat transfer aspects, as well as the thermodynamic aspects of the constitutional supercooling theory. The latter is considered, due to its relative simplicity, and having been verified with experimental results [27]–[34]. The theory predicts the conditions required for the breakdown of a planar S-L interface in alloys with isotropic surface energy, as follows.

The temperature difference across a fusion boundary layer is the equilibrium temperature range, $\Delta T = T_L - T_S$, where T_L and T_S are the liquidus and solidus temperatures respectively. The thickness of the boundary layer at steady state is approximately D_L/R, where D_L is the diffusion coefficient of the liquid and R is the growth rate of the interface. The slope of the tangent to the liquidus temperature distribution is thus $\Delta T/(D_L/R)$ or $R\Delta T/D_L$. For a stable planar S-L interface, the actual temperature gradient, G, at the S-L interface must be at least $R\Delta T/D_L$. The steady state 'criterion for planar growth' is therefore defined as:

$$\frac{G}{R} \geq \frac{\Delta T}{D_L}$$

Eqn. 1

According to the equation, if a high temperature gradient, G, exists at the same time as a low growth rate then there is a higher propensity for a stable planar growth front. Likewise, if a high freezing temperature range exists, ΔT, together with a low diffusion coefficient, D_L, then it becomes more difficult to maintain steady growth of the planar S-L interface.

With increasing constitutional supercooling, the solidification mode will transition from planar, through to equiaxed dendritic solidification. The effect of constitutional supercooling on the mode of solidification is given in Figure 2-4. The region where the dendrites and liquid co-exist, called the mushy zone, is labelled 'M' in the diagram. With very wide mushy zones it may become easier for equiaxed dendrites to nucleate, than for existing columnar dendrites to grow across the whole mushy region.

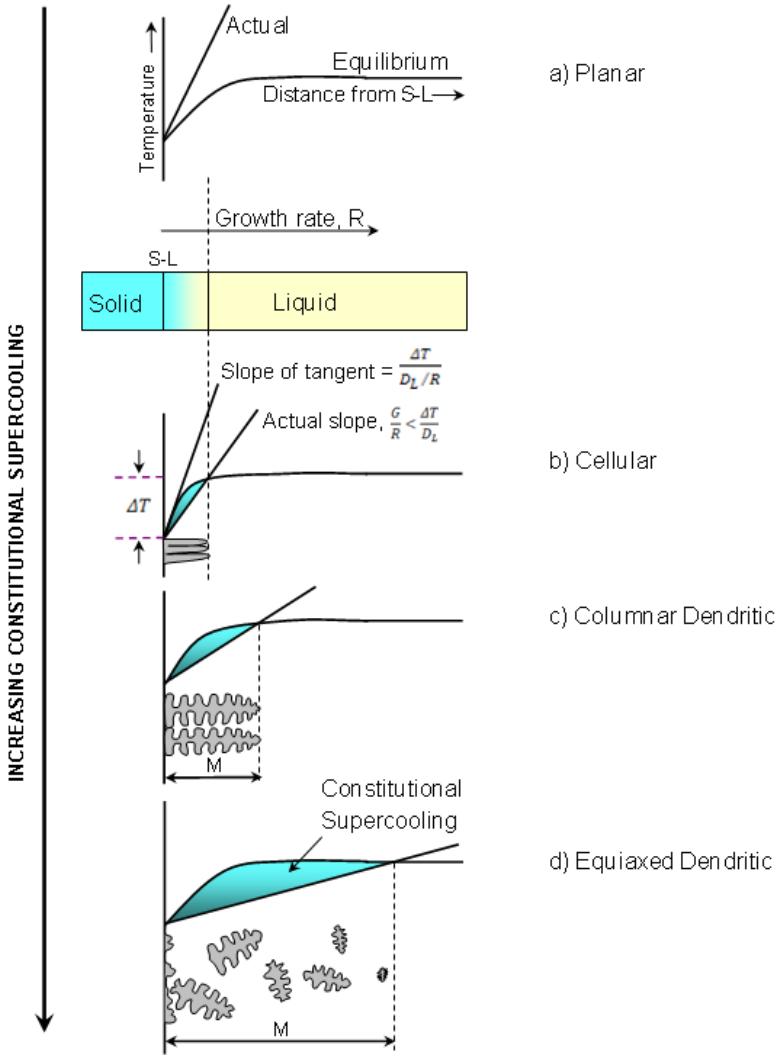

Figure 2-4 – The effect of constitutional supercooling on the mode of solidification. a) planar; b) cellular with illustration of S-L interface; c) columnar dendritic; d) equiaxed dendritic. S, L and M denote solid, liquid and mushy zones, respectively. Adapted from [13]

Solidification mode can vary from weld to weld dependent on the welding process used, however it can also change within a single bead. This phenomenon is explained using Figure 2-5, which shows the relationship between growth rate, R, and the welding speed, V. The distance a point within the weld pool travels in the normal direction, n, within a small time interval, dt, is:

$$R_n dt = (V\ dt)\ cos\ \alpha = (R\ dt)\ cos(\alpha - \beta)$$

Eqn. 2

Which, after division by $dt\cos(\alpha-\beta)$, becomes:

$$R = \frac{V\cos\alpha}{\cos(\alpha-\beta)}$$

Eqn. 3

Where $\propto$ is the angle between the welding direction and the normal to the pool boundary, and β is the angle between the welding direction and the growth direction of a dendrite at the point (which is <100> in fcc and bcc metals) [35]. If the difference between α and β is neglected (at cos 0° = 1) then Eqn. 3 will become:

$$R = V\cos\alpha$$

Eqn. 4

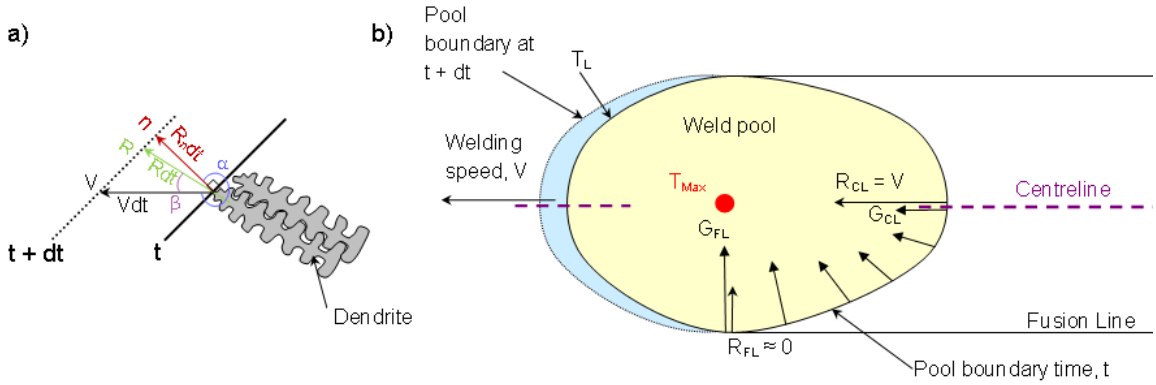

Figure 2-5 – a) Relationship between growth rate, R, and the welding speed, V.; b) Variation in temperature gradient, G, and growth rate, R, at the weld pool boundary. Adapted from [13].

As shown in Figure 2-5, α = 0° at the weld centreline, whereas at the fusion boundary it will be 90°. Thus, the rate of solidification at the fusion boundary is R_{FL}= 0, whilst at the centreline, R_{CL}, it will be at its maximum, R_{CL} = V. The maximum distance from the pool boundary, T_L to T_{max}, is at the centreline of the weld, arising due to the travelling welding torch, which creates an elongated weld pool. As a result, the temperature gradient G_{CL},

which is normal to the pool boundary at the centreline, is less than that at the fusion line, G_{FL}. Therefore, $G_{CL} < G_{FL}$ and $R_{CL} >> R_{FL}$, thus:

$$\left(\frac{G}{R}\right)_{CL} \ll \left(\frac{G}{R}\right)_{FL}$$

Eqn. 5

With reference to the factors controlling solidification growth mode, Figure 2-3a and Eqn. 5 suggests an increased likelihood for equiaxed dendritic solidification of the weld metal at the centreline, compared to the side of the weld pool fusion boundary.

An otherwise circular weld pool becomes elliptical and then teardrop shaped as the speed of the travelling welding torch is increased. The trailing portion of a teardrop shaped pool meets at a small, rounded point, creating two approximately straight lines at the pool boundary. Any columnar grains that are growing arrange perpendicular to the straight lines, hence the columnar grains also appear straight. The same phenomenon is seen in an elliptical shaped weld pool, however columnar grains curve from the fusion line towards the trailing portion of the pool boundary in order to maintain the perpendicular growth relationship.

Axial grains are those that are elongated with the welding direction, appearing in the middle of the solidified weld bead. They can initiate from the fusion boundary, and continue along the length of the weld, blocking columnar grains from growing and meeting at the centreline of the weld. Like the other columnar grains, axial grains also grow perpendicular to the trailing portion of the pool boundary. The trailing portion of an elliptical weld pool has a greater area that is aligned perpendicular to the axial direction, therefore a wider band of axial growth is seen, compared to a teardrop shaped pool, Figure 2-6. Axial grains have been found in aluminium alloys , austenitic stainless steel and iridium alloys [13].

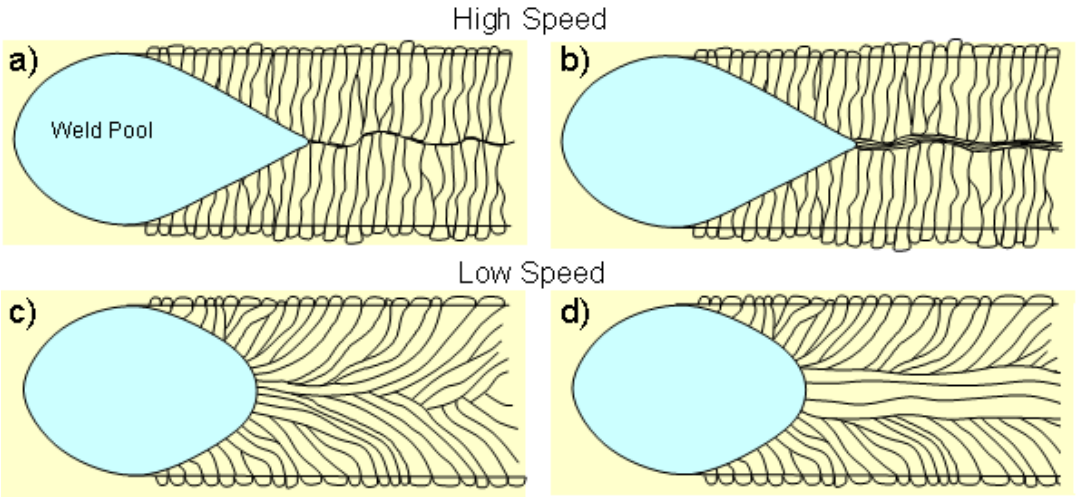

Figure 2-6 - The effect of welding speed on columnar grain structure in weld metal. a) High speed, no axial grains; b) high speed with axial grains; c) low speed without axial grains; d) low speed with axial grains. Adapted from [13].

2.1.3 **Segregation in dissimilar welds.**

Solute redistribution during cooling may result in microsegregation - segregation that occurs at the length scale of cell or dendrite arm spacings [36]. Macrosegregation, on the other hand, is segregation in far larger regions, such as may occur if weld pool mixing is incomplete. In multiple-pass dissimilar welding, macrosegregation can still occur if weld pool mixing is complete in each pass, this is due to the first weld bead having a different mixed composition to subsequent beads which are stacked on top [37].

Macrosegregation has been shown to occur in dissimilar welds in a number of different material combinations and welding processes [38]–[40] which can result in degradation of the quality of the weld. The work of Yang and Kou [39]–[44], has been instrumental in the understanding of four dissimilar weld macrosegregation mechanisms. In the first two mechanisms, verified using dissimilar Al and Cu welds, macrosegregation is described near to the fusion boundary. The filler metal mixes completely with the bulk weld pool, yet a stagnant or laminar flow layer of liquid base metal still forms at the weld pool boundary, solidifying without complete mixing with the filler.

Mechanisms three and four relate to the weld bottom, well within the fusion boundary, in which the filler metal mixes only partially with the bulk weld pool, solidifying near to the bottom of the weld. For simplicity, the case of similar welding is described first.

With the exception of severe undercooling, in arc welding the melting front is at the liquidus temperature of the base metal T_{LB}, and the solidification front is at the liquidus temperature of the weld metal T_{LW}. Because of weak convection near the weld pool boundary, in part because of the 'no-slip' fluid flow condition, a stagnant or laminar flow layer is found at the leading portion of the pool boundary. In fluid dynamics, the 'no-slip condition' states that the velocity of a moving liquid is zero at the interface with a stationary solid wall [45]. Since this liquid layer is composed of base metal, it begins to solidify from T_{LB}. The trailing portion of the weld pool is at T_{LW}, as it is contained predominantly in surrounding weld metal, except when near the fusion boundary where it switches to T_{LB} because of the presence of the liquid layer. In similar welding, the base and filler metals have the same composition, hence the liquid boundary layer solidifies into a beach of the base metal composition. The similarity in composition also means that $T_{LW} = T_{LB} = T_L$, where T_L is the liquidus temperature of the alloy. In this case, the trailing part of the pool boundary is isothermal up to the fusion boundary, and therefore no macrosegregation occurs.

In dissimilar welding, the liquidus temperature of the weld metal, T_{LW} can either be higher or lower than that of the base metal, T_{LB}, depending on the composition of each. Because of this, the stagnant or laminar flow layer at the pool boundary may begin to solidify at T_{LB} as opposed to T_{LW}, as is the case in the bulk weld pool. The boundary layer may then solidify as a filler-deficient 'beach' because of little or only partial mixing with the weld pool, whereas further towards the top of the pool, good mixing may be achieved. The dissimilar welds of interest to this study are such that $T_{LW} < T_{LB}$, the macrosegregation mechanisms relating to this condition are therefore reviewed.

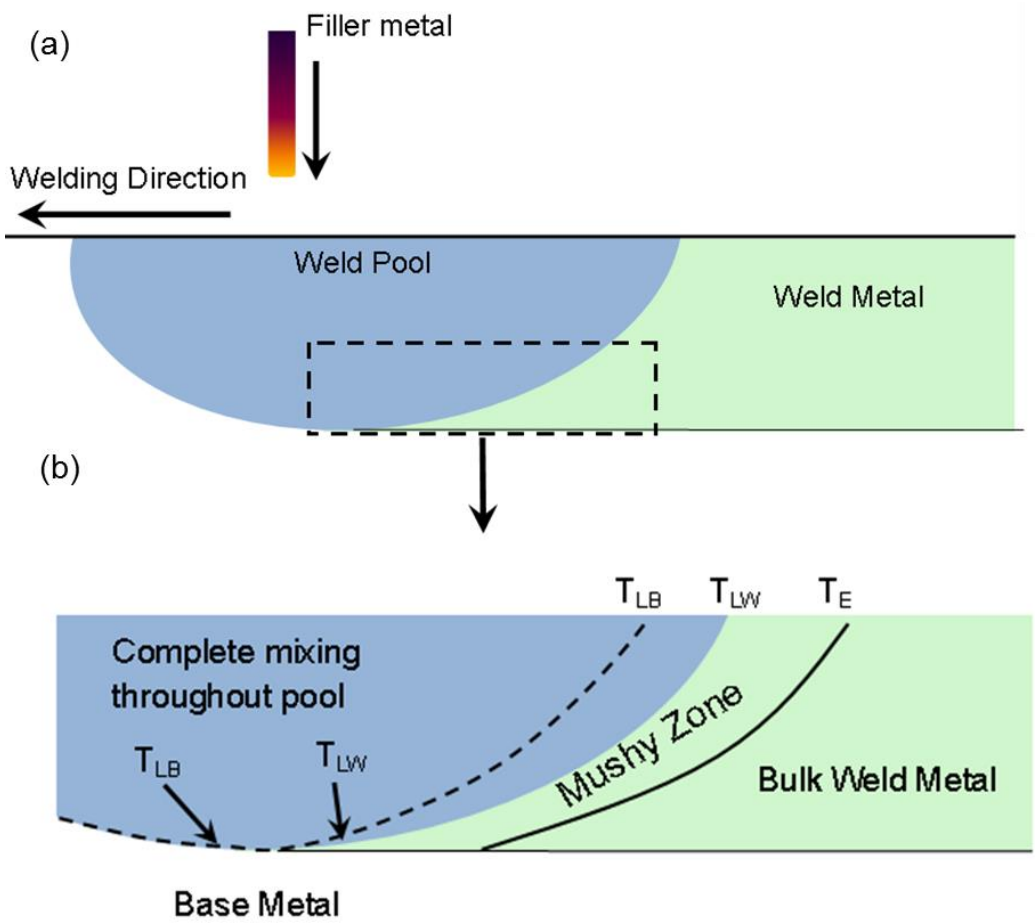

Figure 2-7 –Complete mixing throughout the weld pool with a dissimilar filler metal that makes $T_{LW} < T_{LB}$. a) weld pool and b) bottom of weld pool. Both images illustrate a vertical longitudinal cross-section. Adapted from [43].

Figure 2-7a shows a longitudinal cross-section of an elliptical shaped weld pool. The pool is elongated in the welding direction, as a result of the travelling welding torch. A detailed view of the bottom of the pool, under the assumption of complete mixing of the dissimilar filler metal with the base metal throughout the weld pool is given in Figure 2-7b. The filler metal causes the solidification front to shift backwards (opposite to the welding direction), from T_{LB} to T_{LW} [42]. This means that the region of weld metal in front of the solidification front, T_{LW}, is below the liquidus temperature of the base metal, T_{LB}. A region of solid and liquid, termed the 'mushy zone', is where solidification then takes place, between the weld liquidus temperature and the eutectic temperature, T_E. In this scenario, the weld is

macroscopically homogeneous, however microsegregation still exists at the dendrite-arm scale. Not depicted in the Figure 2-7b is the mode of solidification, which is an important consideration in this thesis. Theoretically, however, if solidification proceeds initially in a planar manner, before breaking down into cellular and dendritic modes (Figure 2-3), then composition gradients may still exist due to solute segregation during cooling.

In Figure 2-8, the proposed mechanism for the formation of a filler deficient zone (FDZ) is illustrated, under the $T_{LW} < T_{LB}$ conditions. The FDZ is described as 'the region in the weld metal where the contribution from the filler metal is less than in the bulk metal' [43]. As before, a stagnant or laminar flow layer exists at the front of the weld pools. In the first condition there is no diffusion between the liquid parent metal and the bulk weld pool, Figure 2-8a. The bulk weld pool begins to solidify at T_{LW}, whereas the layer of liquid base metal solidifies at T_{LB}. By welding with a dissimilar filler metal, isothermal conditions are no-longer present. The weld metal ahead of the T_{LW} front (beginning of mushy zone), is below T_{LB} due to the fact that $T_{LW} < T_{LB}$. At the same time, the layer of liquid base metal near to the pool boundary, solidifies and forms a filler deficient beach of the base metal composition, termed the 'unmixed zone' [46]. Whilst the filler deficient beach illustrated in Figure 2-8a appears uniform, fluctuations in the heat input, for example, can result in discontinuities along the weld length [43].

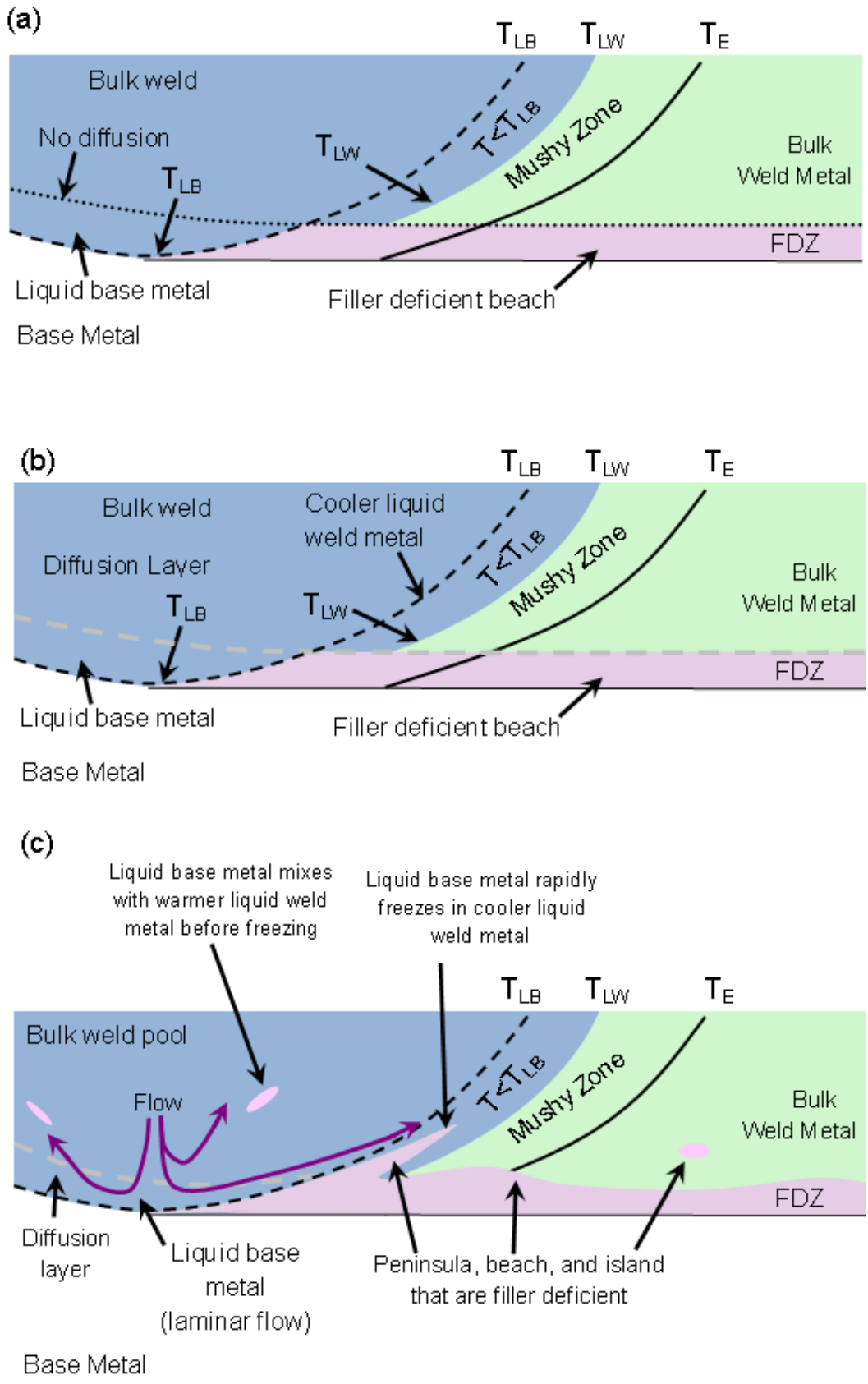

Figure 2-8 - The mechanism for formation of filler deficient zones (FDZ) when $T_{LW}<T_{LB}$ with a) no diffusion between the liquid base metal and bulk weld pool; b) diffusion and c) diffusion and convection. Adapted from [39], [42].

In the second instance, Figure 2-8b, elemental diffusion occurs between the bulk molten metal within the weld pool and the liquid base layer adjacent to the pool boundary. Inevitably, a composition gradient will exist between the two liquids. In the same way as in the no diffusion condition, a filler-deficient beach forms through solidification of the base metal, however in this instance a graded composition is found between the beach and bulk weld metal. If the liquid layer is particularly thin at the pool boundary, or if the solute is such that fast diffusion takes place, then the composition gradient may extend through the thickness of the layer. As a result, the filler-deficient beach will not contain an 'unmixed-zone' as in the previous case.

The more complex case of a weld pool with significant convection is illustrated in Figure 2-8c. Convection currents are able to transport the liquid base metal into cooler regions, for example towards the rear of the pool, on the condition that a velocity component parallel and opposite to the welding direction exists. The liquid weld metal ahead of the solidification is below T_{LB}, meaning that if liquid base metal is swept into such a region, it may begin freezing quickly, without significant mixing with the bulk liquid weld pool.

The strength of weld pool convection is central to the formation of islands and peninsulas that are filler-deficient. In the case where a cross-section for microscopy is prepared, such a peninsula may manifest as a swirl or island, yet is connected to the base metal in the third spatial dimension (i.e. subsurface to the area being examined). In general, the peninsulas tend to be oriented parallel to the fusion boundary due to the direction of convection currents, which transport the liquid base metal to the cooler area, just ahead of the mushy zone.

For the condition where $T_{LW}<T_{LB}$, the greater the liquidus temperature range between the weld and base metal, the wider the cool region ahead of the solidification front. This effectively creates more room for the liquid base metal to solidify amongst the liquid weld

metal, without a high degree of mixing. There is therefore an increased likelihood for a thick filler deficient zone to form when T_{LW} is reduced, relative to T_{LB}.

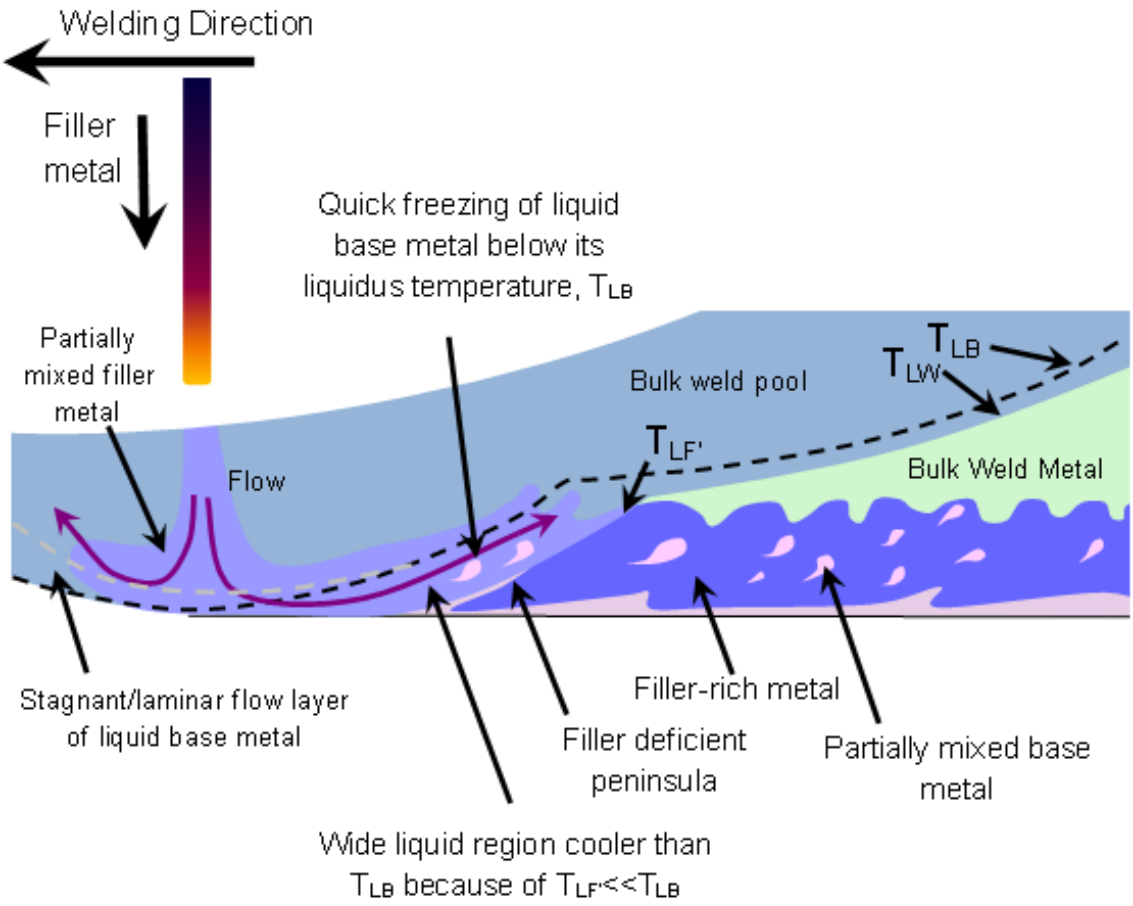

Figure 2-9 – Longitudinal cross-section illustration of the mechanism for macrosegregation formation caused by partial mixing of the dissimilar filler metal, in which $T_{LW}<T_{LB}$. Adapted from [44]

Figure 2-9 illustrates the case of weld bottom macrosegregation [44], where the addition of filler metals makes $T_{LW} < T_{LB}$. The liquidus temperature of the partially mixed filler, $T_{LF'}$, is close to the liquidus temperature of the filler metal, $T_{LF,}$ near to the fusion boundary (where $T_{LF'} << T_{LB}$). Similarly, $T_{LF'}$ is close to T_{LW} near to the bulk weld pool, which also has a lower temperature than the liquidus of the base metal. It follows that for the case where $T_{LW} < T_{LB}$, the liquidus temperatures are: $T_{LF} < T_{LF'} < T_{LW} < T_{LB}$. Referring to Figure 2-9, the trailing solidification front is at T_{LW}, due to compositional homogeneity. At the weld-bottom however, the solidification front is at $T_{LF'}$, because the filler metal is

partially mixed. It solidifies creating a filler rich zone at the bottom of the weld. Again, at the leading edge, the no-slip boundary condition may create a stagnant or laminar flow layer. As already stated, $T_{LF'} << T_{LB}$, and this creates a wide region at the bottom of the pool where the temperature is between the two. With the addition of convection, the liquid base metal layer can be swept into the cooler region, freezing quickly before completely mixing with the bulk weld pool. Therefore the solidified weld may exhibit 'streaks' or 'swirls' with an intermediate composition between the base metal and bulk weld metal. The exact composition of the swirls is dependent on the extent of the mixing before solidification occurs. As suggested in Figure 2-8c, the thin layer of stagnant liquid base metal near the weld pool boundary may still be swept towards the rear of the pool by convection currents. This explains the presence of filler-deficient peninsulas and beaches at the bottom of the solidified weld.

2.1.4 **Grain growth**

Since the liquid weld pool is in contact with parent metal grains at the fusion line, nucleation will take place. In fusion welding without a filler metal, the atoms within the liquid weld will align themselves with the substrate grains without altering the existing crystallographic orientations. This type of growth is known as 'epitaxial growth'. Epitaxial solidification in welding was first discovered by Savage et al. using Laue x-ray back-reflection, for the first time confirming the continuity of crystallographic orientation across a fusion boundary [47]–[49]. However, epitaxial growth has also been shown to occur when the parent material consists of more than one phase. An example of this is given in [50], where both ferrite and austenite were seen to grow epitaxially after welding with an austenitic stainless steel filler.

When joining dissimilar metals, the weld metal composition is different to the composition of the parent metal. Similarly, the crystal structure of the two metals can be different. Under these conditions, it is generally accepted that epitaxial growth is no longer possible and new grains will have to nucleate at the fusion boundary [42]. For example, Nelson et al. conducted studies on the nature and evolution of the fusion boundary in dissimilar BCC/FCC weldments [51], [52]. The authors postulated that when the parent metal and weld metal exhibit two different crystal structures at the solidification temperature, nucleation will occur on heterogeneous sites on the partially melted material. However, this does not rule out the possibility of a particular special orientation relationship between the weld metal and parent metal grains. Indeed, Fenske [14] and Ayer [53] found a Kurdjumov-Sachs orientation relationship at the transition zone between dissimilar low alloy steel-Alloy 625 welds.

Evidence of localised epitaxial solidification at the interface of LAS-Alloy 625 welds was found by Alexandrov et al. [54]. Using electron backscatter diffraction (EBSD), the authors found that a prior austenite grain boundary penetration, that is a region of liquid weld metal that has penetrated the opposing base metal grains during welding, had the same crystallographic orientation as the neighbouring planar solidified region.

2.1.5 **Dissimilar weld compositional gradients**

After depositing a dissimilar filler metal, an intermediate chemical composition between the parent and the weld metal is achieved. As a result of chemical inhomogeneity the corrosion resistance, mechanical properties and weldability are variable across the interface. Weld dilution, D is used to describe the composition of a single point, it is described as the degree of dilution of the parent metal by the base metal [12]:

$$D(\%) = \frac{A_{bm}}{A_{bm} + A_{fm}} \times 100$$

Eqn. 6

Where A_{bm} and A_{fm} are the cross-sectional areas of the base and filler metals, respectively. The composition in the fusion zone depends on the extent to which filler metal is diluted with parent metal. It can be established with knowledge of the composition of the parent metal (C_P), the filler metal (C_f), and the weld metal (C_w) as follows [55]:

$$C_W = C_F + \frac{D}{100}(C_P - C_F)$$

Eqn. 7

This equation predicts that the composition varies linearly from 0 to 100% under the assumption that good mixing has been achieved throughout. The concentration gradients in dissimilar welds have been previously shown to exist over regions of hundreds of microns [56]. Control of dilution is important in Ni-alloy to steel joins in order to prevent embrittling intermediate phases from forming. Segregation can occur, however, which can result in the formation regions highly different to the bulk weld metal, as will be discussed in Section 2.1.3.

Nickel acts as an austenite stabiliser, within weld metals such as Alloy 625, such that LAS to Ni-alloy joints (FCC-BCC) must forego a transition at the interface between the two structure types. The Schaeffler diagram was produced as a means of predicting weld metal constitution [57], but can be utilised for the prediction of phase balance of dissimilar fillers such as ni-alloys deposited on low alloy steel or stainless steel parent metals. An example of the Schaeffler diagram is given in Figure 2-10. The nickel and chromium equivalents are given by Eqn. 8 and Eqn. 9, respectively (expressed as weight percentage):

$$Ni_{eq} = \%Ni + 30(\%C) + 0.5(\%Mn)$$

Eqn. 8

$$Cr_{eq} = \%Cr + \%Mo + 1.5(\%Si) + 0.5(\%Nb)$$

Eqn. 9

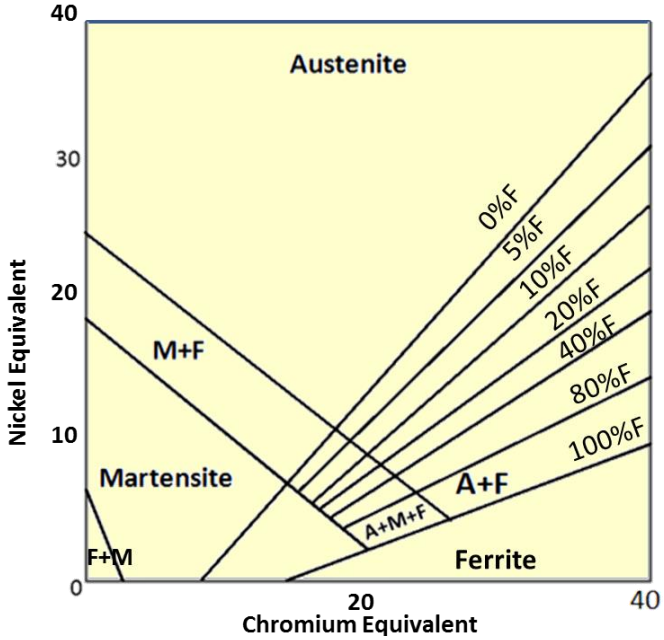

Figure 2-10 - Schaeffler diagram used in the prediction of weld constitution. Adapted from [57].

The Schaeffler diagram is limited in that it can only predict three phases: FCC austenite, BCC ferrite and body-centred tetragonal (BCT) martensite. Phases such as carbides are not found on the diagram, but can potentially form in dissimilar welds. Carbide formation is of interest in dissimilar welds to steels where diluted weld metal can introduce locally high regions of carbon. In order to predict this sort of phase formation, computational modelling is necessary.

2.2 Welding Residual Stress

2.2.1 The origin of residual stress

Residual stresses have been defined as 'self-equilibrating stresses within a stationary body when no external forces are applied' [58], essentially they are the stresses that remain in a body after removal of applied stress. Residual stresses arise due to 'misfits' between parts within a component, or between different phases within the material. Although residual stresses do have a beneficial function, as is the case with tempered 'safety' glass [59], they are generally considered undesirable in welded components. Residual stresses are difficult to determine as they cannot be calculated from forces, impulses or couples, unlike applied stress. They are normally classed according to their origin, such as 'thermal mismatch stress', according to the measurement method used, or by their length scale (e.g. micro- or macrostress) [60].

The HAZ of arc welds is largely associated with regions of concentrated high residual stress – stress that forms upon cooling, after welding. High residual stress, together with HAZ microstructural changes during welding, can result in unexpected failure, and is therefore is an important consideration in the assessment of welded structures [61], [62]. Untreated residual stresses alter the resistance to fracture, by effectively lowering the tolerance to welding defects. Failure may occur by sudden fracture, but has also been associated with stress corrosion cracking and creep. In fatigue failures, the effect of tensile residual stresses may work within the cyclic loading regime, increasing the mean stress, and resulting in damage accumulation. Conversely, for example in high cycle fatigue, compressive stresses may extend fatigue life [63]. Residual stress from welding may be expected, however higher temperature manufacture in which significant distortion exceeds predetermined tolerances, may result in costly rejection.

A simplistic representation of bead on plate transverse welding residual stress formation is shown in Figure 2-11. The changes of temperature profile are shown as a function of time (or alternatively distance), from the passing welding arc. At point A-A, ahead of the weld pool, the unwelded plate is at ambient temperature, the associated stress is therefore zero. At the arc, marked B-B across the weld pool, there is a steep temperature gradient. The stress within the molten weld pool is very low, due to the low associated yield stress. Local plastic deformation is accommodated by local misfits in this area. As a result of expansion, the HAZ near the weld pool experiences compression, and this is balanced by tension within the metal further from the pool. Behind the moving arc, across a welded region that is somewhat cooler (C-C), the temperature gradient from the centreline (X-X) of the weld is not as steep.

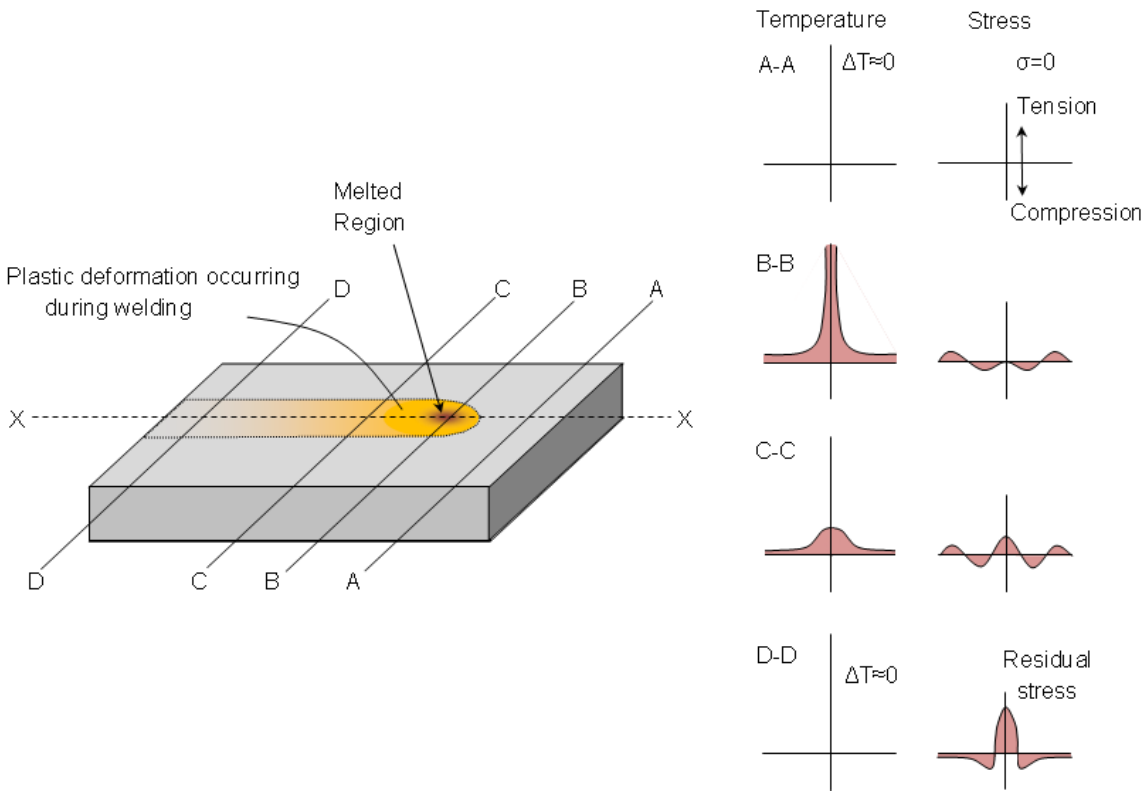

Figure 2-11 – Illustration of a bead on plate arc welding procedure with corresponding temperature and stress profiles. Adapted from [64].

The centre of the weld bead solidifies last, and as it does so, tensile stresses begin to develop. The tensile stresses are introduced due to the formation of the plastically deformed

region during welding, combined with weld metal and HAZ shrinkage during cooling. Once the temperature profile has returned to room temperature after welding (D-D), the final stress distribution is realised: tensile in the weld and HAZ, and compressive further into the parent metal. This means that if the temperature gradient imposed by the travelling heat source was not sufficient to cause plastic deformation, then no residual stresses would form upon cooling.

Inevitably, during welding microstructural changes occur, for example, precipitation hardened metals may suffer from dissolution of the strengthening phases. Similarly, recrystallization and new grain growth will occur in the vicinity of the weld, resulting in HAZ softening. Clearly, thermal and mechanical treatments for residual stress must consider these points to successfully return favourable mechanical properties to the joint.

In the case of buttered dissimilar welds, in which multiple welding passes are involved, the HAZ experiences a heating transient as each weld bead is laid. The formation of residual stress is therefore more complex than the described bead on plate example shown in Figure 2-11. Whilst the HAZ does not melt, the metal within approaches the melting point, and therefore metallurgical changes may be expected: dissolution and re-precipitation, as well as texture changes, may occur with each successive pass [65].

2.3 Hydrogen Embrittlement

The effects of hydrogen on the degradation of mechanical properties of welds is very well documented [6], [66] yet the precise mechanisms of embrittlement are still not fully understood in terms of metallurgical and chemical reactions.

Hydrogen cracking is often referred to as cold cracking, delayed cracking (due to the incubation time before hydrogen induced cracks appear), or underbead cracking. The term ‘hydrogen induced cracking’ (HIC) is used to refer to cracking that occurs through the

evolution of hydrogen whilst the component is in-service. Conversely, the term, 'fabrication cracking' is used to denote cracking occurring through hydrogen ingress during manufacture. In general, hydrogen cracking is associated with a combination of the following four conditions:

i. High hydrogen concentration within the workpiece/weld metal

   The presence of hydrogen may be expected due to absorption into the weld pool whilst in its molten state, followed by diffusion into the HAZ. Sources of hydrogen may be in the shielding gas, for example, or moisture on filler materials.

ii. Stresses acting on the weld

   As previously described, residual stresses may arise due to thermal contraction during cooling from the high welding temperatures. Existing stress problems may be exacerbated by stresses imposed in-service.

iii. Susceptible microstructures

   Within the HAZ, regions which experience a sufficiently high temperature to transform from ferrite to austenite, and back, may solidify into harder, hydrogen susceptible microstructures, such as martensite. Heat-treatment may temper these microstructures, however, microstructural transformation in the weld metal needs to be considered.

iv. Low temperatures

   A high risk of cracking is observed near to ambient temperatures, sometimes several hours after welding. Hydrogen embrittlement is generally associated with temperatures between -100 and 200°C [13].

It is difficult to control the stresses and temperatures in a cooling weld, so measures to reduce susceptibility to cracking normally rely on control of hydrogen level, microstructure, or both [66]. Achieving control of hydrogen content and microstructure relies on the correct

selection of weld combination, welding procedure and treatment, as well as environmental considerations.

2.3.1 **Hydrogen ingress during welding**

Hydrogen cracking is most often associated with the HAZ. An illustration of hydrogen diffusion from the weld metal to the HAZ during welding is given in Figure 2-12. The terms given for the austenite/(ferrite and pearlite) and austenite/martensite transformation temperature are given as T_F and T_B, respectively.

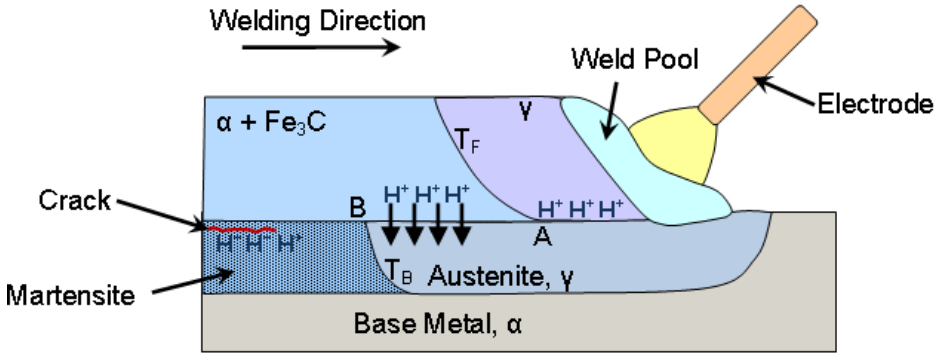

Figure 2-12 - Diffusion of hydrogen from the weld metal to the HAZ during welding. Short arrows indicate diffusion of hydrogen. Adapted from [13], [67].

The passing welding torch traverses across the workpiece, depositing the filler into the molten weld pool, and at the same time, austenitising the base metal. As the weld metal cools, it undergoes a phase transformation from austenite to ferrite and pearlite. At this point the hydrogen, having a higher solubility in austenite than ferrite, is rejected from the austenitic weld metal during solidification. The weld metal is first to undergo the transformation from austenite because the filler metal normally has a lower carbon content to the parent metal. As a result, the weld metal transitions to ferrite and pearlite, ahead of the austenitic parent metal's transformation to martensite. The time difference in structural change between the weld metal and base metal allows for accumulated hydrogen in the weld metal ferrite to diffuse into the austenitic parent metal, near to the fusion boundary. A

comparison of the diffusion coefficients of hydrogen in ferritic and austenitic materials is given in Figure 2-13.

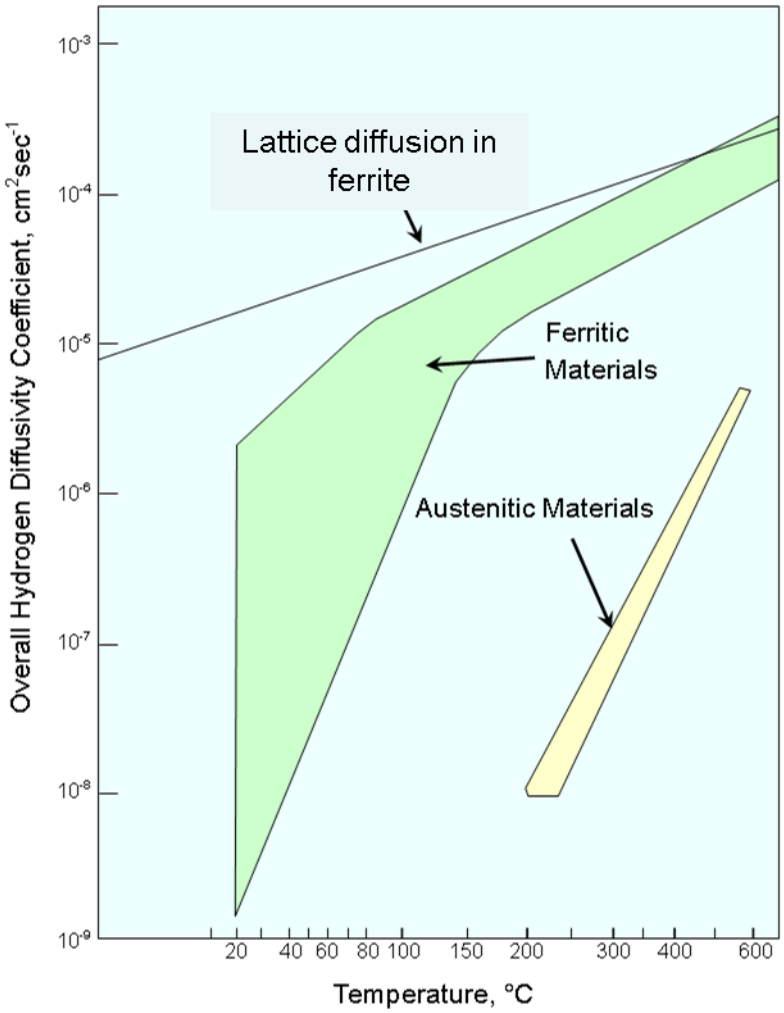

Figure 2-13 - Variations in the measured diffusivities of hydrogen in steel. Adapted from [15], [66], [68].

The diffusion coefficient is much higher in ferrite over the whole temperature range presented, compared to austenite. Hydrogen deposited near the fusion boundary, cannot readily diffuse into the ferritic base metal before the HAZ transforms to martensite. The hydrogen that remains in the HAZ martensite is particularly problematic, and can promote hydrogen cracking [13].

Phase changes in a plot of mean volume per iron atom, Figure 2-14a, and hydrogen solubility, Figure 2-14b, illustrate the crystallographic effect on the solubility of hydrogen.

The BCC structure of α-iron is packed more loosely than FCC γ-iron, the two most commonly used allotropes of iron. The BCC ferrite is stable up to the austenite transformation temperature, A_3 (910°C), at which point it undergoes a BCC→ FCC transition. This transition is accompanied by a reduction in volume per atom, and a concomitant increase in H-solubility. At 1390°C, the γ-iron reverts back to the BCC state: the high temperature δ-ferrite form, which is stable up to the melting point at 1536°C. The formation of BCC δ-ferrite is accompanied by a simultaneous reduction in hydrogen solubility.

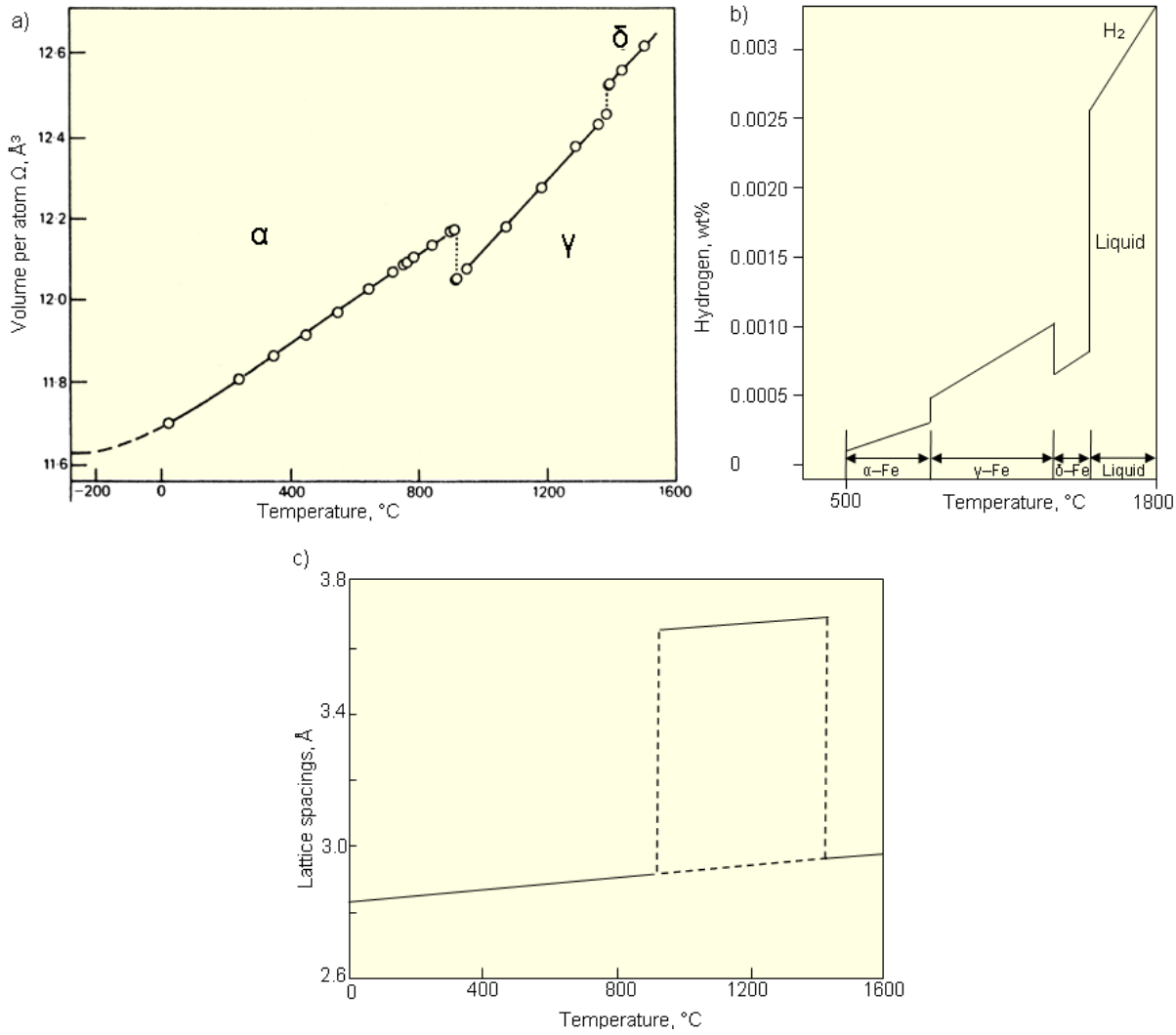

Figure 2-14 – a) Temperature dependence on the mean volume per atom in iron crystals. Adapted from [69] *b) Hydrogen solubility in pure iron as a function of temperature (constant pressure of 1atm). Adapted from* [70]*; c) lattice parameter expansion with temperature, in pure iron. Adapted from* [71].

Increased H-solubility in iron's FCC state is attributed to FCC crystals having a larger central interstice compared to the BCC structures, despite being more closely packed [72]. The largest cavities in BCC crystals are found at the tetrahedral holes between two edge and two central atoms in the structure. The second largest are the octahedral holes which occupy the centre of the faces and the <100> edges of the BCC cube [73]. Larger cavities within the FCC crystals are found at the centre of cube edges. Being surrounded by six atoms in the form of an octagon, these sites are referred to as octahedral holes [72].

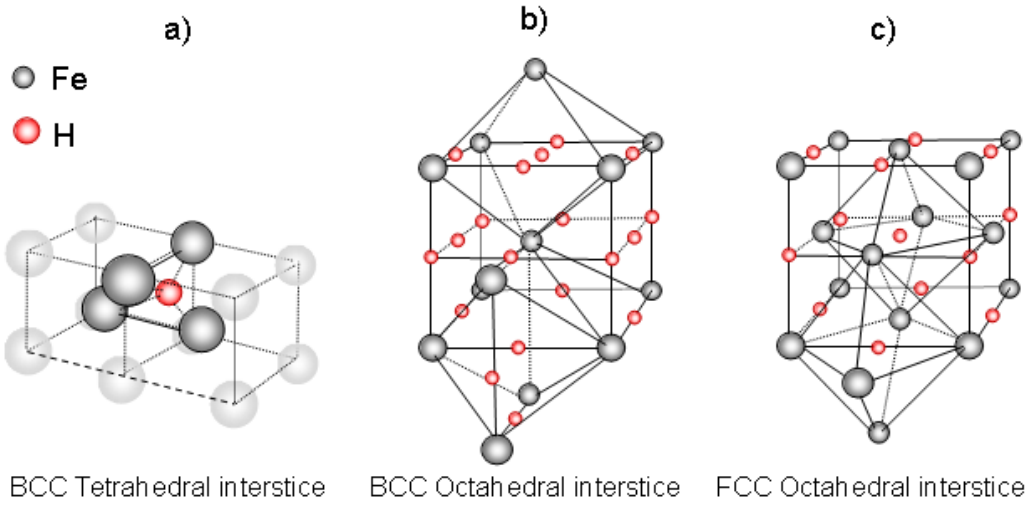

Figure 2-15 – Interstices in Fe structures. a) Tetrahedral interstice in a BCC crystal, with a H atom present; b) Octahedral interstices in BCC crystals; c) FCC octahedral interstice. Adapted from [69], [72]

The transition from γ→α, results in a rapid change in lattice parameter and volume as evident in Figure 2-14a and c [69], [71]. An atomic volume change of approximately 1% during the transition can lead to the generation of internal stresses [72]. The relative low H-solubility in the α form (ferrite/bainite/martensite), accompanied by diffusion of hydrogen to the HAZ, complicates the HIC problem further.

It is well known that interstitial hydrogen adversely affects the properties of steel, but this relationship is also temperature dependent. As shown in Figure 2-16, from Graville et al

[74], hydrogen embrittlement of ferritic steel is most pronounced at temperatures close to ambient. The relationship between notch tensile strength and hydrogen content, suggests that for a fixed displacement rate, it is possible to prevent hydrogen embrittlement by maintaining elevated service temperatures. This is an interesting phenomenon for components that experience temperature fluctuations whilst in-service, such as components within the subsea manifold.

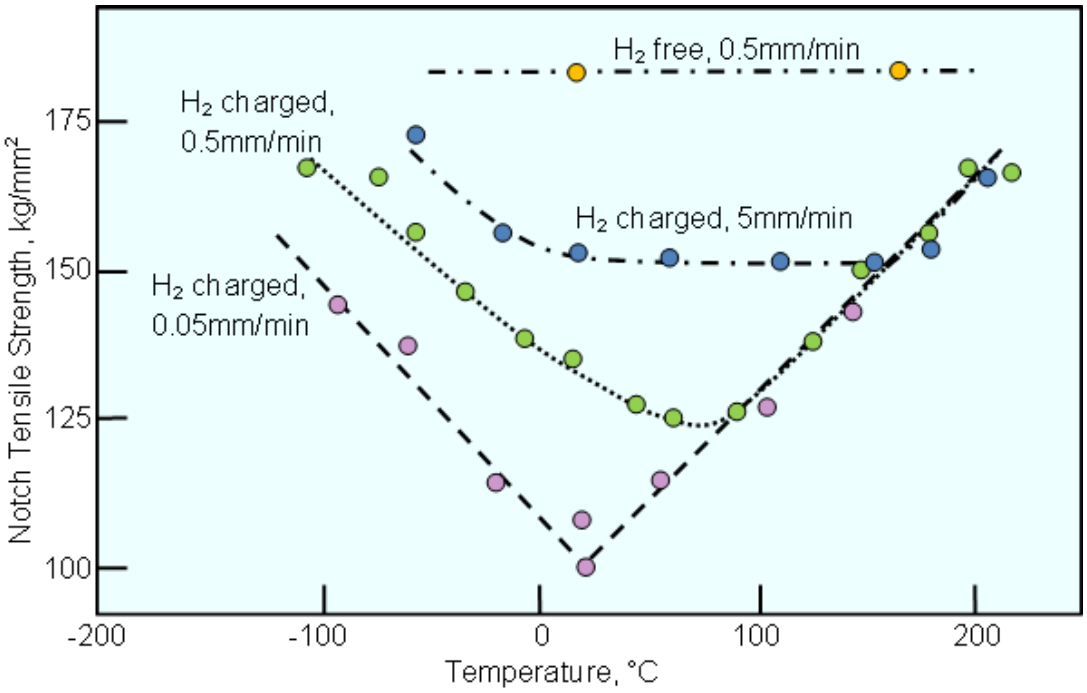

Figure 2-16 - Notch tensile strength of steel (0.22%C, 0.6%Mn, 3.4%Ni, 1%Cr, 0.3%Mo) as a function of temperature and displacement rate, passes through a minimum value close to room temperature. Adapted from [74], [75].

Once the HAZ has completed its transformation from austenite to ferrite, a further increase in temperature above the ambient temperature, will allow hydrogen to diffuse away from the weld. This effect is seen in Figure 2-13 between 20 and 150°C. Therefore, decreasing the cooling rate of the weld is not only beneficial in lowering the amount of martensite that forms, but it allows more time for hydrogen to diffuse away from the fusion zone. Similarly, the thermal cycles from multiple weld passes increases the mobility of hydrogen, allowing it to escape. High hardenability, high yield strength welds are generally

more vulnerable to embrittlement due to the microstructures that form upon solidification [76]. Microstructurally, embrittlement is generally ranked from most to least susceptible in the following order: martensite, spheroidised structures, pearlite, quenched and tempered martensite and lower bainite [77], [78].

Hydrogen cracks are commonly found in the HAZ, due to a combination of high residual stress, hydrogen deposition at the fusion boundary, and the presence of susceptible microstructures. Examples of hydrogen cracks are given in Figure 2-17a, an illustration of a fillet weld. Cracks in the HAZ are normally found at the weld toe, the weld root, or in an underbead position. Cracks in fillet welds are normally oriented along the length of the weld, whereas in butt welds, cracks are often transverse to the weld. Intergranular cracking tends to be the most common type of failure in harder, higher carbon and highly alloyed steel [66] heat affected zones.

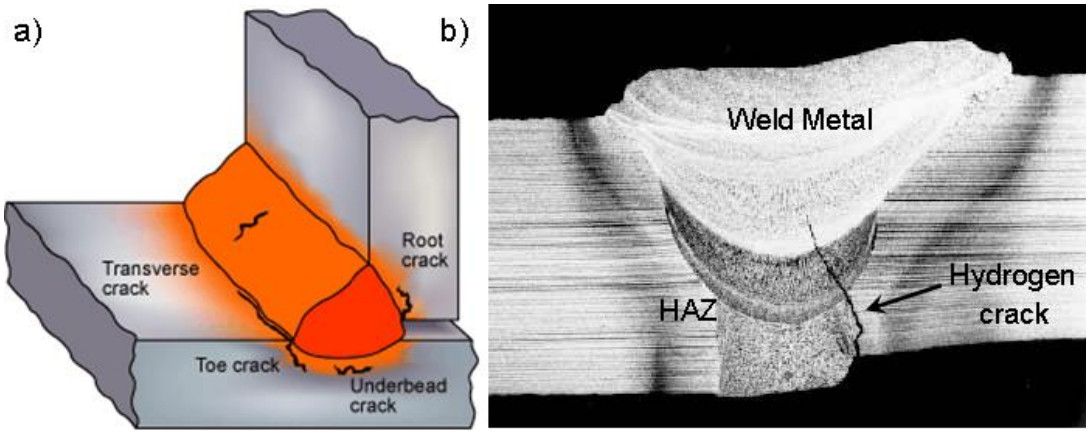

Figure 2-17 – a)Hydrogen cracks originating in the HAZ and weld metal of a fillet weld, note that multiple types of cracking would not be expected to form in the same weld. From [79] *; b) A typical example of a root HAZ hydrogen crack that has extended into the weld metal of a butt welded joint. Adapted from [5] .*

In the weld metal, hydrogen cracks can be oriented longitudinally or transverse to the weld length. Transversely, cracks are often found at an angle (roughly 45°), and are referred to as chevron cracks. An example of a hydrogen crack that had initiated in the HAZ and propagated into the weld metal is given in Figure 2-17b. Generally, the same factors that

influence cracking in the HAZ are applicable to the weld metal, such as stress, high hydrogen content, temperature and susceptible microstructures. However, hydrogen cracking in the weld metal can occur at lower levels of hardness than that of the HAZ [66].

2.3.2 **The evolution of hydrogen**

A brief overview of hydrogen transport and cracking after fabrication has already been given, however in subsea welds another source of hydrogen is problematic: that which occurs due to the use of corrosion inhibitors.

An effective method of corrosion prevention is cathodic protection (CP), which can be used in many situations, and has been known to prevent corrosion entirely. Structures that are commonly protected from corrosion using CP, include pipelines, ports, piers, ships and water storage tanks. The first documented use of CP was by Sir Humphrey Davy on a British Royal Navy ship, HMS Samarang [80], which was launched in 1822. The Samarang's copper body was protected using zinc anodes, with some success. Just 14 years later, further development of corrosion prevention of ships led to the dipping of steel sheets in molten zinc. In this case the zinc is anodic to the steel, protecting the sheeting in the event of any surface damage. However, it was not until the 1920s that the technology reached the oil transportation sector, this time in the protection of subterranean pipelines, used to transport petrochemicals from Gulf Coast oil fields [81].

The role of cathodic protection in inhibiting corrosion is best explained by first explaining how the ferritic parts corrode in water. If two dissimilar metals, connected by an electrically conductive path, are submerged within an electrolyte (such as seawater), then the following reaction will take place at the most active site:

$$Fe \rightarrow Fe^{2+} + 2e^{-}$$

Eqn. 10

The free electrons are conducted through to the less active site, combining with dissolved oxygen and water to form hydroxyl ions (OH^-):

$$\frac{1}{2}O_2 + H_2O + 2e^- \rightarrow 2OH^-$$

Eqn. 11

Recombination of the ions at the active surface produces the following reaction, which results in the formation of iron corrosion products, in this case ferrous hydroxide:

$$2Fe + O_2 + 2H_2O \rightarrow 2Fe(OH)_2$$

$$(steel + dissolved\ oxygen + water \rightarrow ferrous\ hydroxide)$$

Eqn. 12

Simply stated, a structure can become cathodically protected when an alternative external supply of electrons is transported to the metal that needs protecting, turning it into the cathode. The source of electrons can either be impressed current cathodic protection systems, from an external DC power source, or via sacrificial anodes: blocks of metal mounted near to the structure that needs protecting. Sacrificial anodes create a galvanic couple between the material that needs protecting and another metal that is more reactive. The most reactive metal oxidises, and gives up the electrons, protecting the less reactive metal from corrosion. For current to flow through the cathodic protector, there must be sufficient current to overcome the circuit resistance. In the case of aluminium anodes, the reaction at the surface of the sacrificial aluminium is:

$$4Al \rightarrow 4Al^{3+} + 12e^-$$

Eqn. 13

Whereas at the steel surface the reaction is:

$$3O_2 + 6H_2O + 12\,e^- \rightarrow 12OH^-$$

Eqn. 14

In other words, the anodic (active) sites on the steel surface have become cathodic (passive) as a result of the electrons supplied by the aluminium. Because the anodes continually sacrifice electrons, they degrade, needing replacement if corrosion protection is to be maintained. A balance must therefore be achieved between excessive cathodic polarisation, anode life, and service life of the steel components. A consequence of excessive polarisation is the reduction of water, and the generation of hydrogen by:

$$H_2O + 2\,e^- \rightarrow 2OH^-$$

Eqn. 15

The evolution of hydrogen results in the degradation of protective coatings, allowing hydrogen to come into contact with the surface of the metal. A comprehensive summary of adsorption processes is given by Barnoush in [82].

The ingress of evolved hydrogen, generated as a result of excessive CP, may be promoted by the addition of small concentrations of impurity elements [83]–[85]. Typically these 'poisons' encourage the entry of hydrogen atoms into the lattice by inhibiting the recombination of atomic hydrogen to its molecular form. In the petrochemicals industry, one of the most commonly encountered poisons is H_2S, which is found in 'sour' environments. The presence of H_2S has been linked to an increase in hydrogen permeation in steel, effectively reducing resistance to HIC. For example, Kittel et al [86] found that that at a constant pH and H_2S partial pressure (pH_2S), HIC in X-65 (a common grade of LAS used in subsea linepipes), was dependent on exposure time. This suggests that the HIC initiation is dependent on the time it takes to reach a critical hydrogen concentration. Hydrogen promoters include compounds formed, for example, from phosphorus, arsenic and sulphur.

Anions such as cyanide and iodide, and carbon compounds including carbon sulphide and carbon monoxide, are also known to encourage hydrogen permeation [82].

2.3.3 **Hydrogen trapping**

The diffusivity and solubility of hydrogen in ferritic and austenitic alloys, and their respective relationships with temperature have already been discussed in Section 2.3.1. However, it is important to also demonstrate that local variations in hydrogen concentration can exist due to lattice imperfections. An illustration of hydrogen interaction with lattice imperfections in pure metal is shown in Figure 2-18.

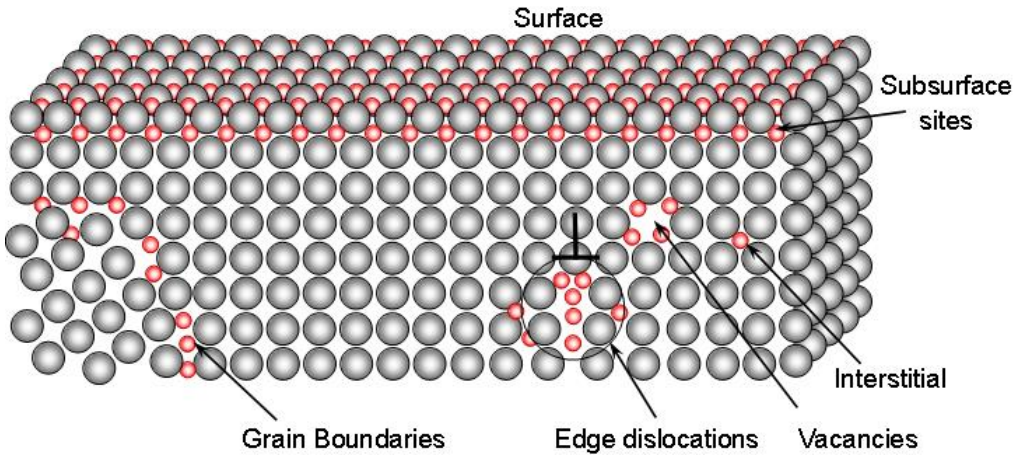

Figure 2-18 – An illustration of hydrogen (red) accumulation at the metal (grey) surface and within subsurface sites, including at grain boundaries and vacancies, as well as through conventional interstitial dissolution. At edge dislocations a cylindrical shaped hydrogen segregation region would be expected. Adapted from [87].

Point Defects

Vacancies are entropically stabilised lattice defects which are always present in materials [87]. Relative to hydrogen, internal vacancies are large, therefore they may be considered as favourable 'open volume defects', similar to an internal surface [88]. Hydrogen is driven to the vacancy site when chemisorption is energetically favoured over interstitial solution, as is normally the case. The presence of hydrogen within the lattice can change the equilibrium vacancy concentration. For example, Fukai and Ōkuma found a lattice parameter decrease

during annealing of Pd-H and Ni-H in hydrogen gas at 5Gpa and approximately 1000K [89]. They related the lattice parameter reduction to an extraordinary high concentration of vacancies, called "superabundant vacancies" (SAVs). The presence of SAVs has been confirmed in many other metals [90]–[92], which has led to the general conclusion that hydrogen atoms, originally at interstitial positions in the bulk metal, become trapped in high numbers at vacancies. At a single vacancy, and ambient temperature and hydrogen pressure, up to 6 hydrogen atoms may become trapped, corresponding to the number of octahedral lattice sites surrounding a vacancy in both FCC and BCC structures.

Dislocations

Dislocations are crystallographic defects which occur during the thermo-mechanical processing of materials (for example during rolling). Dislocations are formed either by homogeneous nucleation, grain boundary initiation, or at the interface between the lattice and the surface and precipitates. The relationship between hydrogen and dislocation dynamics is important due to the ability of hydrogen to reduce fracture toughness. Nevertheless, conflicting results have been reported by authors suggesting that the presence of hydrogen can both decrease and increase the flow stress within the same material systems. For example, an increase in flow stress with hydrogen in nickel was found in [93], whereas the opposite has been found by Kimura and Birnbaum [94].

Birnbaum argued that, in studies supporting an increase in the flow stress, damage via generation of new phases and high dislocation density at the surface may be the true cause (during hydrogen introduction) [95]. In the studies in which a decrease in flow stress was found, care was taken to minimise surface damage, so surface phase formation can be ruled out as an influencing factor. Therefore, it has been argued that the latter studies represent the most probable effect of hydrogen [96]. The decrease in flow stress is caused by hydrogen's

ability to enhance dislocation mobility. The mobilising mechanisms are summarised in [96], but include: a decrease in the effectiveness of solutes as barriers (due to solute clustering), and a decrease in interactions between dislocations and elastic obstacles. The generality of the enhanced dislocation mobility mechanism is demonstrated by it having been observed in a range of crystal systems, dislocation types (edge, screw and mixed), and alloys [96].

Internal Boundaries

Grain boundaries (GBs) are often associated with the hydrogen embrittlement of BCC and FCC systems due to the suggestion that they provide preferable, low energy, pathways for diffusion of hydrogen. This 'short-circuit' diffusion may accelerate hydrogen ingress and transport through the material, and is supported by several studies [97], [98]. However, this position has been challenged due to the realisation that hydrogen may be trapped at dislocations and vacancies within the GBs themselves (albeit in low temperature regimes) [99]. It is difficult to ascertain the exact relationship between hydrogen diffusion through GBs and trapping mechanisms, as often GBs contain non-metallic compounds such as carbide, nitride and oxides, which may bond to the hydrogen. Oudriss et al [100] attempted to isolate the two phenomena, by measuring diffusion of hydrogen in polycrystalline (FCC) nickel with different grain sizes. The authors found that GBs represent short-circuit diffusion pathways in the micrometre grain size range, but that competition between short-circuit diffusion and trapping may exist depending on grain size and the presence of triple junctions (the coming together of three boundaries).

2.3.4 **Mechanisms of hydrogen embrittlement**

A number of mechanisms have been put forward to explain the embrittlement of dissimilar metals. Atomistically, the four main candidates that are commonly used to describe

HIC of dissimilar welds are hydride-induced embrittlement, hydrogen enhanced decohesion (HEDE), hydrogen enhanced localised plasticity (HELP) and Adsorption-induced dislocation-emission (AIDE). A summary of each mechanism is therefore given.

Hydride-induced embrittlement

In hydride-induced embrittlement, hydrides are thought to nucleate in the stress-field ahead of the crack-tip. Within the stress-field of hydrides that have formed, new hydrides nucleate and enlarge. There is a significant body of theoretical and experimental evidence to support this theory, including Robertson et al's ground-breaking transmission electron microscopy studies where β-Ti was charged in a controlled environment in-situ [101]–[103]. In the experiments, small hydrides were seen to grow together, forming larger and larger hydrides. The nucleation and growth of hydrides is likely to be a fundamental cause of embrittlement in the typical hydride formers, such as V, Nb, Ti and Zr. An illustration of the basic hydride-induced embrittlement phenomenon is given in Figure 2-19.

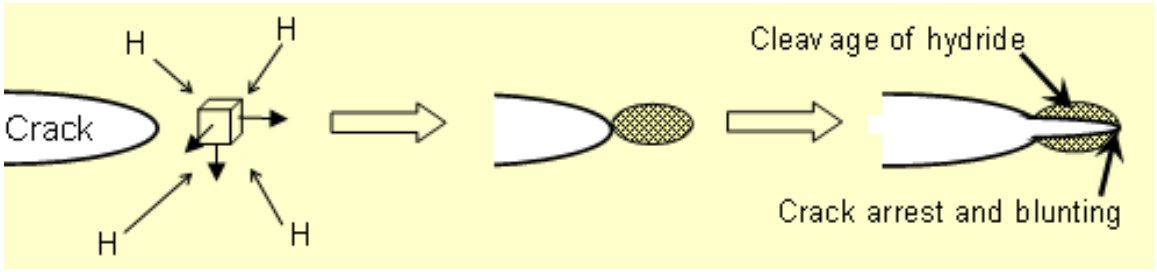

Figure 2-19 – The mechanism of hydride-induced embrittlement. Hydrogen diffuses to regions of high hydrostatic stress ahead of crack tips, at which point the hydride phase nucleates and grows. At a critical size the hydride cleaves, and the crack becomes arrested at the hydride-matrix interface. Adapted from [70].

Hydrogen enhanced decohesion

The hydrogen enhanced decohesion model was first proposed by Troiano [4], [104], [105], and was further developed further by Oriani [106]–[110]. The model suggests that hydrogen accumulates within the material's lattice where it reduces the cohesive strength

between the metal's atoms. Hydrogen accumulation, higher than that of the solubility in the unstressed lattice, is primarily driven by lattice dilation from imposed hydrostatic stress [111]. Subsequent work by Pressouyre found that hydrogen trapping may result in segregation of hydrogen within different regions. Compounding the susceptibility is the suggestion that bond decohesion is further enhanced by the addition of impurities within the lattice [112].

The HEDE model suggests that hydrogen damage occurs in the stress field surrounding the crack tip. Crack propagation succeeds when the crack tip opening tensile stress exceeds the local atomic cohesion strength, which hydrogen lowers. Hydrogen damage is most pronounced ahead of the crack tip, where maximum tensile stress is observed.

The HEDE mechanism is thought to be dominant in hydrogen induced cracking as well as hydrogen environment assisted cracking in high strength steels that do not form hydrides [82]. Within the stressed area ahead of a crack tip, it is thought that hydrogen accumulates, and is also trapped along the crack path, as suggested by [113]. An example of an experiment that supports the model is given in Figure 2-20a, where an increase in the pressure of H_2, as well as a decrease in temperature, is seen to increase how sharp the crack tip, α, becomes in stressed, single crystal, Fe-3wt%Si [114], [115]. In the figure, the red-dotted line represents crack growth exclusively by slip, at an α angle of 70°; the angle between active slip planes in the single crystal, Figure 2-20b. As HEDE becomes more dominant with increasing hydrogen pressure, the crack tip opening angle is seen to decrease, Figure 2-20c.

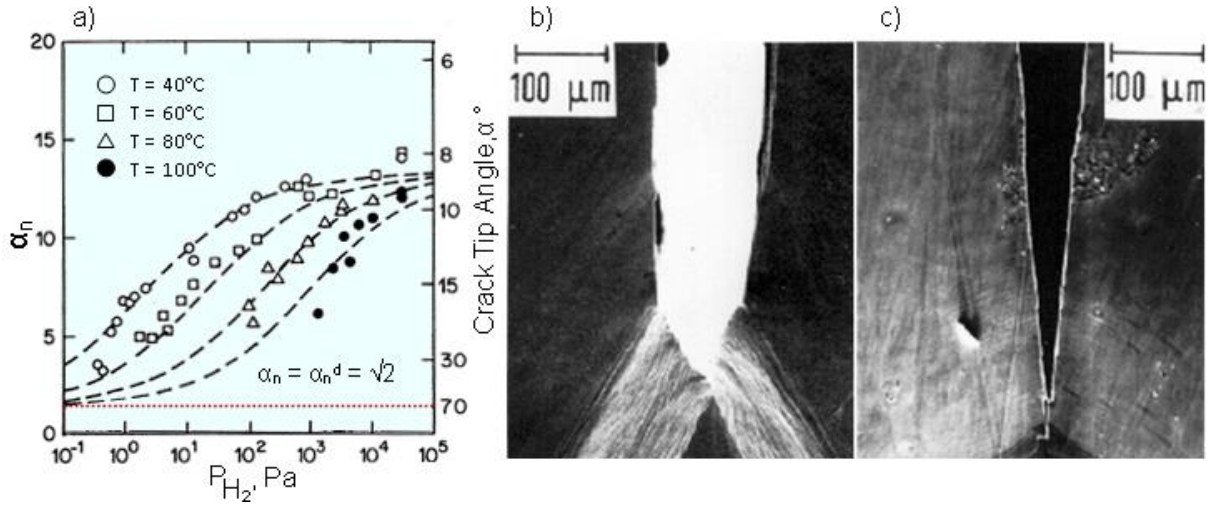

Figure 2-20 – The effect of hydrogen pressure in an Fe-3wt%Si single crystal. a) In-situ measurements of crack tip opening angles, α, under increasing hydrogen pressures and temperatures from 40 to 100°C. α_n is the ratio of crack extension to crack mouth opening ($\alpha_n = \cot(\alpha/2)$). The horizontal-dotted red line represents crack growth by crack tip slip alone; b)crack tip opening angle in a vacuum; c) in hydrogen. Adapted from [115].

The HEDE mechanism is controversial, due to shortcomings in experimental observations. Indeed, there is a lack of direct, a priori, evidence to show that dissolved atomic hydrogen lowers the interatomic force-displacement relationship. The problem is, that the amount of hydrogen able to dissolve in a specimen used for measurement of bulk properties, is far less than that projected to accumulate within the crack tip fracture process zone [82]. Furthermore, the theoretical basis on which HEDE is based, can simultaneously support the hydrogen enhanced localised plasticity (HELP) mechanism [116]–[118].

An illustration of the HEDE mechanism is given in Figure 2-21, illustrating hydrogen's ability to weaken interatomic bonds between matrix, and matrix-particle interfaces.

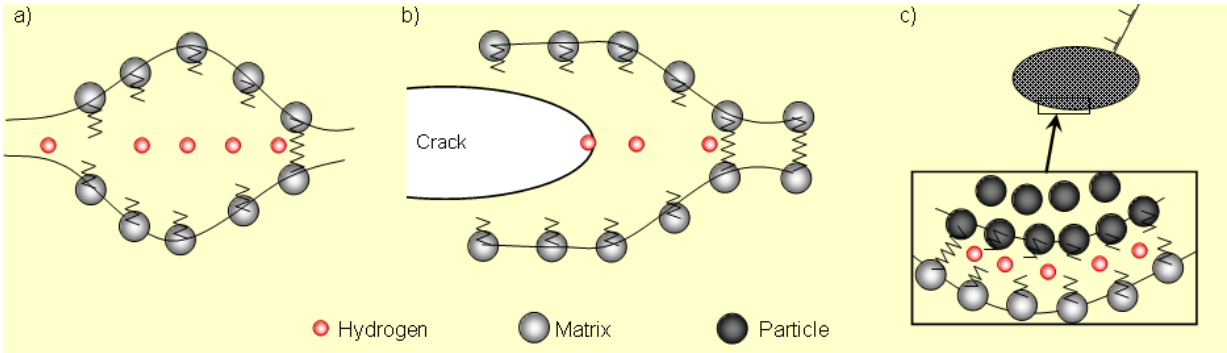

Figure 2-21 – Illustrations of the HEDE mechanism. a) Weakening of interatomic bonds due to hydrogen in the lattice; b) weakening due to adsorbed hydrogen; c) hydrogen interactions with particle-matrix interfaces. Adapted from [70].

Hydrogen enhanced localised plasticity

The hydrogen enhanced localised plasticity (HELP) model takes into account the effect of hydrogen on the dislocation dynamics. Fundamental to the theory, is the seemingly counter-intuitive argument, that rather than reducing plasticity, the effect of hydrogen is to increase localised plasticity, thereby reducing macroscopic ductility. HELP proposes that free hydrogen in solid solution within the material's lattice, is able to shield dislocations from interacting with elastic obstacles [102], [103], [119]–[123] and reduce the stacking-fault energy. The latter point results in a decreased likelihood for cross-clip, by increasing separation distance between partial dislocations[96], [124]–[127].

Beachem is considered to be the first major proponent of the concept, formulating the theory based on fractographic work on AISI 4300 steel, as well as AISI 1020 steel tubes (in torsion), tested in 3.5% NaCl. Beachem compared these electrochemically charged samples with AISI 4340 steel tested in 1atm of dry hydrogen gas [128]. His conclusions were that 'sufficiently concentrated hydrogen dissolved in the lattice just ahead of the crack tip aids whatever deformation processes the microstructure will allow'. Morphologically, the form of the fracture surface, be it intergranular, quasicleavage or microvoid coalescence, is dependent on the concentration of hydrogen, the microstructure, and the stress intensity at the crack tip.

Whilst appearing as localised plasticity on the microscopic scale, the macroscopic characteristics of HELP may at first appear as brittle failure.

The majority of evidence for the HELP mechanism is through in-situ TEM experiments on thin-foil sections, using an environmental cell. These experiments compare the dislocation dynamics in a vacuum as well as that of increasing hydrogen gas pressures, as summarised in [123]. The studies show that in the different materials tested, solute hydrogen can increase the crack propagation rate, decrease stacking fault energy, and increase the propensity for edge character dislocations. The effect was so pronounced that stationary cracks observed in vacuum, continued to propagate as hydrogen was injected into the electron microscope, as seen in Figure 2-22. Similarly, evacuation of the environmental chamber is seen to slow and eventually cease dislocation motion.

Whilst the HELP theory is supported by experimental observations, the environmental TEM method does have critics. In the best case scenario, the electron transparent samples necessitated by transmission microscopy engender a two-dimensional stress state, with a high possibility of dislocation-surface interactions. Dissociation of H_2 in the electron beam may also exacerbate surface issues, oxidising hardening solutes such as carbon and oxygen [82]. Despite these drawbacks, the TEM observations have provided evidence on dislocation motion that support HELP in a number of different crystal structures: BCC [129], [130], FCC [120], [131]–[133], and HCP [134]. In the latter study, the local stress intensity was seen to be critical in the fracture process. At high intensities the process was through HELP, whereas at low intensities titanium hydrides formed, providing a low energy crack path.

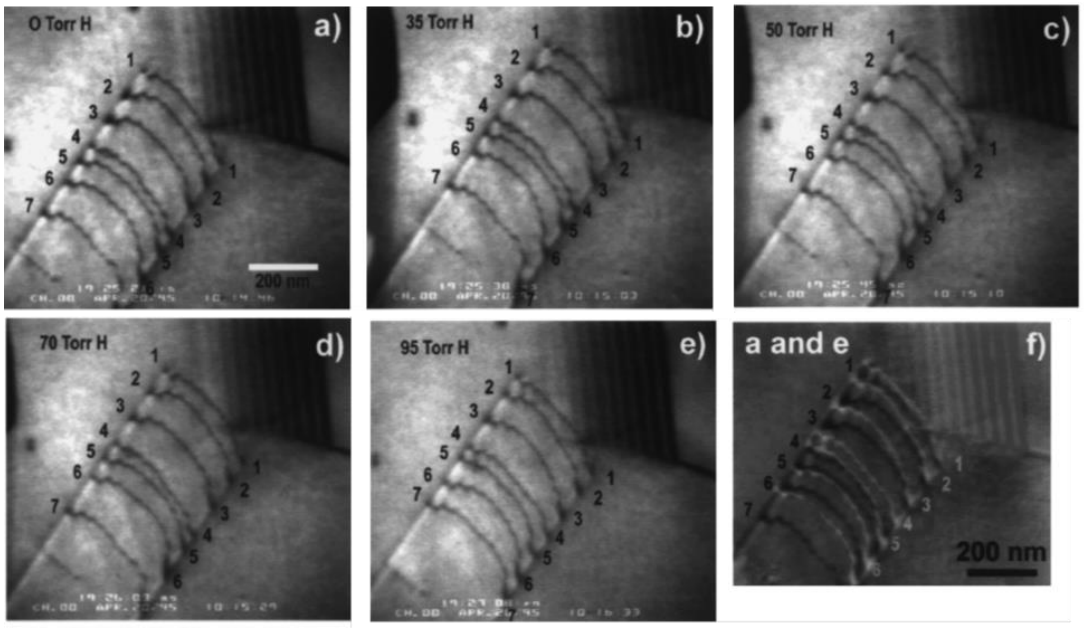

Figure 2-22 – Reduction of separation distance between dislocations in a pileup in 310s stainless steel due to solute hydrogen. Image f is a composite image, made from a positive image of the dislocations in a, together with a negative image of the dislocations in e. From [96], [123].

Bulk specimens have also been the subject of studies of embrittlement experiments, that appear to support the HELP theory [125], [135]–[138]. As demonstrated, a wide range of literature exists on the subject of hydrogen enhanced localised plasticity, however the theory has not yet been developed to the point where quantitative predictions of fracture toughness can be made.

An illustration of the HELP mechanism is given in Figure 2-23. Hydrogen localisation occurs due to hydrogen transport to the crack tip region (either due to high stress or as a result of hydrogen at the crack tip). Accordingly, the localised high hydrogen content results in a region of high localised plasticity. The crack path could be either transgranular or intergranular, depending on the local hydrogen concentrations within the grain and at GBs.

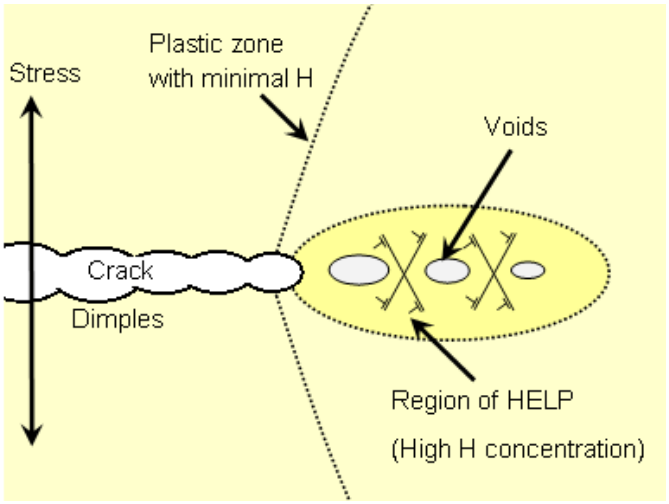

Figure 2-23 - Illustration of the HELP mechanism together with the formation and coalescence of microvoids. Localised plasticity occurs ahead of the crack tip in regions of relatively higher hydrogen concentration. Adapted from[70].

Although the HELP mechanism is well-established, the cleavage-like morphology that is often attributed to it has not been fully explained According to Lynch, the facilitation of localised ductility ahead of cracks would not necessarily result in a change from non-crystallographic ductile fracture to cleavage-like fracture along low-index crystallographic planes [70]. However, despite its implication, the term 'cleavage-like' does not necessarily relate to failure along crystallographic planes, rather it refers to the morphology of the fracture surfaces at relatively low magnifications.

Adsorption-induced dislocation-emission (AIDE)

The principal proponent of the AIDE mechanism is Lynch, having first introduced the idea in 1976 [139], [140]. In the AIDE model, 'dislocation-emission' incorporates the nucleation of dislocations at the crack tip, followed by movement of these away from crack tip area under an applied stress. Critically, the nucleation stage is facilitated by adsorption of hydrogen at the crack tip. The nucleation stage involves the 'simultaneous formation of a dislocation core and surface step by cooperative shearing of atoms' [70]. In other words, in

the presence of hydrogen atomic bonds are weakened and broken at the crack tip over the length scale of several atoms, whilst forming a dislocation core.

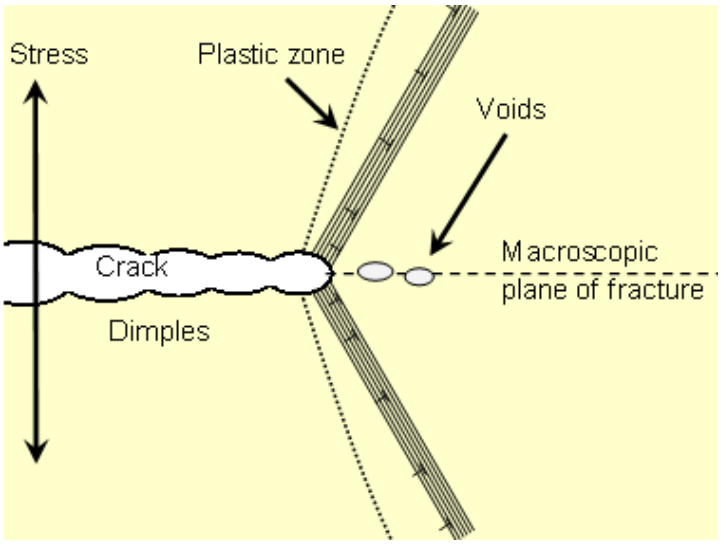

Figure 2-24 - Illustration of the AIDE mechanism, involving the emission of dislocations from the crack tip and facilitating the coalescence of cracks with voids which develop in the plastic zone. Adapted from [140].

In the AIDE model, cracks growing under stress emit dislocations from crack tips. The model also includes the nucleation and growth of voids (micro and nano-scale), ahead of the tip, Figure 2-24. Voids appear ahead of the crack tip at second-phase particles, slip-band intersections or other sites within the plastic zone when stress is high enough to cause general dislocation activity. Void interaction with the crack tip serves to re-sharpen the crack tip radius (minimising crack tip opening angles). It is important to note that, under the AIDE mechanism, hydrogen diffusion to, and adsorption at crack tips is necessary, if HIC is to occur.

Mixed HE Mechanisms

Combinations of all of the mechanisms described could well occur simultaneously [70], depending on the material, microstructure and hydrogen concentration. For example, localised plasticity at a crack tip together with intragranular precipitation (acting as hydrogen

trapping sites) could result in HELP succeeded by HEDE at the particle-matrix interface. Mounting evidence for such a combination is supported by modelling results of chromium-based intragranular M_7C_3 carbide within the austenitic planar solidified zone in dissimilar weldments [141]–[143] , however as yet, there is no direct experimental evidence to support this idea.

2.4 Hydrogen Embrittlement of Subsea Dissimilar Welds

For the past 10 or so years, industrial research into embrittlement of subsea dissimilar welds has gained in popularity, stemming from a number of high profile service failures [2], [3], [144]–[146]. Cracking is often found by remotely operated vehicles (ROVs) during the 'wet-parking' phase, after manifold installation in the field. In one instance cracks were found in 2% of the welds in manifolds [147].

Beginning with rudimentary experiments, the root cause of these failures was determined to be hydrogen embrittlement and 'insufficient material toughness resulting from carbon diffusion across the primary fusion line' [3], leading to the material being unable to meet fracture toughness requirements. However, it was not until the problem reached the academic community that an attempt to understand the underlying failure mechanisms using existing models of HE was made [148].

2.4.1 Microstructure

Low alloy steel – Alloy 625 welds have been the focus of a number of different microstructural studies [14], [54], [143], [148]–[155]. However, a general consensus on nomenclature has not yet been reached between the various authors.

Alexandrov et al. studied 8630-Alloy 625 joints in the as-welded and PWHT conditions [54]. The authors found that on the steel side, after PWHT, a carbon depleted region had formed, having a low hardness of $120HV_{0.1}$. On the weld metal side, a planar growth zone

with an FCC austenitic structure had formed, Figure 2-25, with hardness exceeding 800$HV_{0.1}$. Further into the weld metal, fine precipitates of Mo- and Nb- particles (likely carbides), were found within a cellular dendritic zone. Occasionally, penetrations of Alloy 625 metal with an FCC structure were found along prior austenite grain boundaries (GBs), in the 8630 steel GCHAZ. 'Swirls' of metal with a BCC/BCT structure of partially melted 8630 steel diluted with Alloy 625 were also seen along the cross-section of the weld.

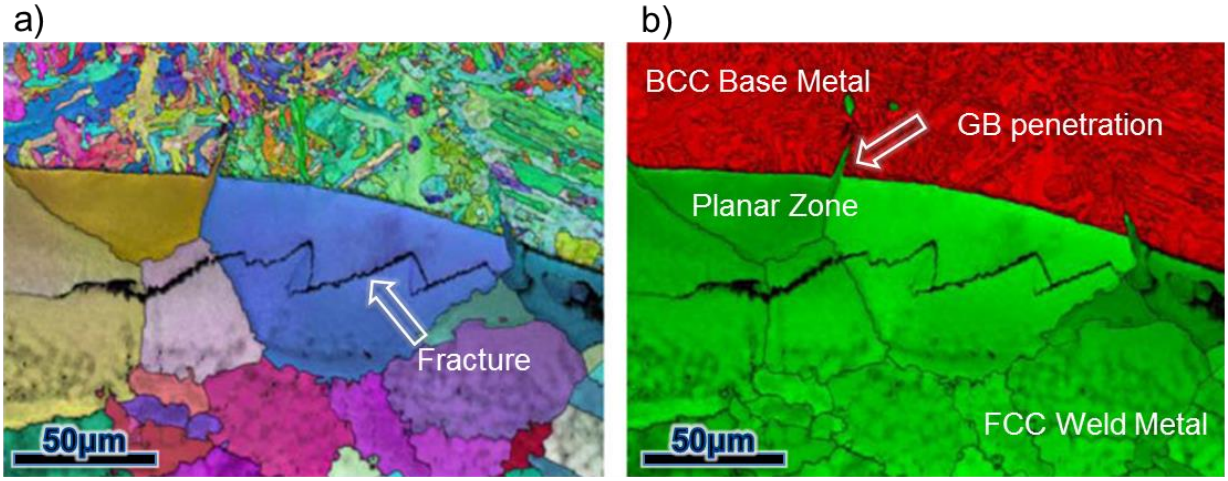

Figure 2-25 - Hydrogen cracking after cathodic charging on a low angle sectioned dissimilar weld between 8630 steel and Alloy 625 (after PWHT). a) EBSD map showing fracture through the planar solidified region within the weld metal and b)Phase content map showing the presence of prior austenite grain boundary penetration. Adapted from [54].

'Swirls' are discontinuities in the partially mixed zone (PMZ) that have likely formed as a consequence of the incomplete weld-pool mixing described in Section 2.1.3, and are a common feature of LAS-Alloy 625 interfaces. An example of these is given in Figure 2-26, which is taken from Fenske's analysis of an F22-Alloy 625 dissimilar interface [148]. The formation of discontinuous PMZs is a consequence of the welding process used. For example, Beaugrand et al found that higher arc energies increased the amount of martensite rich swirls, which is accompanied by a decrease in planar zone width [151].

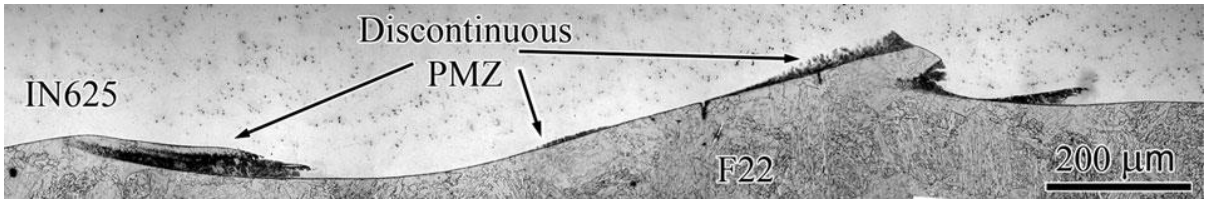

Figure 2-26 – Optical micrograph showing a section of an ASTM A182 (F22) – Alloy 625 weld after 10 hours of PWHT. Taken from [148].

Theoretically, as explained in 2.1.5, it is possible for a band of martensite to exist between the dissimilar metals, not just in discontinuous partially mixed zones. This has been confirmed by Fenske using TEM [14] and by Olden et al [155].

Microstructure after PWHT

The planar solidified region on the Alloy 625 side has previously been called the 'featureless zone', 'white-etching zone' or 'zone ϕ' owing to its particle-free appearance at resolutions afforded by optical and scanning electron microscopy [151], [153], [155]. However, heat-treated samples have been shown to contain nanoscale carbides, such as chromium based M_7C_3 within the planar solidified region. The importance of the M_7C_3 carbide within the incongruously named 'featureless zone' is such that the term 'planar zone' will be used throughout this work.

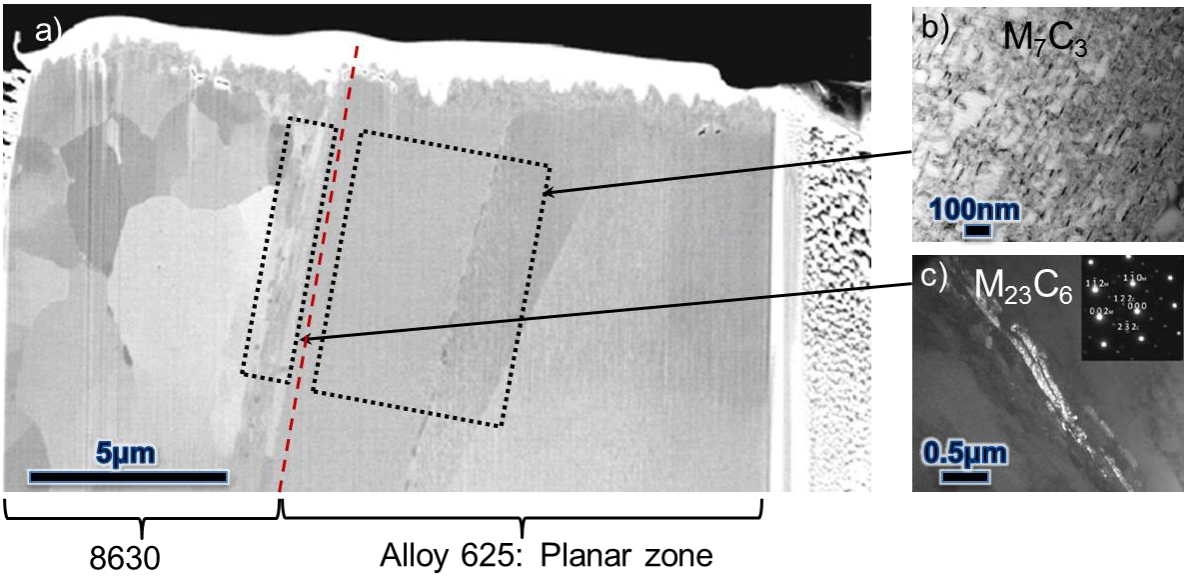

Figure 2-27 - 8630-Alloy 625 fusion zone microstructure after a typical, industry standard PWHT. a) SEM image of a TEM thin-foil showing the fusion zone, fusion boundary denoted by red dashed line; b)M_7C_3 precipitates found within the planar solidification region; c) Darkfield image of $M_{23}C_6$ carbide found within the base metal, inset with selected aperture diffraction pattern. Adapted from [143].

An example of carbide precipitation within the planar zone is given in Figure 2-27b, from research conducted by Kitaguchi [143] on a joint that was retrieved from subsea service. It is important to note that a section from the same ex-service sample is analysed in the present study. The opposing ferritic and austenitic sides shown in Figure 2-27a are easily identifiable, due to the weld metal side having a much greater grain size to the steel (this is also visible in the EBSD images, Figure 2-25). Chromium and molybdenum based $M_{23}C_6$ are visible within the steel side of the interface, and were confined to a lath grained martensitic region. Further into the steel, cementite was found, having preferably formed at the grain boundaries, Figure 2-27b.

In his Thesis, Fenske compared two dissimilar interfaces: F22-Alloy 625 and 8630-Alloy 625, before and after PWHT [14]. He found that after 10 hours of PWHT a dense band of M_7C_3 carbide had formed in the planar zone of the 8630-Alloy 625 joints, however at 15 hours of PWHT, the same carbide was only beginning to nucleate in the F22-Alloy 625.

Carbon migration from the ferritic side into the austenitic weld during heat-treatment results in new phase precipitation [155], martensite formation, and carbon supersaturation [154], [156]. Since the F22 can have up to three times less carbon than the 8630 joint, the result suggest that the higher carbon content is the reason for faster M_7C_3 precipitation. However, in spite of these results, there has been limited further research into determining the relationship between PWHT, microstructure and mechanical properties – the three main themes of this work.

2.4.2 **Mechanical Properties**

In order to compare the fracture toughness in terms of crack tip opening displacement (CTOD) and J-Resistance curves, between samples tested in air and those tested under CP, Milititsky, Gittos et al [157], used single edge notched bend (SENB) testing. A number of 12x12mm sections of a joint between an 8630M and Alloy 625 were notched at the dissimilar interface, through thickness, to a depth of 6mm, using electro-discharge machining (EDM). Complementary specimens were notched to 4.7mm and fatigue pre-cracked a further 1.3mm, to 6mm. The specimens were tested in air at 4°C using the unloading compliance method at the standard test rate [158]–[160], as well as at a low loading rate of 0.018mm/hr.

Further specimens were notched in the same manner as those tested in air, but were subjected to potentiostat driven hydrogen pre-charging at -1100mV_{SCE} in 3.5%NaCl for 48 hours. During testing, an aqueous solution of 3.5%NaCl was recirculated through an environmental cell at -1100mV_{SCE} and a temperature of 4°C, whilst loading was applied at a rate of 0.018mm/hr, to allow for hydrogen diffusion to the crack tip. A representation of these results is given in Figure 2-28

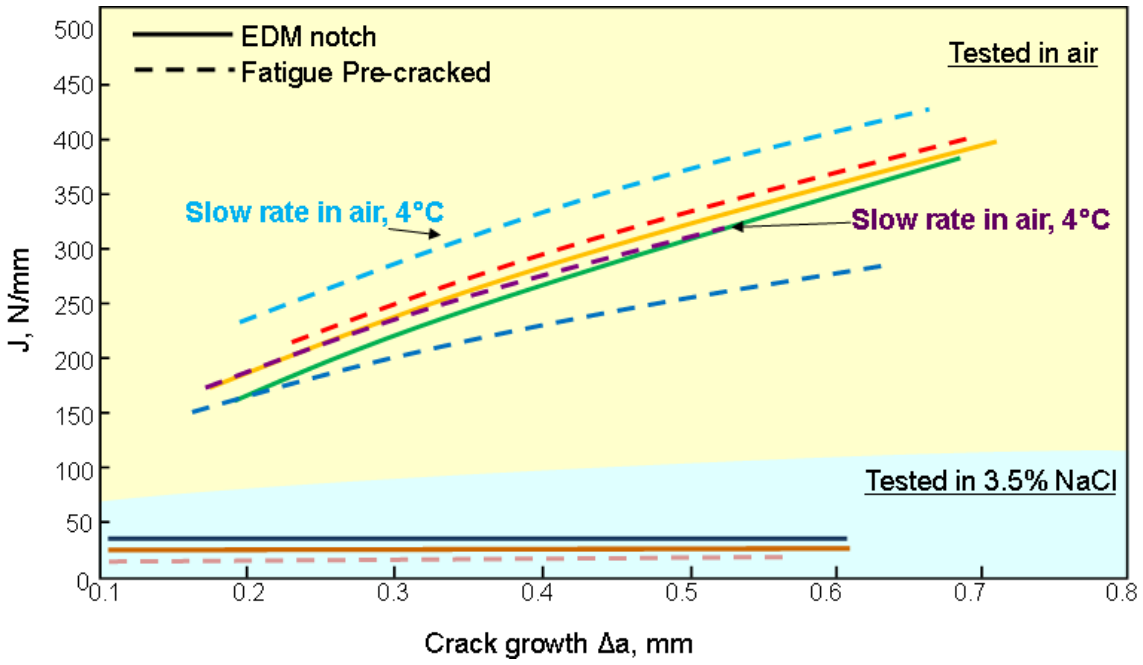

Figure 2-28 –A comparison between unloading compliance J-R curves from 8630M-Alloy 625 specimens tested in air at 4°C and in 3.5%NaCl at 4°C. The diagram shows the difference between notch configurations, and strain rate when testing in air. Samples tested in the NaCl solution were all tested at a slow strain rate. Adapted from [157].

The 'fracture toughness' tests show that the samples tested in a simulated cathodically protected marine environment had far lower J-R curves than those tested in air. The effect of fatigue pre-cracking was also pronounced in the hydrogen charged specimens, which had a lower resistance to cracking than the EDM notched specimens. Although the lowest curve was found in one of the pre-cracked specimens, the effect of notch geometry was less distinct when testing in air.

The two strain rates used for the samples tested in air resulted in comparable J-R curves, suggesting that strain rate itself is not a contributing factor when CP is absent. The result also suggests that significantly lower crack growth resistance when under CP arises due to the presence of hydrogen. However, it should be noted that under CP, slow strain rates are usually associated with lower J-R curves [157].

Different material combinations have also been tested under similar sample preparation and pre-charging conditions. Comparing the alloying content of the base metals,

it is generally accepted that F22-Alloy 625 welds have a higher resistance to cracking (under slow strain rate and CP), than their 8630 counterparts [14].

In a report by Milititsky and Dodge [161] three dissimilar interfaces were tested: 8630, F6NM (a 13%Cr, 4%Ni stainless steel), and F65 (ATM A694, C-Mn steel), all welded with Alloy 625. Accelerated hydrogen crack initiation tests were devised to quantify the resistance to crack initiation. The samples were cathodically polarised in 0.1M H_2SO_4 + 1g/l $Na_2HAs_2O_4$. The sulphuric acid was used to provide a supply of protons, whilst the sodium arsenate was added to promote hydrogen adsorption into the steel by poisoning the recombination of H_2 [83], [162]. The high hardenability 8630M forging was given a PWHT to temper martensite, but as the F65 is far leaner it was not heat-treated after welding. The results of the accelerated hydrogen crack initiation tests showed that whilst no cracking was observed without an applied load, full separation at the dissimilar interface of the F65-Alloy 625 occurred after initial loading to the nominal yield strength of the F65 material. The result suggests that, unlike the notched samples in Figure 2-28, crack initiation and propagation may occur without a pre-existing flaw.

2.4.3 **Fracture**

Mixed mode failures are common in dissimilar welds, due to the varying microstructures that form within a small distance of the dissimilar interface, however it is normally possible to identify a dominant morphology. After heat-treatment, 8630-Alloy 625 specimens subjected to CP, Alexandrov found cracking through the ‘planar solidified zone’, occasionally transitioning to the swirls that are in close proximity to the steel, or through regions adjacent to the planar-cellular transition zone [54]. Failure investigations by Fenske [14] identified similar cracking, referring to failure through the planar zone as ‘terraced cleavage-like’ and failure through discontinuous PMZ swirls as ‘flat’ and ‘featureless’ until

viewed at higher magnification where a ‘bumpy texture’ was observed. Similar observations have been reported separately by Beaugrand and Gittos [152]. These well-known fracture morphologies are consistent with the so-called ‘brittle fracture’ observed in post-mortem examination of failed service specimens [3]. Cleavage-like fracture within the planar zone is intriguing, as the structure of FCC crystals does not accommodate cracking through the crystallographic planes associated with cleavage [163].

Beaugrand, Smith and Gittos investigated the three-point bend specimens under slow strain rate and incremental (dwell) loading conditions, both with and without cathodic protection [150]. In doing so, they discovered that cleavage-like failure did not occur unless CP was present, thus the cleavage-like morphology is attributable to hydrogen ingress. TEM fractography of dissimilar weld fracture surfaces [14], [148], has shown that M_7C_3 can be found subsurface to the cleavage-like surface. The latter point requires further investigation however, in order to establish a link between carbide precipitation and mechanical properties under CP.

A lesser-reported type of failure is ‘interfacial disbonding’; separation at the dissimilar interface itself, as opposed to cracking further into the planar zone or through swirls. This type of cracking was found to be the sole fracture morphology in the accelerated hydrogen cracking tests [161], for the F65-Alloy 625 joint that had no PWHT. It is characterised as an apparently smooth failure, with ridges that correspond to prior austenite grain boundary penetrations, such as those shown in Figure 2-25. Whilst the failure mode has been experienced elsewhere, it is typically accompanied by cleavage-like fracture [151]. It is not yet clear whether interfacial failure is the initiation mode, triggering alternative types of cracking (i.e. cleavage-like) as the stress in the remaining ligament rises during crack extension, or whether the failure is a consequence of the differing microstructure, determined in-part by the lack of PWHT. The contribution of residual stress to the failures is also

unclear, as presumably significant stress relief occurs during sample coupon machining operations, the likes of which is not experienced in full-scale specimens.

As reviewed above, a significant volume of research has been carried out to date on the microstructure and mechanical performance of subsea dissimilar joints. However there is a lack of systematic study to understand the failure of subsea dissimilar joints and how PWHT affects the microstructure and mechanical performance with respect to hydrogen embrittlement. This study aims to:

i. Examine the microstructures present in a typical subsea joint retrieved from service.
ii. To correlate heat treatment with microstructure formation and environmental performance to study how diffusion affects phase change and the susceptibility to hydrogen embrittlement of dissimilar joints.
iii. To characterise the strain relaxation during PWHT and its effect on mechanical performance.
iv. To understand the fracture mechanisms under various heat treatments.

Structure of thesis

In the first Chapter, retrieved specimens act as a benchmark, providing information on the microstructures present in commercially produced joints; a measure by which subsequent laboratory heat-treated specimens may be compared. The material is also used to develop methods for environmental performance specimen preparation and testing (resistance to hydrogen embrittlement). Following Chapters build on these initial observations: thermodynamic modelling is used to assess the extent of carbon diffusion and phase formation under different PWHT conditions, whilst environmental performance testing is used to compare dissimilar joints under varying PWHT conditions. Finally, with knowledge

on the degree of stress relaxation during PWHT, and fracture morphologies from the environmental performance tests, a theory of hydrogen embrittlement is formulated. An illustration of thesis structure and knowledge exchange between Chapters is given in Appendix D.

CHAPTER 3. Characterisation & Performance Testing of Retrieved Subsea Joints

3.1 Introduction

In subsea oil and gas transportation systems, gas tungsten arc (GTA) nickel alloy buttering deposits are commonly deposited on low alloy steel forgings, facilitating in-shop PWHT of the assembly to remove residual stress and temper hard heat-affected zones that form upon cooling, following welding.

During PWHT, carbon migrates from the ferritic steel to the high alloy 'austenitic' weld metal, causing hardening by martensite formation, carbide precipitation and carbon supersaturation [156], [164], [165]. The microstructures within the completed joint have been associated with sensitivity of the dissimilar metal interface to hydrogen-induced cracking. To explore the problem, a number of joints have been retrieved from subsea service, for investigation of the microstructures in greater detail.

An example of a retrieved manifold hub, having been welded to a linepipe, is presented in Figure 3-1a, whilst a detailed view of the dissimilar weld is given in Figure 3-1b. As a consequence of the bevelling procedure, the HAZ of the closure weld lies entirely within the heat treated layers of the initial buttering, thus a narrow (<10mm) band of the buttering is exposed to the outer surface of the joint.

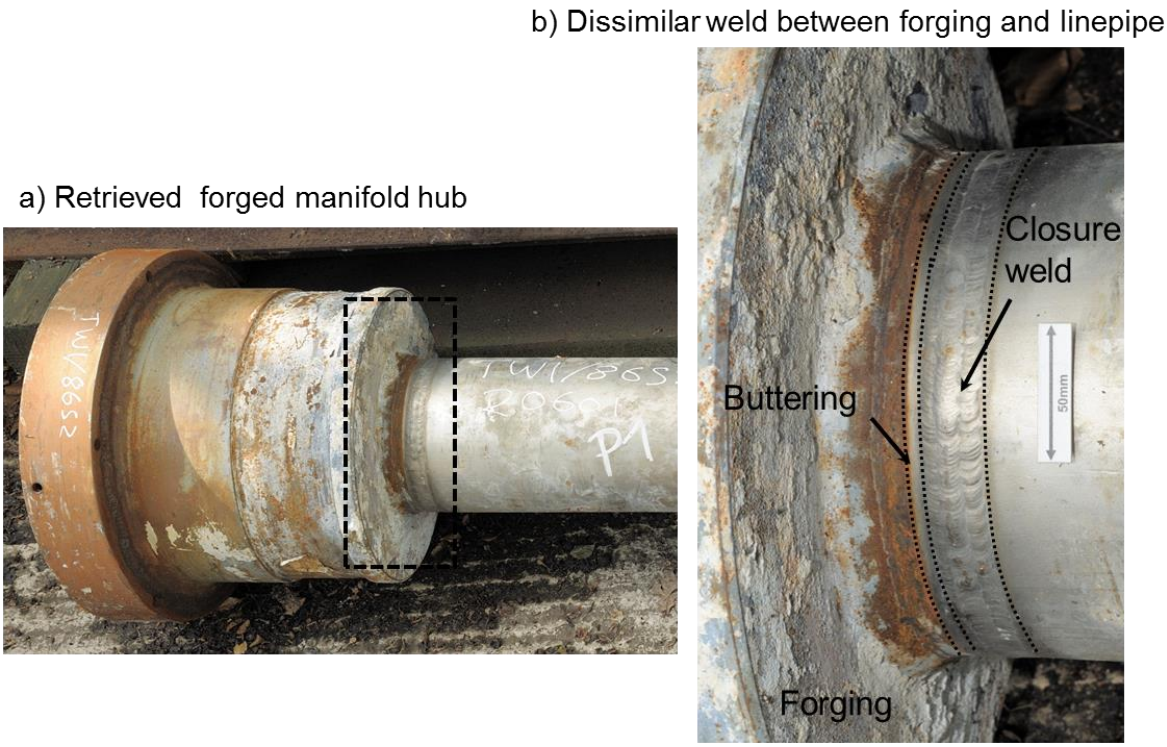

Figure 3-1 – a) A typical commercially produced manifold hub, welded with dissimilar filler metals to a linepipe. b)Detailed view of the dissimilar weld with 50mm scale marker. The forging is composed of 8630 material, whilst the buttering and closure weld are Alloy 625.

A subsurface cross-sectional photomacrograph of the dissimilar joint is presented in *Figure 3-2*. In this instance an internal Alloy 625 cladding, the same material as the buttering and closure weld, is present on the internal face of the forging.

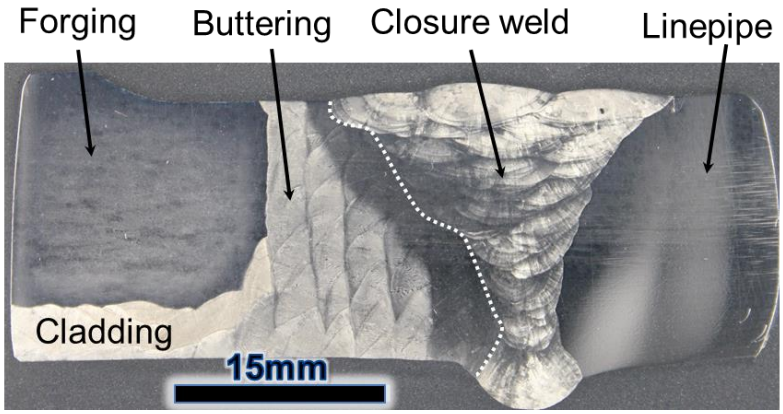

Figure 3-2 – A photomacrograph of a cross-section of the commercially produced 8630-Alloy 625 dissimilar joint, as shown in Figure 3-1. Sample is pictured after a 5%Nital, and electrolytic sulphuric acid etch.

An important consideration to the service-life of these components subsea, is the environmental conditions. Therefore, the joints are subjected to fracture toughness testing: J-R curve generation under the influence of cathodic polarisation, within a simulated marine environment. A testing programme has been developed to represent commissioning and service temperatures of 4 and 80°C, respectively. The developed method will be used in subsequent Chapters in order to rank the resistance to hydrogen embrittlement under different PWHTs in Section 5.3.2. The fractured specimens, from the various types of joint will be compared and analysed in Chapter 7.

3.2 Experimental Procedure

3.2.1 Materials

Four specimens were retrieved from subsea service for comparison of microstructures. All of the forgings were 8630 low alloy steel, buttered with Alloy 625. The specimens were retrieved due to structural integrity concerns, following failures under similar service conditions, however none of the joints were thought to contain flaws.

Specimens 2, 3 and 4 were retrieved from the same field, after approximately 9 months of 'wet-parking'. After retrieval they were subsequently stored outside for a period of several years. Due to coming from the same field, they are assumed to have been fabricated under similar conditions.

Specimen 1 was also retrieved from subsea service, however the exact service history was not provided. Prior to sectioning, the joint had been stored outside for a period up to 9 years. Due to having been retrieved from different fields, it is possible that the welding procedure differed slightly, however all four specimens would have been given an industry standard PWHT of between 5 and 10 hours, between 650-675°C. In Table 2, specimen origin and history is presented, whilst in Table 3 the nominal composition of the forging and weld metal is given.

Table 2 – Origin, history and analysis methods for the retrieved dissimilar joints.

Sample ref.	Combination	Origin and History	Analysis method
Specimen 1	8630 - Alloy 625	Retrieved from subsea service (unknown). Typical PWHT 650-675°C, 5-10 hours	Microstructural characterisation: SEM, TEM
Specimen 2	8630 - Alloy 625	Retrieved from subsea service (9 months). Typical PWHT 650-675°C, 5-10 hours	Microstructural characterisation: SEM, Nanoindentation
Specimen 3	8630 - Alloy 625	Retrieved from subsea service (9 months). Typical PWHT 650-675°C, 5-10 hours	Microstructural characterisation: SEM, Nanoindentation testing. Environmental performance testing
Specimen 4	8630 - Alloy 625	Retrieved from subsea service (9 months), Typical PWHT 650-675°C, 5-10 hours	Microstructural characterisation: SEM, Nanoindentation testing. Environmental performance testing

Table 3 – Specified composition of parent (8630) and weld metal (Alloy 625), wt%.

Material	C	Mn	Ni	Cr	Mo	Si	Nb	Fe
8630 (AISI 8630)	0.28-0.33	0.70-0.90	0.40-0.70	0.40-0.60	0.15-0.25	0.15-0.30	-	Bal.
Alloy 625 (ERNiCrMo-3)	0.01-0.1	0.125-0.5	>58.0	20.0-23.0	8.0-10.0	0.125-0.5	3.15-4.15	5.0 max

3.2.2 **Sample preparation**

Transverse sections for microstructural characterisation were machined from each joint before manually grinding using SiC paper abrasives. Initially the joints were ground using a linisher, ensuring a flat surface, with the cross-sectional bead profiles visible. Manual rotary grinding, using 160, 320, 400 and 1000 grits ensured the progressive removal of material. During each grinding step, the samples were rotated, and scratch marks observed, in order to prevent uneven grinding. Furthermore, after each grinding step, the samples were rinsed with methanol and dried at room temperature. An optical microscope was used after each polishing step, to inspect for flaws, and to ensure that no polishing artefacts (such as debris) remained on the surface.

Cloths were used to polish with fine diamond pastes: 9, 3, 1 and 0.25μm, followed by a diluted suspension of colloidal silica (OP-U), as the final polishing step. Where necessary, samples were etched using a two stage process. Initially the specimens were submerged in a 2% Nital solution (Nitric acid and methanol), before rinsing thoroughly with water. The procedure was repeated until the desired etching level was reached, at which point the sample was rinsed in water and methanol, before being allowed to dry. The samples were left for an hour, allowing the newly etched ferritic parts to develop a protective corrosion layer. As the austenitic side (particularly in the case of Alloy 625), remained relatively unaffected by the Nital etch, electrolytic etching in 5% sulphuric acid was then used.

3.2.3 **TEM sample preparation using Focussed Ion Beam (FIB)**

Focussed ion beam (FIB) based methods are becoming increasingly popular in the preparation and analysis of samples, largely due to their ability to extricate material, for either subsurface examination, or analysis by other means. For example, Lozano-Perez has

described a method by which stress corrosion cracks may be removed for both TEM and atom-probe analysis [166]. Similarly the samples can be analysed in-situ using FIB slicing, in which material is removed layer-by-layer, resulting in a three-dimensional tomographic image [167].

In this study, specimens for transmission electron microscopy were created from the polished sections by adopting the focussed ion beam in-situ thin-foil lift out procedure, variations of which are described in [168]. All TEM samples were created using an FEI Nova 600 nanolab dual beam system. It was not necessary to etch the polished sections prior to insertion in the vacuum chamber, instead a retractable, solid-state, backscatter detector was used, enabling location of specific sites for examination. An Omniprobe micromanipulator, equipped with a tungsten needle, facilitated the placement of ion-milled thin-foils on copper lift-out grids. The general procedure used to extract from a polished section is described in Figure 3-3.

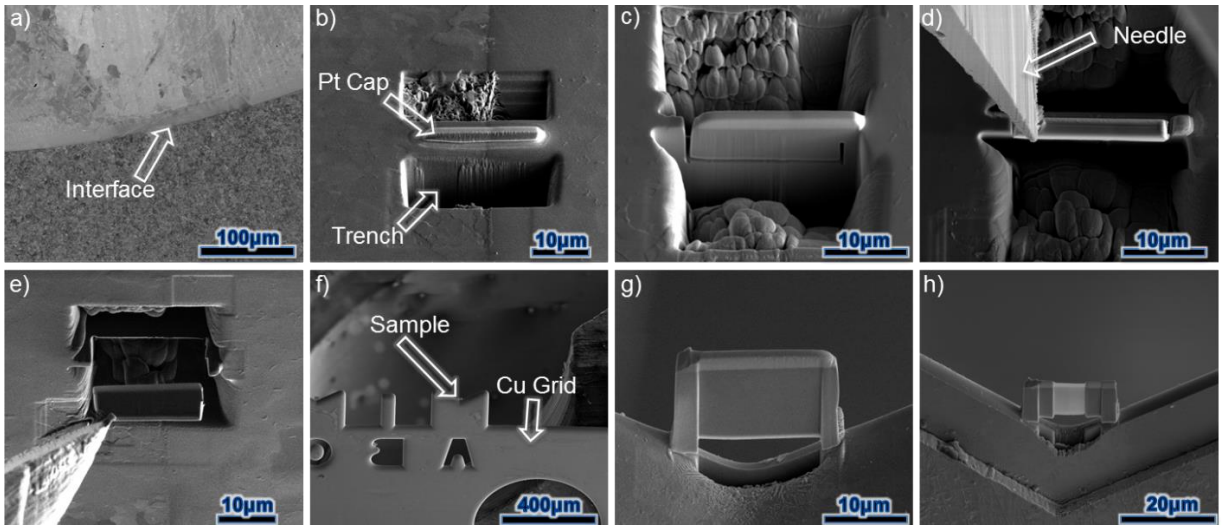

Figure 3-3- TEM sample preparation using the FIB lift-out procedure. a) locating the area of interest; b) deposition of platinum cap and milling of trenches using the ion beam; c) preparing the wafer for extraction; d) attachment of W needle to the sample; e) removal of wafer; f) placement of wafer on Cu grid using Pt deposits; g) thinning of sample h) sample thinned to electron transparency

Initially, the area of interest was located using the backscattered electron detector, Figure 3-3a. In this instance a section across the dissimilar interface of a retrieved 8630-Alloy 625 joint (specimen 1) is shown. Using a gaseous injection system, a platinum 'cap' measuring approximately 20x3x2μm was placed on top of the region to be extracted. The Pt cap served to protect the subsurface material from ion beam damage during subsequent milling operations, Figure 3-3b. After milling trenches either side of the protective Pt cap, the sample was released using a 'J' shaped cut, effectively freeing the sample on three sides, Figure 3-3c. Following this, the tungsten Omniprobe needle was moved into place, the tip of which is indicated in Figure 3-3d. After affixing the W needle to the edge of the wafer using a Pt deposit, the ion beam was used to mill the sample free from the bulk material. Next the sample stage is lowered, bringing the bulk material out of view, in preparation for mounting to a TEM sample grid, Figure 3-3e. Samples were attached to the centre of the 'V' shape attachment points on copper Omniprobe lift out grids using two platinum deposits at the bottom corners of the wafer. Copper was selected for all TEM grids as it is not a constituent element of the materials that underwent compositional analysis. Once the thin-foil was attached, the W needle was milled free, and retracted, Figure 3-3f. In order to reduce sample thickness, the sample was thinned in-situ, using progressively lower ion beam currents, Figure 3-3g. At this point the surface of the thin-foil wafer was placed parallel to the incident ion beam. A 'window' was then selected, for final thinning to electron transparency. In order to thin the sample without incurring surface damage, the stage was tilted and either side of the foil thinned, at angles of <1.5° from the window surface normal.

3.2.4 **Nanoindentation testing**

Due to the fine scale of the various microstructures in the dissimilar weld fusion zone, nanoindentation testing was selected, to measure the variation in hardness across the steel –

buttering interfaces. A Micromaterials Nanotester, equipped with a Berkovich tip, was used at room temperature to determine hardness. Arrays of 10x10 indents, angled acutely across the interface were used, providing a high point-to-point resolution. Measurements extended between 15 and 60μm into the steel and weld metal. Indentations were performed at a maximum load of 1.5mN using loading/unloading rates of 0.05mN/s, with a 10 second dwell at maximum load. Hardness was calculated by Oliver and Pharr analysis [169].

3.2.5 **Environmental Performance Testing**

SENB Sample Preparation

The resistance to hydrogen embrittlement was investigated for retrieved specimens that had been subsea for 9 months, however, joint 2, which was found to contain subsurface cracks, was excluded from experiments. Blank specimens were electro-discharge (ED) machined from the partial joints, creating sections 12.5x12.5x120mm long. The specimens were further ground and polished progressively up to a 5μm finish and 12x12±0.1mm square section. Following this, the blank coupons were etched in 2% Nital in order to reveal the dissimilar interface. All specimens were engraved at the ends, indicating the outer diameter of the forging.

Typically, notching procedures use ED machining with wires that are 0.25mm in diameter. However, 'missing the interface', which occurs due to the undulating welding profile and unrefined notching procedures, can result in high wastage. A limited amount of retrieved material was available for mechanical testing, necessitating a higher yield, high accuracy notching method. As a result, a method of notching with fine gauge (0.15mm) wire was developed, ensuring notch intersection and stress localisation at the dissimilar interface. Essentially, each blank specimen was ground on one end, creating a square datum from which measurements could be made. The specimens were then placed on a knife-edged jig,

mounted on a Mitutoyo shadowgraph. Measurements were made in the y-direction, in order to establish sample thickness, such that a notch could be placed to a depth of 50% sample thickness (6.0mm for a 12.0mm sample), Figure 3-4.

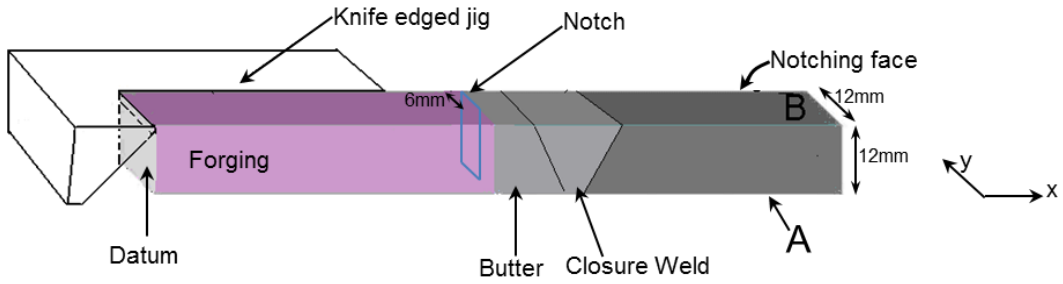

Figure 3-4 - Illustration of SENB specimen notch placement. Side B corresponds to the outermost diameter of the forging.

Measurements in the x-direction, from the datum end to the dissimilar interface, at half sample thickness, were made on two sides (labelled A and B), perpendicular to the notching side. Calculated grinding angles, G, were then applied to the datum end, according to the formula:

$$G = \tan^{-1}\left(\frac{Measured\ difference\ between\ A\ and\ B\ in\ the\ x\ direction}{Sample\ Width}\right)$$

Eqn. 16

After grinding the calculated angle onto each blank specimen, they were placed back on the shadowgraph and inspected to ensure that the measurements from the datum end were the same on both faces (A and B). Before machining the notch, it was necessary to apply a correction factor, taking into consideration the angles imposed on the specimen during machining. The corrected distance, D, is equal to the measured distance from the datum to the interface, I, multiplied by the cosine of the grinding angle, plus half of the ED wire thickness, W:

$$D = I\ \cos G + 0.5W$$

Eqn. 17

Half of the width of the wire diameter is added, as on the ED wire machining apparatus, readings are zeroed at the point where the wire initially begins to touch the surface being notched. The correction factor, D, will be very small for low grinding angles (G <1°), but becomes significant above this. After notching, satisfactory notches were checked by placing back on the shadowgraph and inspecting intersection of the notch with the interface on both sides. Samples with notches which did not intersect the interface, due to machining errors, were discarded. An example of an ED machined notch using fine gauge wire is given in Figure 3-5.

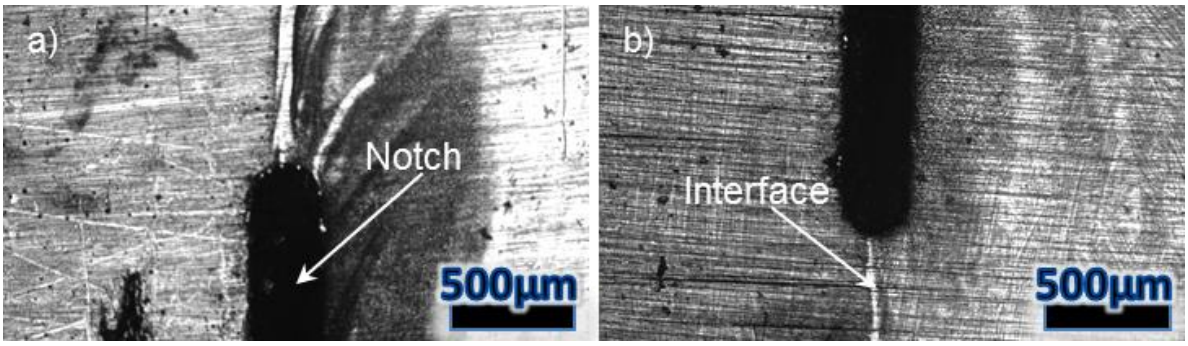

Figure 3-5 – a and b) Optical micrographs of EDM notch placement, using thin gauge wire on opposing sides of a retrieved 8630-Alloy 625 dissimilar joint (specimen 2). The micrographs demonstrate the accuracy of the notching method.

SENB Pre-charging and testing

The notched samples were pre-charged with hydrogen by holding them at -1100mV$_{SCE}$ in 3.5% NaCl solution. The potentiostatic charging was applied to simulate cathodic protection. A testing programme, reflecting subsea commissioning (4°C) and service (80°C), was designed. Two samples were then tested for each of the following conditions:

i. CP pre-charging at 4°C for one week, testing at 80°C

ii. CP pre-charging at 4°C for one week, testing at 4°C

iii. CP pre-charging at 80°C for one week, testing at 80°C

iv. CP pre-charging at 80°C for one week, testing at 4°C

Three-point bending rigs were instrumented for single specimen unloading compliance tests, using a modified version of BS7448 [158]–[160]. A slow strain rate (SSR) loading rate of 0.018mm/h (plastic) was used, with crack tip opening displacement measured by two knife edge clip gauges, located at the notch mouth, Figure 3-6.

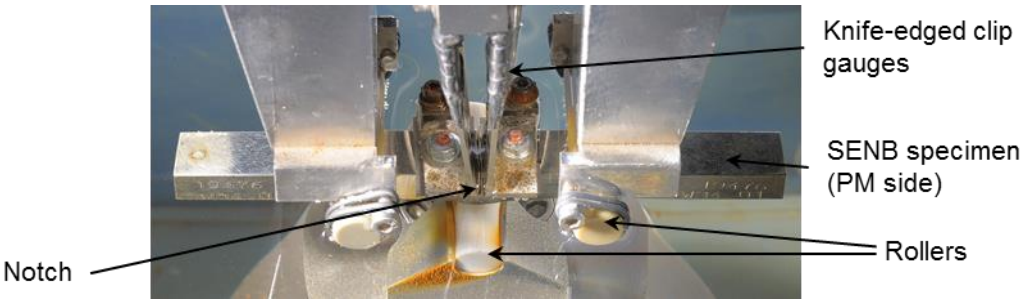

Figure 3-6 - Single edge notched bend specimen instrumented for testing in a simulated marine environment. Sample is approximately 120mm long.

Ten elastic loadings were used as instrument calibration (0.1mm/min), before the test began. To minimise testing time, an unloading rate of 0.05mm/min was selected. After each environmental performance test, a number of test validation checks were performed; essentially the SENB specimens were heat-tinted in a furnace at approximately 300°C, allowing a light oxidation layer to form. Following this, the samples were immersed in liquid nitrogen and broken open.

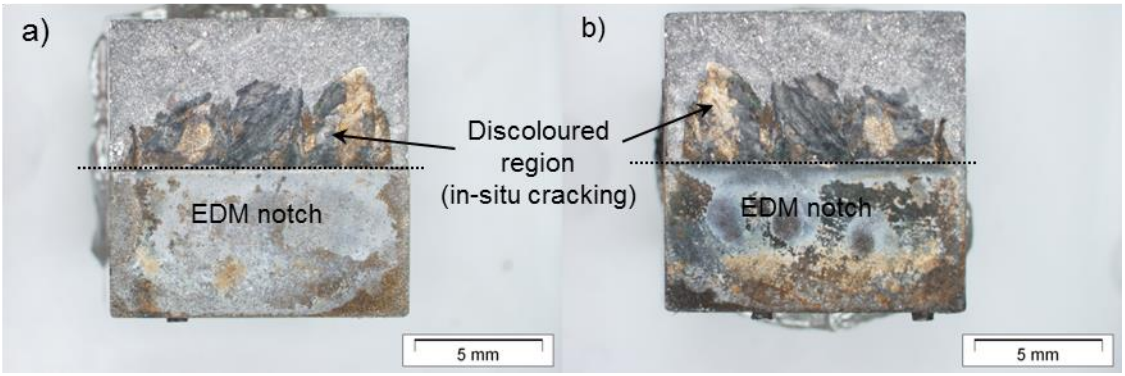

Figure 3-7 – Photographs of a typical SENB fracture surface after 'heat-tinting', submersion in liquid nitrogen, and breaking open. The discoloured region corresponds to cracking during slow strain rate testing in the simulated marine environment. a) the Alloy 625 portion of the specimen and b)the 8630 side.

In accordance with BS7448-4 [160], crack advancement was then measured from the notch-tip to the crack tip (corresponding to the edge of the discoloured region), at 9 points along the specimen width using a light microscope, Figure 3-7. The exception to this is one retrieved specimen, which was sectioned by ED wire machining, such that the crack path was visible in cross-section. In this instance, test qualification checks were measured at 5 points using a light microscope, and the remaining 4 measurement points were line averaged. This is explained in greater detail in Chapter 7.

3.3 Results

3.3.1 Microstructural and Chemistry of the dissimilar joints

SEM Microstructure and Chemistry

The retrieved specimens exhibited interfacial zones consistent with a number of other studies [14], [148], [150], [151]. As mentioned in Section 2.4, these may be broadly divided into two types based on solidification structure morphology: continuous and discontinuous partially mixed zones (PMZs), Figure 3-8a and b, respectively. In the former, the HAZ remains ferritic up to the fusion boundary. The weld metal has then solidified in a planar manner, resulting in an apparently particle-free, 10-20µm wide austenitic band - the planar

zone that has previously been termed the ‘featureless zone’. Further into the weld metal, Nb and Mo based carbides decorate the regions between dendrite arms, probably as a result of the rapid transition to cellular, followed by cellular-dendritic growth.

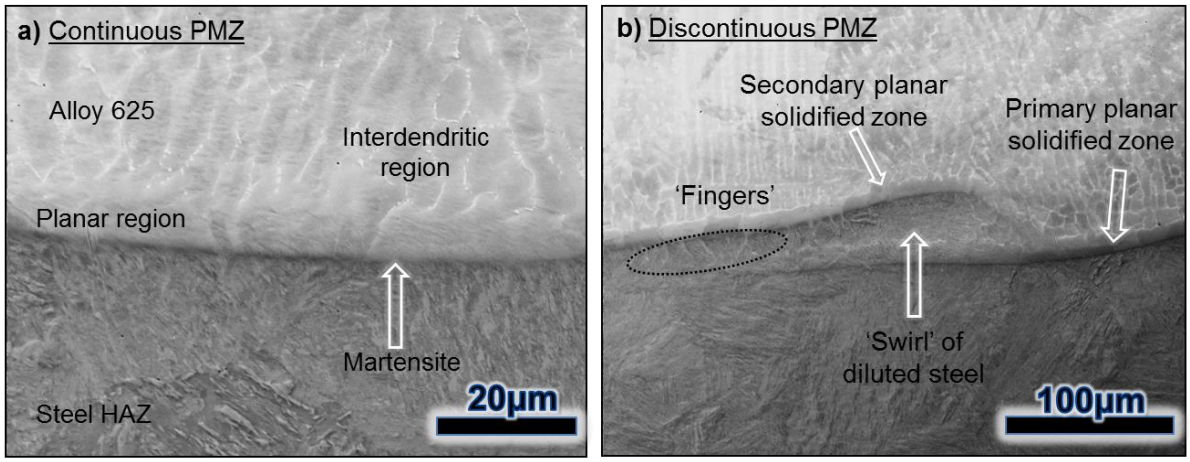

Figure 3-8 - SEM backscatter images of a retrieved 8630-Alloy 625 joint in cross-section. a)a continuous PMZ exhibiting the austenitic planar zone and b) a discontinuous partially mixed zone, showing a ‘swirl’ of steel that has penetrated into the weld metal.

In the discontinuous PMZs, a ‘swirl’ of diluted steel has penetrated the weld metal, resulting in a martensite-rich peninsula, which constitutes a disturbance in the otherwise continuous interface. The weld metal above the swirl has solidified in a planar manner, as has the weld metal beneath it. As a result, a primary and secondary planar region has formed, each solidifying from the steel towards the undiluted weld metal. It can also be observed that ‘fingers’ of weld metal that had penetrated a few microns of the prior austenite grain boundaries (GBs) in the HAZ, during welding. It is important to clarify at this point, that ‘swirls’ are not the only type of discontinuous PMZ that exists at the fusion boundary; beaches and islands may also form depending on the extent of weld pool mixing, as explained in Section 2.1.3. An example of discontinuous PMZs is given in Figure 3-9a, whilst an example of prior austenite GB penetration, at higher magnification is given in Figure 3-9b.

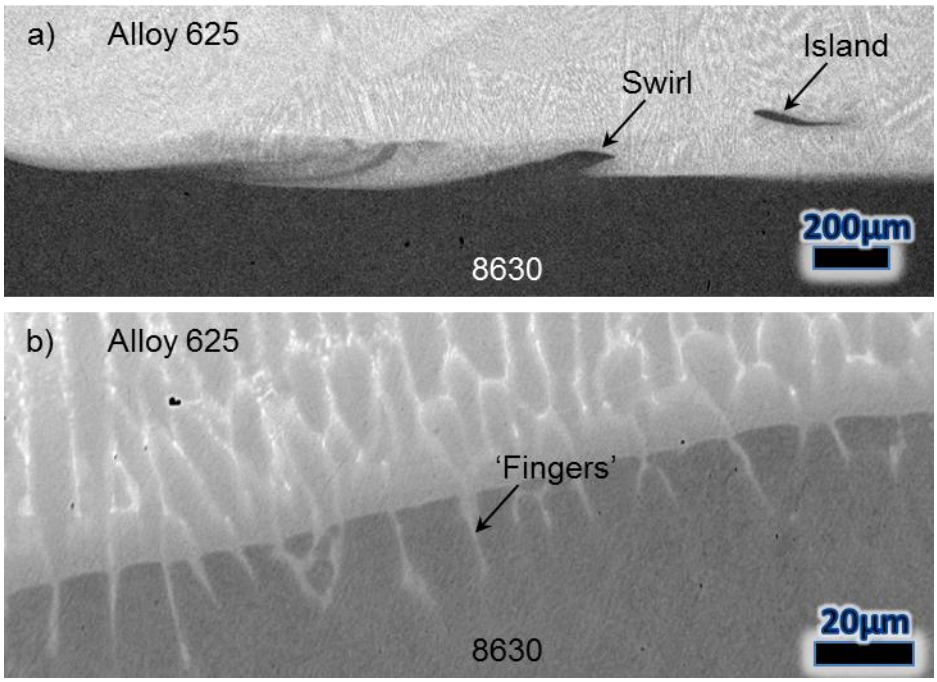

Figure 3-9 - SEM BS images of typical interface regions. a) Discontinuous PMZ manifesting as swirls and islands of parent metal within the austenitic weld (retrieved specimen 3) and b)Prior austenite GB penetration, or 'fingers' of fused weld metal having penetrated the opposing side during welding (retrieved specimen 4).

During metallographic preparation of one of the retrieved specimens (specimen 2), a number of cracks were found, Figure 3-10. The cracks were predominantly confined to the planar zone, rather than to the adjacent, prior austenite GBs or steel HAZ. Moreover, there were several secondary cracks apparently unconnected to the main crack. There was also some crack branching between primary dendrite arms. It is notable that these cracks, which had apparently formed during seabed exposure, were all subsurface.

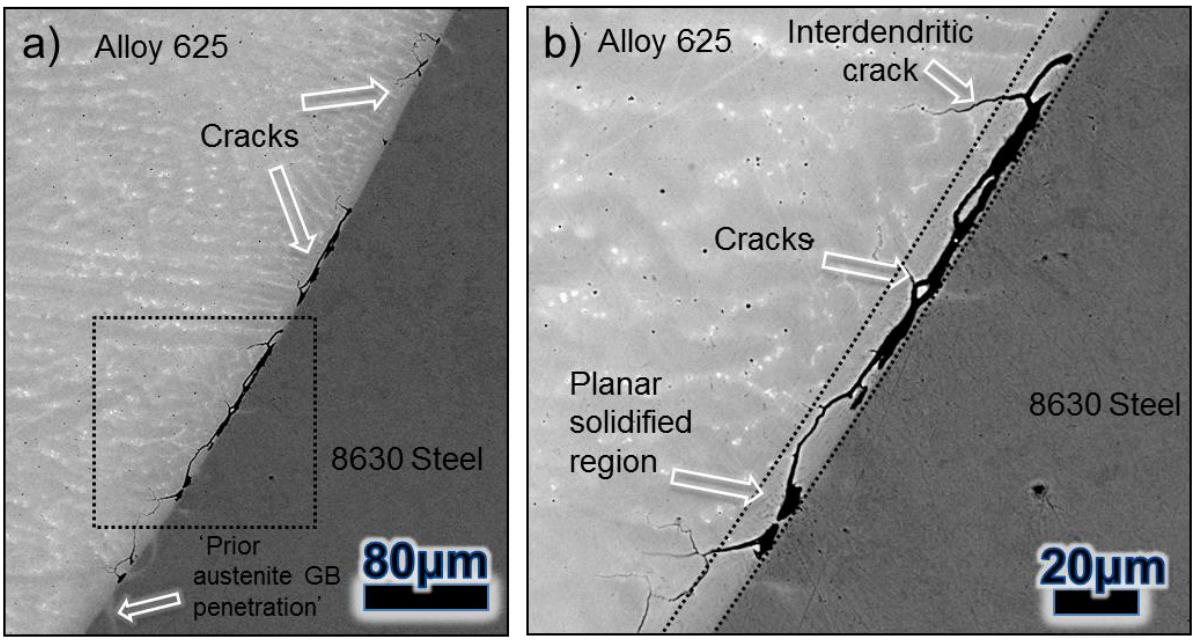

Figure 3-10 – SEM backscatter images of a retrieved 8630-Alloy 625 joint (specimen 2), retrieved from subsea service. a) crack linking within the planar zone and interface and b) a higher magnification image from the region shown in a.

TEM Microstructure and Chemistry

An approximately mid-wall thickness position in a continuous (therefore mid-weld bead position) PMZ from specimen 1 was selected for TEM analysis. Three extractions were made, two across the interface, and one towards the outer edge of the planar zone, Figure 3-11. TEM sample 1 was selected from a region towards the edge of a weld bead, close to a discontinuous PMZ (bead overlap swirl). Sample 3 was selected from a mid-bead position.

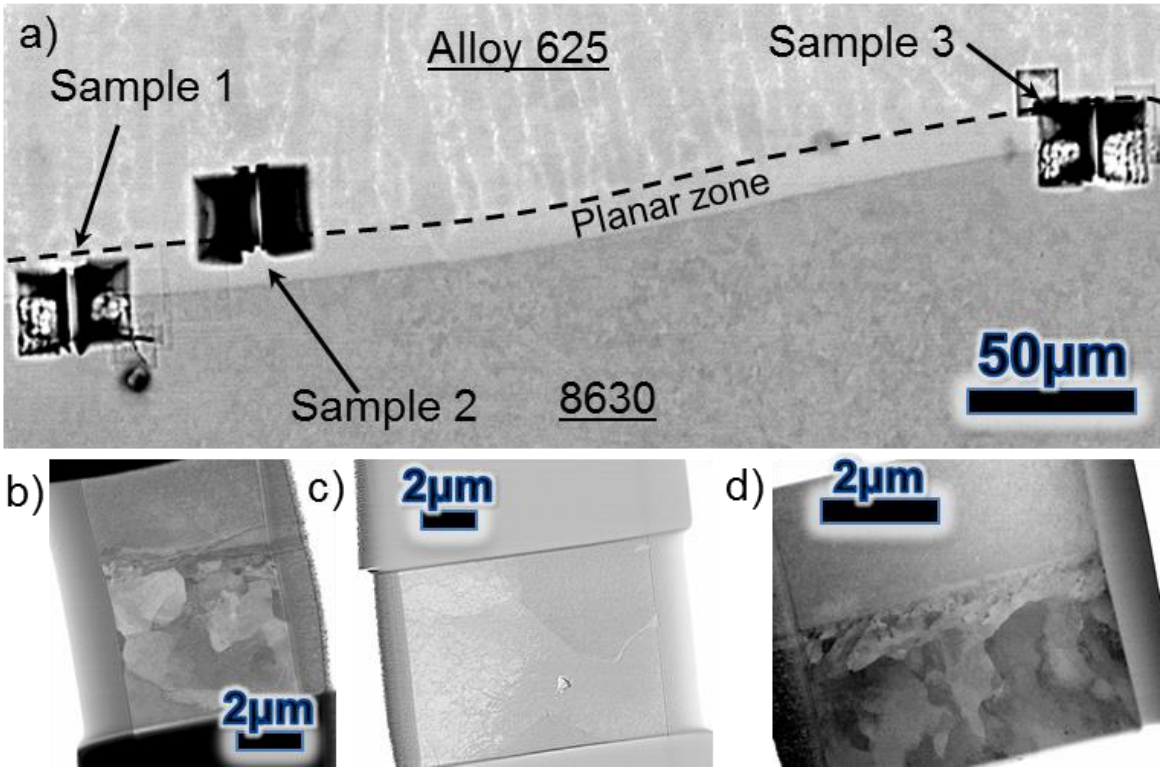

Figure 3-11 – a) Positioning of TEM samples with respect to the dissimilar interface in a retrieved 8630-Alloy 625 joint; b) FEGSEM-STEM images of TEM sample 1; c) TEM sample 2 and d) TEM sample 3.

Along the interface of the first sample, lath-like martensitic grains were seen running vertically through the thin-foil, Figure 3-12a. Immediately adjacent to this was a transition zone, typified as a carbide-free region near to the protective Pt cap. The nickel rich planar zone appeared featureless in the SEM but, at this magnification, nanoprecipitates were visible. It is suggested that they were M_7C_3, having been well-documented as forming within the planar zone of LAS-Alloy 625 weldments, in accordance with [148], [170].

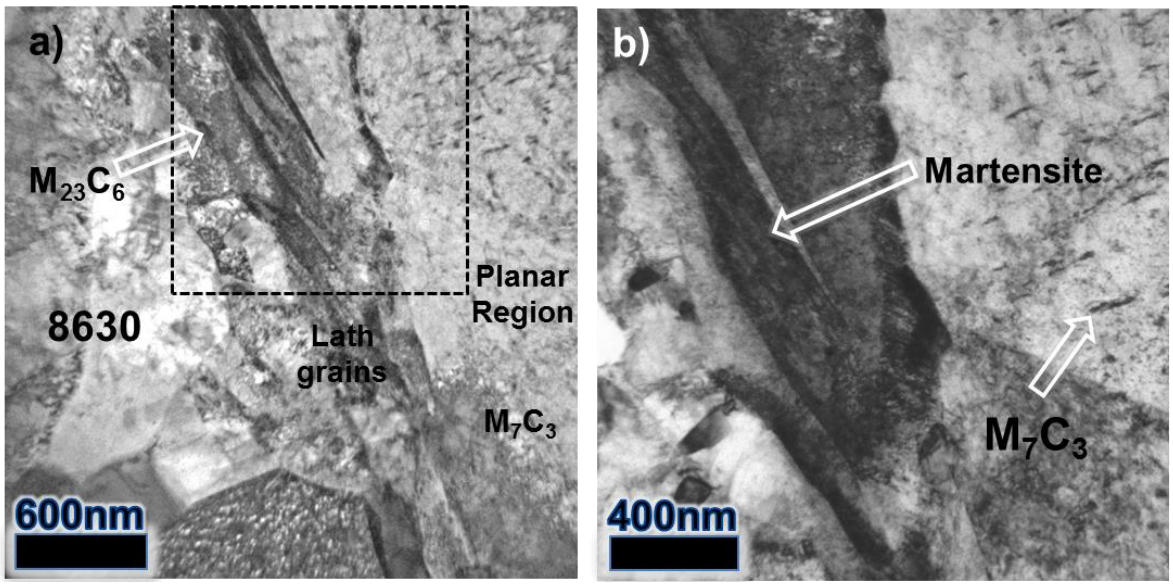

Figure 3-12 - TEM images of retrieved 8630-Alloy 625 joint, sample 1. a) overview of the fusion boundary and start of the planar zone (indicated); b) Tilted, higher magnification image of the region at the top of the TEM foil showing martensite and M_7C_3 growth.

At higher magnification, tilted images Figure 3-12b, revealed the lath structure more clearly, as well as a narrow band of particles, given in Figure 3-14a to be rich in chromium and molybdenum. These particles are principally chromium based $M_{23}C_6$, having previously been identified by diffraction [143]. The dark precipitates, found on the GB obliquely crossing the planar zone are also thought to be carbides, although point electron diffraction did not confirm this. Sample 3, Figure 3-14, further away from the discontinuous PMZ at the bead overlap position, had a considerably narrower lath martensite zone, but displayed a more pronounced carbide-free region in the Alloy 625 next to the interface.

The interface between the austenitic and ferritic sides in TEM sample 3 is seen running diagonally through the micrograph in Figure 3-13a. Within the Alloy 625 planar zone, a carbide-free transition zone, was observed adjacent to the BCC/FCC boundary followed by a band of ordered, intragranular nanoprecipitates, visible as dappled specks within an FCC matrix. The precipitates, shown in Figure 3-13b, had nucleated approximately 500nm from the fusion boundary, and were identified by diffraction and energy dispersive x-

ray spectroscopy (EDX) as being predominantly chromium based M_7C_3 carbide. The small size of the precipitates (20x80nm) explains the previous naming conventions such as 'featureless zone'.

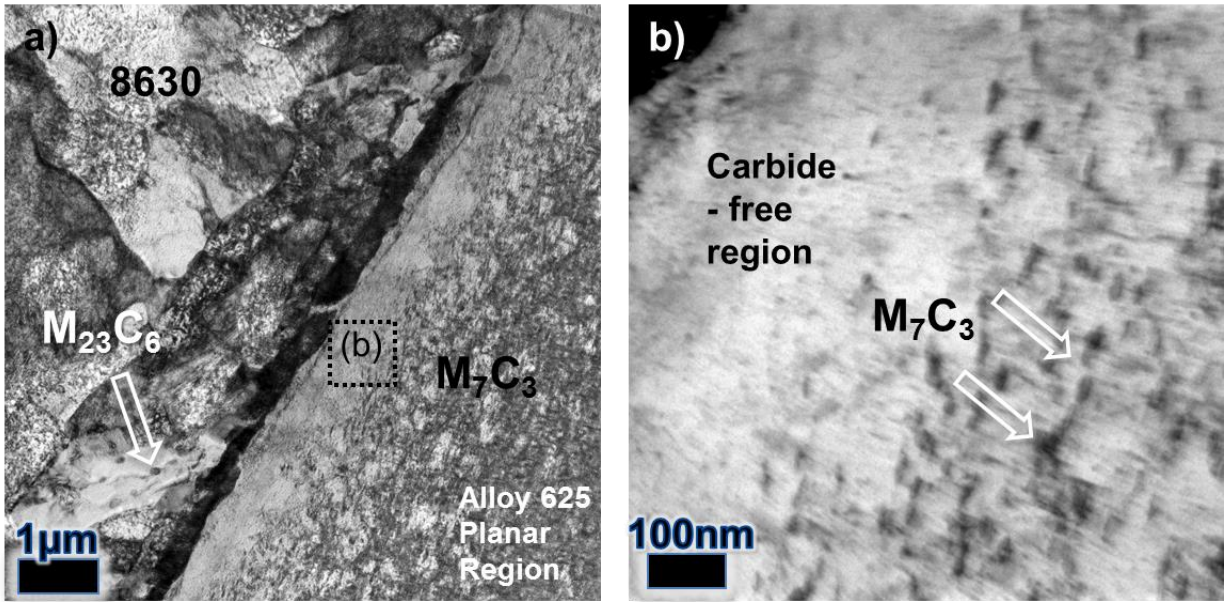

Figure 3-13 - TEM images of retrieved 8630-Alloy 625 joint, specimen 3. a) overview of the fusion boundary within a continuous PMZ; b) Higher magnification image from the region indicated in a, showing M_7C_3 carbide growth bordering a carbide-free region.

A scanning transmission electron microscopy (STEM) image from part of the interface region is presented in Figure 3-14a, together with an EDX chemical distribution map. The intensity maps for iron and nickel indicate significant localised dilution of the austenitic weld metal occurring within the planar zone, corresponding to the carbide-free region. With this in mind, a normalised intensity plot was produced by averaging the element counts in 250nm increments across the apparent dissimilar interface, Figure 3-14b.

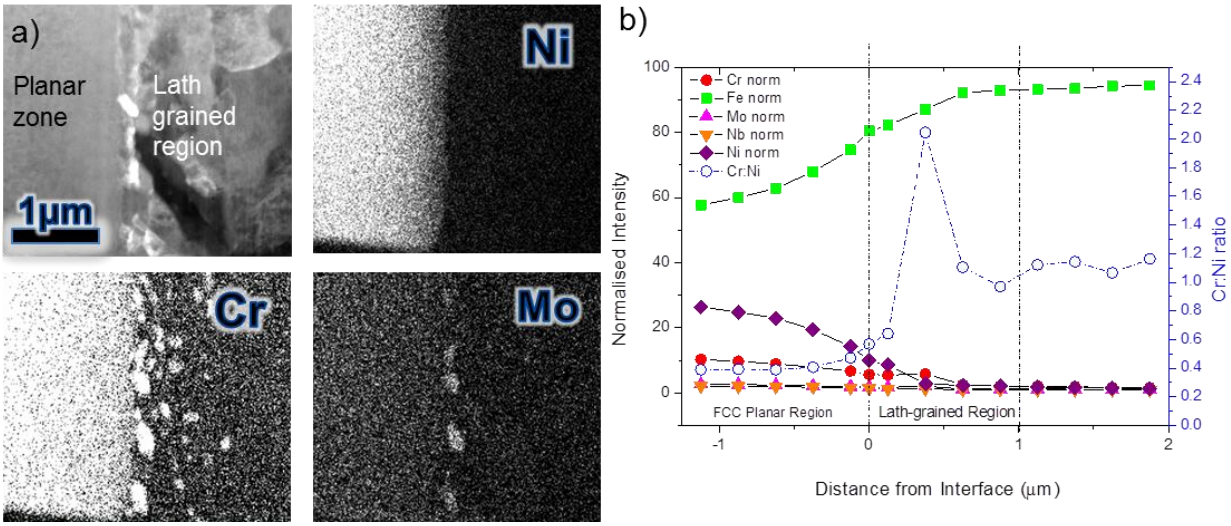

Figure 3-14 - TEM chemical analysis of sample 3. a) STEM image and EDX-mapped chemical distribution across the fusion zone; b) Normalised chemical distribution across the fusion boundary, including the ratio of Cr to Ni.

The results clearly show a steep gradient in composition across the 3µm wide PMZ, however the composition difference, within the first 250nm either side of the FCC/BCC interface, was relatively small. Therefore, the emergence of the carbide-free zone is a result of the rapid chemical changes that occur through planar growth, which in turn, modifies the local carbon solubility, inhibiting carbide precipitation immediately adjacent to the fusion line.

As previously mentioned, the chemical maps reveal a narrow band of chromium and molybdenum-rich $M_{23}C_6$ within the lath-like structure on the BCC side of the FCC/BCC boundary (<1µm from the start of the carbide-free region). At typical PWHT temperatures, chromium is not very mobile and for this reason the carbides seen here are likely to have formed during welding, necessitating TEM analysis of as-welded specimens (Section 5.3). The relative abundance of boundaries within the lath-structured region may afford a fast diffusion pathway for chromium to travel from the parent side. However, as chromium is seen at the fusion boundary, it may have diffused to the region from the austenitic side, as it has a tendency to partition to ferrite.

The loss of chromium, either by diffusion to neighbouring regions, or through in-situ carbide precipitation, could elevate the martensite start temperature (Ms) in those regions. Considering the chemical distribution and morphology, the lath-structured region is consistent with tempered lath martensite. Virgin martensite, found in sample 1, is consistent with the extraction area, which is adjacent to a discontinuous PMZ where iron rich swirls, within the weld metal, may undergo reaustenitisation during PWHT.

The size of the planar zone is determined by weld pool fluid flow, which is in turn determined by the welding procedure. The size of the planar zone can be defined as the distance between the BCC/FCC fusion boundary and the breakdown of stability of the planar front, where higher atomic number particles are found. An example of this is the niobium based precipitate found in sample 2, (most-likely niobium carbide) from the TEM wafer that bridged the planar zone/cellular region.

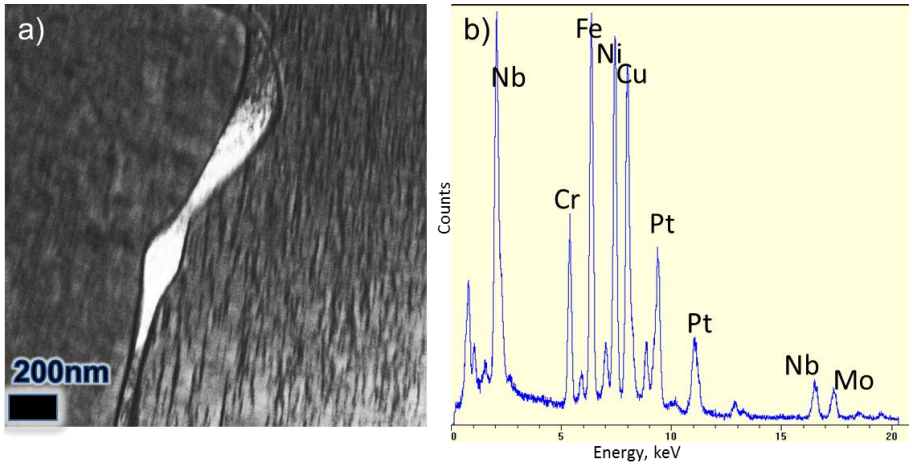

Figure 3-15 – a) TEM image of the retrieved 8630-Alloy 625 joint showing interdendritic niobium carbide adjacent to the planar zone and b) EDX spectrum from frame in a. Note that Cu is present due to the composition of the TEM grid.

3.3.2 **Nanoindentation testing**

In an attempt to overcome indent spacing limitations, nanoindentation arrays were set at a shallow angle to the fusion line. In doing so, an effective spacing of 0.5µm perpendicular to

the interface was created without interference from the plastic zone of neighbouring tests. A field emission gun (FEG) SEM was used to measure the perpendicular (±1°) distance from the centre of each indent to the fusion line. An example of an indentation array, overlaid with hardness values (GPa) is given in Figure 3-16.

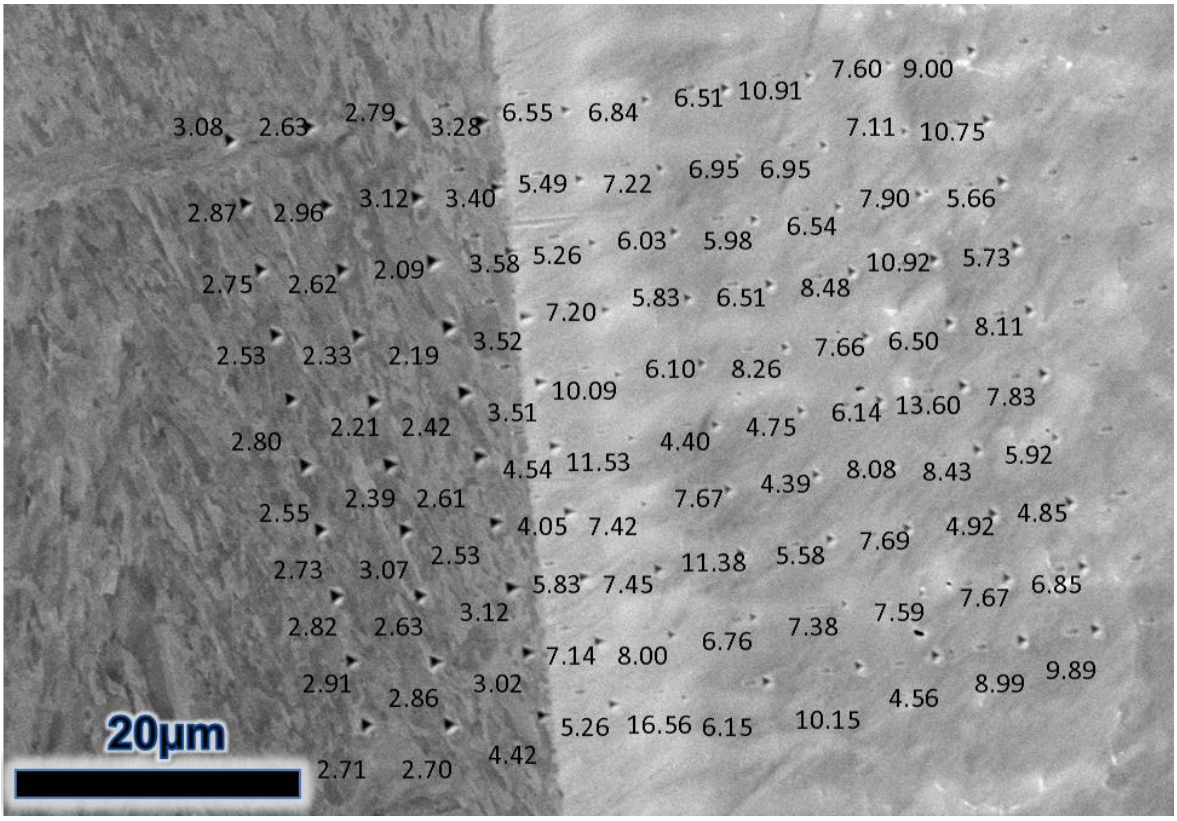

Figure 3-16 – SEM image of nanoindentation array on a retrieved 8630-Alloy 625 joint (Joint 4, array B), overlaid with hardness values (GPa).

The perpendicular measurements allowed hardness profile results to be plotted as a function of distance from the apparent fusion line. Each array was also accompanied by an SEM EDX linescan from the interface towards the bulk weld metal, between the middle columns of indents, in order to assess the extent of weld metal dilution.

Hardness profiles for retrieved joints 2, 3 and 4 are given in Figure 3-17 and Figure 3-18. The highest hardness values are given furthest from the interface, and are associated

with interdendritic regions. Discounting these regions, in general high hardness was observed immediately adjacent to the interface in both the ferritic and austenitic sides.

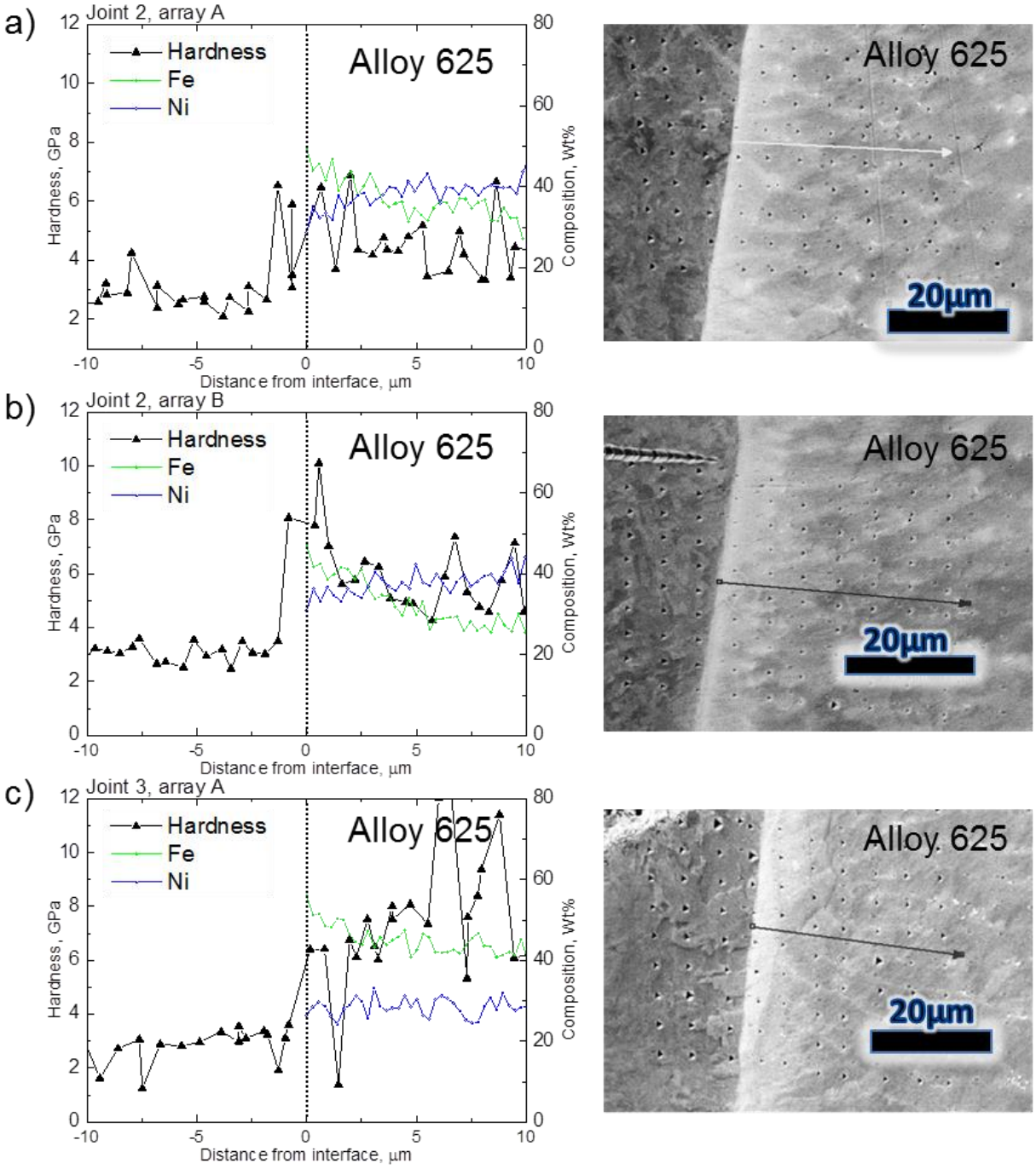

Figure 3-17 – Nanoindentation arrays with accompanying chemical analysis across the dissimilar interface in retrieved 8630-Alloy 625 joints. a) Joint 2, array A; b) Joint 2 array B; c) Joint 3, array A (discontinuous PMZ) beach.

The EDX traces showed an apparent difference in the chemical gradients at the interfaces of joints 2 and 4, despite the fact that the bulk dilution of the beads seemed to be levelling out at a similar composition (further away than depicted in the figures). The EDX chemical distribution for joint 3, Figure 3-17c, showed a highly different chemical gradient to the other joints. Considering its morphology, the placement of the indentation array is consistent with a filler deficient beach (lighter region). The result of this is a more gradual reduction in iron content (and increase in nickel content) with distance. The data for this array also contains a high amount of scatter, due to diverse microstructures that occur within a smaller distance to the resolution achieved by the indent spacing.

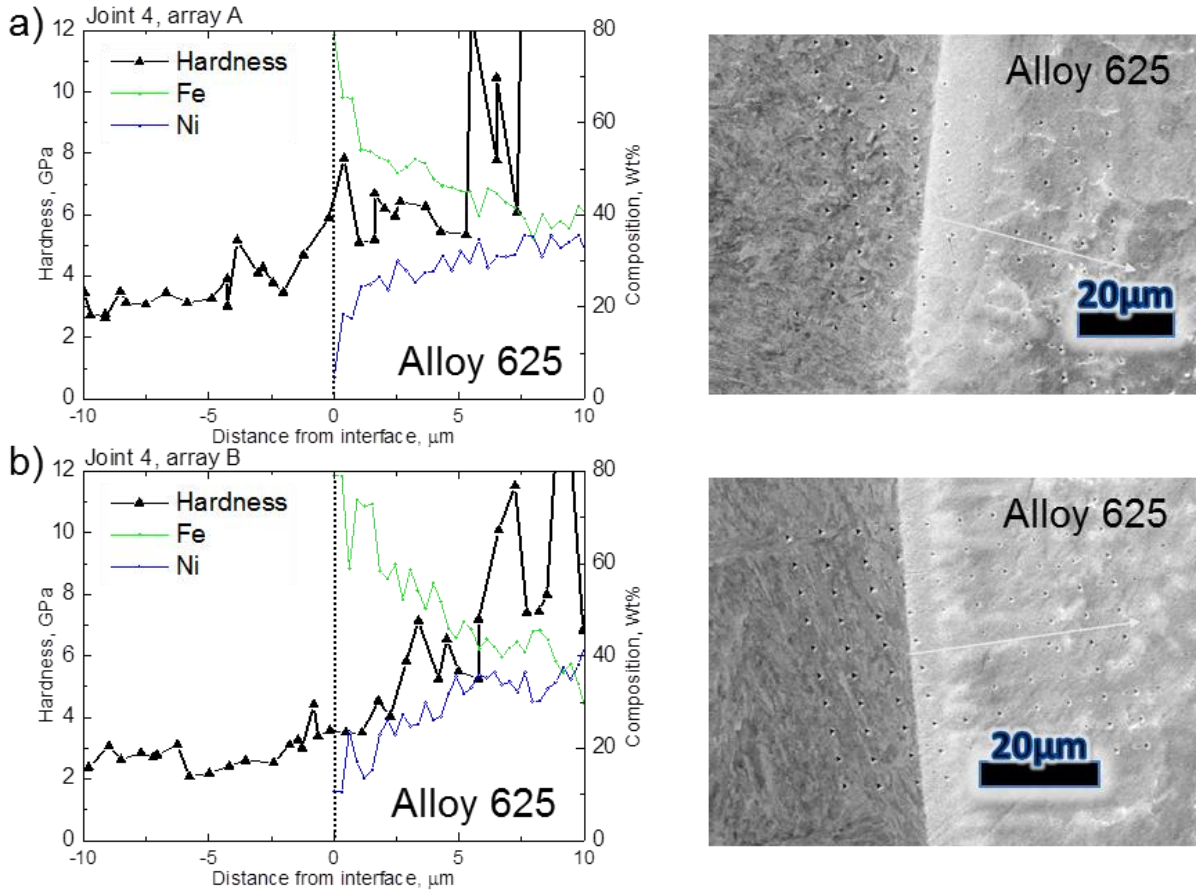

Figure 3-18 – Nanoindentation arrays with accompanying chemical analysis across the dissimilar interface in retrieved 8630-Alloy 625 joints. a) Joint 4, array A and b) Joint 4 array B.

3.3.3 **Environmental Performance Testing**

The results of the slow strain rate testing at 4 and 80°C show considerably more resistance to crack growth, when testing at the higher of the two temperatures, Figure 3-19. However there was no clear difference between the pre-charging temperatures.

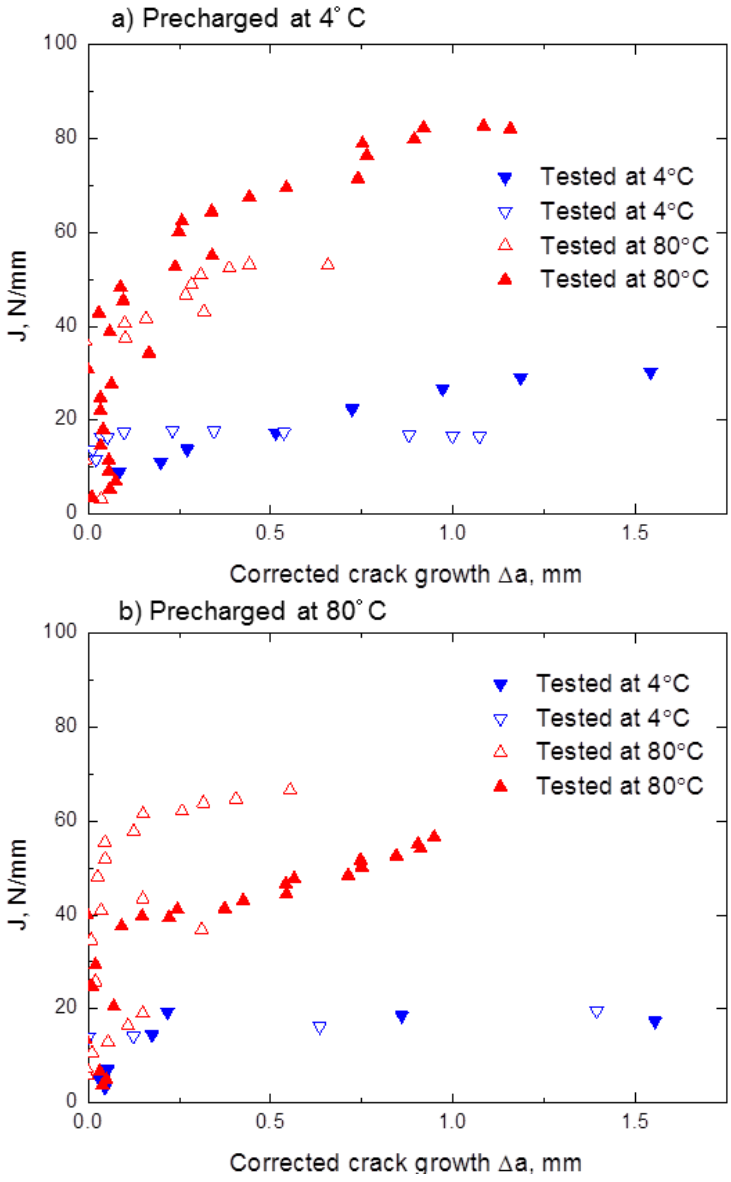

Figure 3-19 - Single specimen unloading compliance J-R curves for retrieved 8630-Alloy 625 joints, having been pre-charged (one week) at a) 4°C and b) 80°C. Tests were performed in a simulated marine environment at 4 and 80°C (3.5% NaCl solution, -1100mV$_{SCE}$ via potentiostat).

An important response is that of the simulated 'shut-down' condition, whereby the system may have been producing petrochemicals for some time, before standing at the lower

temperature of 4°C. The limited test results presented here indicate that this condition is at no greater risk of cracking, despite the fact that, in theory, more hydrogen should be able to accumulate at the interface due to the faster diffusion rates associated with the higher temperature charging condition.

3.4 Discussion

The resistance to hydrogen embrittlement has been demonstrated to increase dramatically with temperature, independent of hydrogen pre-charging conditions. These J-R curve results are consistent with observations that hydrogen lowers the fracture toughness (Section 2.3), but is temperature dependent.

Interestingly, the joint that exhibited the highest fusion boundary hardness was also found to have a number of subsurface cracks. These cracks were found within the planar zone, having propagated incrementally, rather than in a single large event, with some evidence of crack linking ahead of the primary crack front. These observations dispute the fast 'brittle' fracture described in post-mortem examination of other retrieved ferritic-austenitic subsea joints [3] and warrants further investigation. Recent publications on the subject endorse this view, supporting theories of a localised plasticity process, accelerated in the presence of hydrogen [148], [149], [170] (HELP), or a combination of HELP with decohesion (HEDE) at carbide-matrix interfaces within the planar zone [141], [142].

3.5 Chapter Summary

The planar zone in the 8630-Alloy 625 buttering interfaces retrieved from subsea service, and having presumably been given an industry standard PWHT, are decorated by fine M_7C_3 precipitates. The formation of these is attributable to carbon diffusion during PWHT, and will be explored in the following Chapters.

Hardness peaks at the interface between the forging and weld metal arise from either martensite or carbide particles, or a combination of both. The fine scale of these features warrant examination at higher magnifications, if possible, under different PWHT conditions, to establish a correlation between microstructure and mechanical properties.

Using partial sections from retrieved joints, sample preparation and testing methods have been established. These techniques are based on established procedures [158]–[160], albeit modified to suit dissimilar joints tested under the influence of hydrogen charging. These methods will be used to characterise the resistance to CP-induced cracking in future sections.

Based on this Chapter, and reviewed literature (Section 2.4), a summary of LAS to Alloy 625 weld interface microstructures can be made, these are illustrated in Figure 3-20, and are described as follows:

i. The body centred cubic ferritic microstructure of the parent low alloy steel forging containing carbides and inclusions.
ii. A mainly ferritic, decarburised, grain-coarsened heat-affected zone (GCHAZ), immediately adjacent to the interface, with fingers of fused weld metal that have penetrated into prior austenite grain boundaries.
iii. A martensitic region at bead overlap positions (where ‘swirls’ normally occur) that extends into the PMZ, labelled as a ‘discontinuous PMZ in Figure 3-20.
iv. A thin band of martensite at the fusion boundary between the dissimilar metals.
v. An austenitic, apparently particle-free region (at low magnifications), that has solidified in a planar manner, into which carbon may diffuse during PWHT – the ‘planar zone’.
vi. An austenitic region further into the PMZ containing higher atomic number interdendritic particles.

vii. The bulk weld metal away from the fusion zone that is FCC and presents a less diluted chemistry.

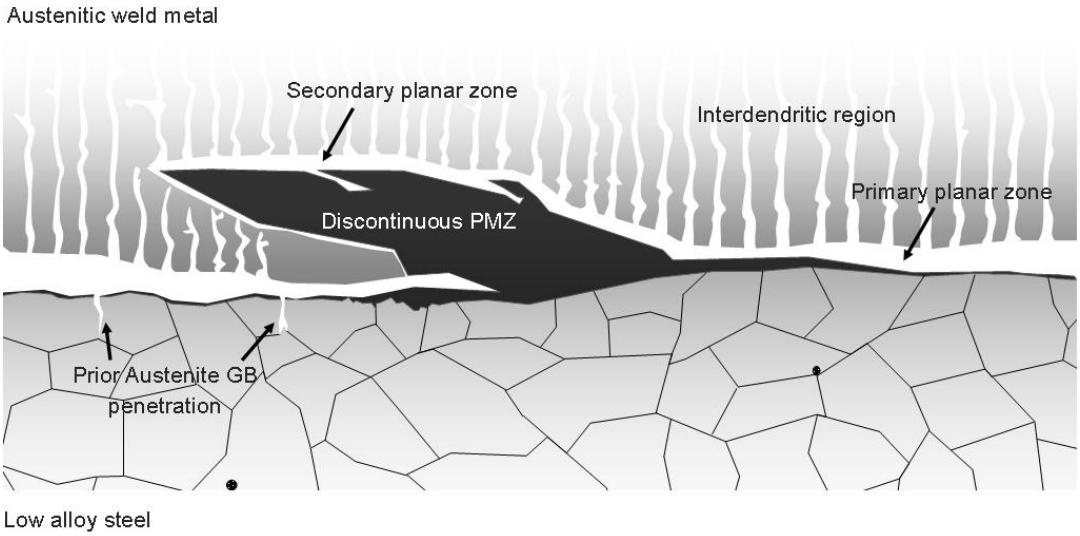

Figure 3-20 - Illustration of typical microstructures at the fusion boundary of a typical austentic-ferritic dissimilar joint.

CHAPTER 4. Modelling of Chemistry and Phase Change in Dissimilar Joints during PWHT

4.1 Introduction

In the previous Chapter, a summary of the microstructures that are present in a typical joint, retrieved from service in a marine environment, was presented. Assessment of the microstructure is useful, not just in comparing specimens fabricated for investigation of mechanical performance under varying PWHT, but in the modelling of the fusion zone. In this Section, microstructural models are formulated based on the observations made in the previous Chapter. The microstructural models compare the material combination used for the retrieved joints, 8630-Alloy 625, with two further dissimilar weld combinations. In doing so, the forging and weld metal compositions, and their effect on fusion zone morphology, can be compared.

To begin with, the three dissimilar joints are evaluated, using laboratory fabricated specimens. Elemental characterisation (SEM EDX) is used to assess dilution of the weld metal in the as-welded condition and again, after heat treatment. EBSD is then used to characterise typical interface microstructures in greater detail. Together, the results highlight the limitations of the thermodynamic and thermo-kinetic simulations, modelled in Thermo-Calc and Dictra, respectively. The results of the diffusion simulations aid in determining the heat treatments that result in excessive decarburisation of the HAZ, followed by carbon enrichment and new phase precipitation in the planar zone.

4.2 Experimental Procedure

4.2.1 Materials

The three dissimilar weld specimens (F22-Alloy 625, F22-309LSi and 8630-Alloy 625) were provided in the as-welded condition. The exact welding procedures, and therefore details of the heat-inputs, are given in appendix A. The selection of the LAS-Alloy 625 joints is based on their current usage as manifold-based hub forgings. Whilst the F22-309LSi joint is not a proposed solution to the problem of in-service hydrogen cracking, it is included, for comparison of the metallurgical aspects that relate to failure. The nominal compositions of the parent and weld metals is given in Table 4. The 8630 and F22 forgings were heat treated for 10 hours at 675±5°C and 665±5°C, respectively.

Table 4 – Specified nominal compositions (wt%) of the components of the three dissimilar weld combinations

	Parent metals		Weld metals	
	8630 (AISI 8630)	F22 (ASTM A-182)	309 (ER309LSi)	Alloy 625 (ERNiCrMo-3)
C	0.28-0.33	0.08-0.15	max 0.03	0.01-0.1
Mn	0.70-0.90	0.30-0.60	1-2.5	0.125-0.5
Ni	0.40-0.70	0.5 max	12-14	>58.0
Cr	0.40-0.60	2.0-2.50	23-25	20.0-23.0
Mo	0.15-0.25	0.90-1.10	max 0.75	8.0-10.0
Si	0.15-0.30	0.15-0.50	0.65-1.0	0.125-0.5
Nb	-	-	-	3.15-4.15
Fe	Bal.	Bal.	Bal.	5.0 max

4.2.2 Microstructural analysis

After electro-discharge machining, all metallographic specimens were manually ground using 80 to 1000 SiC papers, as described in the previous Chapter, Section 3.2. Cloths were used for polishing, together with 3, 1 and 0.25μm diamond suspensions. Final finishing included polishing using colloidal silica (OP-U).

The fusion zone microstructure, of all joints, was examined using an FEI Sirion SEM. Both backscatter (BS) and secondary electron (SE) modes were used. As hydrogen-assisted failure, within planar solidified zones, is commonly associated with the Steel-Alloy 625 joints, these joint types were also subjected to EBSD analysis, using a HKL Nordlys EBSD detector. Quantitative EDX analysis was performed, using a Princeton Gamma Tech detector. All SEM studies were performed using a 20kV accelerating voltage. All EDX linescans had a 0.5µm point resolution.

4.2.3 **Thermodynamic Simulations**

Thermodynamic simulations for the three dissimilar welds were conducted using the **cal**culation of **pha**se **d**iagrams approach, or 'Calphad'. Calphad has become a widely recognised tool in the development of new materials and processes, since its first inception in the 1970s by Kaufman and Bernstein [171]. Calphad is based on the law that states that a system with a given composition, temperature and pressure attains that state of lowest Gibbs energy, under these conditions [172]. Provided that the Gibbs energy is known for the individual phases, the overall equilibrium state may then be calculated using an energy minimisation procedure. In particular, the Thermo-Calc^{TM} software was used. Thermo-Calc is a powerful tool, allowing for the calculation of, for example, phase diagrams (binary, ternary and multi-component), transformation temperatures and solidification using the Scheil-Gulliver model [173][174].

Weld metal dilution (as explained in Section 2.1.5) was calculated using the medians of the specified composition ranges of each joint, in 10% increments. For enhanced detail at the extreme ends of the dilution range, dilutions between 0 to 10% and 90 to 100%, calculations were made in 2% increments. Thermodynamic simulations were then conducted for each calculated dilution point, using Thermo-Calc^{TM}. The fusion zone microstructure, in

a dissimilar 8630-Alloy 625 joint, has previously been evaluated by Alexandrov et al, using similar methods [54], albeit with different thermodynamic databases. In this work, the updated TCS Steels/Fe-Alloys Database Version 6.2 (TCFE6) [175] was used, in simulations above 50wt% iron. Simulations with 50wt% nickel or higher were conducted, using the Thermotech Ni-DATA database, version 7 (NIDAT7) [176]. Lowering the principal database component to near 50wt% carries increasing inaccuracy, due to the databases being evaluated with substantially lower alloying content. The lower accuracy simulations are therefore indicated.

The Scheil-Gulliver (S-G) solidification module, within the software package, was used to calculate the solidification mode. Solidification range was determined within the Scheil-Gulliver module, assuming equilibrium conditions at the solid-liquid interface. Under S-G solidification, the solid-liquid (S-L) interface is in equilibrium, such that no diffusion occurs within the solid. It also assumes complete mixing within the liquid phase. In order to calculate phase equilibria for the F22 and 8630 parent metals, liquid, BCC, FCC, $M_{23}C_6$, M_7C_3, M_6C, M_5C_2 and M_3C_2 phases were added. The temperature was lowered from 2000 to 400°C and calculations made at 1°C intervals, until the solid fraction reached 0.99.

4.2.4 **Diffusion simulations**

Non-equilibrium, **Di**ffusion **c**ontrolled **tra**nsformations during PWHT were calculated using Dictra™[173]. Dictra is a programmable software package for the calculation of diffusion and phase transformation in multicomponent alloys. It is particularly useful in assessing microstructural stability between two metals at elevated temperatures. An example of this was published by Anand et al [177], who used Dictra to successfully predict microstructure formation during high temperature exposure of dissimilar ferritic steel weldments. The authors found that the formation of hard and soft zones was attributable to

carbon diffusion towards the higher chromium metal, and their models showed a strong correlation with experimental observations.

The software combines the thermodynamic data used within Thermo-calc, with a kinetic 'mobility' database – a database that contains information about the atomic mobility of individual components in relevant phases [178]. The accuracy of Dictra is highly dependent on database accuracy, however choice of geometry is also an important factor [179]. In this work, a 'sharp' dissimilar interface method was selected, which is analogous to two materials placed side-by-side, with no prior mixing.

The modelling of dissimilar welds, especially where two major constituent phases are present, necessitates the use of a homogenisation function – a means of averaging kinetic properties.

To make the correct choice of homogenisation function, prior knowledge of the microstructure and phase constitution is required [180]. As a result, diffusion modelling was conducted with prior knowledge of the microstructure [143], [148], together with knowledge of phase equilibrium from Thermo-calc computations. The Hashin-Shtrikman (H-S) bounds were deemed most appropriate for the diffusion models. Geometrically, the H-S bounds can be considered as groups of concentric spherical shells of phases.

A variety of bounds exist within the set of H-S homogenisation functions. These arise from modifications to the geometrical properties, and consist of:

i. The H-S bound with predefined matrix phase. In some systems there is a continuous matrix phase (for example in a diffusion couple between two ferritic steels). It is therefore appropriate to use this bound, setting the matrix phase as the 'α-phase'.
ii. The majority phase as the matrix phase, in which the phase with the highest local volume fraction becomes the local 'α-phase'.

iii. The upper and lower bound with excluded phases. These bounds may be used when a few phases make up majority of the volume, with a small volume fraction of dispersed phases distributed within. Where necessary, the dispersed phases may be excluded from the simulation.

Despite the added computational complexity compared to the other options, the H-S function with the locally highest phase as the matrix (majority) phase was deemed most appropriate. This is because a continuous phase is not present throughout the whole dissimilar joint (bound i), nor was enough phase fraction information available to implement bound iii.

To assess phase equilibria, the TCFE6 database was used, whilst mobility (thermo-kinetic) data was assessed using the mobility database V.2 (MOB2) [181]. Simulations were carried out at an assumed temperature of 665°C for up to 100 hours. The FCC, BCC, $M_{23}C_6$ and M_7C_3 phases were added to the simulation of the F22 and 8630-Alloy 625 joints, in line with the observed fusion zone phases.

4.3 Results

4.3.1 Experimental Results of Microstructure and Chemistry

The microstructures observed in the three dissimilar joints were consistent with the cross-section illustrated schematically in Figure 3-20, Section 3.5. The joints had varying amounts of discontinuous PMZ, due to welding procedure and compositional differences. To aid comparison, only continuous PMZ were selected for analysis. SEM BS electron images, together with EDX linescans, across the three fusion boundaries, are presented in Figure 4-1, in the as-welded condition. Values corresponding to the dilution of iron in the weld metal, are indicated on the micrographs. The arrows on the diagrams show the linescan traces, in which the composition in the corresponding graphs, were measured.

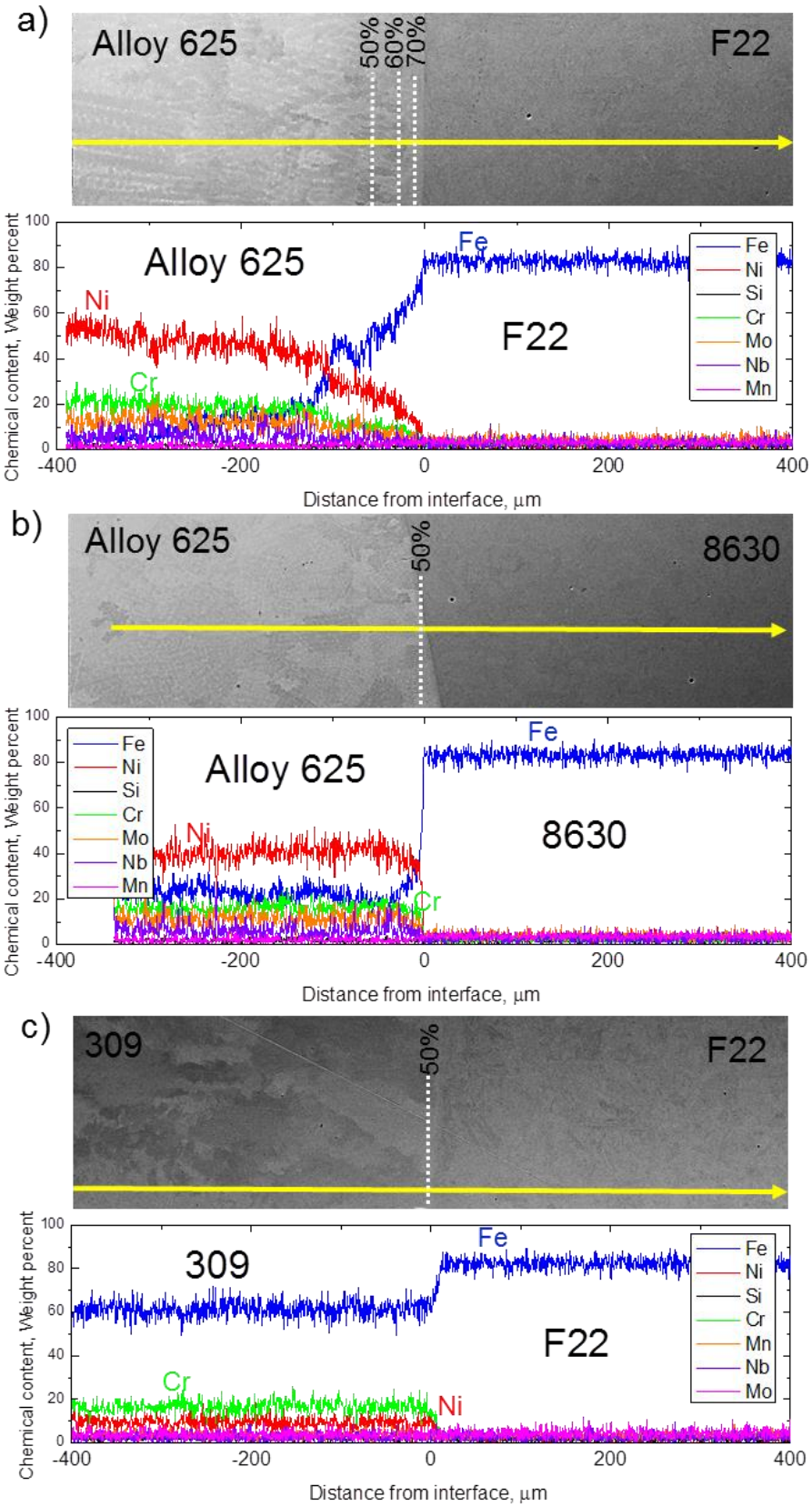

Figure 4-1-Low magnification SEM BS electron images with accompanying EDX linescans (yellow arrow) across the fusion boundaries of a) F22-Alloy 625; b) 8630-Alloy 625 and c) F22-309LSi dissimilar joints (as-welded condition).

Regions of partial mixing were observed as transitional changes from the parent to weld metal. PMZ width is determined by factors including heat-input and filler feed rate. Therefore, the two Alloy 625 joints, having been fabricated under the same welding conditions, can be compared. In the F22-Alloy 625 joint, the PMZ width was approximately twice that of its 8630 counterpart, although the width of the PMZ is likely to vary across the thickness of the weld, due to localised differences in weld pool mixing, as discussed in Section 2.1.3.

To elucidate near-interface regions, higher magnification linescans, from the same continuous PMZ regions as in Figure 4-1, are presented in Figure 4-2.

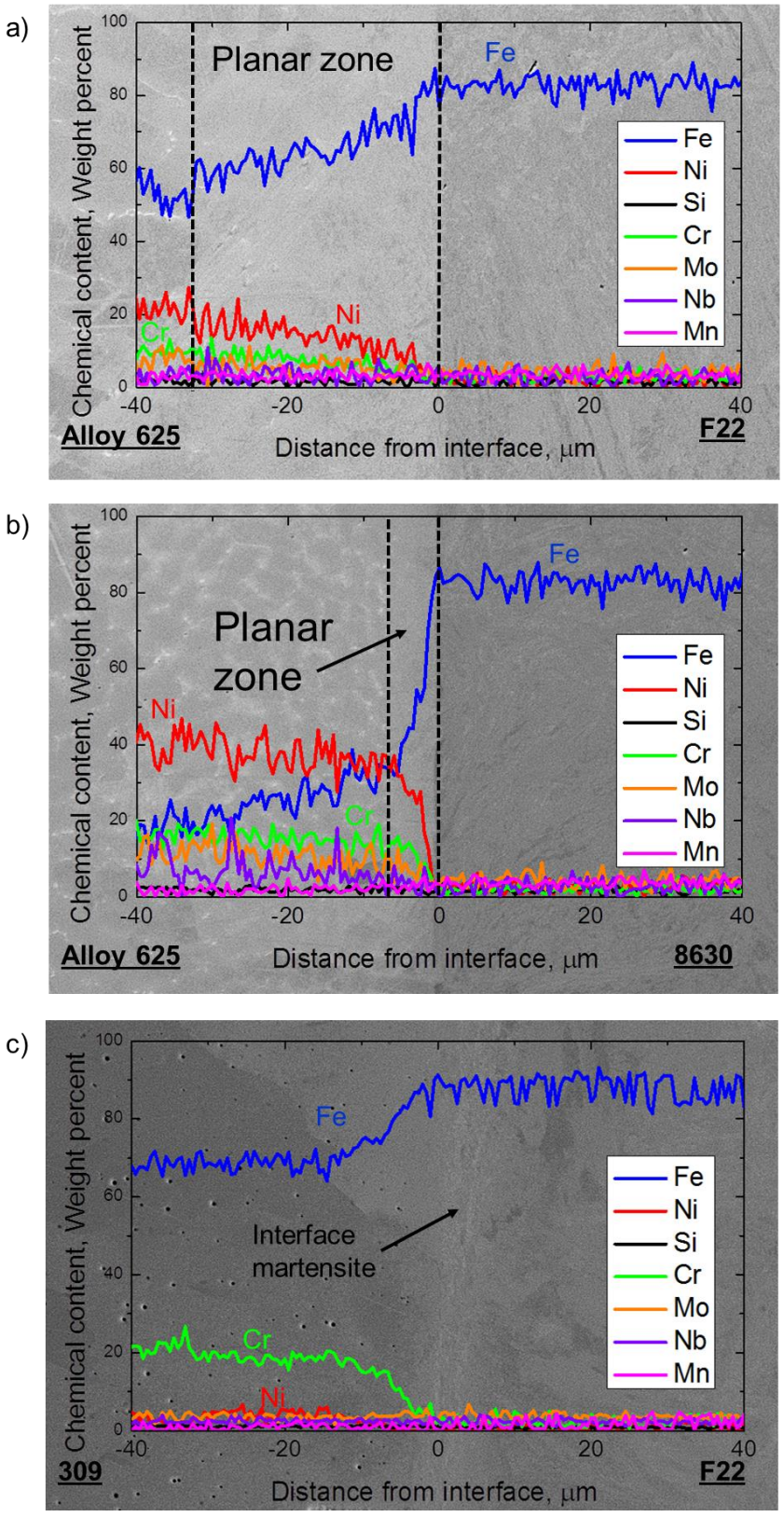

Figure 4-2 – SEM BS electron images of the dissimilar joint fusion boundaries (in the as-welded condition), overlaid with corresponding EDX chemical distribution linescans, for the three dissimilar joints: a) F22-Alloy 625; b) 8630-Alloy 625 and c) F22-309LSi.

The most significant composition changes occur within the planar zone of both of the Alloy 625 butterings. Of these two joints, the steepest composition gradient was observed to occur across the 8630-Alloy 625 interface, and was associated with a reduced planar zone width. In the 8630 and F22-Alloy 625 interfaces, the planar zone widths were approximately 8 and 32μm, respectively.

The nickel content across all three dissimilar joints decreases from the weld metal PMZ towards the parent metals. During cooling, the reduced nickel content results in a weaker driving force for the stabilisation of austenite to lower temperatures. Together with the high carbon content of the forging, this creates a scenario whereby martensite is likely to form even under slow cooling conditions. As explained in Section 2.1.5, the Schaeffler diagram can be used to predict microstructure formation, in the transition region between two dissimilar metals, under the cooling conditions associated with arc welding. To illustrate this, the nickel and chromium equivalents have been superimposed on the diagram in Figure 4-3.

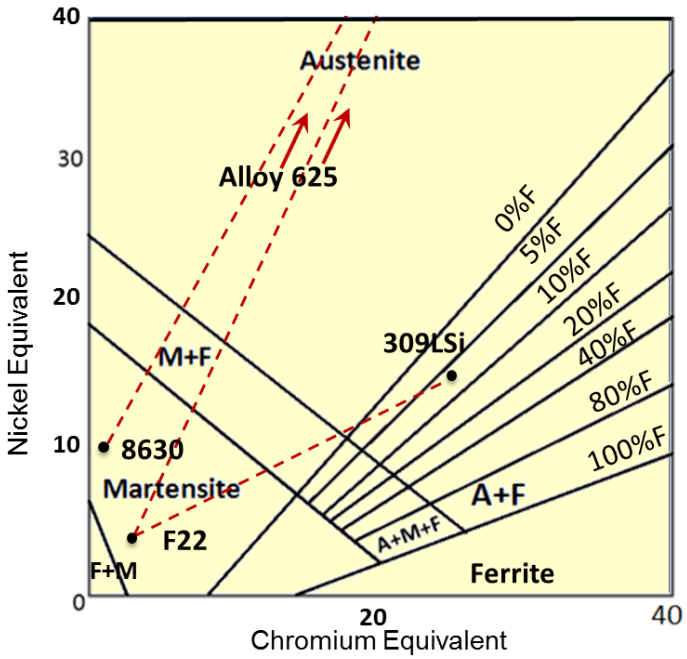

Figure 4-3 - The Schaeffler diagram, with superimposed lines for the composition range of the three dissimilar joints. Adapted from [57].

The partially-mixed zone may consist of all compositions connecting each pair of points together. In all three pairings, the composition traverses through a martensitic region, such that martensite may be expected at the interface between the two materials. A complete assessment of the chromium and nickel equivalencies over the whole dilution range is given in the Appendix C, together with predicted phase percentages. Due to the higher nickel concentration of the joints prepared with Alloy 625, a steeper composition gradient is found within the PMZ, compared to the 309LSi combination. Consequently, there is a reduced compositional band, over which, martensite is stable, hence resulting in the formation of a thinner band of martensite.

In the as-welded condition, martensite was present in its virgin form, whereas after PWHT, the structure presented a tempered morphology. Although the width of the martensitic band varied along the length of the interface due to weld pool mixing, in general the F22-Alloy 625 combination had a broader martensitic band than that of the 8630 joint. Micrographs of interface martensite are presented, at higher magnifications in section 5.3.3. Differences in martensite band width between the F22 and 8630-Alloy 625 joints are attributed to the higher nickel equivalency in the 8630 joint, as well as higher hardenability. In both of the Alloy 625 joints, interface martensite typically measured less than 1μm, whereas in the F22-309LSi combination the same structure measured approximately 4μm, as indicated in Figure 4-2c.

EBSD analysis of the interfacial regions was used to determine phase constitution and grain texture. The polished sections were analysed using a 0.5μm sampling interval. Inverse pole figure plots are given relative to the observed surface plane. In each plot the FCC phase is shown in red, whilst the BCC phase is shown in blue. For clarity, the phase maps are overlaid with associated electron band contrast images. Figure 4-4 shows two continuous PMZ sections from the F22-Alloy 625 joint, in the as welded condition.

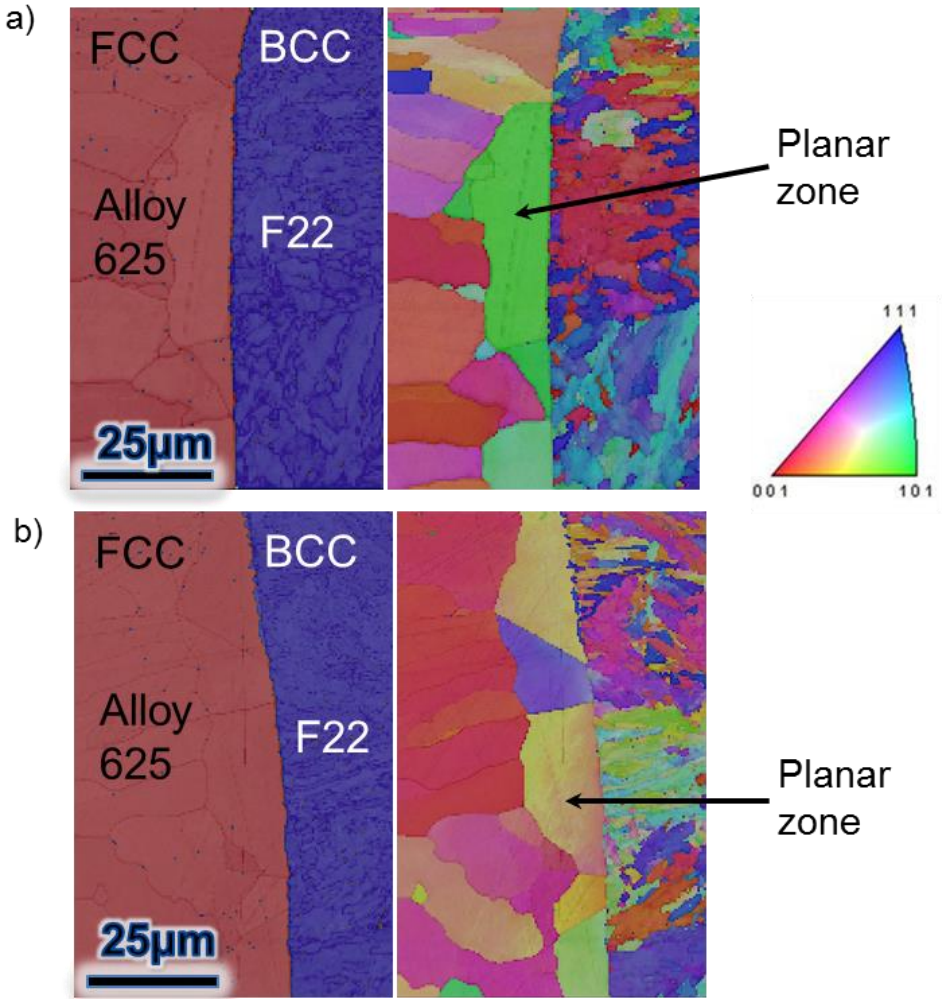

Figure 4-4 – Phase constitution (overlaid with band contrast image) and EBSD maps for a and b) F22-Alloy 625 joint, continuous PMZ in the as-welded condition.

In the F22 joint, the iron-rich parent metal was determined to be BCC. Within the continuous PMZ, the BCC/FCC fusion boundary appears to be nominally flat, however the same is not true within discontinuous PMZ regions, Figure 4-5.

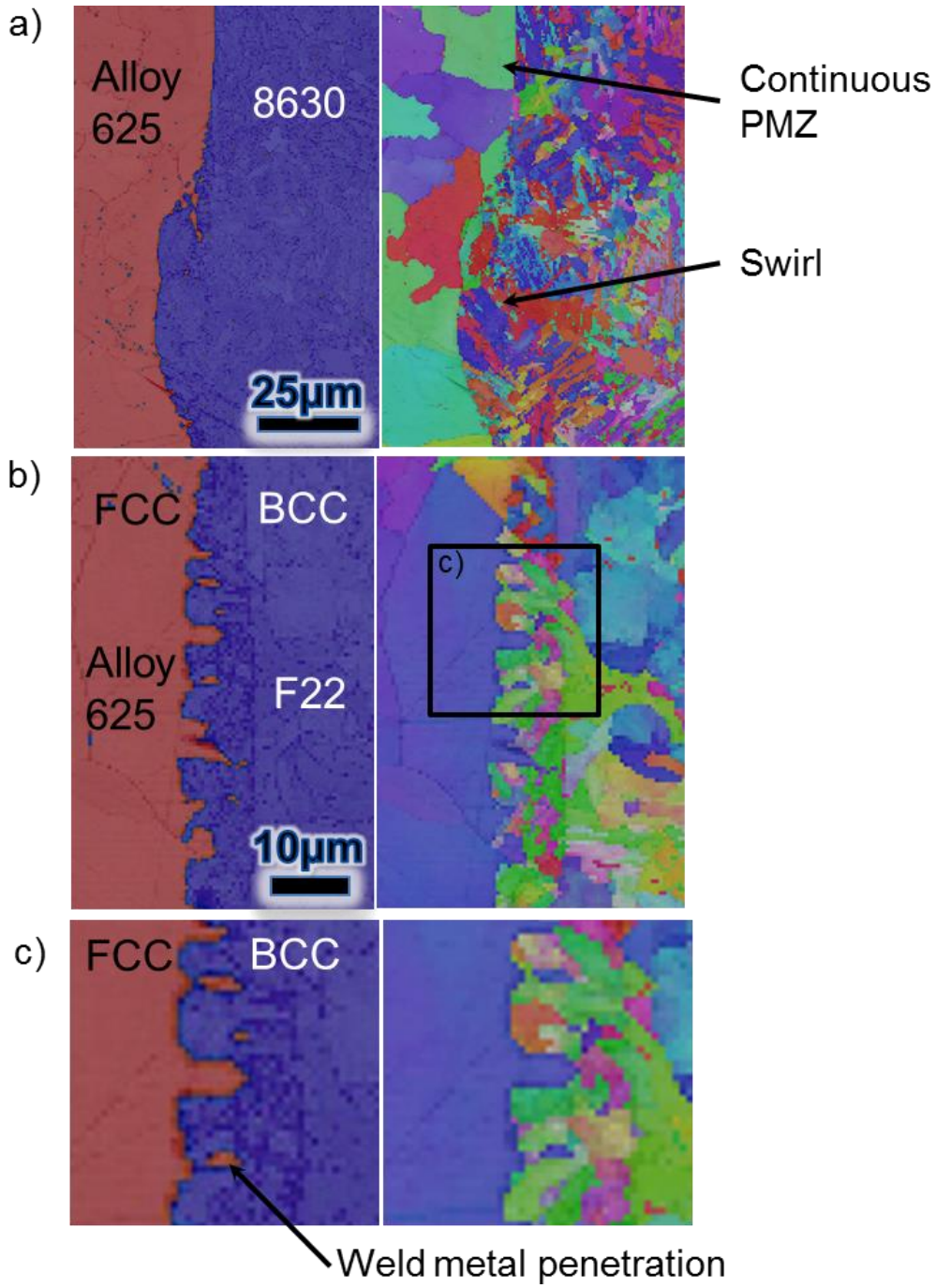

Figure 4-5 – Phase constitution and EBSD maps for a) 8630-Alloy 625 joint after 10 hours of PWHT showing a swirl adjacent to a continuous PMZ; b) F22-Alloy 625 dissimilar joint in the as-welded condition showing a discontinuous region with weld metal penetration; c) the inset region from b, showing weld metal penetration in greater detail.

The interfaces presented in Figure 4-5 show discontinuous partially-mixed zones, in which the BCC/FCC boundary is irregular in shape. In particular, the weld metal has penetrated the GBs of the ferritic side, probably during welding as opposed to during PWHT.

The penetrations are shown to have an FCC structure before PWHT, Figure 4-5b and c, and are likely to remain so after PWHT, due to the selection of PWHT temperature.

The parent metal, and molten metal, within the GB penetration, are likely to lie within the steep composition gradient. Both near-interface sides of the fusion zone are predicted to form austenite, initially, with overlapping austenite temperature ranges, appendices, Table 10 - Table 12, and Figure 4-8. In accordance with Alexandrov et al [54] the solidification sequence and temperature ranges of both sides may promote localised epitaxial solidification of the weld metal from the neighbouring steel HAZ grains.

In all the EBSD maps presented, a planar solidified zone is seen, regardless of PMZ type. Grains within the planar zone had a high aspect ratio; the long sides were aligned parallel to the dissimilar interface. High angular misorientation, is observed between planar zones and neighbouring dendritic regions. Elongated grains, perpendicular to the fusion boundary, indicated grain growth towards the centre of the weld pool, during solidification.

4.3.2 **Results from Thermodynamic Models**

The predicted phase equilibrium calculations for the 8630 parent metal, Figure 4-6, show that above the martensite transformation temperature, complete dissolution of the $M_{23}C_6$ and M_7C_3 phases is possible. The chemistry differences between the F22 and higher carbon content 8630 forging result in dissimilarities in phase content; cementite is not stable in the F22 forging, whereas M_6C carbide is not stable in the 8630 forging. At a typical PWHT temperature of 650°C, complete dissolution of $M_{23}C_6$ is not predicted in the F22 forging.

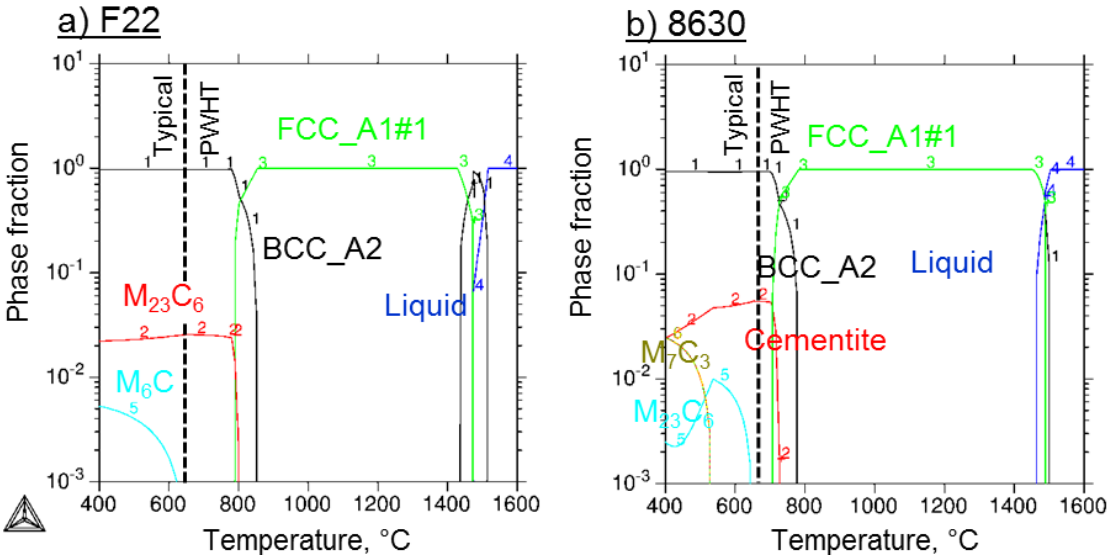

Figure 4-6 - Thermo-Calc prediction of phase equilibrium in a) the F22 and b) 8630 parent metals

The Thermo-Calc prediction of phase stability in Figure 4-6 considers the unmixed parent materials only. In dissimilar welds, within discontinuous partially mixed zones containing austenite stabilising elements, the selection of PWHT temperature may be sufficiently low, such that localised regions undergo the BCC-FCC transition. To illustrate the point, consider a 'swirl' of parent metal that has penetrated into the weld metal, such as that in Figure 4-7. Two indicated points were measured quantitatively, for the following elements Fe, Ni, Cr, Nb and Mo. A carbon percentage of 0.3wt% (assumed), corresponding to the nominal forging composition was included, such that the thermodynamic models are simplified and do not include fully specified elements, as indicated in Table 5.

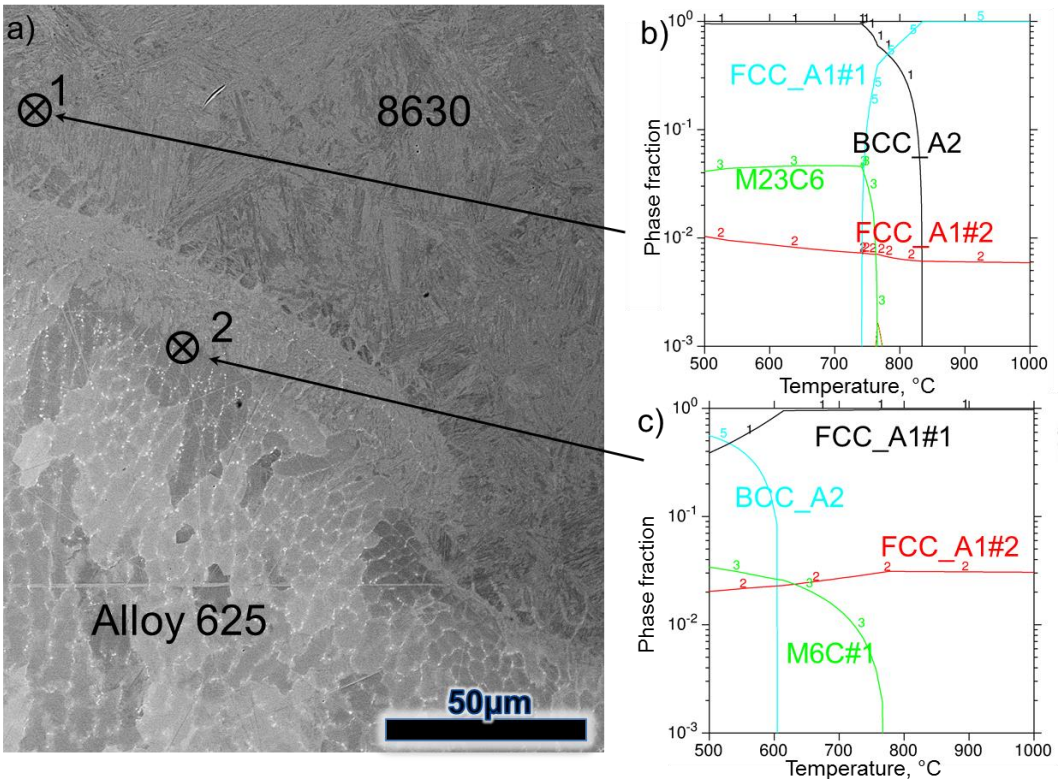

Figure 4-7 – A PMZ swirl at the boundary between 8630-Alloy 625, after 10 hours of PWHT. a) SEM BS image of swirl; b) Thermo-Calc prediction of phase constitution in point 1 and c) in point 2.

Table 5 – EDX measured weight percentages for the points indicated in Figure 4-7. Values for carbon were assumed, based on the nominal composition of the parent metal.

Measurement Point	Fe*	Cr	Ni	Mo	Nb	C*
1	Bal	0.63	0	0.77	0.5	0.3
2	Bal	6.5	13.07	2.37	3.61	0.3

*Assumed weight percentages

The BCC_A2 values are far higher in the forging side, point 1, compared to the within the swirl, point 2. The effect is pronounced, such that at a typical PWHT temperature of 650-675°C, within the swirl, the metal consists solely of M_6C and FCC phases. Whilst the phase diagrams are simplistic and consider equilibrium aspects only, they highlight that the formation of virgin martensite within discontinuous PMZs may be possible following cooling from typical PWHT temperatures.

The predicted solidification ranges, for the three dissimilar joints, are given in Figure 4-8. Overlaid on the graph is the percentage of δ-ferrite at solidification, over the dilution range. For the 8630 joint, the undiluted parent metal initially solidifies as 36% δ-ferrite, reducing to 14% at 98% dilution of the filler wire. In the F22-Alloy 625 joint, δ-ferrite formation is extended further into the dilution range. In its undiluted state, a phase percentage of 84% δ-ferrite was calculated. 27% δ-ferrite was calculated at 92% dilution. In the F22-309LSi joint, δ-ferrite extends throughout the whole dilution range, although it is reduced by mixing with the 309LSi filler metal.

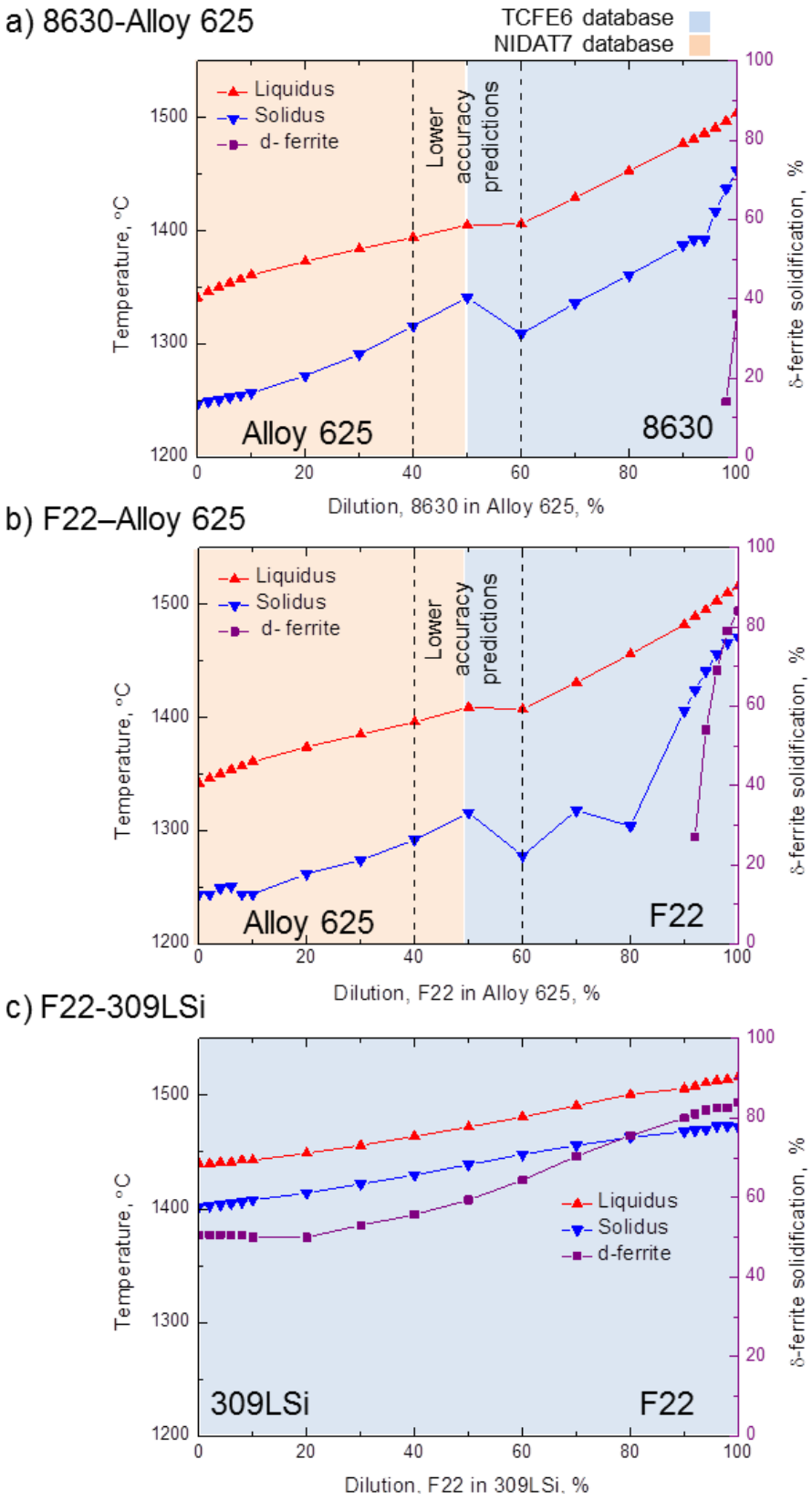

Figure 4-8 – Thermo-Calc predictions of the solidification temperatures over the calculated concentration range (linear dilution) for the three dissimilar combinations, using the S-G module. a) 8630-Alloy 625; b) F22-Alloy 625 and c) F22-309LSi

For all three dissimilar weld combinations, a decrease in the dilution of the filler metal by the LAS parent metal, results in a similar decrease in both liquidus and solidus temperatures. Due to the relative compositional similarity between the materials, the F22-309LSi joint has a lower liquidus-solidus temperature range throughout the dilution range. In general, however, the solidification range increase with decreasing dilution of the filler metal.

EDX measured compositional gradients indicate, that in the planar zone of the F22-Alloy 625 joint, the dilution range is approximately 100 to 68%. In the 8630-Alloy 625 joint, planar zone dilution is between 100 and 46%. By comparing the solidification range with these measured values, a sharp temperature gradient would be expected within the planar zone after welding. The results suggest that, in the F22-Alloy 625 joint, from the parent metal at the fusion boundary, a 32μm thick planar band is predicted to exist, which has a liquidus temperature gradient of approximately 150°C. In the 8630 joint, the planar zone is narrower, at approximately 10μm, yet also has a liquidus temperature gradient of approximately 150°C.

Temperature dependency on carbon thermodynamic activity, for the parent and weld metals, is presented in Figure 4-9. Compared to the weld metals, carbon activity is far higher in the F22 and 8630 parent metals. Carbon is likely to diffuse in the direction of its thermodynamic activity gradient. High carbon activity in the parent metals, combined with high concentration gradients, will encourage diffusion of carbon from the LAS forging, towards the weld metal. The higher heterogeneity between the diffusion couple, the higher the likelihood of carbon redistribution during PWHT.

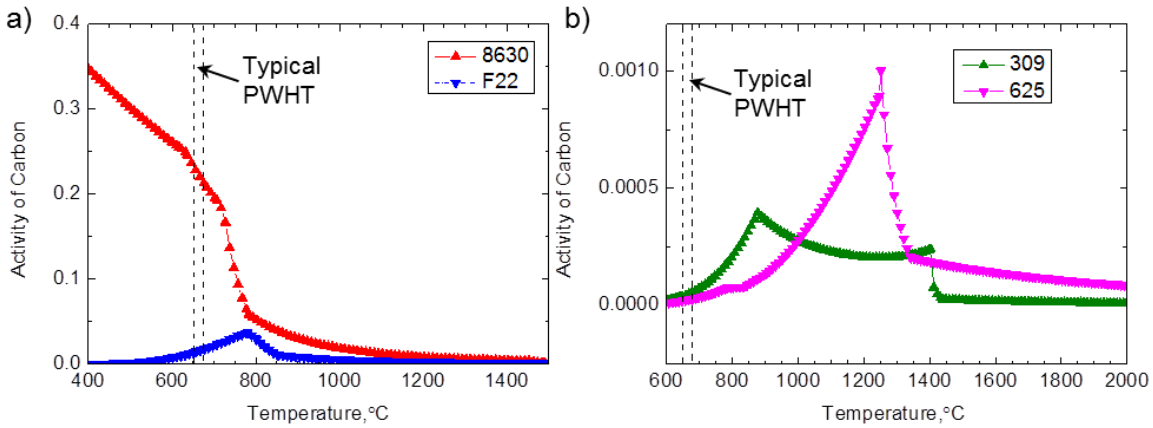

Figure 4-9 - Thermo-Calc prediction of carbon activity for a) the F22 and 8630 parent metals and b) the weld metals. Typical PWHT temperature ranges are indicated.

The activity of carbon in F22 is seen to increase with temperature from 400 to 780°C. Conversely, over the same temperature range, the carbon activity decreases considerably, in the 8630 material. Despite the contrasting carbon activity trends, at typical PWHT temperatures, the carbon activity in the 8630 is approximately 12 times higher than in the F22 material.

In the weld metals, the carbon activity remains comparatively low, at typical PWHT temperatures. This is attributed to the diffusivity in austenite being considerably lower than in ferrite and the carbon solubility being higher. The reduced nickel content in the 309LSi, results in a higher carbon activity at typical PWHT temperatures, compared to the Alloy 625.

4.3.3 **Results from Diffusion Models**

Quantitative measurements of carbon concentration profiles are difficult due to the low atomic number of carbon, however they were modelled in Dictra, as presented in Figure 4-10.

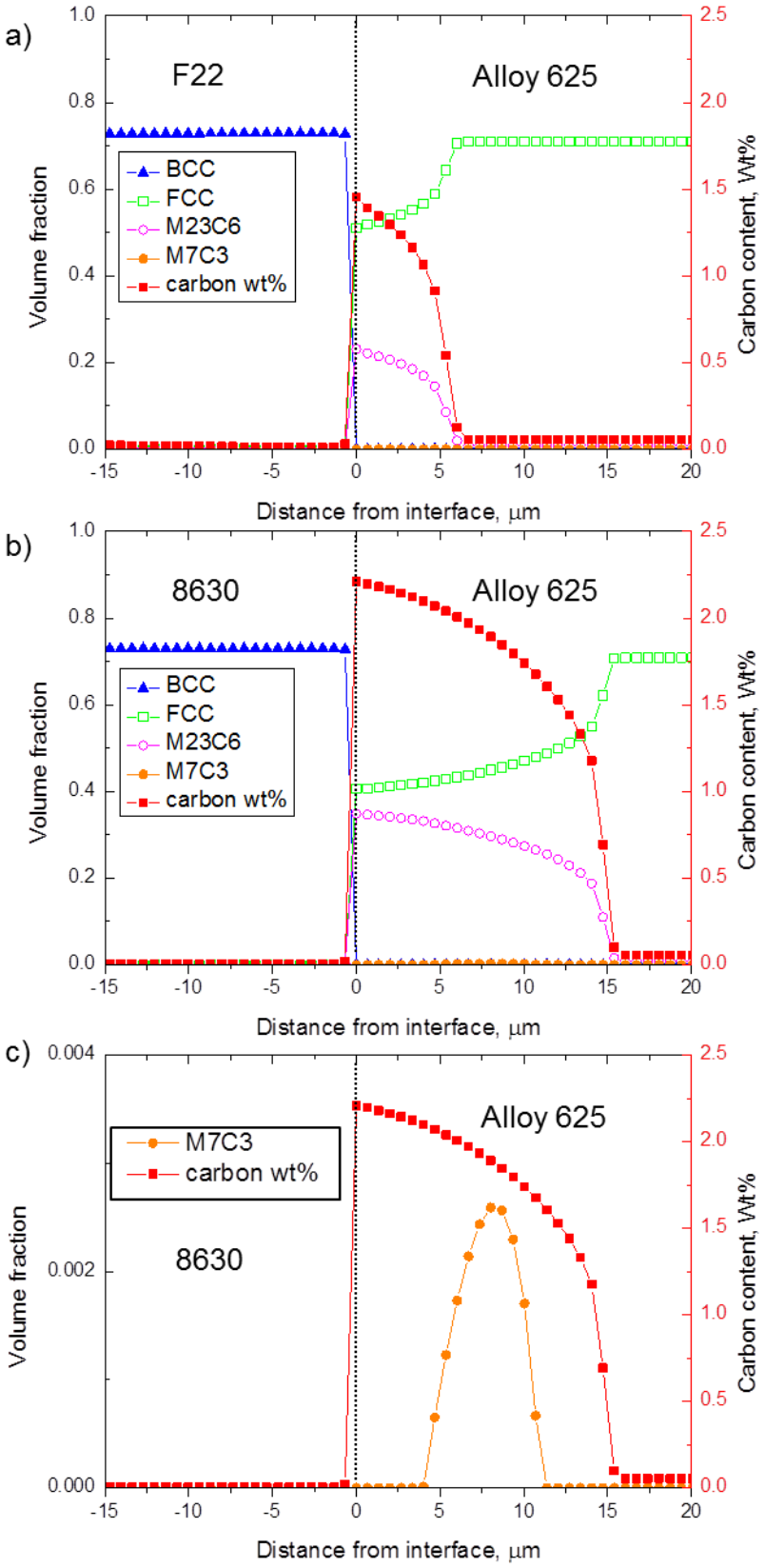

Figure 4-10 –Calculated phase distribution and carbon weight percentage values for the LAS-Alloy 625 joints after 10 hours of PWHT at 665°C. a)F22-Alloy 625; b)8630-Alloy 625 and c)8630-Alloy 625 showing the formation of M_7C_3.

The Dictra models were performed under the assumption of an abrupt transition between the two materials before PWHT. In practice, however, chemical gradients between the two dissimilar metals, are present, in which a transitional increase in chromium within the weld metal is observed. Chromium is known to lower the chemical potential of carbon [182], [183], thus a discontinuity in chemical potential of carbon would be expected across the interface.

In the models, diffusion of carbon during PWHT resulted in 1.5% and 2.25wt% carbon in the weld metals of the F22 and 8630-Alloy 625 dissimilar joints, respectively. The high rate of diffusion stems from a higher diffusivity of carbon in ferrite than in austenite. Diffusion of carbon into the weld metal also resulted in the formation of a carbon-depleted region in the ferritic side, which would result in a reduction in HAZ hardness. To exaggerate the decarburisation phenomenon, calculated carbon distributions during PWHT up to 100 hours are given in Figure 4-11.

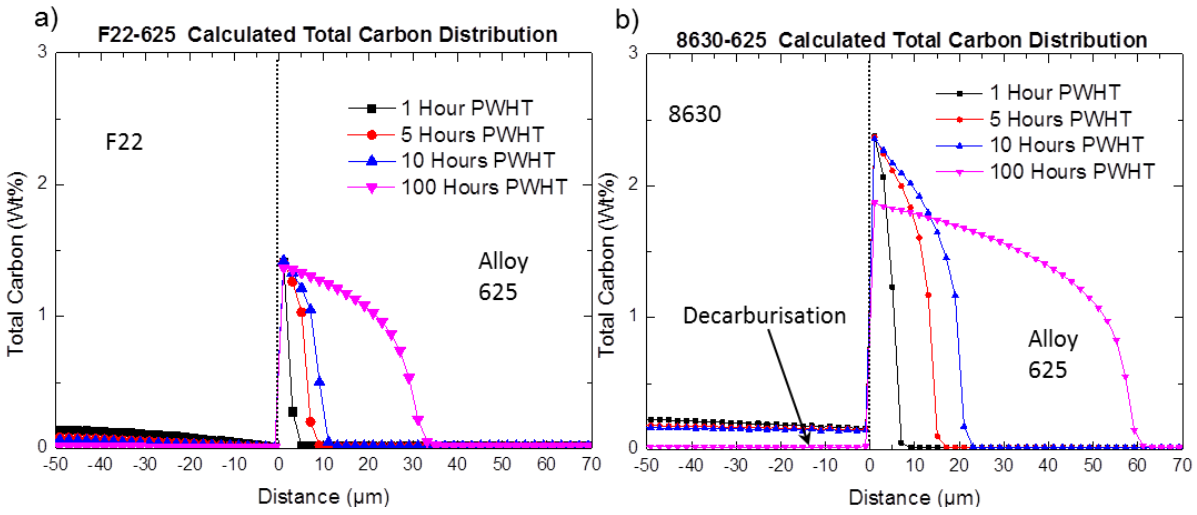

Figure 4-11 – Calculated distribution of carbon across the dissimilar interfaces under various lengths of PWHT. a) The F22-Alloy 625 and b) the 8630-Alloy 625 joints, showing decarburisation of the LAS with increasing PWHT time.

Carbon diffusion into the austenitic side of the Alloy 625 joints resulted in the solubility limit being reached, causing the precipitation of new phases. $M_{23}C_6$ carbide is predicted to form, in the austenitic side of both dissimilar joint types. The formation of this carbide has been observed in LAS-Alloy 625 joints [14], [143], [148], but not in the austentic side immediately adjacent to the interface (i.e. not in the planar zone). The M_7C_3 carbide is predicted to form, within the weld metal, of the 8630-Alloy 625 joint after 10 hours of PWHT. This is an interesting observation, as the simple diffusion couple does not account for the morphology and chemical gradients that are present in real dissimilar welds. The prediction of the formation of M_7C_3, after 10 hours of heat treatment, in the 8630 weld, but not in the F22-Alloy 625 joint, is consistent with the TEM observations of Fenske [14], as well as those presented later in this work. However, with further PWHT, beyond that typical of industry practice, M_7C_3 precipitation within the weld metal is likely, due to further diffusion of carbon from the LAS side. Results to confirm these findings are presented in Section 5.3

4.4 Discussion

The formation of embrittled weld fusion boundary regions, is determined primarily by the welding process used, and the parent/weld metal combination. The F22-309LSi joint was selected solely as a metallurgical comparison to the LAS-Alloy 625 joints. In the 309LSi combination, the relative similarity between the PM and weld metal, reduces the chemical gradient with consequent broadening of zones exhibiting transitional microstructures. This is perhaps most evident when comparing interface martensite; the highly dissimilar 8630-Alloy 625 combination, produced the narrowest martensite band and planar zone.

The steep weld metal composition gradient, appeared linked to planar zone width. The F22-Alloy 625 weld had a considerably broader planar zone and a less sharp

compositional change, than the 8630-Alloy 625, despite the use of a similar welding procedure. The steepest composition gradients, might be expected within the planar zone, due to the fact that larger composition changes occur in planar solidified regions, compared to cellular or dendritic areas [184].

During PWHT, carbon saturation in the planar zone is accompanied by the formation of M_7C_3 [14], [148]. The width and morphology of the planar zone might therefore play an important role in the formation of these phases. The EBSD analysis has demonstrated that grains within the planar zone have a high aspect ratio, the long sides of which are parallel to the dissimilar interface. The relative scarcity of GBs within the planar zone, compared to the bulk weld metal, may alter the diffusion dynamics of carbon. Grain boundaries further into the weld metal may represent preferable diffusion pathways, so that intragranular M_7C_3 precipitation ceases, in preference of a different phase. The extent of carbon diffusion, further into the weld metal than the planar zone, has been predicted by the diffusion models, however these do not account for the wide range of microstructures in the transition region, such as the existence of the planar zone. Similarly, diffusionless structures such as martensite, are not included in Dictra, thus tempering, and interface martensite's effect on long range diffusion are not accounted for.

As well as redistributing residual stresses, PWHT also tempers virgin martensite and increases HAZ ductility. Synchronously, peak hardness associated with interface martensite, may be reduced, provided the PWHT temperature is kept below the A_{c1} transformation temperature. Thus, it is proposed that during PWHT there are a number of different mechanisms taking place: 1) martensite tempering 2) redistribution of residual stress, and as demonstrated in this Section, 3) the formation of phases in the interfacial transition zone which might exacerbate hydrogen embrittlement, such as M_7C_3 and 4) some degree of de-carburisation of the forging HAZ. The latter point suggests that lengthy PWHTs,

in which a significantly de-carburised zone forms within the HAZ, can cause loss of strength and toughness.

4.5 Chapter Summary

Along with welding procedure, the chemical composition of the forging and weld metal influence the formation of hydrogen-assisted cracking, susceptible microstructures. Diffusion of carbon may result in the formation of the detrimental M_7C_3 carbide phase within the planar zone of the LAS-Alloy 625 welds, where a steep composition gradient exists after welding. At typical PWHT temperatures, there is reduced carbon activity in the F22 PM, compared to that in the 8630 steel. Therefore, the extent of carbon diffusion into the weld was also reduced.

Hydrogen-assisted cracking of the planar zone might be mitigated by altering the forging chemistry. Unlike the 8630-Alloy 625 combination, PWHT of the F22-Alloy 625 joint for 10 hours, did not result in the formation of M_7C_3. On this basis, the F22 forging represent a possible solution to cracking within the planar zone of heat-treated LAS-Alloy 625 welds. However, to confirm the latter point, mechanical performance testing under simulated service conditions, is required, along with post-mortem fractographic examination, as explored in the following Chapters.

CHAPTER 5. The Effect of PWHT on Resistance to Hydrogen Embrittlement

5.1 Introduction

The microstructures that occur within a typical (industry standard) dissimilar joint between an 8630 forging and Alloy 625 weld metal were explored in Chapter 3. The results indicated that, during PWHT, carbon migrates to the planar zone where it may form new precipitates. A method of testing the resistance to hydrogen embrittlement, via mechanically driven cracking under the influence of CP, was also established. Following this, in Chapter 4, the microstructures that form during welding, and subsequently during PWHT, were modelled. The driving force for new phase precipitation was found to be partially dependent on the composition of the parent metal.

Building on the above observations, in this Section a testing programme is used in order to rank the resistance to hydrogen embrittlement of the 8630-Alloy 625, and the lower carbon content F22-Alloy 625 joint. A series of heat treated sample coupons are subjected to SEM and TEM analyses in order to verify the extent of carbon diffusion, and to assess the microstructures responsible for the observed mechanical responses.

5.2 Experimental Procedure

5.2.1 Materials and sample preparation

Plate specimens, from ex-hub forging F22 and 8630 material, were water-jet machined to create 'L' shaped parent samples. Each specimen was welded using a buttering technique with Alloy 625, according to the process detailed in appendix A. The nominal compositions of the forging and weld metal is given in Table 4. To confirm conformance to compositional specifications, independent UKAS accredited, optical emission spectroscopic

(OES) analyses were performed on the forging material. The OES results are available in Appendix B. Slightly elevated molybdenum, nickel and chromium values for the 8630 material indicate the provided 8630 hub may fit the criteria for an 8630M forging – a modified form of the low alloy steel.

5.2.2 **Environmental Performance Testing**

Environmental mechanical tests were used to rank the resistance of the dissimilar joints to hydrogen embrittlement, according to the duration of heat treatment to which they were subjected. A series of 120mm long, blank, single edge notched bend (SENB) specimens, with a 12.5x12.5mm square section, were ED machined from each of the F22 and 8630-Alloy 625 interfaces. The specimens were furnace heat-treated with air cooling for 1, 10 and 100 hours at 650±5˚C and 675±5˚C, respectively. Following PWHT, the specimens were ground and polished to a 12x12±0.1mm square section to remove oxidation layers, and etched in 2% Nital to reveal the dissimilar interface.

Butter weld interfaces are not planar, but when viewed on a transverse cross-section, the weld typically displays an undulating penetration profile. The SENB specimen notches needed to be cut to intersect as much of the non-planar surface as possible. This was achieved using the notching method that was developed in Section 3.2.5, further aiding in comparison of resistance to hydrogen embrittlement between the two sample types. The notches were cut in the plane of the interface in the through-thickness direction of the joints to a depth of 6mm using Ø0.15mm wire.

Hydrogen pre-charging and testing temperatures were selected in accordance with the lowest performing crack-growth resistances from the retrieved specimens. Prior to testing, each sample was pre-charged with hydrogen for one week at -1100mV_{SCE} in a 3.5% NaCl solution. The solution was recirculated through a chiller to replicate typical subsea

commissioning temperatures of 4±2˚C and a potentiostat was used to simulate cathodic polarisation conditions. The same test parameters as for the retrieved specimens, were used for single edge notched bend testing: a loading rate of 0.018mm/hr, unloading at 0.05mm/min and ten elastic unloadings before beginning the test (0.01mm/min). Fracture surfaces, corresponding to in-situ cracking, were revealed after heat-tinting. A fractographic comparison between the retrieved joints and those fabricated for investigation of PWHT, is given in Chapter 7.

5.2.3 **Microstructural Analysis**

In Section 4.2.4, carbon was found to diffuse towards the weld metal during PWHT - the extent of the diffusion is dependent on the length of time at the PWHT temperature. To verify the relationship experimentally, additional sample coupons were prepared from F22 and 8630-Alloy 625 specimens and subjected to the same PWHT conditions as above, with the addition of a further sample that was heat treated for 1000 hours. The 1000 hours heat treatment was applied to further demonstrate the effect of excessive heat treatment.

Each interface sample was placed in a Zeiss E-SEM, equipped with EDAX EDX equipment. Initially, the bulk material was used to optimise the working distance, accelerating voltage, current and amp time. A region within a continuous PMZ was then selected for incremental ‘carbon scans’ perpendicular to the interface. A selected area of 10x100µm, placed immediately adjacent to the dissimilar boundary in the base metal, was selected for analysis. Pre-set EDX scan times of 20s were used and the net peak intensities (NPIs) for carbon and nickel were recorded upon completion. The stage was traversed incrementally by 10µm after each scan. Consequently, the corresponding carbon NPI values can be considered to be averages over each 10µm distance. After completion of the scans in

the HAZ, the analysis box was positioned adjacent to the interface inside the weld metal and the procedure repeated. Due to inaccuracies inherent with carbon quantification by EDX, the values obtained from the scans were normalised to the average of three carbon NPI values within the bulk weld metal, far away from the interface (therefore away from regions of high carbon activity).

SEM images were taken of each dissimilar interface whilst conducting the EDX carbon scans. However, in order to assess the nanoscale features, it was necessary to prepare TEM samples. To do this, an FEI Nova 600 nanolab dual beam system was used, using the same procedure described in Section 3.2.3. TEM samples were selected based on observations of the mechanical performance tests: the as-welded, highest performing, and 'over-aged' conditions. All TEM analyses were performed on Jeol 2010 and 2100 microscopes, operating at 200kV. Princeton Gamma Tech EDX equipment was used for elemental and phase identification.

5.3 Results

5.3.1 The Effect of PWHT on Carbon Diffusion across the Dissimilar Interface

The results from the carbon diffusion scans are presented in Figure 5-1. In the 8630-Alloy 625 system, all applied heat treatments had the effect of creating a measurable carbon-enriched region within the first few microns of the weld metal, thus corresponding to the planar zone. PWHT also had the effect of reducing the carbon concentration in the steel next to the interface - evidence of HAZ decarburisation. Whilst less pronounced, the F22 also exhibited near-interface carbon enrichment, despite having a much reduced carbon content compared to the 8630. The effect of carbon diffusion in the F22 combination is most evident as decarburisation in the HAZ after 1000 hours of heat treatment.

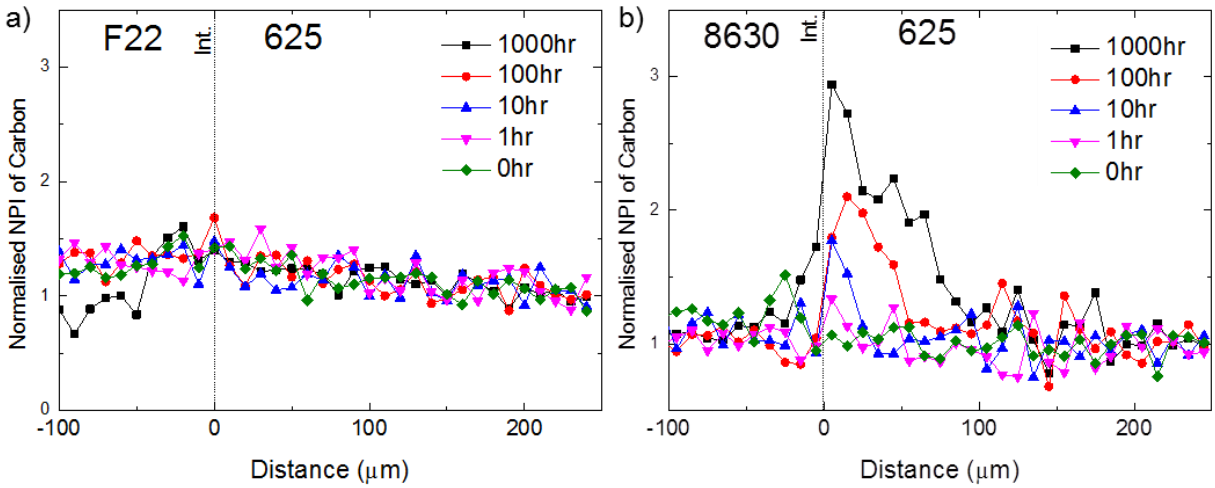

Figure 5-1 –Normalised net peak intensities for carbon for PWHTs from 0 to 1000 hours. a) The F22-Alloy 625 and b) The 8630-Alloy 625 dissimilar joint.

In the 8630 joint, elevated carbon levels were seen to extend further than the planar zone; high intensities were seen up to 55μm, and beyond 100μm into the weld metals, for the 100 and 1000 hours PWHT conditions, respectively. Whilst these results are not quantitative, in terms of diffusion distance, a consensus is apparent between experimental results and thermo-kinetic predictions, Figure 4-11. Typically, industrial manifold hubs are heat treated for between 5 and 10 hours. Although the point-to-point resolution is limited, for the 8630 joint, elevated carbon levels were observed extending approximately 25-30μm into the buttering: beyond the width of the planar zone.

The measured carbon intensities in the as-welded condition for both joints show a peak just before the interface. After PWHT, the peak is no-longer present. The measured peak in carbon may be as a result of the formation of interface martensite. The formation of martensite is not dependent on diffusion, thus it is not predicted using the CALPHAD approach.

5.3.2 **The Effect of PWHT on the Resistance to Hydrogen Embrittlement**

The F22 and 8630-Alloy 625 joints were tested using the same general procedure as the retrieved joints in Section 3.2.5, however in this instance, all joints were tested at 4°C. The effect of PWHT time on resistance to hydrogen-assisted crack propagation under CP is presented in Figure 5-2. The crack growth resistance curves for these joints were in line with those of the retrieved specimens. Interestingly, it was found that all applied heat-treatments either maintained or improved the mechanical performance, compared to the as-welded conditions. Relatively short PWHTs, comparable to industry practice, were observed to be the most beneficial, though the response was dependent on the material combination used.

For the heat treatment times selected, the F22 – Alloy 625 showed greater sensitivity to PWHT, as evidenced by the greater crack growth resistance to the equivalent 8630 tests. In the F22 combination the best performance was associated with a 10 hour heat treatment. A shorter heat treatment time appeared to provide only marginal improvement in the properties of the 8630-Alloy 625 combination and, interestingly, any further heat treatment time appeared to reduce the resistance to crack propagation back to the levels observed in the as-welded combination.

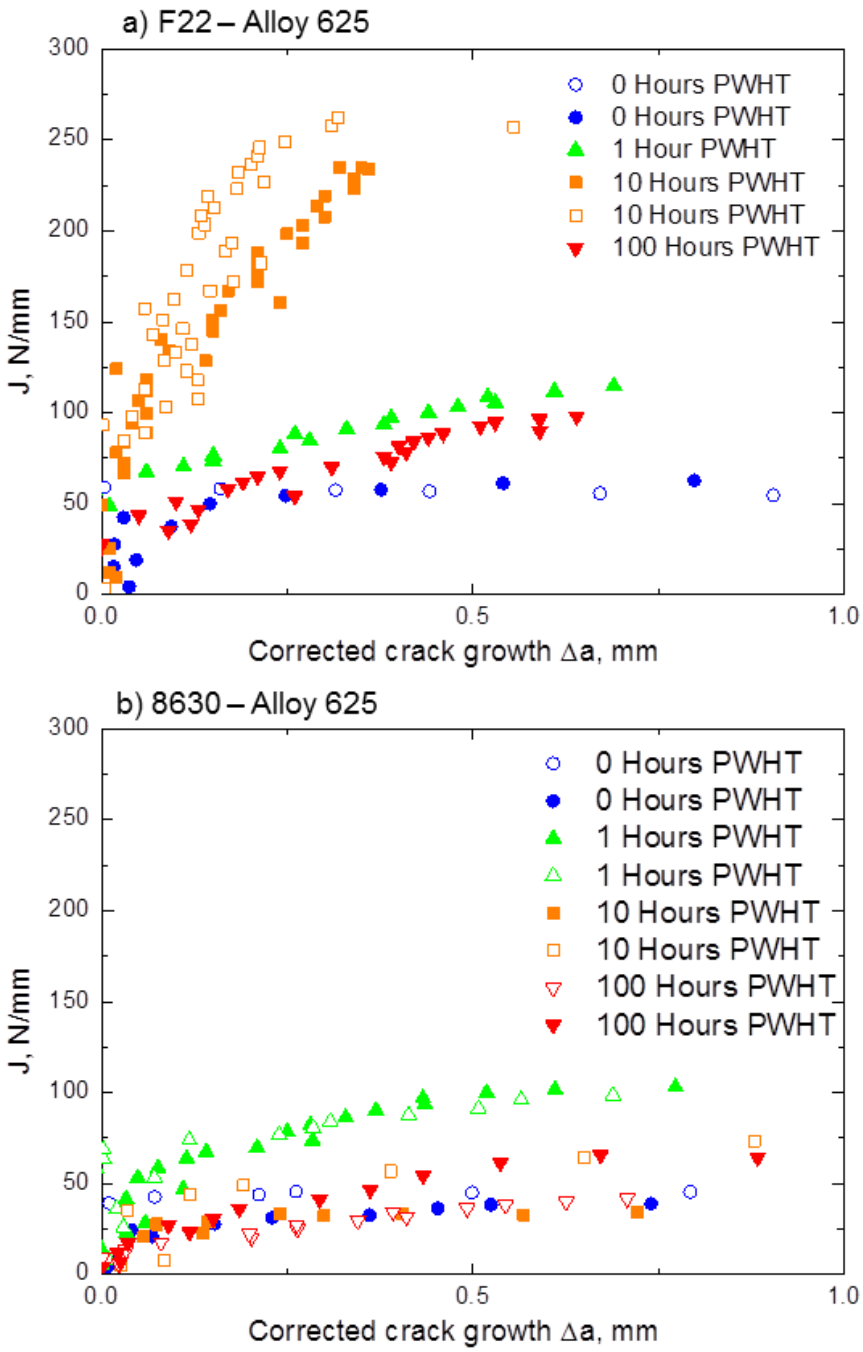

Figure 5-2 - Single specimen unloading compliance crack growth resistance curves for a) the F22-Alloy 625 and b) the 8630-Alloy 625, laboratory heat treated specimens. Note the repeat tests (points which are shaded).

5.3.3 **The Effect of PWHT on Microstructure of Dissimilar Joints**

The TEM thin-foil analysis from heat-treated sample coupons was selected to coincide with the three most significant mechanical responses in each joint: the as-welded, highest performing and 'over-aged' conditions.

In the as-welded condition, the F22 joint, Figure 5-3, exhibited a large, low-angle lath-structured band. Within this untempered region, precipitates, thought to be $M_{23}C_6$, had formed. The untempered microstructure within the ferritic side, and the absence of M_7C_3 carbide (which was present in retrieved, heat treated joints), was notable, as the application of PWHT was seen to change these microstructures significantly in successive TEM extractions.

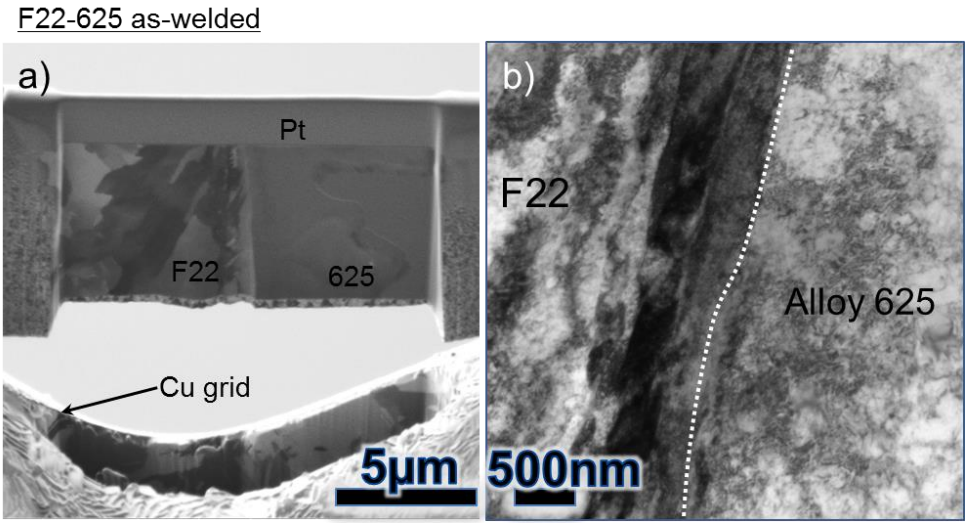

Figure 5-3 - TEM analysis of the F22-Alloy 625 joint in the as-welded condition. a) ion beam image of the TEM thin-foil and b) TEM image of the fusion zone showing an apparently featureless planar zone

A continuous PMZ region, from the F22-Alloy 625 sample coupon in the 10 hours PWHT condition, was selected for TEM analysis due to it having the highest resistance to hydrogen induced cracking. After 10 hours of heat-treatment, partial decomposition of martensite was observed (narrow, white interfacial band in Figure 5-4b) yet no new phase precipitation was seen in the austenitic planar zone, Figure 5-4c.

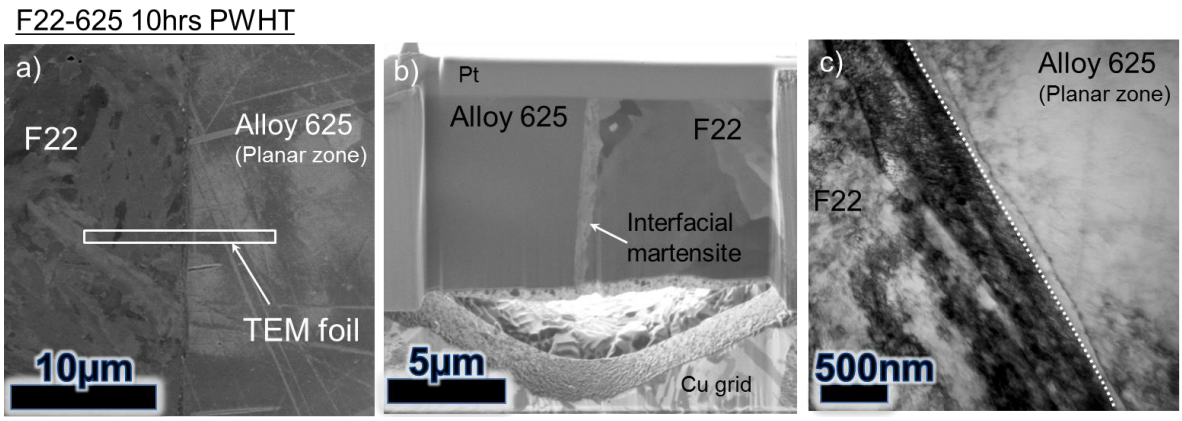

Figure 5-4 - TEM analysis from F22-Alloy 625 after 10 hours of PWHT. a)FEGSEM BS image of TEM sample region; b) ion beam image of TEM foil and c) TEM image of fusion boundary showing no new phase precipitation within the planar zone

After 100 hours, however, the effect of element diffusion was clear. A dense band of M_7C_3, was seen occupying a significant volume fraction of the planar zone and this was accompanied by almost complete decomposition of the martensite. Although texture analysis was not conducted, the long sides of the M_7C_3 carbides appeared aligned approximately parallel or perpendicular to the fusion boundary. TEM analysis from the F22-Alloy 625 joint after 100 hours is presented in Figure 5-5. The dense band of M_7C_3, begins at a distance of approximately 0.5µm from the steel grains. A higher magnification image of the carbides in close-proximity to the fusion boundary is given in Figure 5-6. As demonstrated, the regular oval shape of the M_7C_3 had approximate dimensions of 98x28nm. The density of the carbides did not vary significantly throughout the sampled region, however the TEM foil did not extend throughout the whole planar zone. An EDX linescan, consisting of net counts per second versus distance is presented in Figure 5-6b. Composition analysis indicated a predominantly chromium based carbide with additions of molybdenum, the concentration of which is reduced from the centreline of the 'oval' shaped precipitate. It is important to note the M_7C_3 carbide has a three dimensional morphology, the dimensions of which may extend

beyond the thickness of the TEM sample. Therefore, irregularities in shape throughout the planar zone may be partially due to viewing the precipitates in cross-section.

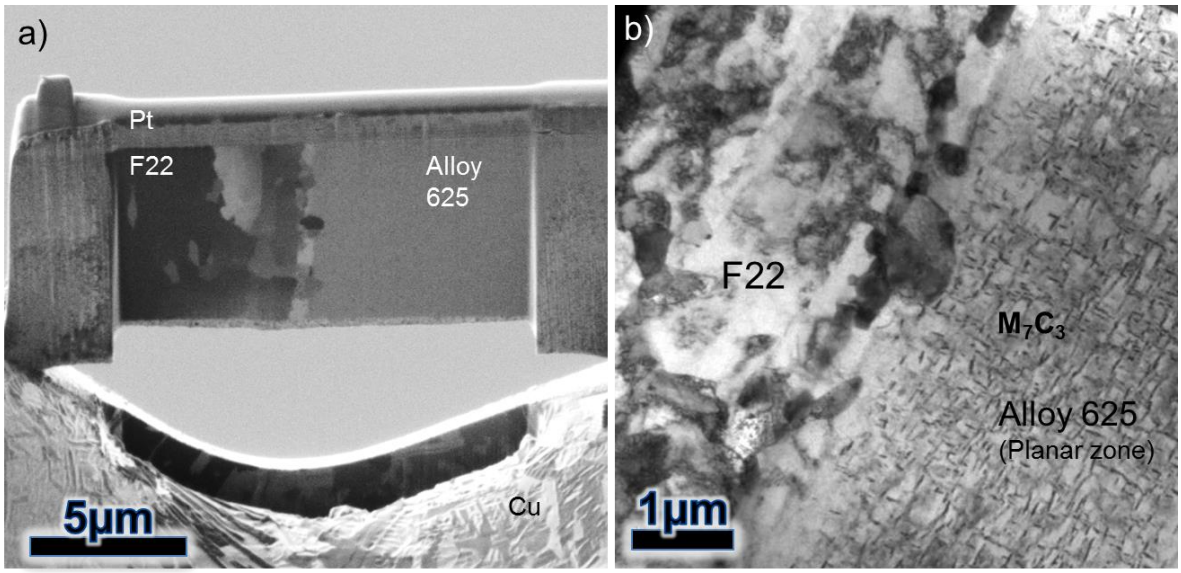

Figure 5-5 – TEM analysis of F22-Alloy 625 in the 100 hours PWHT condition. a) SEM image of the TEM thin-foil prior to analysis, and b) TEM image of the fusion boundary region, showing dense precipitation of carbide within the planar zone.

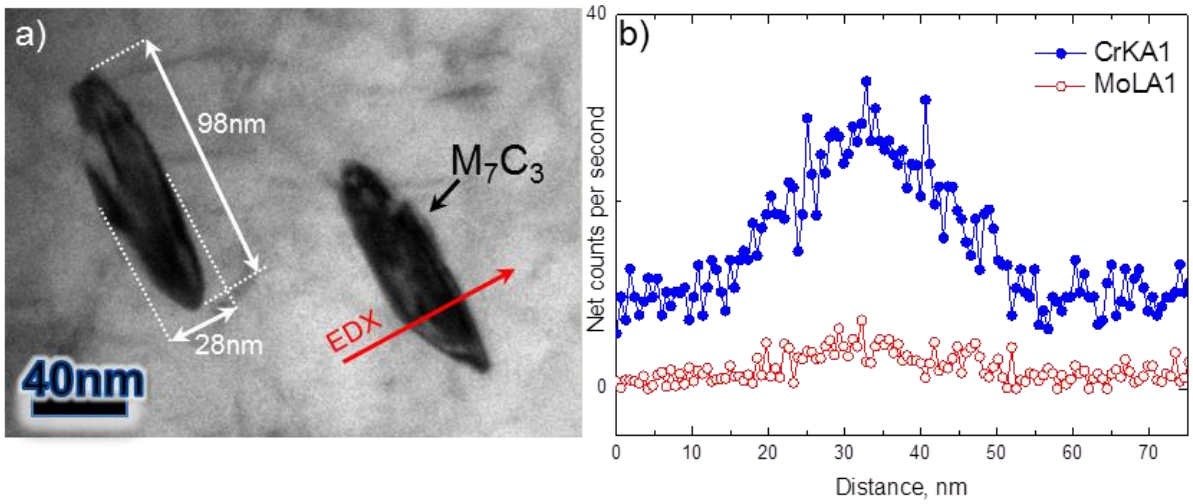

Figure 5-6 – TEM chemical analysis of M_7C_3 carbide, showing: a) approximate dimensions of two typical carbides adjacent to the fusion boundary and b) EDX analysis from region highlighted in a, illustrating a predominantly chromium-based carbide with additions of molybdenum.

An example of an M_7C_3 carbide, having an altered (diamond shaped) morphology, is presented in Figure 5-7a. The planar zone matrix was identified as FCC [100] zone axis

using selected aperture diffraction pattern (SADP) analysis. Due to the small size of the precipitate, nanobeam diffraction pattern (NBDP) analysis was necessary to isolate the M_7C_3 precipitate from the surrounding matrix, inset to Figure 5-7b. The carbide and matrix were indexed, according to the combined diffraction pattern presented in Figure 5-7c. Carbide, C, diffraction spots were partially concealed by the higher intensity matrix spots, M. Indexing of the NBD pattern was also difficult due to low intensity diffraction, however the pattern suggests a M_7C_3 carbide [312] zone axis.

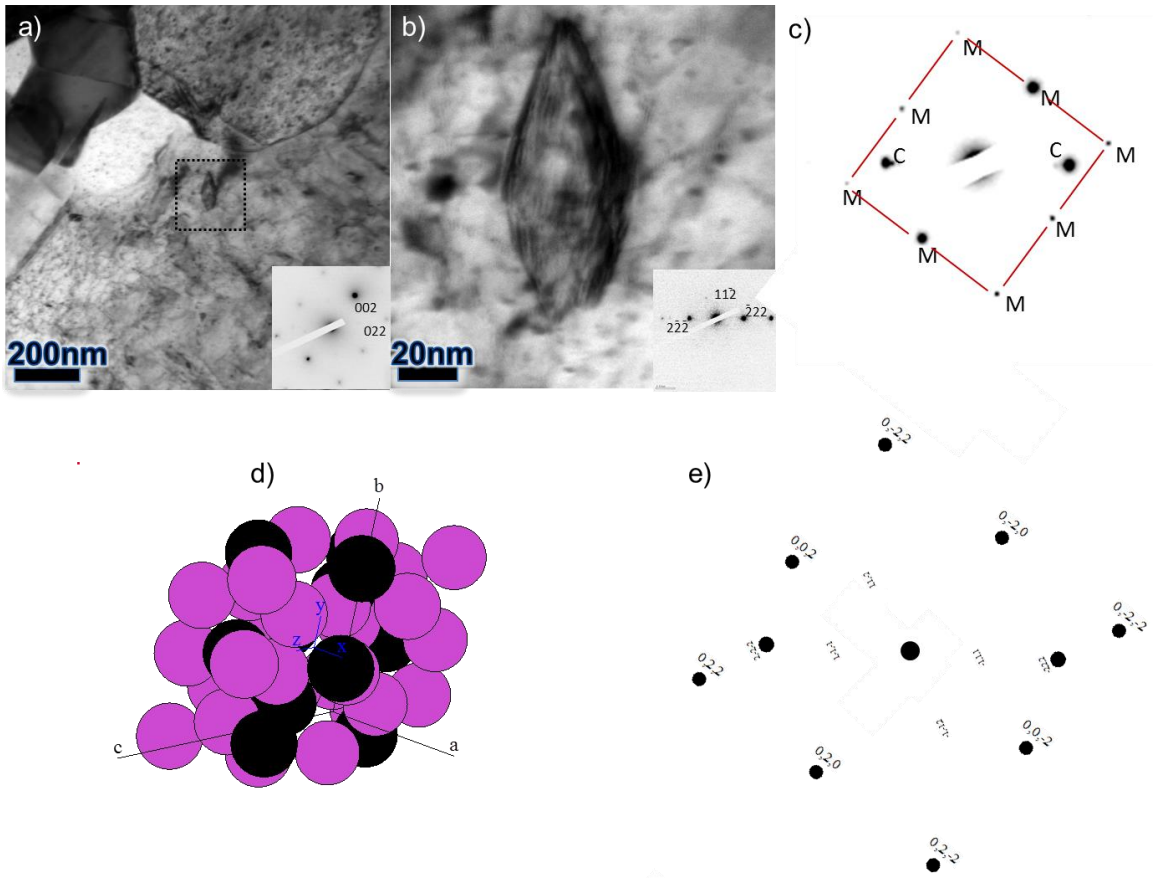

Figure 5-7 – TEM analysis of M_7C_3 nearest the fusion boundary. a)carbide with SADP of FCC matrix ([100] zone axis); b) Carbide with nanobeam diffraction pattern ([312] zone axis); c) SADP of matrix and precipitate; d)calculated M_7C_3 precipitate and e) calculated diffraction pattern for matrix and precipitate.

A three-dimensional representation of M_7C_3 is given in Figure 5-7d, calculated using orthorhombic Cr_7C_3 cell data [185]. CaRIne crystallography software [186] was used to construct a primitive orthorhombic unit cell (a=0.4526, b=0.7010 and c=1.2142nm), which

was converted to a Pnma space group (62). The calculated diffraction pattern arising from the construction of a Cr_7C_3 precipitate within an FCC nickel matrix is presented in Figure 5-7c. Considering the difficulties experienced with low intensity diffraction, and the chemical analyses (which suggest a complex $(Cr, Mo)_7C_3$ carbide), the computed structure factor is likely to vary significantly from that of the observed carbide. Further work is necessary if an orientation relationship between carbide and matrix is to be determined unequivocally.

Microstructural observations in the 8630 system were consistent with those in the F22 joint. In the as-welded state, Figure 5-8 , an untempered lath martensitic structure was visible adjacent to the FCC/BCC boundary. The planar zone consisted of FCC austenite but was lacking in the M_7C_3 precipitates, which were found in the retrieved joints that had received heat treatment.

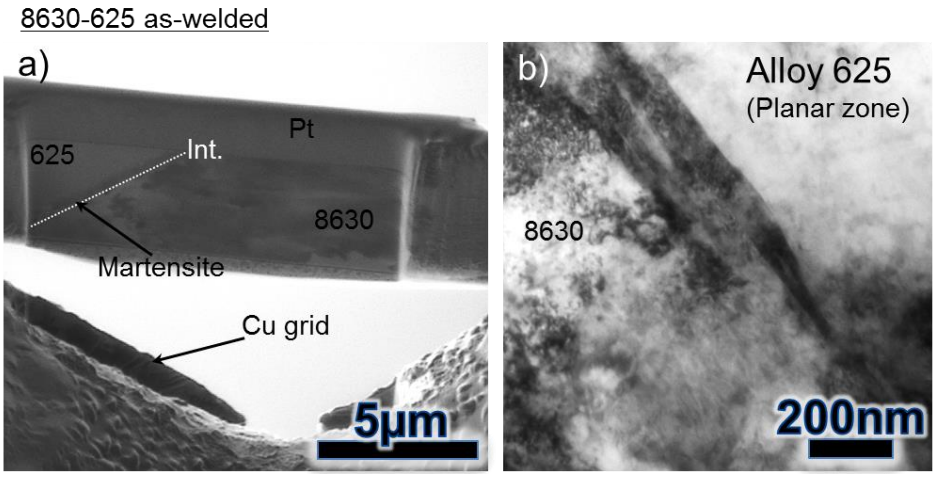

Figure 5-8 - TEM analysis of the 8630-Alloy 625 joint in the as-welded condition. a)ion-beam image of the TEM foil and b) TEM image of fusion boundary showing precipitate-free planar zone

A typical tempered region is shown after 1 hour of heat treatment in Figure 5-9. Characteristic to its environmental performance, and the microstructural observations in the F22 system, no new phases were present in the planar zone of the 8630 joint in this PWHT condition. Interestingly, a GB protrusion was partially contained within the TEM foil, due to

the sample being selected from an interface highly interspersed with 'fingers'. Though the sampled region was small, the lath structured region was significantly wider adjacent to the GB protrusion.

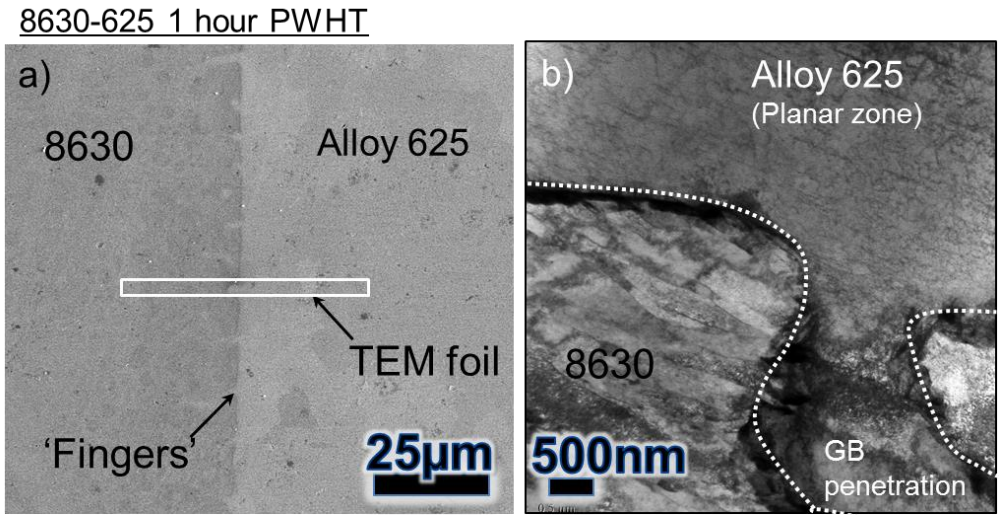

Figure 5-9 - TEM analysis of the 8630-Alloy 625 joint in the 1 hour PWHT condition. a) SEM SE image of sample selection from a PMZ containing prior-γ GB penetrations. b)TEM image of fusion zone containing a 'finger' of fused weld metal penetration. The BCC/FCC fusion boundary is delineated by the dashed line. The absence of M_7C_3 is notable.

Whilst the M_7C_3 carbide was not present after 1 hour, a band of the precipitates was visible after 10 hours of heat treatment, Figure 5-10. The precipitation of the carbide correlates to a synchronous reduction in resistance to hydrogen embrittlement, as observed in the J-R curve results.

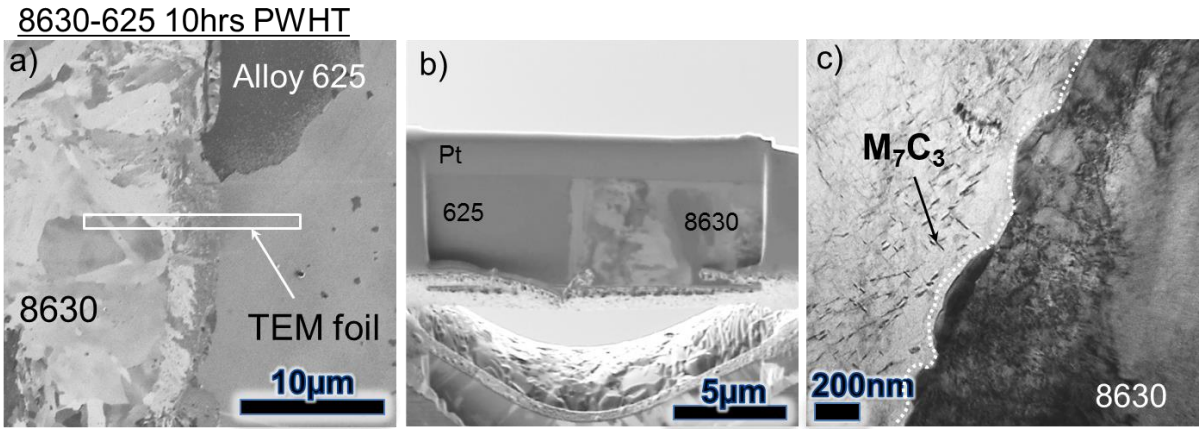

Figure 5-10 - 8630-Alloy 625 TEM analysis. a) FIB image of fusion boundary showing TEM sample selection; b) TEM sample mounted on Cu-grid for analysis and c) TEM image of sample showing M_7C_3 precipitates within the planar zone of the Alloy 625. Fusion boundary delineated by the dashed line.

5.4 Discussion

The planar region in both joints in the over-aged condition revealed a particle-free transition region close to the fusion boundary, followed by a band containing carbides. The emergence of this carbide-free region is due to the selection of the PWHT temperature, local chemistry and atomic structure, all of which influence the carbon solubility. Carbon solubility in Fe-based ferrite is considerably lower than the carbon solubility in austenite. Whilst the atomic structure either side of the interface is different, the chemical composition is not likely to vary significantly. The net effect of this is a relatively low carbon concentration in the steel, followed by a large peak in carbon in the austenite, slightly into the planar solidification region, where the amount of iron remains elevated. Further towards the bulk weld metal there is a less diluted chemistry (dilution of the weld metal by the parent) and the solubility for carbon decreases, increasing the propensity for carbide nucleation.

Decomposition of the martensite is therefore accompanied by the growth of carbides at the dissimilar interface within the steel and, simultaneously, further into the planar region.

The carbide-free region is likely to represent an area of carbon in solid-solution which, having not yet become saturated, has not nucleated M_7C_3.

The susceptibility of the joint to hydrogen embrittlement is clearly linked to microscopic regions, such as the planar zones and discontinuous PMZs adjoining the interface. However, it is be possible to eliminate the formation of the planar zone by modifying the welding procedure. Lower arc energies, for example, have been shown to reduce propensity for solidification to proceed in a planar manner, however this is associated with the formation of unfavourable martensitic structures [151]. This emphasises that whilst mechanical performance has been linked to competition between HAZ tempering and new phase precipitation, resistance to hydrogen embrittlement is also dependent welding process variables. An experimental programme to examine the connection between length of PWHT, joint combination, microstructure *and* welding process is essential. Moreover, whilst a dissimilar joint testing programme, based on J-R curve generation in a synthetic marine environment, has been developed, it is not clear how representative these tests are to in-service failure of full-scale components. Indeed the nature of subsea failures raises questions about the validity of the mechanically driven cracks used in the generation of J-R curves. Whilst the SENB tests may readily produce failures along the dissimilar interface replicating those of in-service specimens, the critical step may be initiation, as-opposed to propagation. Moreover, the mechanically driven three point bending tests that were used, accelerate the failure at an artificial rate, based on selected cross-head displacement. Hydrogen embrittlement has been shown to be a strain rate sensitive process [74], [75], thus the rankings provided herein are not necessarily representative of in-service failure.

5.5 Chapter Summary

The importance of PWHT in increasing the resistance to hydrogen embrittlement in LAS to Alloy 625 dissimilar joints has been examined through a combination of microstructural analysis, normalised carbon EDX profiles across the fusion zone, and mechanical performance testing. The results suggest that whilst PWHT is necessary, 'over-ageing' can prove almost as harmful. The resistance to hydrogen-assisted crack growth for the F22- and 8630-Alloy 625 interfaces showed a tri-modal split in response to an applied stress, as the length of PWHT was varied. In the 8630-Alloy 625 joint, 1 hour of heat treatment almost tripled the resistance to crack growth. The low PWHT time avoided formation of a critical concentration of carbon in the planar zone, such that no new phases formed. Prolonged heating resulted in the formation of M_7C_3, and was accompanied by reduced mechanical properties.

In the F22-Alloy 625 combination, the same phenomenon was observed: PWHT was seen to temper the HAZ, resulting in improved mechanical properties whilst under CP. Excessive PWHT resulted in decarburisation of the steel, carbon saturation in the planar zone, and the precipitation of M_7C_3. Due to having a reduced carbon concentration compared to the 8630 material, the F22 system has a similar reduction in mechanical performance, but it occurs later in the PWHT cycle. In the F22-Alloy 625, reduced resistance to HE was only observed after a tenfold increase in PWHT time, compared to the 8630. Further testing, under more PWHT conditions, would be beneficial in increasing the sampling resolution, such that an optimal PWHT may be found in each joint. A summary of microstructural changes, as PWHT time is increased, and its correlative impact on mechanical performance is illustrated, schematically, in Figure 5-11. In the as-welded condition, Figure 5-11a, the joint has the poorest resistance to HE due to the untempered structures, particularly martensite. In Figure 5-11b and c, tempering returns ductility to the HAZ, improving resistance to HE, and

resulting in carbon diffusion into the austenitic weld metal. The reduced mechanical performance, Figure 5-11d, is associated with further carbon diffusion, and the nucleation and growth of M_7C_3 in the planar zone.

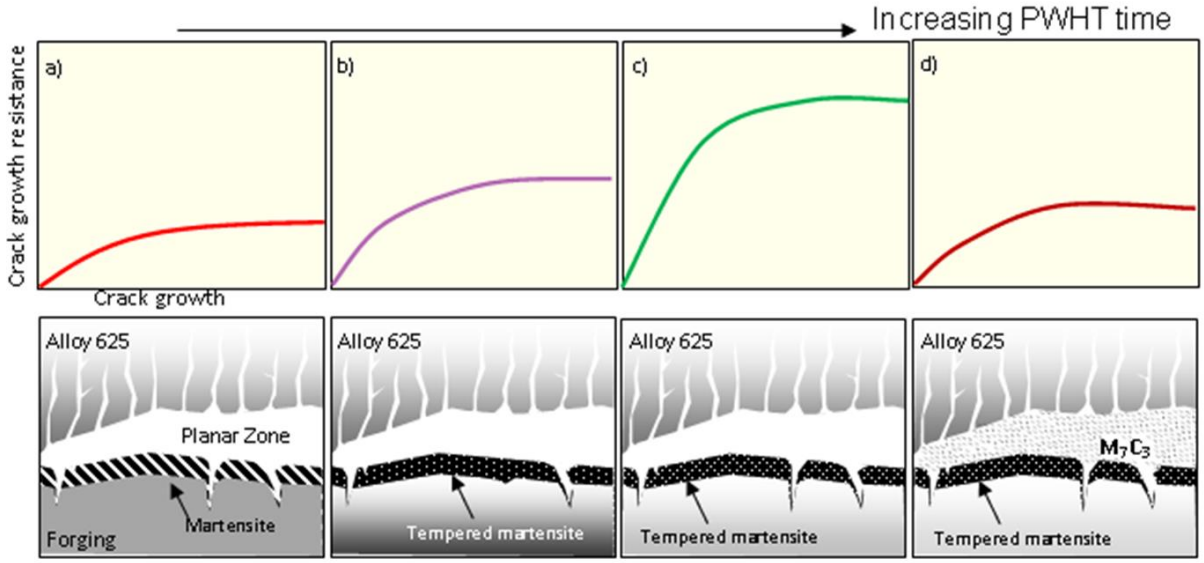

-Untempered HAZ
-Martensite is susceptible to HE
-Poor resistance to HE

-Tempered HAZ
-Decarburisation in HAZ
-Carbon diffusion into planar zone
-Improved resistance to HE

-Tempered HAZ
-Decarburisation in HAZ
-Planar zone approaching carbon saturation
-Further improvement in resistance to HE

-Tempered HAZ
-Extensive decarburisation in HAZ
-Planar zone is supersaturated with carbon, M_7C_3 forms.
-Reduction in resistance to HE

Figure 5-11 - An illustration of the relationship between resistance to hydrogen embrittlement and microstructure, as PWHT time is increased from the as-welded condition

CHAPTER 6. In-situ Measurement of Strain Evolution during PWHT

6.1 Introduction

The favoured methods for the characterisation of welding residual stress tend to be those that are non-destructive, such as neutron diffraction; however these are often associated with high-cost and lengthy experimental planning. Masabuchi [64] has classified stress characterisation techniques into three categories:

i. Stress-relaxation
ii. Cracking-related methods
iii. Diffraction based methods

Examples of stress-relaxation characterisation techniques include sectioning, hole drilling and contour methods, though variations do exist. Using the sectioning technique, strain gauges are mounted on the sample before machining takes place. By cutting, the stress within the sample is released, whereupon it may be measured. The basic principle of hole drilling is similar, a strain gauge rosette is placed on the sample to measure strain relaxation, and the stresses are calculated from the strain changes after the hole is drilled. Subsurface stress information is available, but is usually limited to less than 1mm from the surface [58]. In the contour method, the section is cut by electro-discharge (ED) machining, and the topography of the surface is measured to determine one or more components of residual stress [187]. The method is based on inferring prior residual stresses from the deviation of the cut from flatness [58]. Though limited examples are shown, the disadvantages of the techniques are obvious – they are destructive. Stress determination using hydrogen or stress-corrosion induced cracks is also a destructive process. The basic principle is to qualitatively determine the two-dimensional stress distribution by assessing the number density of cracks on a surface.

Diffraction techniques, such as X-ray diffraction, high-energy synchrotron x-ray diffraction, and neutron diffraction differ in that little sample preparation is necessary (except

for in experiments requiring stress free reference samples). Both the synchrotron x-ray and neutron methods require large scale facilities, with a high associated cost. However, the benefits, in terms of both the ability to perform in-situ experiments non-destructively, such as deformation experiments, or heat-treatments, is unparalleled. Another advantage of using neutron diffraction is a high penetration power (centimetre scale in most engineering materials). The spatial resolution is also adaptable during the experiment, enabling macroscopic engineering stresses, average phase specific stress and intergranular stress to be determined.

6.1.1 **Measurement of residual stress by diffraction**

Most metals consist of crystallites (grains), that are fused together to form the bulk material. When such a material is placed under an externally applied stress, elastic strains are produced within the crystal lattice (distributed between individual crystallites). The same principal applies to residual stress; stresses that are below the yield point of the material are accommodated by the interatomic strains in the grains within. Measuring the interatomic strains, with knowledge of the material properties of the component being measured, leads to calculation of stress. X-ray and Neutron diffractometers can be used to measure the atomic lattice parameter within a material, then, by measuring the stress-free lattice parameters, the degree of deformation may be determined. The advantage of neutron diffraction methods is a larger penetration depth, compared to X-ray diffractometers [188]. Penetration depths up to a few centimetres inside a metal is possible using neutron diffraction, however it is still possible to measure near-surface strains; in fact, typical sampling (gauge) volumes can range from 0.2 to 1000mm^3 [189].

6.2 Experimental Procedure

6.2.1 General Procedure

The primary objective of the work described is to use neutron diffraction to quantify competitive strain evolution at more than one point during heat treatment of the dissimilar joint. Monitoring multiple points is, however, complicated by the multiphase nature of the sample. Secondary to this, ex-situ measurements are carried out to measure residual stress relaxation before and after heating. The heat treatment parameters are selected to be comparable to industry standard PWHTs. Heating is applied using controllable, electric heating blankets.

In selecting the appropriate sampling times, the limited PWHT period must be considered. These sampling times must feature a compromise between the number of points that can be measured during the heat treatment, and an acceptable degree of measurement error. Additional measurement complexity is caused by interfacial regions, in which more than one phase is present within the sampling volume of the neutron beam. The described procedure can be considered an expansion on the in-situ heat treatment method described by Chen et al [190], in which a single point in a ferritic steel was monitored during PWHT. In the current study, three measurement points are monitored during the heat treatment: the ferritic side, the austenitic side, and the dual phase interface region.

In the case of buttered dissimilar welds, in which multiple welding passes are involved, the HAZ experiences a heating transient as each weld bead is laid. Whilst the HAZ itself does not melt, the melting point is approached, close to the fusion boundary, and metallurgical changes may, therefore, be expected. Dissolution and re-precipitation, as well as texture changes, may occur with each successive pass [65]. To assess the extent of mixing in sampling regions expected to be dual-phase, microstructural analysis is carried out using a

scanning electron microscope (SEM). Chemical analysis was facilitated by using SEM electron dispersive X-ray spectroscopy (EDX).

6.2.2 **Materials and Sample Preparation**

An ex-service AISI 8630 low alloy steel forged hub was water jet machined to create an 'L' shaped component (a plate with backing bar) approximately 250mm long. The hub was metal inert gas (MIG) welded with Alloy 625 (ErNiCrMo-3) using a layering procedure. The nominal compositions of the joint and welding procedure are the same as those used in the fabrication of specimens for the investigation of PWHT, Chapter 5.

The welded specimen was electro-discharge (ED) machined to create two 100mm long plates. Sample thickness is an important consideration when preparing a specimen for strain measurement using neutron diffraction (ND). By shortening the length of the beam path the counting times are reduced, meaning the point-to-point measurement resolution can be increased. Typical industry PWHT times are between 5 and 10 hours, hence a compromise had to be found. The sample thickness had to be small enough such that the number of points during the hold temperature could be maximised whilst minimising stress relaxation through the machining operations. With this in mind, the pair of plate samples was further ED machined to 99x100x14mm, with the dissimilar-interface situated in the middle. The width of the sample therefore contained 2-3 weld beads. Maximum stress relaxation due to machining was also likely to be found in the normal direction. A diagram of the dissimilar joint design, welding sequence, and the region extracted for ND measurements, is given in Figure 6-1.

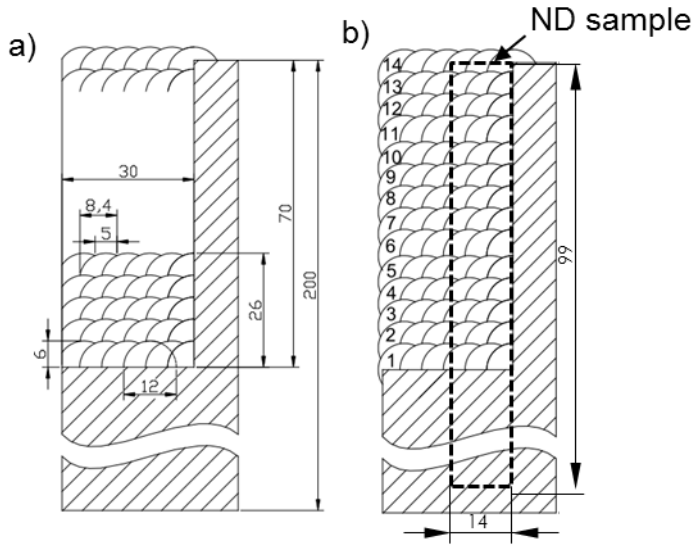

Figure 6-1 - a) Joint design and b) welding sequence used in the fabrication of the dissimilar joint. Outlined is the 14mm wide specimen used in the ND measurements

The main challenge for accurate measurement of stress fields in weldments using neutron diffraction lies in the accurate determination of strain- free lattice spacing [58], [191]. For this experiment, stress free (d_0) sample combs were designed to accommodate a gauge volume of 3x3x3mm (and hence a diagonal of 4.24mm). Two stress-free combs were created; one with vertical and one with horizontal teeth allowing for measurement of the three principal stress directions. ED cutting with Ø0.25mm wire enabled the precise machining of the sample comb with 5x5mm teeth, Figure 6-2. Additional teeth were machined in order to allow the d_0 samples to be isolated when clamped in place during the strain measurements.

Figure 6-2 - Photographs of ED machined specimens prior to testing, together with scale bar (cm)

After the ND experiment, a transverse section was ED machined from the joint in preparation for microstructural analysis. The specimen was ground using SiC paper abrasives. Cloths were used to progressively polish with fine diamond pastes of 9, 3 and 0.25µm. A diluted suspension of colloidal silica (OP-U) was used for the final polishing step. The morphology of the polished section was examined using the backscatter imaging mode of an FEI Sirion scanning electron microscope. Princeton Gamma Tech EDX spectroscopy equipment was used to perform chemical analyses across the interface.

6.2.3 **Neutron Diffraction**

Non-destructive strain measurements were made using neutron diffraction on the ENGIN-X time-of-flight diffractometer at ISIS, Rutherford Appleton Laboratory in Harwell, UK. The instrument concentrates a pulsed neutron beam which comprises of a continuous spectrum of thermal neutrons. Two fixed time-of-flight detectors located at a 2θ angle of ±90 degrees record diffraction patterns corresponding to two orthogonal components of strain simultaneously, Figure 6-3.

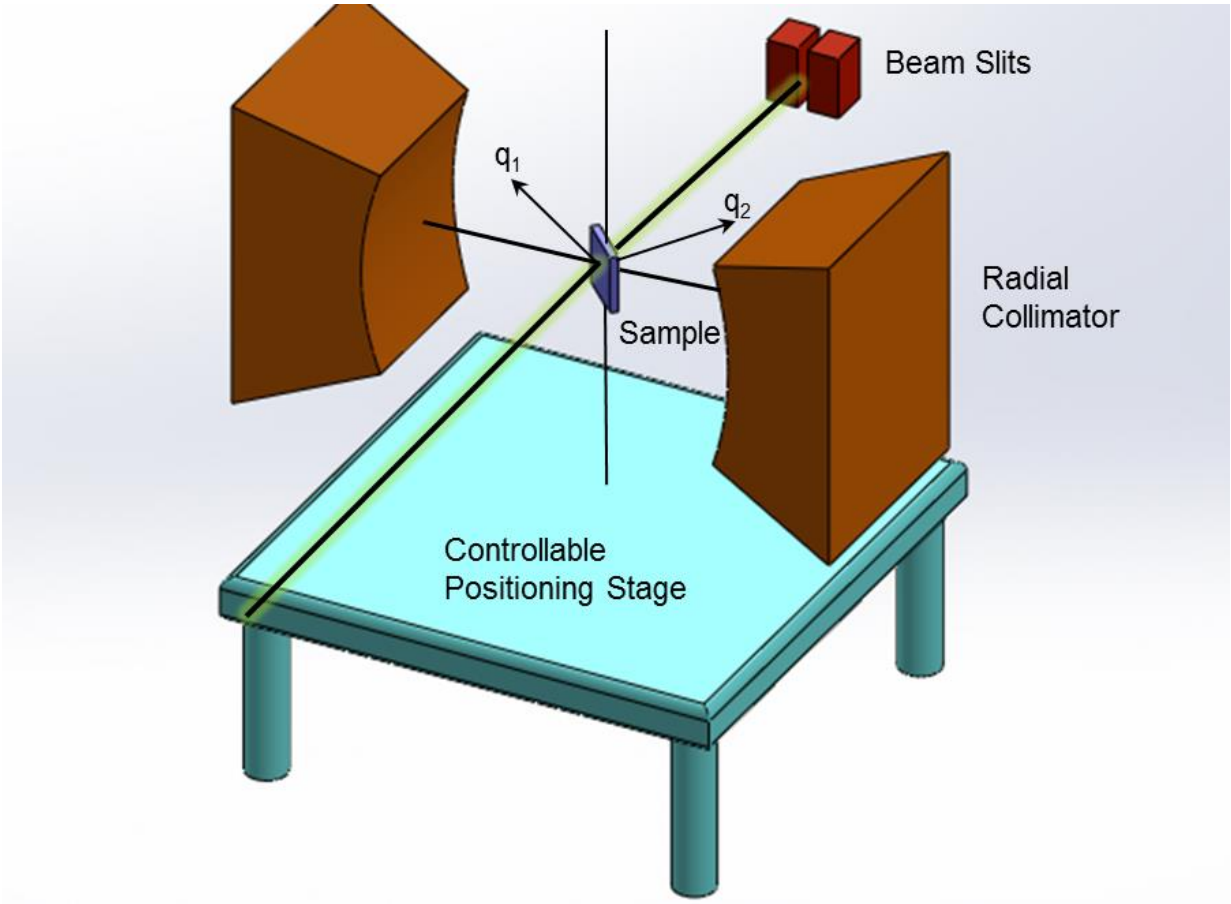

Figure 6-3 - A 3D model of the ENGIN-X instrument at ISIS. Radial collimators are shown at a 90° scattering angle, each of which would be positioned in front of a bank of neutron detectors. q_1 and q_2 indicate the strain directions measured by the instrument. Adapted from [192].

In order to measure the third component the sample needs to be rotated by 90 degrees to bring the sample direction which was previously vertical into the plane of diffraction. Since the PWHT process is irreversible, in this study, two separate, identical samples were used to measure all three strain components in-situ using neutron diffraction.

Heat treatment was facilitated by designing two individually controllable, ceramic sintered alumina heating elements. The heating elements were positioned and clamped in place adjacent to the ND measurement location, creating a 'neutron transparent' window. Temperatures were monitored in regions near the fusion zone, but away from the regions subject to stress measurement. Holes were drilled to mid-thickness of the sample and

thermocouples placed inside, creating an interference fit. Calcium-magnesium silicate insulation was placed on the specimens and manipulated in order not to interfere with the beam path. The whole assembly was secured to the positioning stage using a water-cooled sample holder, Figure 6-4. Specimen alignment was ensured by incrementally rotating the specimen and measuring the sample position with a pre-calibrated theodolite.

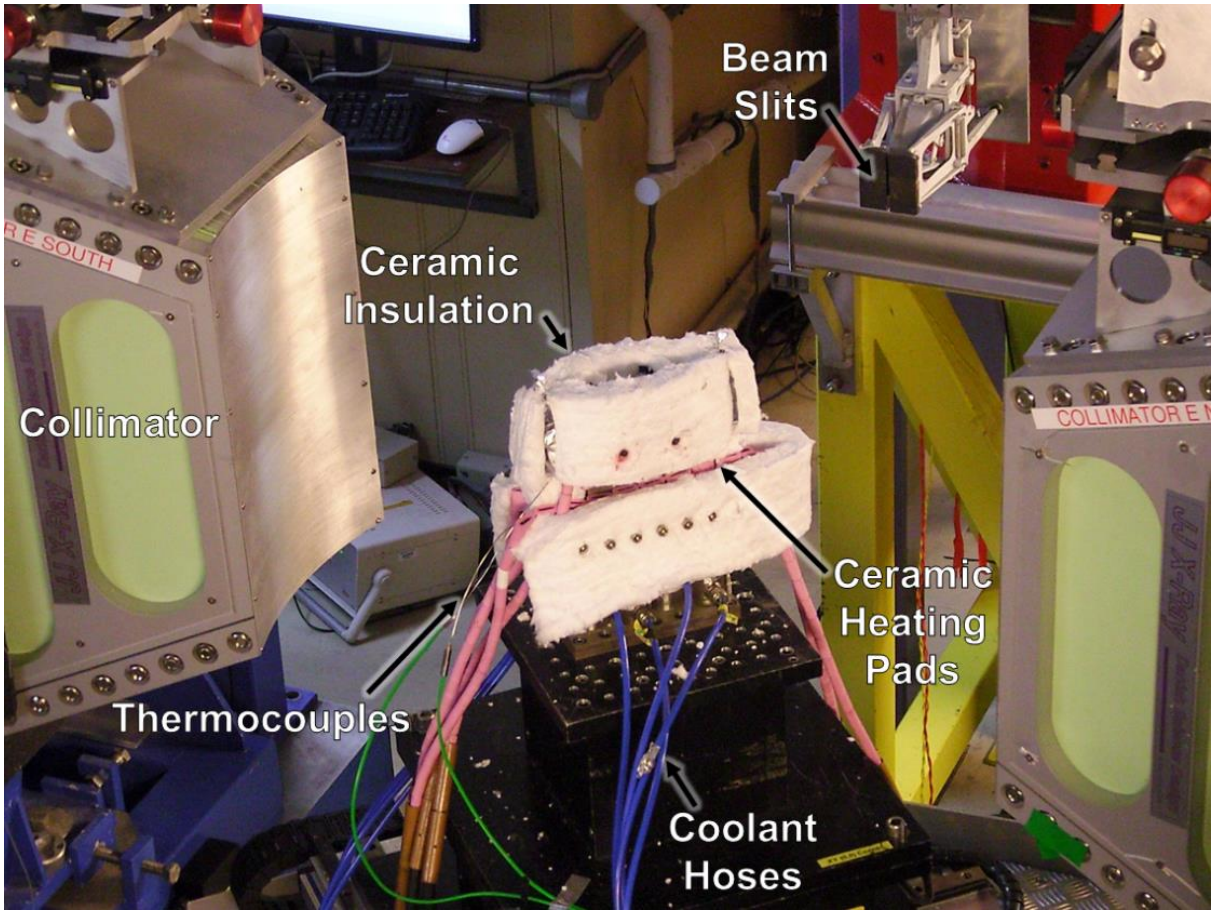

Figure 6-4 - Photograph of experimental set-up during PWHT of the as-welded sample

Three measurement points were selected for monitoring during heat treatment: one at the interface and two at 2.67mm from the interface on either side into the parent and weld metal. In order to monitor competitive strain during the experiment, the positioning stage was set to alternate between the steel and the nickel sides during the temperature ramp. During the PWHT holding period, all three measurement points were monitored. A holding time of 345 minutes was used for each test. After heat treatment, the heating pads were

removed and the sample was allowed to cool in air. During cooling, the stage was again set to alternate between the steel and Alloy 625 measurement points. A plot of measured temperature and the respective materials being measured is seen in Figure 6-5.

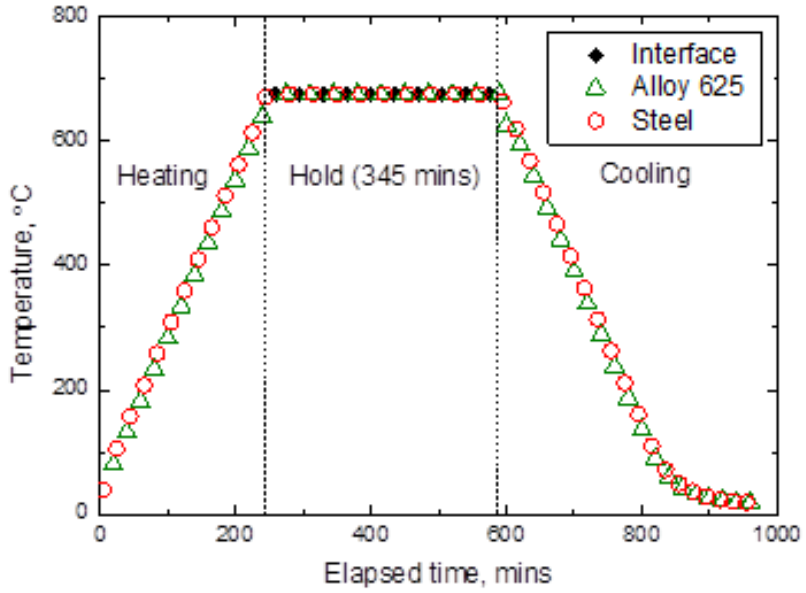

Figure 6-5 - Measurement points and temperature during the PWHT cycle

Ex-situ measurements across the interface were made before and after each heating-experiment. A schematic of the points measured in-situ and ex-situ, and their placement with respect to the interface, is shown in Figure 6-6. Lattice parameter measurements in the stress-free samples followed the same general procedure as the stressed samples; however, the holding time was reduced. A summary of all necessary measurements for the ex-situ and in-situ experiments is given in Table 6.

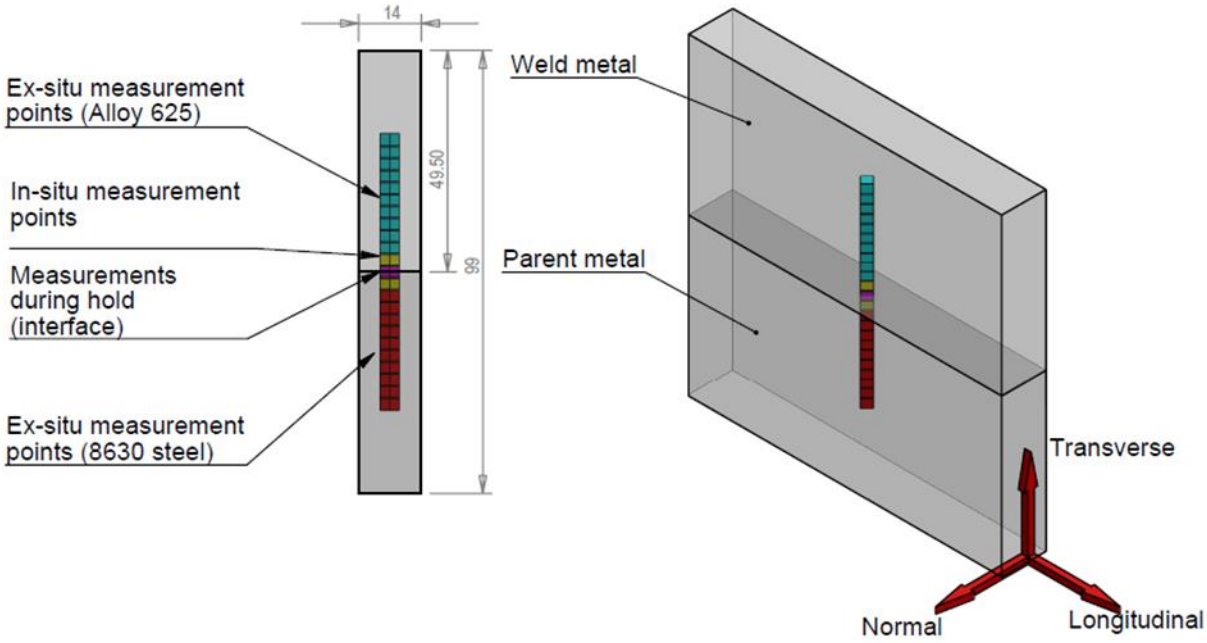

Figure 6-6 - Sample geometry and measurement points. Plates were welded in the longitudinal direction

Table 6 – Ex-situ and in-situ experimental measurements

Measurement Reference	Sample Description	Measurement Type	Principal Measurement Directions
1	D_o stress-free comb (vertical cuts)	Before PWHT	Longitudinal and normal
2	D_o stress-free comb (vertical cuts)	During heat treatment	Longitudinal and normal
3	D_o stress-free comb (vertical cuts)	After PWHT	Longitudinal and normal
4	D_o stress-free comb (horizontal cuts)	Before PWHT	Transverse and longitudinal
5	D_o stress-free comb (horizontal cuts)	During heat treatment	Transverse and longitudinal
6	D_o stress-free comb (horizontal cuts)	After PWHT	Transverse and longitudinal
7	As-welded sample 1	Before PWHT	Longitudinal and normal
8	As-welded sample 1	During heat treatment	Longitudinal and normal
9	As-welded sample 1	After PWHT	Longitudinal and normal
10	As-welded sample 2	Ex-situ, before PWHT	Transverse and longitudinal
11	As-welded sample 2	During heat treatment	Transverse and longitudinal
12	As-welded sample 2	After PWHT	Transverse and longitudinal

6.3 Data Analysis

6.3.1 Calculation of Residual Stress

The process behind residual stress measurement during in-situ heat treatment is more complex than that of ex-situ tests. The general procedure for testing at a fixed temperature involves the determination of the d-spacing spacing d_{hkl} using Bragg's Law:

$$d_{hkl} = \frac{\lambda_{hkl}}{2\ sin\ \theta_{hkl}} = \frac{ht_{hkl}}{2m_n L\ sin\ \theta_{hkl}}$$

Eqn. 18

for which h, k and l denote the crystallographic planes, λ_{hkl} is the wavelength of the diffracted neutrons, θ_{hkl}, is the angle of diffraction, h is the Planck constant, m_n is the neutron mass, L is the length of the neutron's flight path and t_{hkl} is the time of flight (ToF). The measurement volume was bounded by the intersection of the diffracted and incoming beams and values that arose from such a measurement corresponded to the average elastic strain within. The elastic strain ε_{xx}, or change in the lattice parameter, encompassed the measurements of the d_0 sample comb for each specific point and direction such that:

$$\varepsilon_{xx} = \frac{d_{xx} - d_0}{d_0}$$

Eqn. 19

However, this simplistic approximation does not consider elastic anisotropy in the measurements.

ENGIN-X permits the collection of simultaneous diffraction peaks from multiple crystals. The average strain can therefore be obtained using a Rietveld refinement of the entire diffraction spectrum [193]. By measuring more than one diffraction peak, the associated strain uncertainty was lowered, effectively improving counting times [194]. Based on continuum mechanics, the calculation of residual stress was achieved using Hooke's law. Stress was calculated from the strain measurements, in the three mutually-orthogonal directions, and takes the general form:

$$\boldsymbol{\sigma} = \mathrm{c}\,\mathbf{A}\,\boldsymbol{\varepsilon}$$

Eqn. 20

Where:

$$\boldsymbol{\sigma} = \left[\sigma_{\mathrm{trans}}, \sigma_{\mathrm{long}}, \sigma_{\mathrm{norm}}\right]^{\mathrm{T}}$$

Eqn. 21

$$\mathbf{A} = \begin{bmatrix} 1-\nu & \nu & \nu \\ \nu & 1-\nu & \nu \\ \nu & \nu & 1-\nu \end{bmatrix}$$

Eqn. 22

$$\boldsymbol{\varepsilon} = \left[\varepsilon_{trans}, \varepsilon_{long}, \varepsilon_{norm}\right]^{T}$$

Eqn. 23

The constant, c, is defined as:

$$\mathrm{c} = \frac{\mathrm{E}}{(1+\nu)(1-2\nu)}$$

Eqn. 24

Where E is the Young's modulus and ν is the Poisson's ratio of the material.

6.3.2 **Interface Stress Calculations**

In dual-phase materials, the gauge volume may intersect material with two highly differing lattice parameters and phase fractions. To account for this, the strain was calculated separately for each material, thus the true strain within the gauge volume lay between two single-phase data points. As a result of differences in material properties, however, an interpolated lattice parameter (and therefore strain) could not be used to calculate a single value of interface stress. A modification of Eqn. 20 was therefore necessary:

$$\boldsymbol{\sigma}_{int} = p\,[\mathrm{c}_1\mathbf{A}_1\,\boldsymbol{\varepsilon}] + (1-p)[\mathrm{c}_2\,\mathbf{A}_2\,\boldsymbol{\varepsilon}]$$

Eqn. 25

Where p is the proportion of the gauge volume lying within the parent material and $\boldsymbol{A}_1 = \{\boldsymbol{A} : v = v_1\}$ and $\boldsymbol{A}_2 = \{\boldsymbol{A} : v = v_2\}$, similarly, $c_1 = \{c : v = v_1 and\ E = E_1\}$, and $c_2 = \{c : v = v_2 and\ E = E_2\}$ where E_1 and E_2 are the Young's moduli and v_1 and v_2 are the Poisson's ratios in the parent and weld metals, respectively. For both materials, a Poisson's ratio of 0.3 was used. Young's moduli of 207 GPa and 200 GPa were used to calculate stress in the steel and Alloy 625 sides, respectively. Interface data points were calculated under the assumption that the sample volume intersected the two sides equally.

6.3.3 Strain Calculations during Heating

For the in-situ experiments, the general strain calculations at each temperature point, T, proceeded under the assumption of linear thermal expansion and contraction of the stress-free samples. Therefore, Eqn. 20 becomes Eqn. 26 where the $d_0(T)$ values are determined from a plot of lattice parameter versus temperature for a given strain direction:

$$\varepsilon_{xx}(T) = \frac{d_{xx}(T) - d_0(T)}{d_0(T)}$$

Eqn. 26

By monitoring the thermal expansion and contraction, and applying a least-squares fit, interpolated $d_0(T)$ values could then be calculated for each material system and temperature.

6.4 Results

6.4.1 Microstructure and chemistry

A cross-sectional image from the heat-treated plate specimen after the ND experiment is presented Figure 6-7a. The microstructure of the interface regions included a coarse-grained HAZ within the ferritic steel, and a 10μm wide, apparently featureless, planar zone

within the FCC nickel alloy side Towards the bulk weld metal, cellular and columnar dendrites were found, which had formed due to a breakdown in the stability of the planar front. A small fraction of the interface was occupied by discontinuous partially mixed zones, or 'swirls' of parent metal that had penetrated into the weld as a result of localised fluid flow during welding. 'Fingers' of weld metal, which had penetrated short distances along prior austenite grain boundaries in the steel, were also present

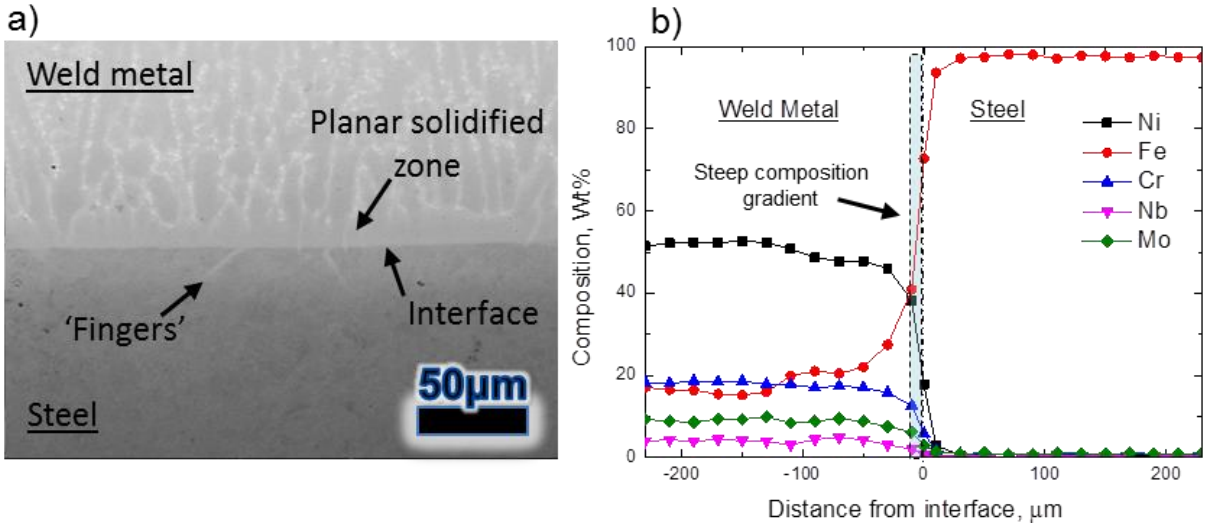

Figure 6-7 - SEM microstructural examination a) backscatter image of the fusion zone and b) EDX chemical distribution across the interface

Chemical analyses were performed by rastering the SEM electron beam over 20x80µm regions and collecting EDX spectra from successive zones, after traversing the stage by increments of 20µm. Therefore, each point in the graph, Figure 6-7, corresponds to the average chemical composition within a 10µm region either side of the data point. Bulk weld metal was present <200µm from the interface. The position of partially-mixed weld metal was sufficiently far from the first ND measurement point in the Alloy 625. Similarly, the first point within the steel does not contain elevated levels of nickel. As a result, multiphase fitting of the ND spectra was only considered necessary for the interface regions. A steep composition gradient was found within the weld metal that corresponds to the planar

solidified region. This region was characterised by a rapid increase in nickel and chromium, with a concomitant reduction in iron. The composition at the planar/cellular region corresponded to weld dilution of approximately 45%.

6.4.2 **In-situ monitoring of strain redistribution**

In order to differentiate between lattice parameter changes due to stress-relief and those due to thermal expansion in the plate sample, it was necessary to measure the stress-free sample under the same heating and cooling conditions. As an example, a plot of stress-free (d0) lattice parameter changes during heat treatment is shown in Figure 6-8, for the steel and Alloy 625 sides in the transverse direction.

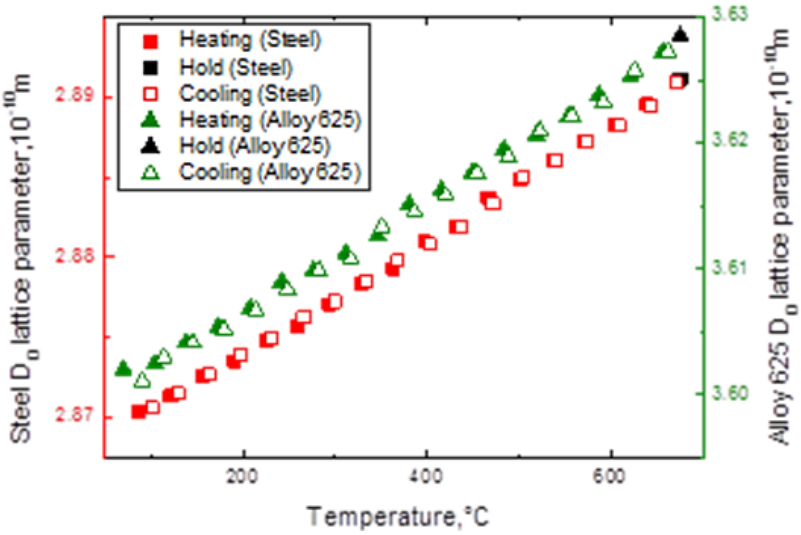

Figure 6-8 - Stress-free measurements of the lattice parameter in the transverse direction in the steel and nickel sides

Assuming no auxiliary phase precipitation within the metals, a sample which has been sufficiently stress-relieved will exhibit linear thermal expansion and contraction. A linear regression fit was applied to the data, allowing for d0 values to be calculated as a function of temperature. The calculated fitting parameters are given in Table 7.

Table 7 - The parameters used to calculate a linear regression fit to the stress-free lattice parameter during heating and cooling

Sample Reference	Measurement Direction	Position	m (10^{-15}m/°C)	c (10^{-10}m)	R^2
d_0 1	Longitudinal	2.67mm into steel	4	2.8661	0.9991
d_0 2	Transverse	2.67mm into steel	4	2.8669	0.9988
d_0 3	Normal	2.67mm into steel	4	2.8669	0.9986
d_0 4	Longitudinal	2.67mm into Alloy 625	6	3.5949	0.9952
d_0 5	Transverse	2.67mm into Alloy 625	4	3.5976	0.9972
d_0 6	Normal	2.67mm into Alloy 625	6	3.5973	0.9976

The parameters for the linear regression line of best fit given in Table 7 are defined by the equation:

$$d_0 = mT + c$$

Eqn. 27

Where T is the temperature in °C. Calculated R^2 values approaching unity for all d0 temperature plots indicated a highly linear relationship between the lattice expansion and temperature. Differences in offset, c, were attributed to slight variations in chemistry between measurement points.

Plots of the lattice parameter expansion in the longitudinal, normal and transverse directions, during the heating cycle, are given in Figure 6-9. To monitor competitive expansion and contraction between the two different metals, each graph shows the opposing steel and Alloy 625 sides. The two measured regions lie 2.67mm into the steel and Alloy 625 sides. Due to insufficient neutron counts (and therefore high error), a significant portion of data from the Alloy 625, normal direction measurements was unavailable. Weak diffraction patterns in the Alloy 625 may arise from insufficient counting time or from the creation of highly textured material during solidification, following welding [195].

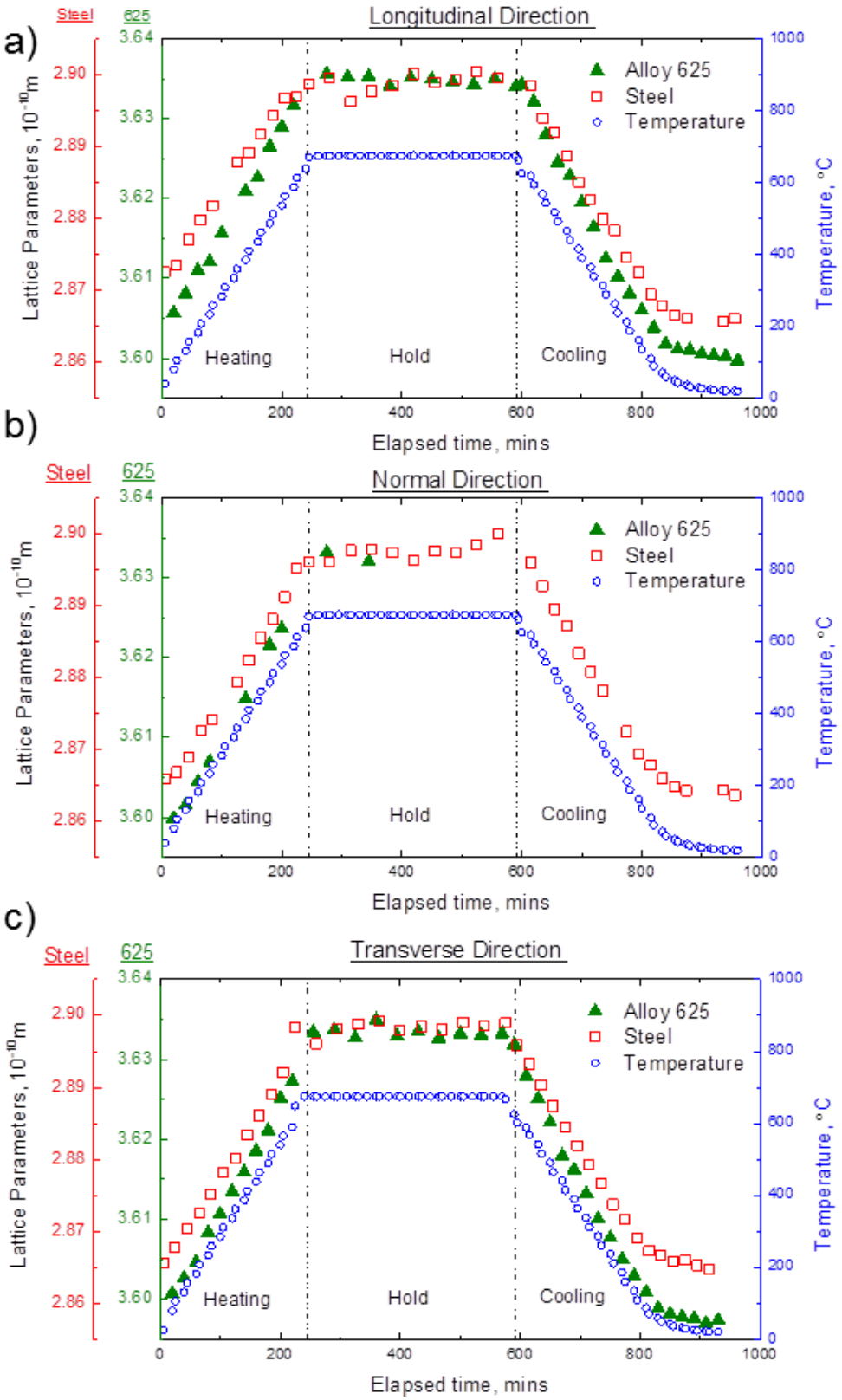

Figure 6-9 - Measurements of lattice parameter either side of the dissimilar interface during PWHT a) longitudinal b) normal and c) transverse directions

In Figure 6-10, plots of measured strain are presented during the heating cycle, after application of calculated stress-free lattice parameters, given in Eqn. 26. Individual error bars are presented for each point during heating and were determined using associated Rietveld refinement errors.

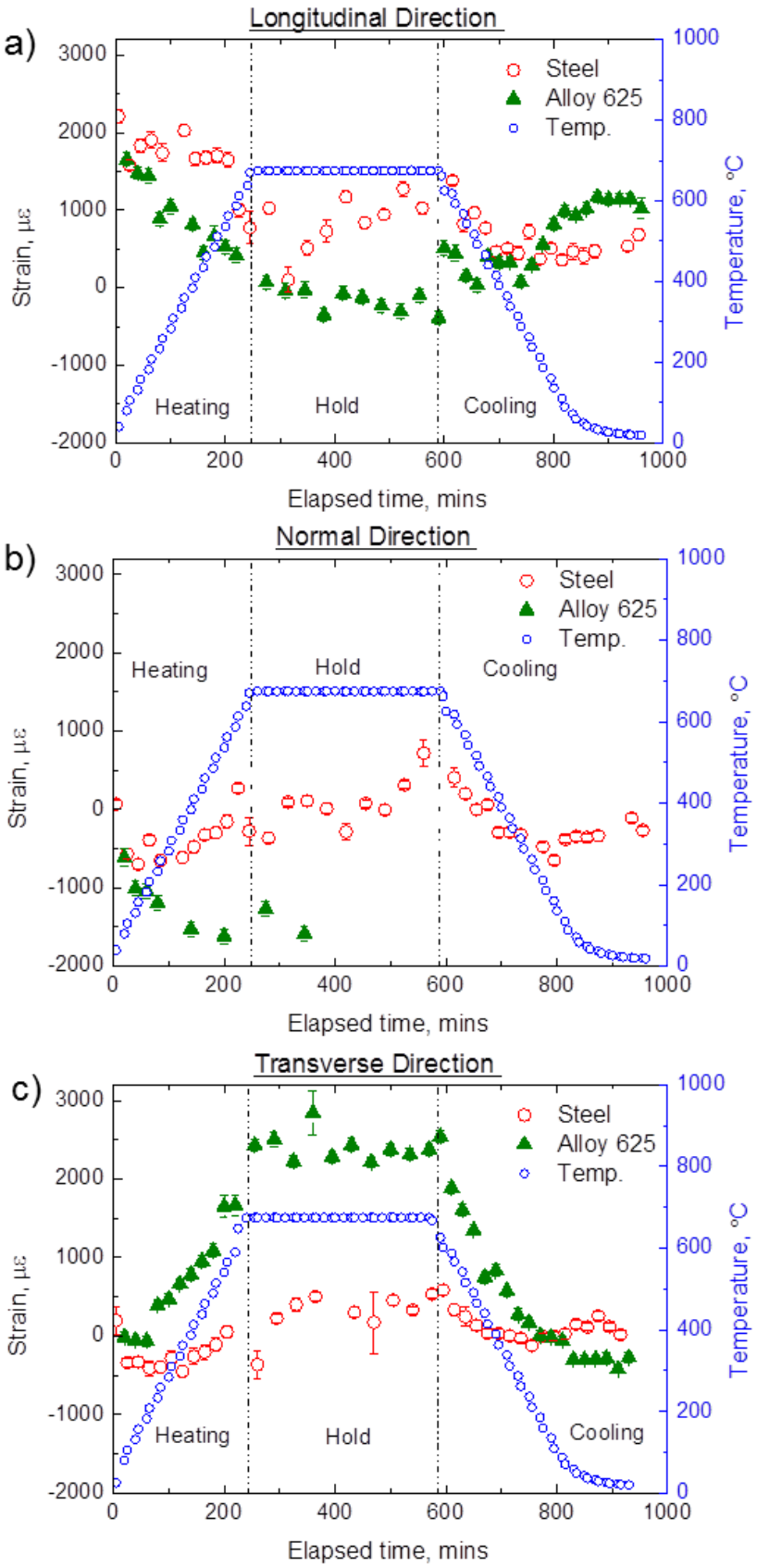

Figure 6-10 - Measurements of residual strain either side of the dissimilar interface during PWHT a) longitudinal b) normal and c) transverse directions

By alternating between the two measurement points either side of the interface, a satisfactory plot of strain evolution during PWHT was achieved. In the longitudinal direction, Figure 6-10a, the Alloy 625 had a continuous strain reduction throughout both the ramp and holding periods. During the PWHT hold period, the longitudinal Alloy 625 direction came out of tension and started to become compressed. At the same time, the opposing steel side remained in constant tension throughout the hold. Upon cooling, at a temperature of approximately 380°C, the Alloy 625 side re-entered a state of tension. Subsequent cooling to room temperature saw an overall strain reduction on both sides, however the Alloy 625 became the more highly strained material, whereas before PWHT the opposite was true. In the transverse direction, within the steel side of the sample, the degree of strain reduction was lower, compared to the longitudinal strain measurements. The Alloy 625 did, however, move from a condition of low strain to a slightly compressed state during the heat treatment.

Residual strain profiles up to 27.5mm either side of the fusion boundary are presented in Figure 6-11. The measurements were completed independent of the in-situ tests, and at room temperature. Each data point is associated with similar room temperature measurements of stress-free lattice parameter, Eqn. 19. At the interface, where two major phases were observed, three calculated strain points are present. The three points assume the following i) Rietveld fitting to the austenitic (Ni) phase only ii) fitting to the ferritic (Fe) phase only iii) strain values, with a 50% strain contribution from each material. The same method was not used away from the interface, as microstructural analyses indicated that the data points lay within unmixed regions. Before PWHT, the highest strain was associated with the interface region, in the longitudinal direction. The mutually orthogonal directions are most strained 5-

15mm into the weld metal, which translates to the highest degree of stress relaxation after PWHT.

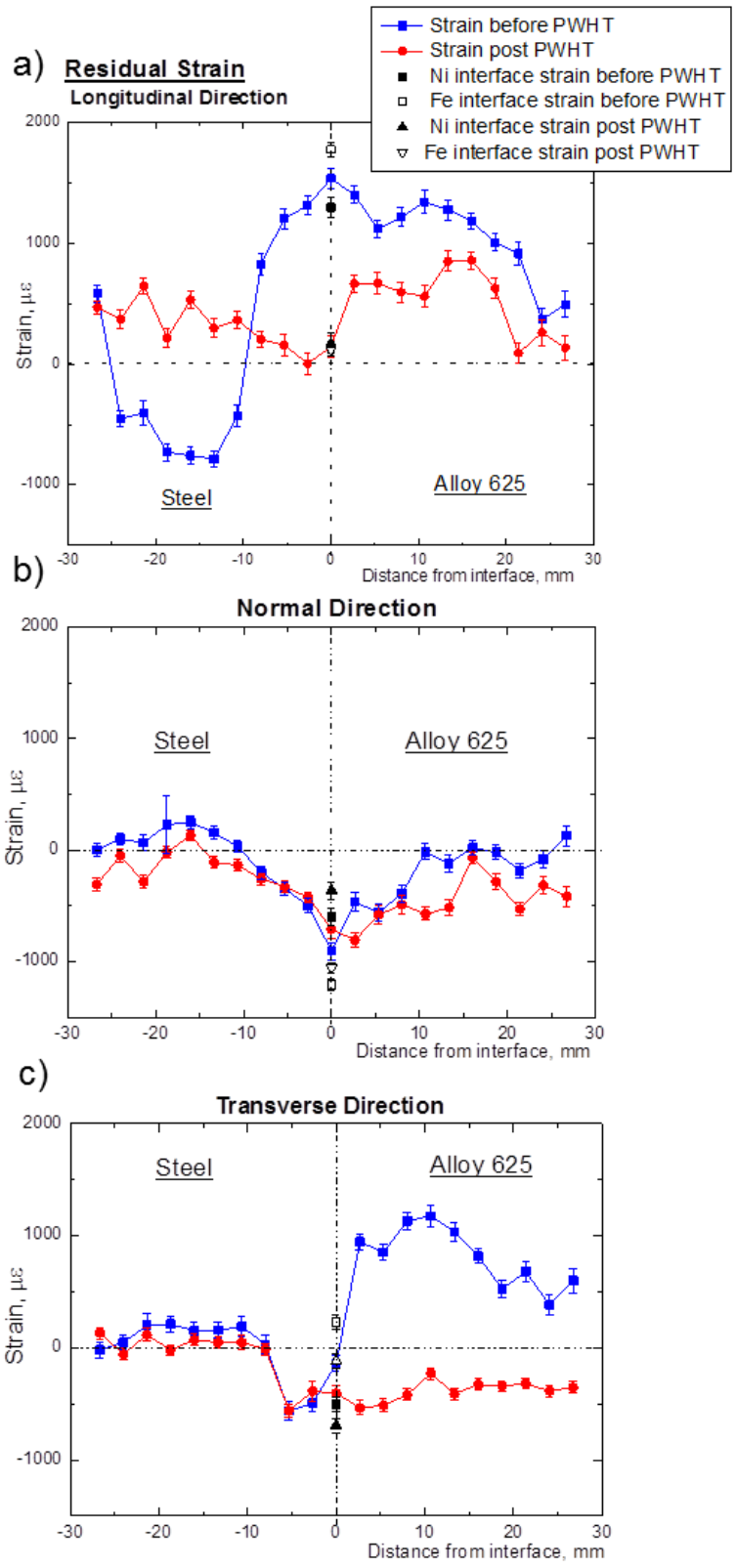

Figure 6-11 - Measured strain before and after PWHT. Fusion boundary is located at 0μm. Unmixed interface points have been calculated and placed at the dual-phase region.

Residual stress profiles across the dissimilar joint are presented in Figure 6-12, before and after heat treatment. Strain errors from the Rietveld analysis are combined, so that individual stress error bars account for the three strain directions. Interface error bars were calculated using the maximum error from the three measured strain points. The results indicated a considerable degree of stress relaxation for all three measurement directions. The highest relative and absolute stress relaxation occurred within the Alloy 625. In the transverse and longitudinal (welding) directions, an approximately 700MPa stress range was reduced to 300MPa, after PWHT.

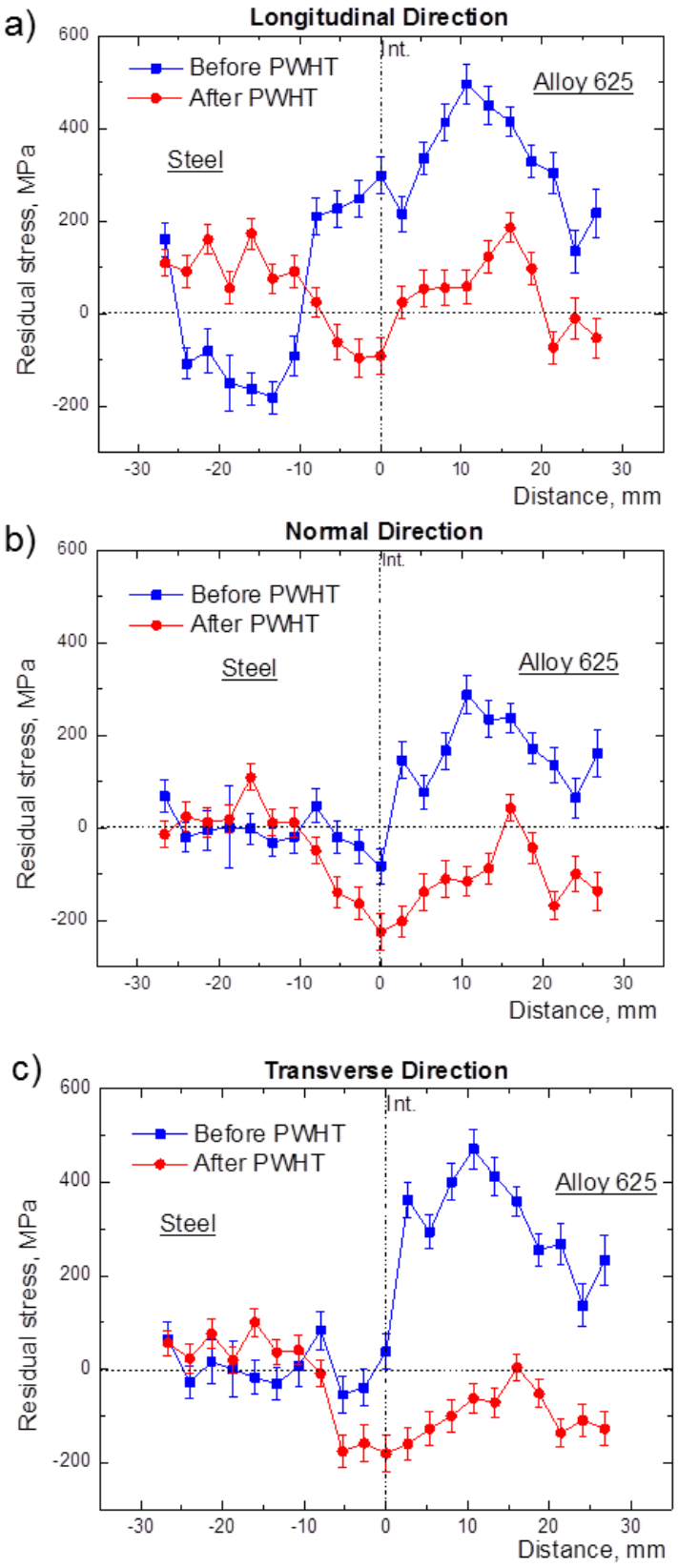

Figure 6-12 - Calculated residual stress values before and after PWHT. Fusion boundary is located at 0μm.

Of the two points either side of the interface that were monitored throughout the PWHT thermal cycle, the highest degree of stress relaxation was found to occur in the Alloy 625 side, in the transverse direction. This was evidenced by the lattice parameter gradients, which were shallower during cooling in the unstressed condition when compared to the stressed condition, Figure 6-9c and Figure 6-8. Corresponding strain plots showed that this was due to the state of the location changing, from tension to compression, after PWHT. Residual stress is redistributed in this region such that the monitored point in the Alloy 625 transforms from 363MPa to -160MPa, after heat treatment. A summary of the average stress in both the Alloy 625 and 8630 is shown in Table 8.

Table 8 - Average residual stress values in each of the weld and parent materials, before and after PWHT

	Longitudinal Stress (MPa)		Normal Stress (MPa)		Transverse Stress (MPa)	
Material	As-welded	PWHT	As-welded	PWHT	As-welded	PWHT
Alloy 625	331.1	46.5	168.2	-105.6	319.2	-94.1
8630	7.4	62.7	-1.9	-17.6	0.0	0.8

6.5 Discussion

Upon rapid cooling from high temperatures, such that the steel base metal is in its austenitic state, high alloy steel joints can form unfavourable martensitic structures of high hardness. As a result of this, PWHT temperatures are generally kept below the $A1_c$ transformation temperature. However, in a dissimilar steel-nickel alloy weldment, discontinuities in the interface can result in localised areas of relatively higher nickel content. Such regions have been referred to as ‘discontinuous partially mixed zones’ (PMZs), manifesting as ‘swirls’, ‘peninsulas’, or ‘islands’ of parent material that have been swept into the weld metal adjacent to the interface. Within these regions, some alloying with nickel can have the effect of stabilising the austenite to a temperature lower than that of the heat

treatment temperature. Phase changes may therefore be expected during PWHT. In addition to quantifying residual stress, ND is advantageous as it allows for the quantification of phase volume fractions by means of measuring relative peak intensities [58]. To verify this phenomenon, the equipment monitored the interface at room temperature and at the PWHT temperature. Either side of this, the two regions neighbouring the interface were also monitored during the whole PWHT cycle. Despite a relatively high PWHT temperature, no evidence of the re-austenitisation phenomenon was found when comparing room temperature and 675°C time of flight spectra. The thermodynamic simulations, Section 4.2.3, indicate that a further increase in PWHT temperature (above 700°C) would create a scenario where a phase change would be observed. However, due to beamline availability PWHT above 700°C was not tested in this study. Heat treatment experiments that encompass different temperatures constitute future work.

In order to monitor competitive strain evolution, two points at 2.67mm either side of the dissimilar interface were monitored throughout the whole of the heat treatment. Ex-situ measurements have, however, shown that the highest degree of stress relaxation was approximately 10mm into the weld metal. In order to monitor strain evolution at more points during heating, the described procedure would have to be modified. There are two possible methods by which this could be achieved: (i) manufacture and measure additional plate samples (ii) reduce the width of the plate specimens in order to improve (reduce) counting times. In the former method, it is necessary to assume an identical stress distribution in each sample, however this is unlikely. Furthermore, realising identical heating and cooling rates over multiple samples is problematic. To address the second point, the relief of residual stress by the machining operations would need to be accounted for. It should be noted that whilst error bars are present on the ex-situ stress profiles across the interface, these do not account for any differences in strain between the two plates used. In practice, residual stresses

have been shown to vary from point to point, even within a single component [195]. It may therefore be the case that the error associated with using two plates is far greater. In instruments where two directions of strain can be measured at once, as in the case in ENGIN-X, rotating the stage allows for the third strain direction to be measured. Whilst this reduces the error associated with using two plates, it also reduces the number of strain points measured during the heating cycle.

A 'rule of mixtures' approach was used to calculate the residual stress at the interface regions, Eqn. 25. The method assumed that, following individual measurement of strain in each side, the sampling volume intersected both sides of the interface equally. Whilst the calculations may allow for modification of phase volume fractions, the method may be developed further where higher accuracies are required. For example, exact determination of phase constitution in dual phase regions would be beneficial.

In this experiment, the weld metal was shown to have solidified, initially, in a planar manner. Whilst the planar region is small, it is important to note the lack of homogeneity across the fusion boundary. The steepest composition gradient was found within the planar solidified zone, rather than neighbouring cellular and dendritic areas. This gradient might have been magnified by the solidification mode, as cellular and dendritic solidification modes are associated with smaller composition changes [184]. The textured nature of the weld metal is likely to be the cause of low intensity diffraction peaks, which resulted in increased fitting error, for the set-counting times. This phenomenon was more pronounced at the fusion boundary.

The J-R curves, Section 3.3.3 and 5.2.2, generated by SSR bend testing in a chloride environment, were machined and ground to a 12x12mm square cross-section. However, the contribution of residual stress to the resistance to hydrogen cracking, when generating J-R curves, had not yet been confirmed experimentally. The ND samples were machined to a

width of 14mm in the normal direction. In this direction, the degree of strain relaxation was pronounced, with a marked effect on overall residual stress reduction. With this in mind, the J-R curve specimens, having reduced longitudinal and normal dimensions, would likely experience a reduced strain in all but the transverse direction (therefore across the dissimilar interface). The result of this is a large difference between full-scale stress state and that observed in laboratory test coupons; an important consideration in assessing the fracture mechanics of full scale components.

One limitation of the ND method used, is the averaging of properties across a very large sampling volume (3x3mm), compared to the micro-scale regions at the fusion boundary. With knowledge of the macroscopic stress state, it would be beneficial to establish a means of characterising strains between grains and inter and intra-granular precipitates, in both sides of the dissimilar joint.

6.6 Chapter Summary

Measurements of residual stress have been made in a machined plate specimen of 8630 low alloy steel, buttered with Alloy 625, before and after heat treatment. A summary of the results of this work are as follows:

i. Using neutron diffraction techniques, it is possible to non-destructively monitor the evolution of strain in fusion welded dissimilar metals, during heat treatment, and to quantify competitive strain redistribution between the two materials.

ii. Reduction of stress in the vicinity of the weld is critical. In the present study, an industry standard heat treatment has been shown to significantly improve the degree of localised (interfacial) strain in all three principal strain directions. The highest stress reduction was associated with the Alloy 625 side, where it fell by as much as 400MPa.

iii. Sample width and extraction orientation are fundamental to the pre-existing stress state within mechanical bend specimens. Full scale testing will not alter the triaxial stress distribution as far as that of machined specimens. Fracture toughness experiments with small-scale test coupons must consider the loss of residual stress due to machining, which may have otherwise been crucial to the propagation of hydrogen-induced cracks.

CHAPTER 7. Fractography – The Effect of PWHT on Fracture Morphology

7.1 Introduction

Chapter 3 discussed how partial sections from retrieved 8630-Alloy 625 joints were retrieved from subsea service, and used to develop a method to assess the resistance to hydrogen embrittlement. Single edge notched bend test rigs were instrumented to simulate a 4°C marine environment (3.5%NaCl solution), with cathodic polarisation applied using a potentiostat at -1100mV_{SCE}. Testing temperatures of 4°C and 80°C, corresponding to the 'wet-parking' and production phases of the life-cycle of the joints, revealed a reduced environmental performance when testing at the lower temperature. In Chapter 5, F22 and 8630-Alloy 625 specimens were heat treated in a laboratory and tested using the same methods as per the retrieved joints. A tri-modal split in mechanical performance was observed between as-welded, PWHT, and 'over-aged' specimens. Whilst the poorest performance was attributed to untempered, hydrogen-sensitive martensite in the as-welded state, a less-than-optimal performance was attributed to planar zone M_7C_3 carbide in the 'over-aged' condition. Within this section, a comparison is made between the retrieved and the laboratory heat treated specimens. Further to this, the fracture modes associated with differing lengths of PWHT are assessed, in terms of both surface and subsurface features.

7.2 Experimental Procedure

7.2.1 SENB sample preparation

After environmental performance testing, crack length measurements were taken using a light microscope. The SENB fracture surfaces were then sprayed with an oil based lubricant (to prevent further oxidation) and stored at room temperature. Prior to electron microscopy, the individual fracture surfaces were prepared by ultrasonic cleaning in

methanol, followed by air drying. One exception to this procedure was the analysis of a retrieved 8630-Alloy 625 specimen, used in environmental performance testing after 4°C pre-charging and testing. The sample was measured, ED-machined, mounted in thermo-set resin and then ground and polished so that 5 cross-sectional measurement points were visible along the width of the sample. The samples were prepared so that with five out of the nine measurement points specified in the test validation checks (BS 7448-4 [160]) were visible. In order to conform to the SENB test checks as far as reasonable, the remaining 4 measurements points were line-averaged according to the neighbouring crack length values.

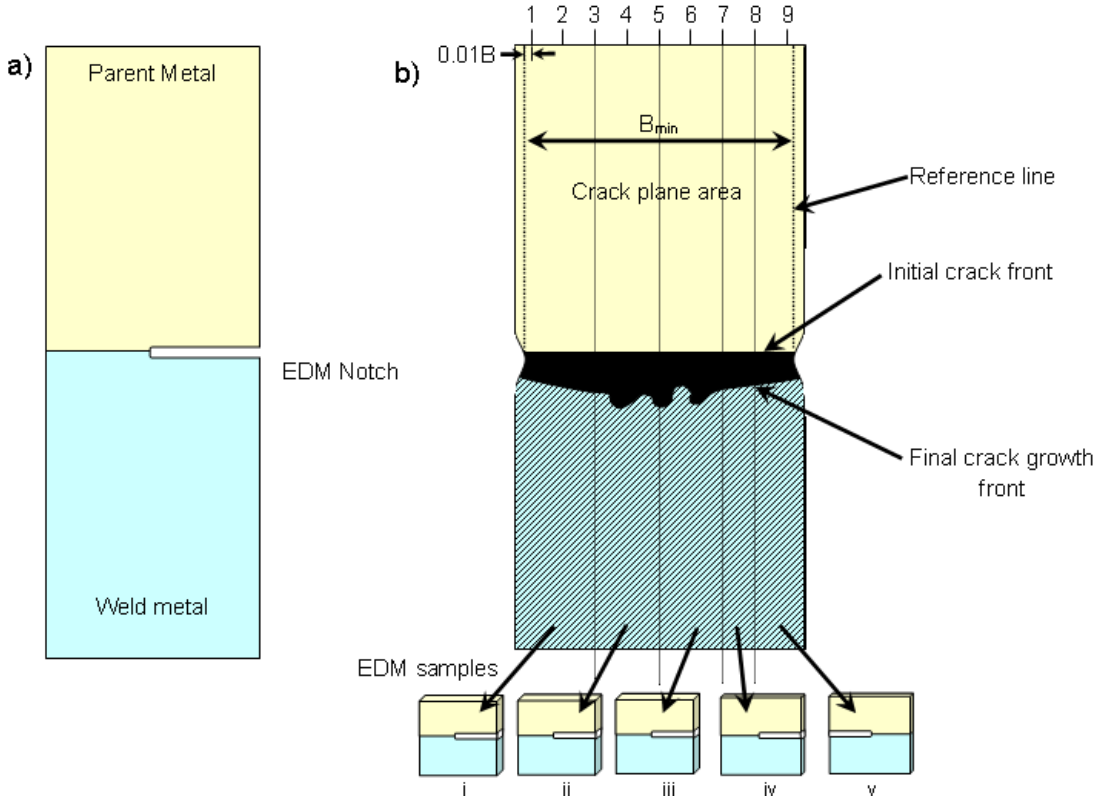

Figure 7-1 - Measurement of crack lengths on single edge notched bend specimens a) notched SENB specimen, b) SENB test validation check measurement positions and cross-sectional cracking profile sample generation. Adapted from [160].

TEM analysis was facilitated using the FIB-SEM procedure described in Section 3.2.3, however, due to the undulating profile of the surfaces, often a deeper protective Pt layer was necessary.

7.3 Results

7.3.1 Fracture Morphology of Retrieved joints

After heat-tinting and breaking open, the samples were placed in an SEM. Features corresponding to in-situ cracking (oxidised surfaces), were easily discernible when viewed in backscatter electron mode. A number of different fracture modes, depending on the position of the crack path with respect to the dissimilar interface, are shown in Figure 7-2. The fracture surface observed is from the steel side of the broken SENB specimen. A flat fracture region was identified adjacent to the steel (area 1).

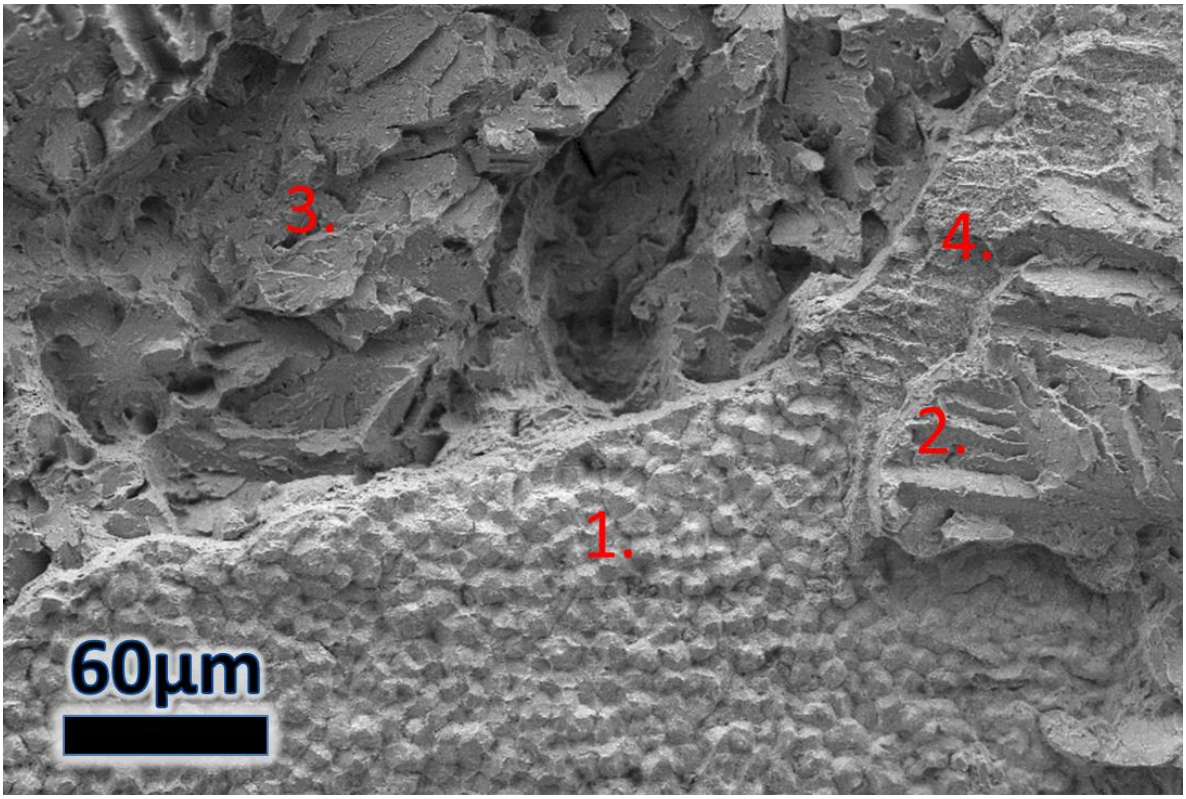

Figure 7-2 - SEM fractograph of multiple morphologies occurring at different distances from the fusion boundary: 1) a flat fracture region with crater-like features, 2) a terraced cleavage-like region, 3) failure within the steel HAZ and 4) a transition region

Upon closer inspection, a grainy, crater-like morphology was observed. The hexagonal craters typically had a number of ridges radiating from a distinct central node. A higher magnification image of such a region is presented in Figure 7-3.

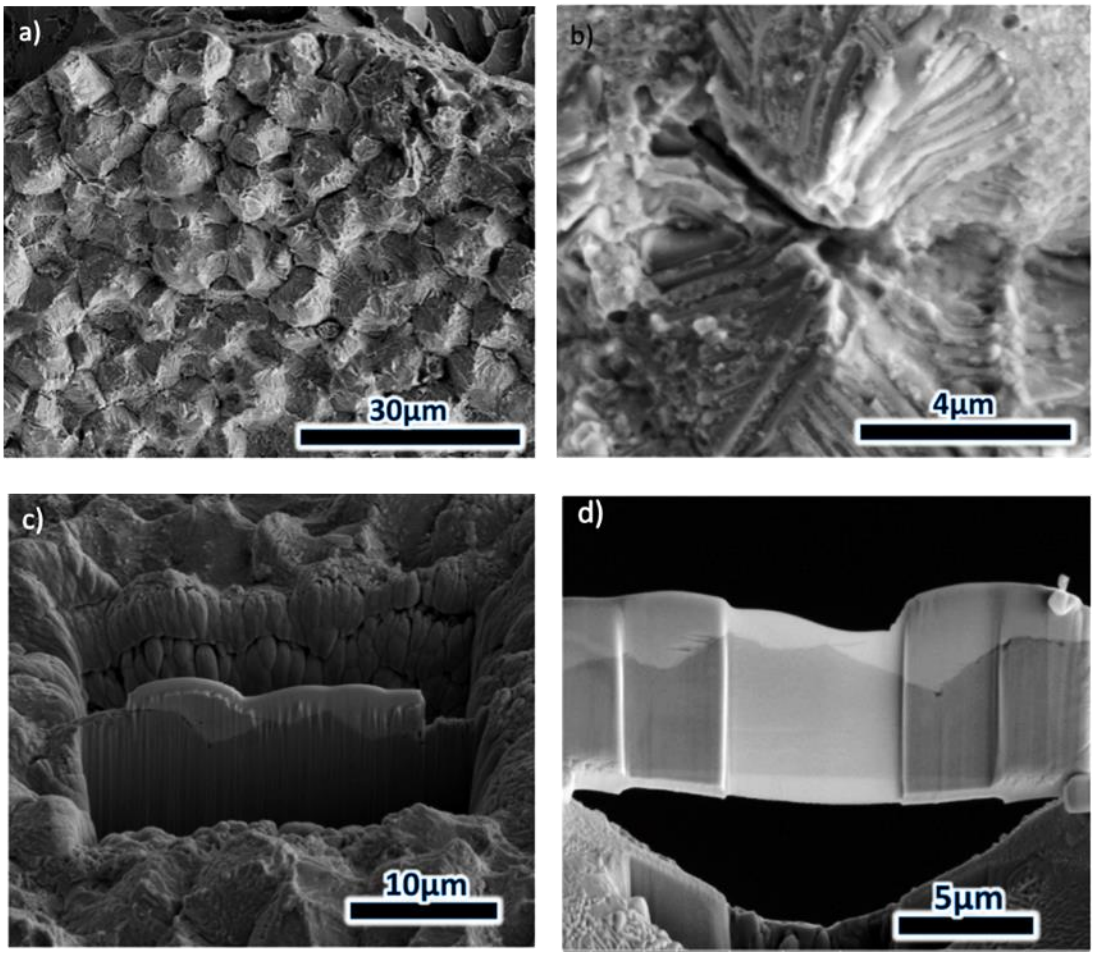

Figure 7-3 - 8630-Alloy 625 specimen fracture surface: a) SEM image of 'flat' and grainy-like crater morphology; b) a higher-magnification image of a single crater with a central node, c) TEM wafer selection and d) thinned TEM wafer mounted on a Cu grid.

A typical area of fracture morphology, for example shown in region 1 of Figure 7-2, was selected for TEM analysis in order to confirm its location in relation to the fusion boundary. Images of the site selection and electron transparent TEM thin foil are shown in Figure 7-3c and d, respectively.

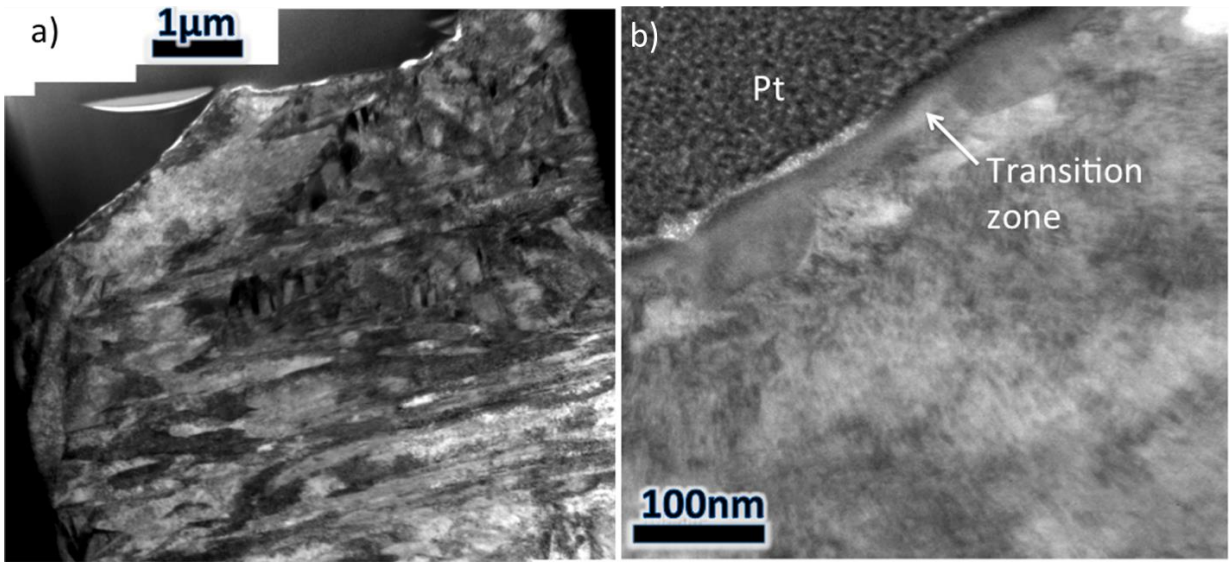

Figure 7-4 - TEM montage of the crater-like region and the sub-surface lath-like structure and b) a TEM image from a region directly below the fracture surface showing a transition zone adjacent to a ferritic grain.

Below the fracture surface, delineated by the protective Pt cap, the TEM foil showed a lath-like structure, elongated and parallel with the plane of the thin foil, Figure 7-4a. Closer to the fracture edge it was apparent that the orientation of the laths differed, with a number running perpendicular to the foil surface. It is this microstructure that is responsible for the ridges on the faces of the crater surfaces. The existence of a narrow transition zone, at all interfaces between the BCC and FCC microstructures close to the fusion line, has been previously described by other authors [148], [170]. The presence of this zone, immediately adjacent to the protective platinum cap at the fracture edge, Figure 7-4b, suggests that the flat fracture region lies at the interface between the planar zone and a 'swirl' (discontinuous PMZ). In Figure 7-5, an image of the opposing fracture surface to that seen in Figure 7-2 (i.e. the Alloy 625 side), shows that this flat fracture morphology is observed at the interface between the planar zone and the iron rich side of the interface, be it a swirl or not. This is evidenced by the flat crater regions existing at different elevations.

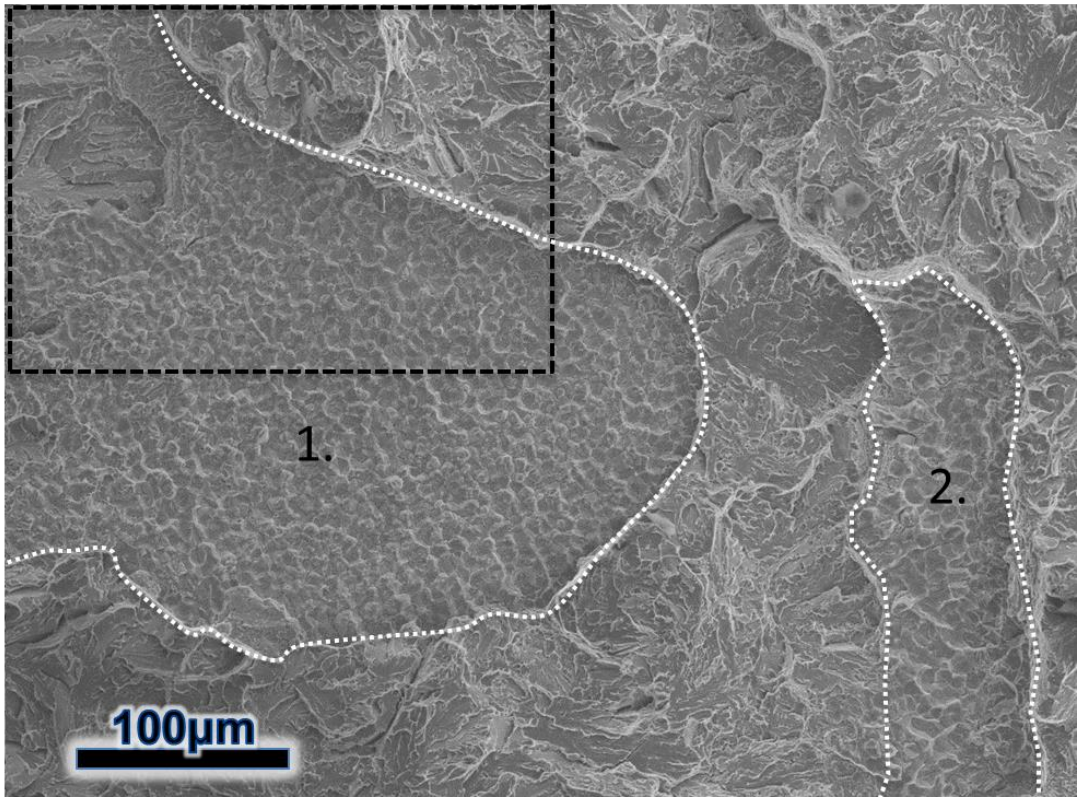

Figure 7-5 - SEM SE fractograph of the Alloy 625 side of the retrieved 8630-Alloy 625 SENB specimen. The opposing side to that shown in Figure 7-2 is outlined. Crater-like regions 1 and 2 are seen at a different elevation, corresponding to an area further towards the weld metal and nearer the steel, respectively.

The terraced cleavage region of Figure 7-2 (region 2), was found to contain a number of 'steps' and ridges on the terraced faces. The observed steps are perhaps evidence of a localised plasticity process and were therefore extracted for further scrutiny by TEM, as shown in Figure 7-6. Thin-foil TEM sample creation was facilitated by milling perpendicular to the macroscopic fracture surface, rather than in the apparent plane of the cleavage surface, Figure 7-6c. At the location of the step, a dark region measuring 400x100nm was found (Figure 7-7b). EDX analysis of this region gave a similar spectrum to that of the surrounding iron rich matrix. The differences in diffraction contrast intensity may therefore have arisen due to local changes in crystal orientation, such as would occur from defects or bending, or grain misorientation.

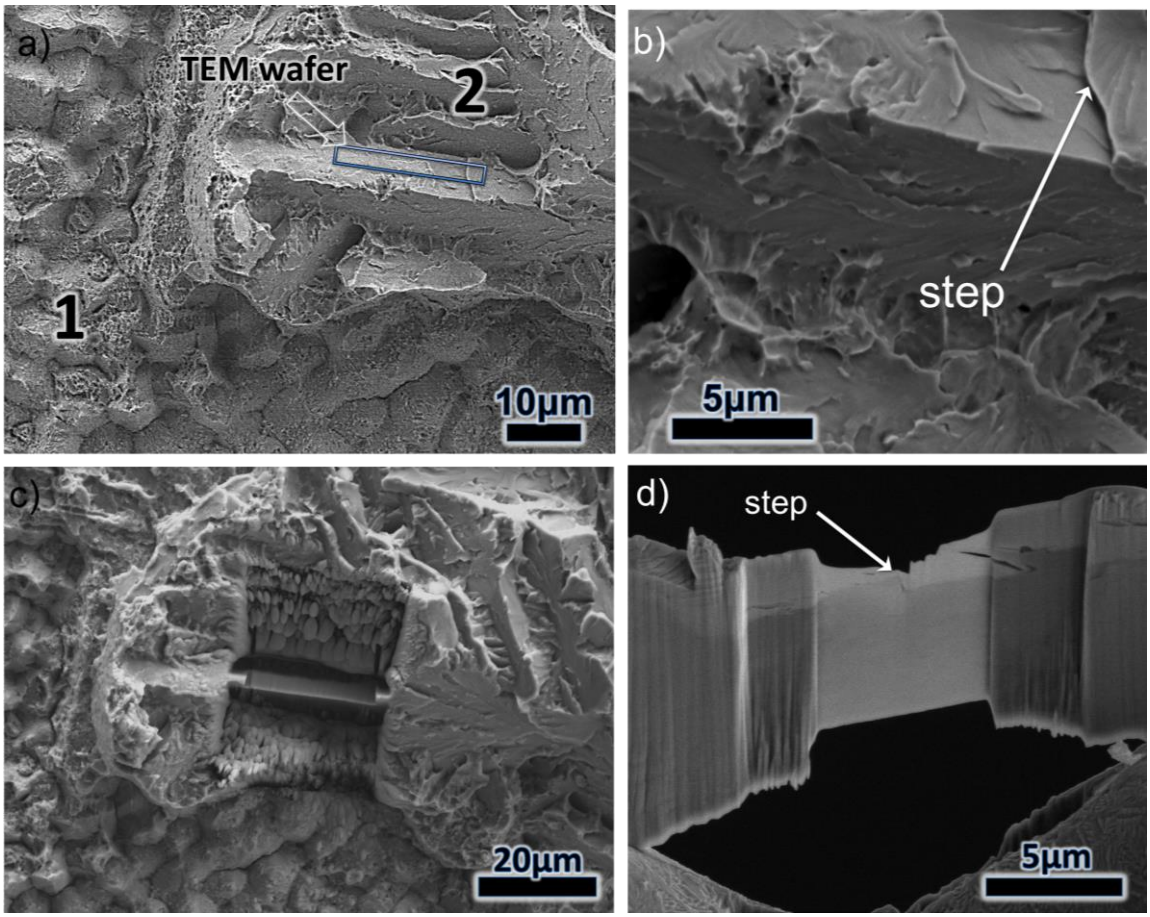

Figure 7-6 – Retrieved subsea 8630-Alloy625 specimen fracture surface after SENB testing showing a) the 8630 steel side with crater-like failure (1) terraced cleavage-like failure (2), and b) a higher magnification image of the 'step"; c) Fracture surface after TEM thin-foil extraction and d) TEM sample mounted on Cu grid.

The terraced cleavage like sample also exhibited a lath-like structure, but not immediately below the fracture surface, Figure 7-7a. The terraced cleavage-like failure exists at a greater distance into the fused zone than the lower, flat fracture (i.e. further towards the nickel alloy). Consequently, one would expect the structure to be fully austenitic, as is the case in the planar zone. However, the cleavage-like morphology observed was within an iron-rich region. The presence of ferritic grains above the flat fracture can be explained by the positioning of this region. The terraced cleavage-like failure exists at the edges of the crater-

like interfacial fracture and may exist at the transition between the two fracture mechanisms: a mixed-mode failure.

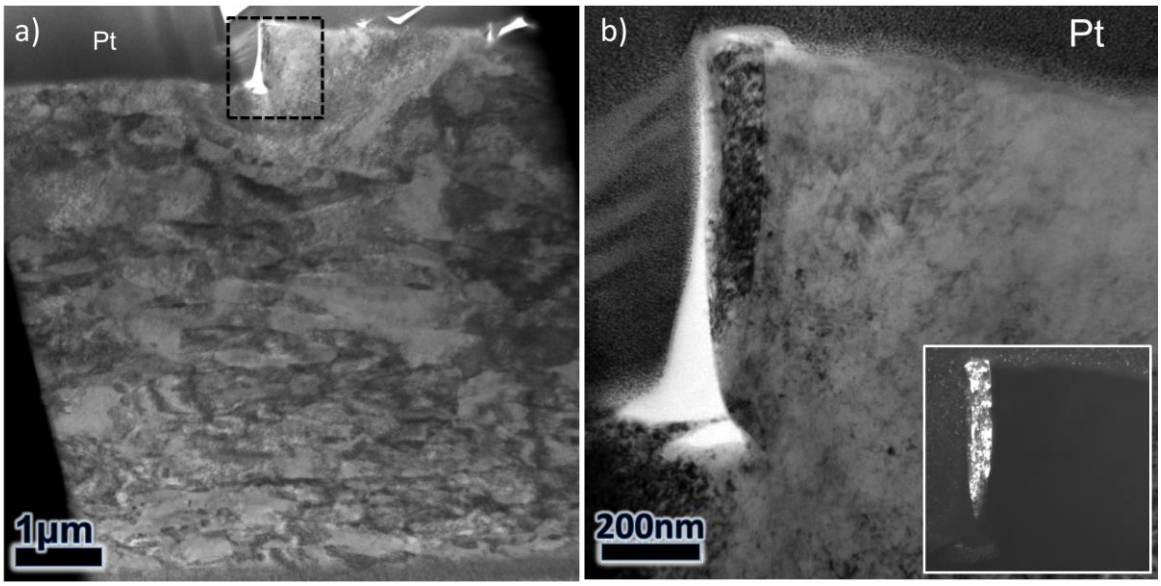

Figure 7-7 – TEM images of the wafer extracted from the terraced surface, a) overview of wafer showing lath structure and b) a higher magnification image of the region outlined in a, showing the stepped nature of the fracture surface with associated darkfield image of the frame in b (inset)

A region that is more typical of the cleavage-like failure that occurs within the planar zone of dissimilar joints [14], [148], [153] is presented in Figure 7-8. In this region, the cleavage-like faces are much more pronounced and exist within the planar zone of a continuous PMZ.

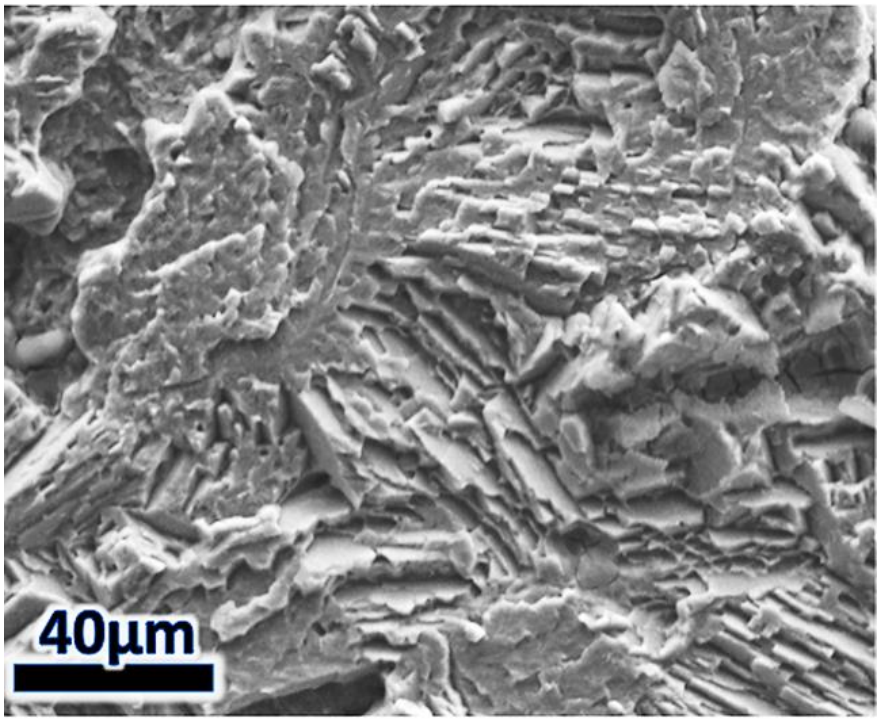

Figure 7-8 - Typical cleavage-like fracture in the Alloy 625 planar zone, adjacent to the interface

A crack emanating from the deformed notch of a SENB specimen after bending, and having been ED-machined into at several positions across the width of the sample, is presented in Figure 7-9. The notch is seen to intersect with the interface, and despite the primary crack apparently initiating in the Alloy 625, multiple crack initiation sites were observed in the HAZ, as indicated in the figure. Following propagation through primary dendrite arms, the crack transitioned to that of a cleavage-like failure mechanism bordering the planar-cellular morphology. The crack occasionally transitioned to that of ductile tearing within the steel, before reverting back to the planar zone. Interface disbonding was also evident, as shown towards the left of the figure.

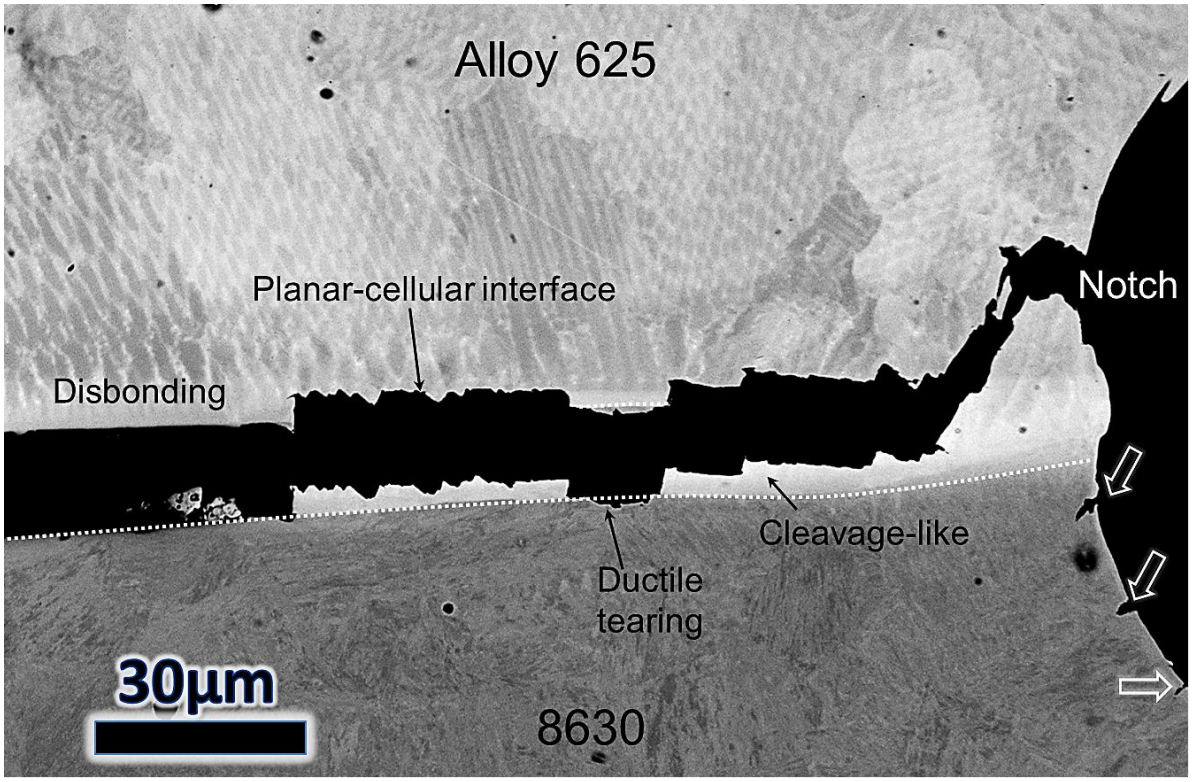

Figure 7-9 - SEM BS image of a retrieved 8630-Alloy 625 SENB specimen after EDM sectioning and polishing (specimen iv). Pictured are crack initiation sites, indicated by the arrows near to the notch tip.

Upon encountering a discontinuous PMZ, Figure 7-10, the crack is deflected towards the weld metal, from an apparently cleavage-like mode of failure. A planar zone was not easily discernible, and at this point, the cleavage-like cracking mode diminishes. The crack then propagated via a terraced quasi-cleavage mechanism through the steel, before transitioning to a flat fracture immediately adjacent to the fusion boundary, within the HAZ. The low energy crack path within the secondary planar zone then becomes favoured, and the crack propagates through the discontinuous PMZ to link the secondary planar zone which has formed on the other side of the swirl. It does this through another, in this case lower, region of crater-like failure. Thus, the crack path, viewed here in cross-section, is similar to the fracture features observed in Figure 7-2.

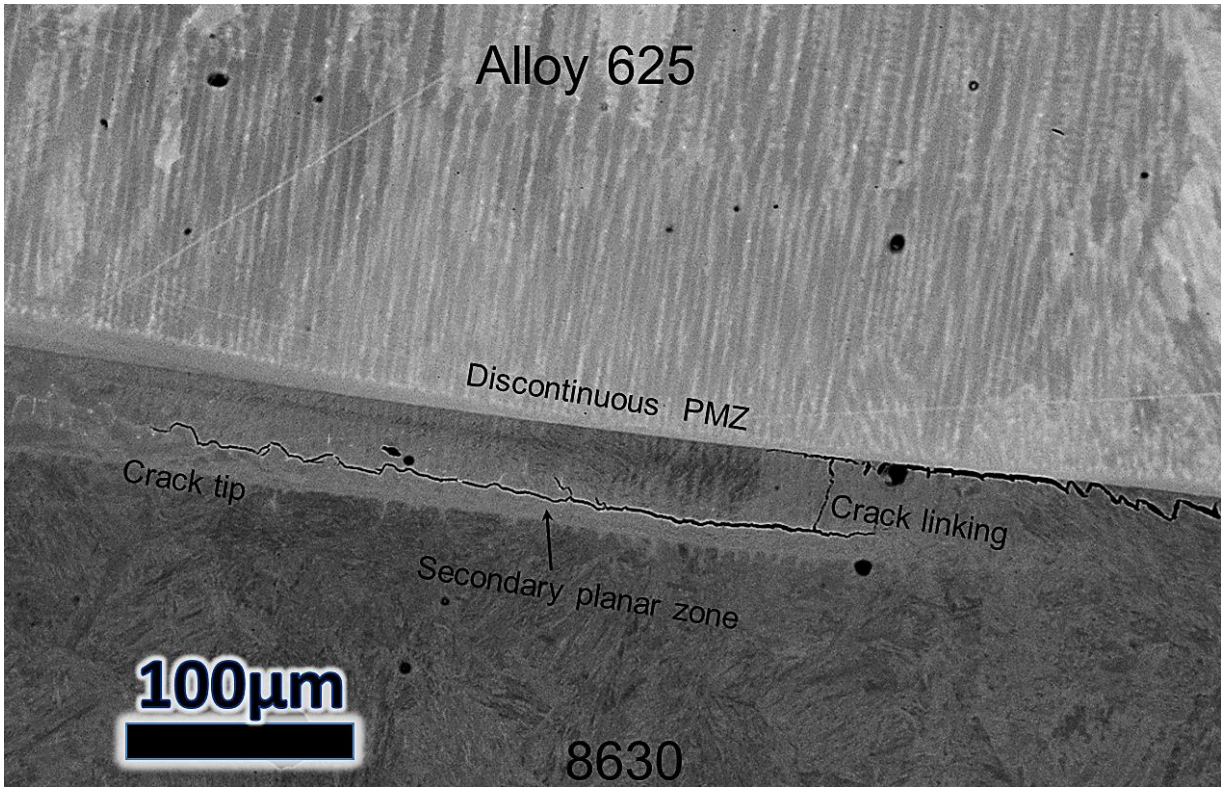

Figure 7-10 - SEM BS image of a retrieved 8630-Alloy 625 SENB specimen after EDM sectioning (specimen iv). Pictured is the crack tip which has arrested at a discontinuous PMZ, during propagation in a flat, crater-like manner. Crack linking through the discontinuous PMZ is also present.

The observations of fracture paths from Figure 7-11 were made through a two-dimensional analysis, however, it is important not to rule out the three-dimensional crack path characteristics. It is possible that cracks may link around discontinuous PMZ as well as through them.

7.3.2 **Fracture Morphology of Laboratory PWHT specimens**

As-welded specimens

The 8630-Alloy 625 specimen was selected for SEM analysis in the as-welded and PWHT conditions. The as-welded specimens clearly exhibited different fracture morphologies from the equivalent PWHT specimens.

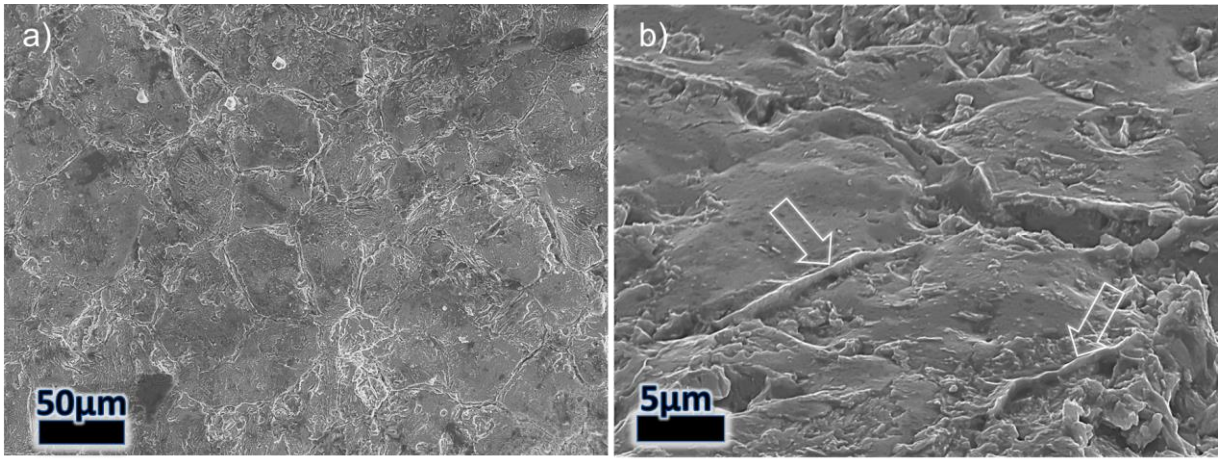

Figure 7-11 – SEM images of the 8630-Alloy 625 fracture surface in the as welded condition (alloy 625 side) showing a) interfacial failure and b) tilted, higher magnification image of the GB protrusions, indicated by the arrows.

Both specimen types exhibited occasional regions of flat crater-like failure as described in Figure 7-5, however, the as-welded specimen showed a greater surface area of flat interfacial fracture, similar to that observed by Milititsky in [161]. Ductile tearing within the steel was also present, together with localised regions of terraced cleavage-like fracture. The dominant failure mode was characterised by flat fracture that followed the macroscopic welding bead profile, Figure 7-11a. The outline of what appeared to be grain boundaries, was visible, as indicated in the tilted image, Figure 7-11b. These were in fact, prior austenite grain boundary penetrations, formed due to the penetration of molten weld metal through the GBs of the opposing side during welding.

To confirm the position of the GB penetrations with respect to the fusion boundary, a continuous interface region from an 8630-Alloy 625 joint in the as-welded condition was selected. Care was taken to examine the exact opposing GB penetration, so that the analyses presented in Figure 7-12 and Figure 7-13 are 'mirror images'. On the 8630 side, Figure 7-12, the protective platinum cap was deposited in a manner that preserved the internal features: incremental rotation of the sample at acute angles during deposition. Complete penetration of platinum within the overhanging features was not possible due to the profile of the surface.

The result of this is a cavity in the sample, where high intensity (white) features correspond to the unimpeded electron beam.

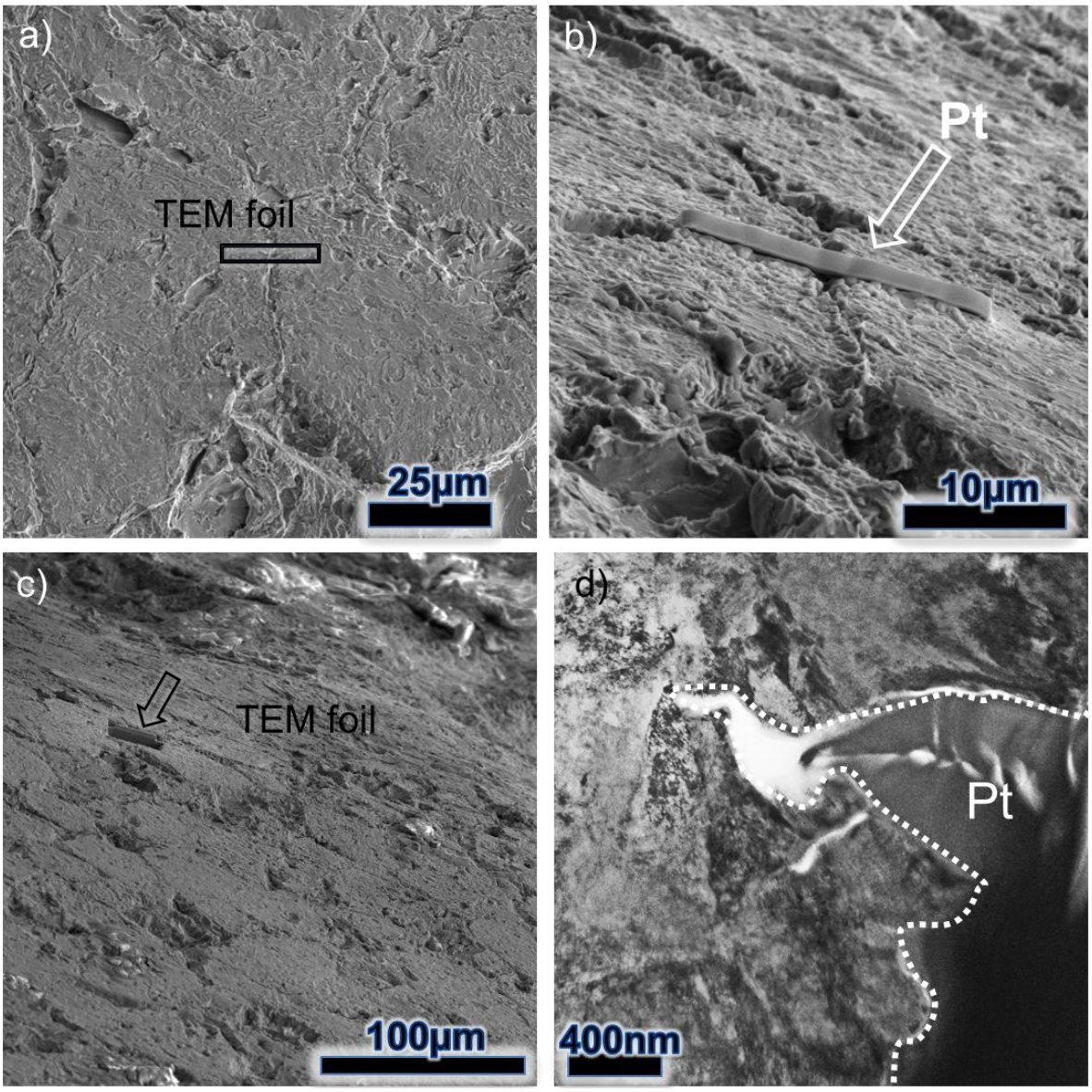

Figure 7-12 –The 8630-Alloy 625 fracture surface (8630 side) in the as-welded condition showing a) SEM SE image of the prior austenite GB penetration; b) tilted SEM SE image of deposited Pt cap for TEM thin foil generation; c) low magnification, tilted image of extraction area and d) TEM image of penetration through lath boundaries (outlined).

Outlined in Figure 7-12d, the penetration is seen to extend approximately 2.5µm into the ferritic side. The microstructure adjoining the platinum-filled recess exhibited extensive plasticity in the form of intense slip bands amongst the lath boundaries. No residual

austenitic weld metal was found, indicating separation at the BCC/FCC interface and necessitating investigation of the opposing side, Figure 7-13.

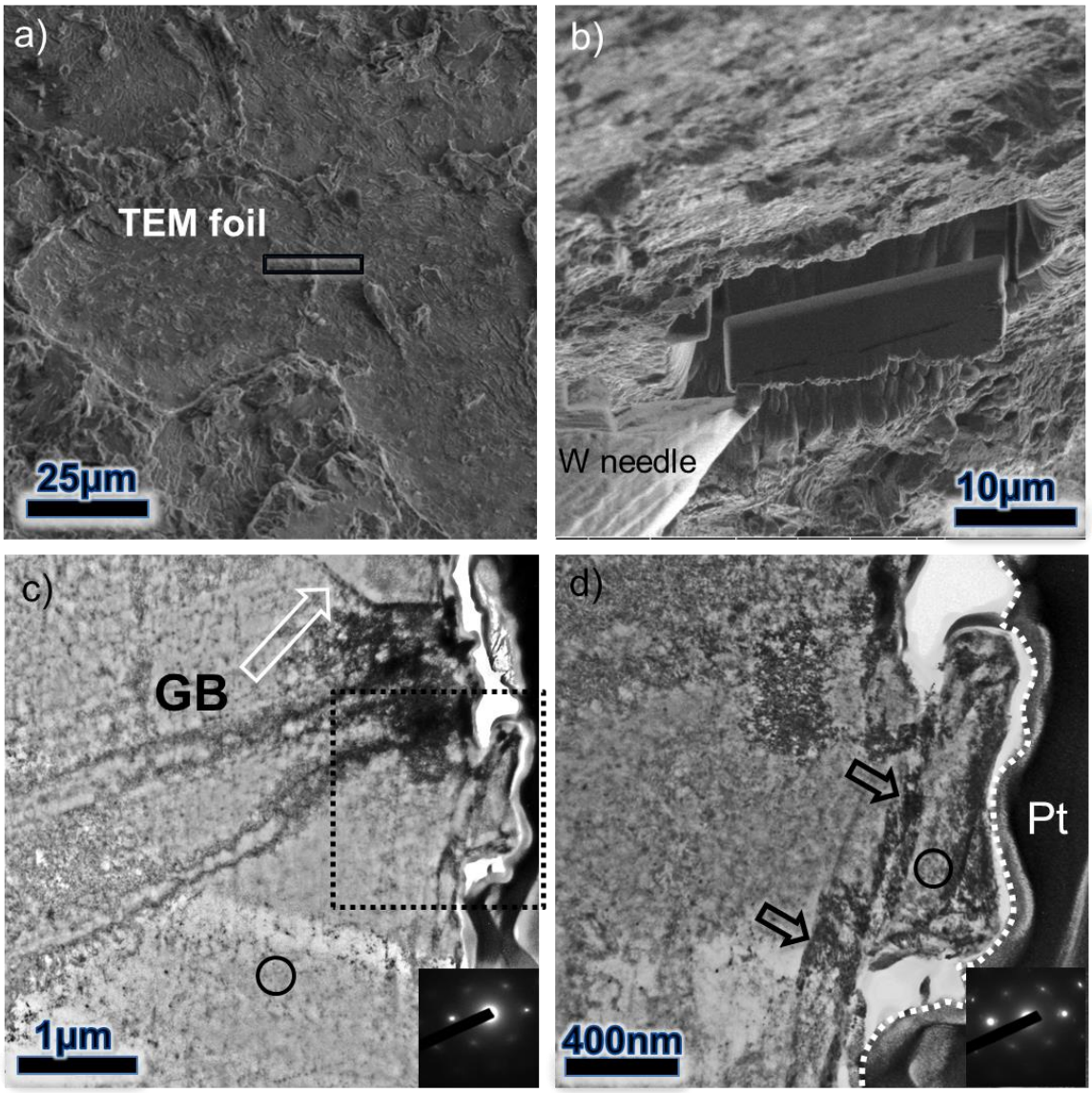

Figure 7-13 – The 8630-Alloy 625 fracture surface (Alloy 625 side) in the as-welded condition showing a) SEM SE image of prior austenite GB protrusion of the opposing side to that of Figure 7-13; b) tilted SEM image of TEM thin-foil creation; c) TEM image of the protrusion and d) higher magnification image of region highlighted in c with inset SADPs from circled regions (FCC [110] zone axis).

In Figure 7-13a, the opposing matching features to those seen in Figure 7-12a are presented. As far as possible, the thin-foil was created to intersect the convex features responsible for the imprints seen. TEM analysis, Figure 7-13c, revealed that subsurface, and extending towards the bulk weld metal, was the austenitic planar zone. In common with

previously analysed as-welded specimens, there was a complete absence of M_7C_3 carbide. A separate planar zone GB was present in the sample. The protruding prior austenite GB indicated in the figure is seen at higher magnification in Figure 7-13d. The slip bands, indicated by the arrows in the figure, converge at the GB protrusion. The dislocation density was low compared to the opposing ferritic side. EBSD analysis conducted in Section 4.3.1, showed that weld metal protuberances remain austenitic after PWHT. The TEM analysis shown here is evidence that the penetrations are also austenitic before PWHT, and are therefore consistent with those observed in a study by Alexandrov et al [54]. In this instance, the penetration was contained within a single grain on the planar solidified side of the joint, as confirmed using selected aperture diffraction pattern analysis.

Heat treated specimens

Despite revealing many different fracture modes, the ten hour PWHT SENB fracture surface exhibited a predominantly cleavage-like mode of failure. The SEM images of Figure 7-14 are typical of such a region. Interestingly, this area exhibited a fine network of cracks that often appeared to follow the facets of the cleavage-like fracture. Again, at higher magnification, the cleavage facets did not appear perfectly flat, each displaying a number of fine surface ridges, 7-12b.

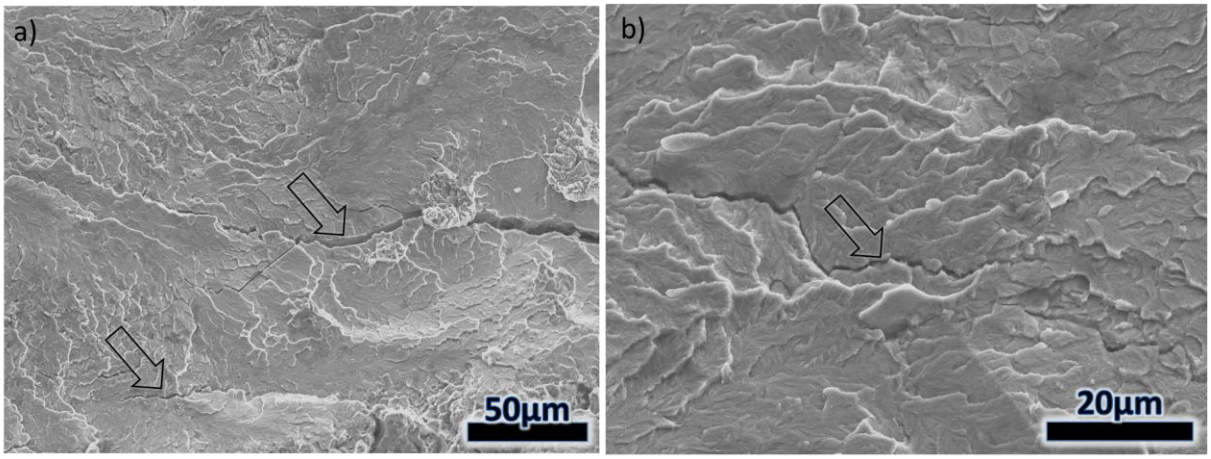

Figure 7-14 - SEM SE images of the cleavage-like morphology from the 8630-Alloy 625 joint after 10 hours of PWHT showing a) morphology of cleavage-like facets and b) higher magnification image of cracking. Secondary cracks are indicated in the figure by the arrows.

A 'cleavage-like' fracture region is also presented in Figure 7-15, which has a slightly different morphology to that seen in Figure 7-14. In the latter figure, the cleavage-like facets are clearly visible, but assume a more cellular structure. As indicated in the figure, a TEM thin-foil was positioned and thinned to create a specimen containing a number of the cleavage-like ridges, Figure 7-15b and c. The specimen was milled as deep as practicable, so that the fracture path in relation to the FCC/BCC interface was visible, whilst maintaining specimen quality.

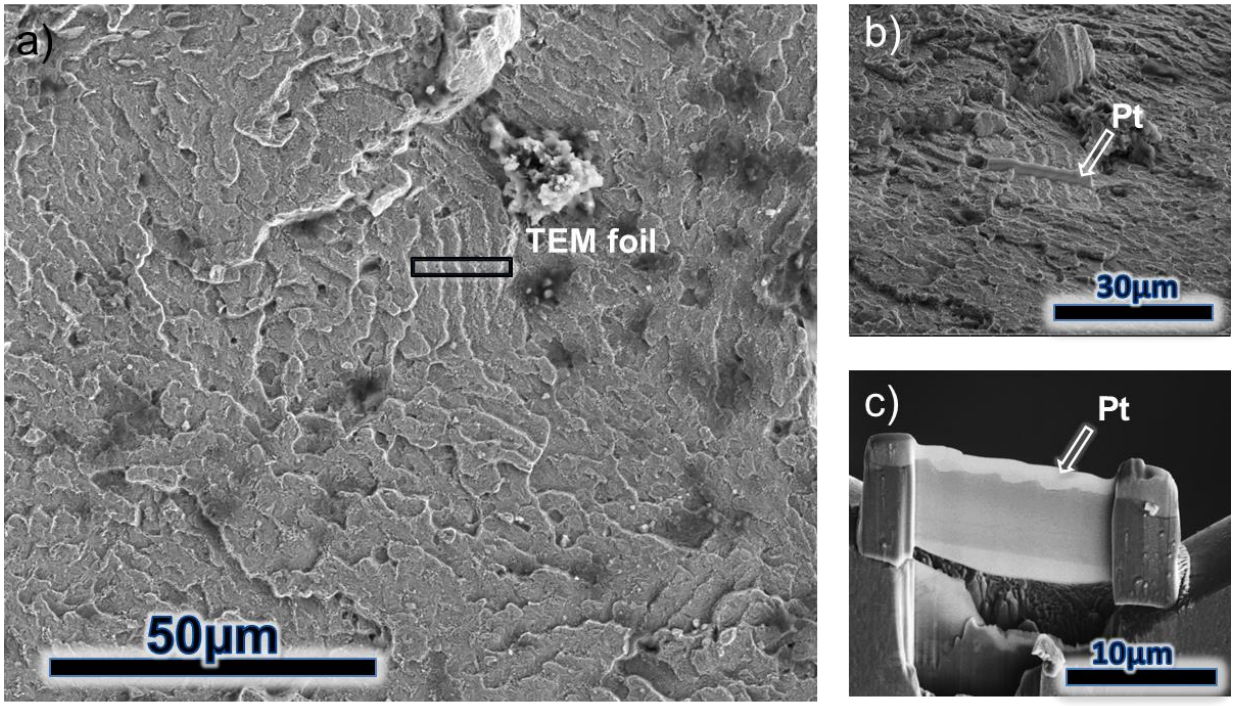

Figure 7-15 – SEM SE images of the 8630-Alloy 625 fracture surface (8630 steel side) after 10 hours of PWHT showing a) cleavage-like cracking within the planar zone; b) a tilted image showing the deposited Pt cap for thin-foil creation and c) the placement of the TEM thin-foil on a Cu grid, having been machined to 'electron transparency'.

A reconstructed TEM montage, showing the fracture surface between 6 and 8µm from the interface is presented in Figure 7-16. A high dislocation density, characterised by the dark region extending 4-5µm from the fracture surface, was found within a band of what appeared to be M_7C_3 carbide. There was no obvious gradient in the dislocation density extending from the fracture surface towards the dissimilar interface, except where the precipitates become scarce. The dislocation-free region corresponds to the precipitate free zone which has increased carbon solubility.

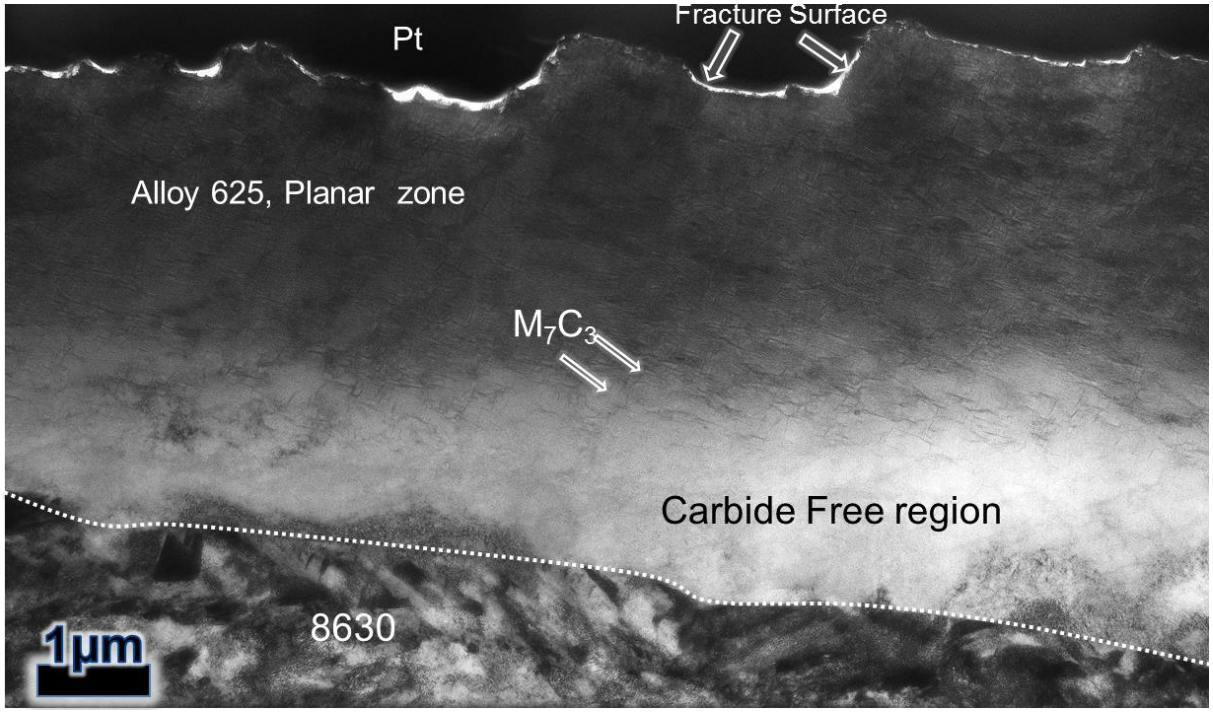

Figure 7-16 – Reconstructed TEM montage subsurface to the cleavage-like fracture within the 8630-Alloy 625 joint, following 10 hours of PWHT. A dense dislocation structure is observed amongst the band of M_7C_3 precipitates within the planar zone.

In this specimen, the long sides of the rod-shaped carbides appear elongated, and are aligned both perpendicular and parallel to the dissimilar interface. This feature may explain the fracture morphology, which appeared to run parallel to the long sides of the precipitates, as illustrated in Figure 7-17.

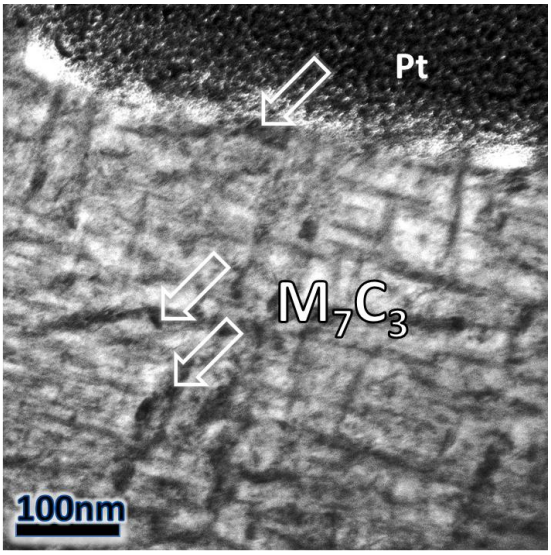

Figure 7-17 - TEM image from immediately below the fracture surface of Figure 7-16. Arrows indicate precipitates within the planar zone

7.4 Discussion

As the stress is applied during bend testing of the heat treated joints, the dominant cleavage-like failure mode acts as the low energy crack path. Upon encountering a discontinuous PMZ, or perturbation in the interface, the crack path is deflected away from the direction of applied stress, as it attempts to continue within the primary planar zone. The crack thus follows the interface between the two, creating the crater-like morphology along lath boundaries.

Cracks may develop ahead of the primary crack front, as evidenced by the discovery of progressive cracking in the retrieved joint recovered from service, Figure 3-10, and by the numerous secondary cracks observed in the laboratory heat treated specimens, Figure 7-12. Nevertheless, failure occurs across the discontinuous PMZ, as a means of linking cracks in the planar solidified, low energy, carbide rich regions. It is possible that crack-linking between neighbouring carbides within the planar zone is responsible for the 'cleavage-like' surfaces and the presence of fine surface ridges upon them.

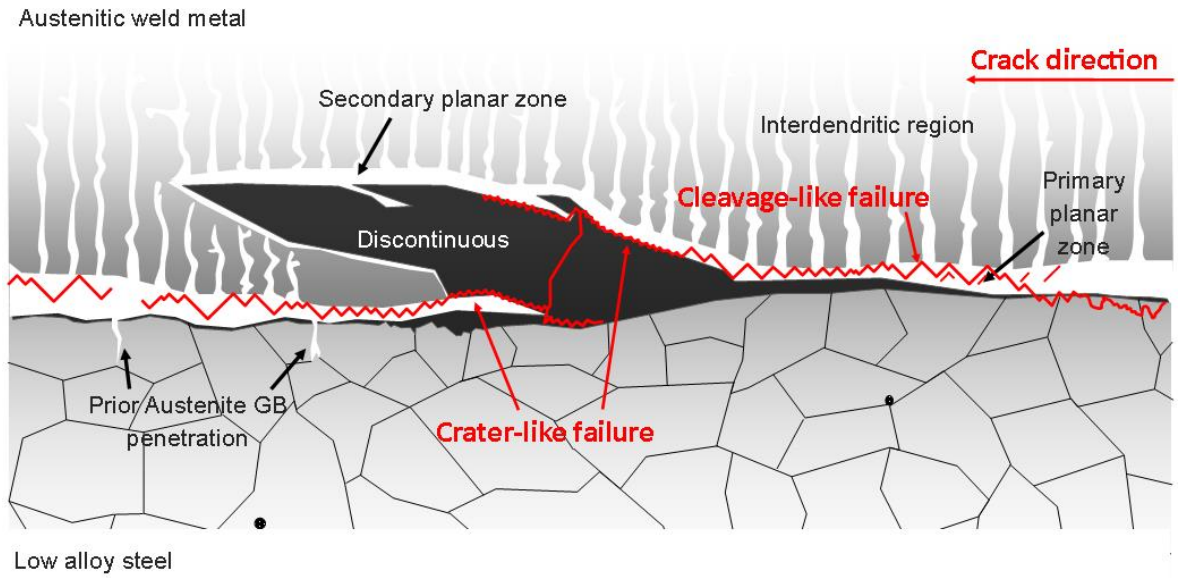

Figure 7-18 - Illustration of proposed dominant fracture morphology in cross-section for an in-service joint, having been subjected to excess PWHT (precipitation of carbide within the planar zone).

As a result, crater-like failure can exist at different points, above and below discontinuous PMZ regions, as failure mode transitions from cleavage-like to flat, crater-like failure, and vice versa. The observations of crack path characteristics for the heat treated joints are illustrated, schematically, in Figure 7-18. However, it is important to note that the fracture surfaces were generated by a mechanically driven stress, and may therefore not be completely representative of in-service failures of full-scale specimens. Indeed, the residual strain measurements presented in Section 6.4, indicate a significant reduction in stress in the direction (normal), having been machined to a 14mm wide section. The SENB samples were prepared to a 12x12mm section, and therefore a similar reduction in residual stress may be expected. Although significant stress relaxation may occur during PWHT, the failure of full-scale service components may have a significant contribution from residual stress, in the presence of hydrogen.

Whilst interspersed with regions exhibiting small amounts of the various fracture morphologies presented, in general the dominant failure mode in the as-welded condition was

through interfacial failure. This failure mode is typified by large swathes of flat morphology that follows the macroscopic bead profile. At resolutions afforded by SEM, it is possible to identify the outline of prior austenite GB penetrations, resulting from the penetration of weld metal through the opposing side during welding. This is possible in part, as the liquidus temperature of the weld metal is lower than that of the parent steel ($T_{LW} < T_{LB)}$. A schematic of the dominant as-welded failure morphology is presented in Figure 7-19.

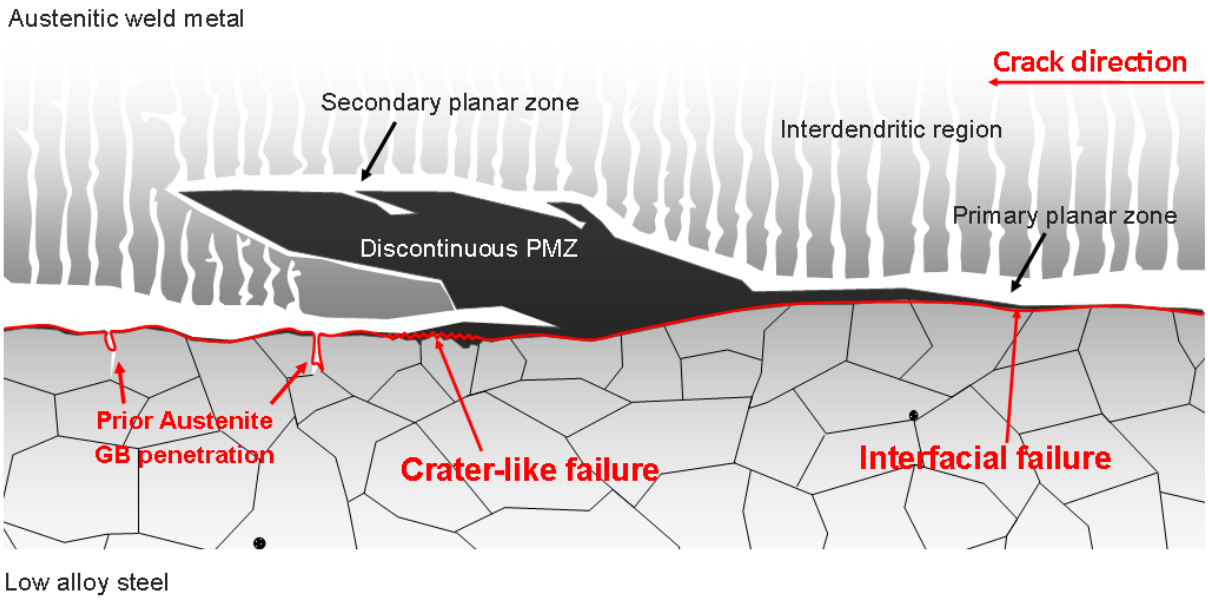

Figure 7-19 - Illustration of proposed dominant fracture morphology in cross-section for a hydrogen-charged dissimilar joint in the as-welded condition.

7.5 Chapter Summary

By comparing retrieved and laboratory heat treated specimens, the fracture surfaces of which were generated under similar testing conditions, the following conclusions can be made:

i. Despite evidence of multiple fracture modes, the dominant failure mechanism in the LAS-Alloy 625 joints after PWHT, is through a cleavage-like failure, rather than major interfacial failure in the as-welded condition. Discontinuities in the PMZ

disrupt cleavage-like cracking along the planar zone, deflecting the crack path and resulting in crater-like failure along lath boundaries.

ii. Subsurface to the cleavage-like cracking within the planar zone, a number of carbides, thought to be M_7C_3, were found. The precipitation of M_7C_3 coincided with a region of high dislocation activity, the degree of which was not observed in the carbide-free region adjacent to the dissimilar interface.

iii. Microscopic ridges on 'cleavage' surfaces, combined with cracking observed in the retrieved service specimen subjected to CP, (Section 3.3.1) are evidence of a localised plasticity process, rather than fast, brittle fracture.

CHAPTER 8. Discussion

8.1 Microstructure

8.1.1 As-welded Microstructure

All of the specimens that were investigated exhibited interfacial zones consistent with those found in literature [54], [148], [150]–[152], [170], [196]. These are broadly divided into two types based on the solidified morphology: continuous and discontinuous partially mixed zones. In the latter, swirls of parent material are swept into the weld metal by fluctuating welding pool convection currents. Similarly, beaches may form due to incomplete mixing within the weld pool. The result of this is an inconsistent interface, typified by regions of varying local composition gradients, and therefore microstructure. Within discontinuous PMZ swirls, a higher proportion of hydrogen sensitive martensite may be expected, forming as a consequence of the welding procedure [151].

In continuous PMZ regions, following welding, the reduced nickel content within the steep composition gradient results in a weak driving force for the stabilisation of austenite to lower temperatures. Therefore, interface martensite forms at the fusion boundary between the dissimilar materials, even under slow cooling conditions. Post weld heat treatment is applied primarily to temper these hydrogen sensitive microstructures. Additional microstructures found within the fusion zone of a continuous PMZ in the as-welded condition between LAS-Alloy 625 joints may be summarised as follows: the BCC ferritic microstructure of the parent steel, containing carbides and inclusions. Further towards the fusion boundary, a partially decarburized grain-coarsened heat-affected zone is present, with fingers of fused weld metal that have penetrated the opposing side during welding. These prior austenite GB protrusions remain austenitic, before and after PWHT. At the dissimilar interface, a thin band of martensite may be visible, the width of which varies due to

compositional fluctuations. Within the austenitic side, an apparently ‘featureless’ or ‘planar zone’ is found, having apparently solidified in a planar manner. However, whilst precipitates may not necessarily be found in the as-welded condition, the naming convention ‘featureless zone’ is misleading, due to the presence of nanoscale precipitates that form during PWHT. Towards the undiluted bulk weld metal, and associated with the instability of the planar solid-liquid interface, higher atomic number interdendritic particles (Nb and Mo based carbide), are observed.

The F22-309LSi joint was selected solely as a metallurgical comparison to the low alloy steel – Alloy 625 joints. In the 309LSi combination, the relative similarity between the PM and the weld metal reduced the chemical gradient. This was accompanied by a broadening of transitional fusion boundary microstructures. The result of this is pronounced when comparing interface martensite; the most dissimilar joint, the 8630-Alloy 625, produced a very narrow band, <1µm wide, which was in stark contrast to the approximately 4µm wide band observed in the F22-309LSi combination. The steep weld metal composition gradient also appeared linked to planar zone width, visible when comparing the F22 and 8630-Alloy 625 combinations.

The microstructural models have demonstrated that the liquidus temperature of the weld metal is less than that of the base metal over all of the dissimilar joints used. Indeed, the microstructures that formed following welding are consistent with those presented by Yang and Kou [39]–[44] for the case where $T_{LW} < T_{LB,}$ as discussed in Section 2.1.3. The ‘no-slip’ boundary condition for fluid flow [45] may be satisfied at the pool boundary, resulting in a stagnant laminar flow layer with weaker convection currents. This can result in a thin layer of unmixed or ‘filler deficient’ base metal that solidifies before the bulk weld pool.

Despite having been fabricated under the same conditions, the F22-Alloy 625 had a considerably broader planar zone, and a shallower compositional change than the 8630 counterpart. In the F22 and 8630-Alloy 625 joints, having a planar zone width of approximately 32 and 10μm respectively, a liquidus temperature range of 150°C was found. However, the average compositional gradient along the cross-sectional bead profile and weld length was not assessed. Compositional gradient severity is likely to vary due to fluctuating weld pool convection currents. Therefore, changes in dilution may occur as a consequence of both solute segregation and partial mixing. Indeed, the steep compositional changes at the pool boundary may be partially present due to increasing shear forces approaching the pool boundary as well as larger compositional changes occurring in planar solidified regions [184].

8.1.2 **Microstructure Evolution during PWHT**

During heat treatment, carbon diffuses in the direction of its thermodynamical activity gradient, which for the dissimilar joints was towards the austenitic weld metal. The higher the degree of heterogeneity between the forging and weld metal, the higher the degree of carbon redistribution during heating. The diffusion models presented in Section 4.3.3 and the carbon analysis results presented in Section 5.3.1 reveal the extent of this phenomenon and, subsequently, the cause of new phase precipitation within the planar zone. Carbon saturation in this planar solidified region is accompanied by the formation of M_7C_3 carbide; however saturation is reached after differing time periods, depending on parent metal composition. Comparing the two LAS-Alloy 625 joints, the F22, having less than half of the carbon content compared to the 8630, does not precipitate M_7C_3 until far later in the PWHT cycle. While limited results are presented, the density of the carbide band also appears to be linked to PWHT time - a greater proportion of M_7C_3 was found as PWHT time was increased.

Although not quantified, the size of the carbides also appeared to increase with longer heating durations. The relationship between carbide size and fracture morphology was not examined, and warrants further study.

The width and morphology of the planar zone may play an important role in the formation of M_7C_3. For example, the long aspect ratio of the planar zone grains, combined with their large size relative to neighbouring regions, will influence the mechanism for carbon diffusion and, additionally, the crack path characteristics. Further into the weld metal, where the grain size is reduced and chemical composition becomes less diluted, GB diffusion may be preferable such that intragranular M_7C_3 carbide precipitation ceases. It would be beneficial to investigate the effect of carbon diffusion in less diluted regions.

Nanoscale analysis, afforded by transmission electron microscopy, revealed a carbide-free region within the planar zone of dissimilar joints. Whilst M_7C_3 was commonly found away from the interface, the carbide-free region remained featureless even after extended heating. The emergence of the carbide-free region is likely a result of the rapid chemical changes that occur within the first few microns of the planar zone, which in turn modifies the local carbon solubility. The carbide-free band is highly diluted, indicating that M_7C_3 carbide formation is sensitive to the composition of the planar zone matrix.

PWHT temperature is normally selected at a high temperature, but below the austenite transformation temperature, A_{1c}, such that, upon cooling, undesirable martensitic structures do not form. Whilst equilibrium modelling results indicate the complete dissolution of forging $M_{23}C_6$ and M_7C_3 phases in the 8630 material, complete dissolution of $M_{23}C_6$ was not achieved in the F22. However, considering the susceptibility of martensite to hydrogen embrittlement, of perhaps greater importance is the prediction of BCC-FCC transition temperatures. In the F22 material, reversion to austenite was predicted at a far higher temperature to that of the 8630 (approximately 790 versus 710°C). Therefore, as a

consequence of having its PWHT temperature (650-675°C) closer to the austenite transformation temperature, there may be a higher propensity for reaustenitisation to occur during PWHT in the 8630 material. This is providing there are localised regions which contain a sufficient amount of austenite stabilising elements. Within these regions, it may be possible to form martensite during cooling from PWHT. In the weldments analysed, ferritic discontinuous PMZ swirls, islands and peninsulas, contain nickel. The nickel may stabilise austenite to temperatures lower than that of a typical PWHT, as demonstrated for the simplified case in section 4.3.2. A modification of the PWHTs may therefore be beneficial: lower temperatures and slower cooling rates may reduce the amount of discontinuous PMZ martensite.

8.2 Mechanical Properties

8.2.1 Resistance to Hydrogen Embrittlement

The resistance to hydrogen embrittlement was assessed for retrieved joints under temperatures typical of commissioning and service, 4 and 80°C respectively (Section 3.3.3). An important consideration is the simulated 'shut-down' condition, whereby the manifold had been operating at the higher temperature, before standing at the lower temperature whilst offline. Although test data was limited, the results of these slow strain rate SENB tests indicated that when testing at the higher of the two temperatures, a considerably higher resistance to cracking was found. However, this result appeared to be independent of the pre-charging temperature, such that the 'shut down' condition appeared to be at no greater risk of cracking. This occurred despite the fact that, theoretically, more hydrogen should be able to accumulate at the interface due to faster diffusion rates associated with the higher temperature, as discussed in Section 2.3.

Under pre-charging and testing temperatures of 4°C, the resistance to CP-induced hydrogen embrittlement was explored in F22 and 8630-Alloy 625 joints, for varying lengths of PWHT. The J-R curve tests were accompanied by heat treated sample coupons in order to correlate environmental performance with the microstructures present in each heat treatment condition. The coupons also allowed for normalised carbon distribution profiles to be created, demonstrating the carbon diffusion trends. The most prominent microstructural changes occurred at the fusion boundary and within the planar zone due to the tempering of martensite and the precipitation of M_7C_3. Tempering of the HAZ was accompanied by an increase in resistance to embrittlement. In fact, for all PWHTs applied, an increase in crack growth resistance was found. However, the results also showed that an optimal solution exists at the junction of competing mechanisms. During HAZ tempering, excessive carbon diffusion from the steel occurs. This is accompanied by the precipitation of M_7C_3 within the austenitic planar zone, at which point the crack growth resistance is dramatically reduced. Therefore, in mitigating M_7C_3 precipitation, careful control of carbon diffusion and saturation within the planar zone is necessary. As demonstrated, employing a lower carbon content forging may be beneficial as it affords greater control of PWHT whilst potentially reducing the amount of martensite that can form after welding. Evidence for this is seen in the F22-Alloy 625 joint, which suffered losses in mechanical performance far later in the PWHT cycle in comparison to the 8630 combination.

The susceptibility of the dissimilar joints to hydrogen embrittlement has been assessed using slow strain rate testing in a simulated marine environment under CP. Whilst the susceptibility to HE is clearly linked to microscopic fusion boundary regions, it is not yet clear how representative the SENB tests are of full-scale, in-service failure. The notched test coupons had 12x12mm sections, with crack lengths up to 3mm. As a result, high variability may be expected between specimens created from a single partial joint due to localised

microstructural variation interspersed along the weld length. As discussed in Section 5.4, the microstructure is also heavily dependent on welding process [151], which can alter the ratio of discontinuous to continuous PMZ. As a result, the mechanical response is also likely to vary between manufacturers due to slight differences in welding processes. Mitigation of martensite-rich swirls is likely to improve the environmental performance in the as-welded condition, whereas the restriction of planar zone formation may be preferable when employing lengthy PWHTs due to the lack of favourable M_7C_3 carbide growth sites.

8.3 Fracture

Cracks found in the retrieved 8630-Alloy 625 joint (Chapter 3) indicate subsurface initiation, secondary crack coalescence, and propagation in a progressive manner. This opposes the idea of propagation in a single, large event. In keeping with those of the fracture surfaces generated after environmental performance testing, the cracks were predominantly confined to the planar zone and fusion boundary.

In the as-welded condition, interface disbonding was dominant. Yet 'swirls' of steel with a highly diluted chemistry were observed in which flat, crater-like failure, was found. The swirls, having a highly diluted chemistry, promote the formation of martensite, which is particularly susceptible to embrittlement. The swirls form, in part, due to the large difference in liquidus temperatures between the parent and base metals. At bead overlap positions, interpass swirls are common. Therefore, a semi-continuous fracture path may be found around the weld length, depending on butter welding procedure.

In the dissimilar joints that were given extended PWHTs, cleavage-like morphologies were present. Whilst subsurface to these a band of M_7C_3 carbide was found, its high carbon content and steep chemistry gradient may also be responsible for the cleavage-like

appearance. Therefore, using the subsurface analysis methods described herein, it would be beneficial to assess whether this fracture morphology can form in the absence of the carbide.

Hydrogen is often associated with dislocation motion as well as the modification of dislocation velocity and separation distances [197][198]. It is also widely recognised as being transported to the interfaces between traps, such as precipitates or GBs, where decohesion events can initiate [199]. Therefore, when considering the cleavage-like fracture surfaces, the interaction between the M_7C_3 particles and dislocations must be considered. It is possible that the cohesive strength at the interface between precipitates and the matrix is lowered due to hydrogen ingress. Hydrogen diffusion is succeeded by hydrogen accumulation at the particles, especially in the locally stressed, dislocation-rich region ahead of the crack-tip, causing decohesion (HEDE) events in neighbouring precipitates. Cracks that have nucleated at M_7C_3-matrix interfaces in this stressed region link-up [141], creating the cleavage-like surface. An increase in the amount of localised stress in systems with intergranular precipitates has been seen to encourage decohesion at carbides [200]. A similar interplay between the HELP/AIDE and decohesion mechanisms could also be present in hydrogen assisted failure in the intragranular M_7C_3/austenite system. Evidence of this has been found in mesoscopic finite element based microstructural models of the austenite-M_7C_3 system [201].

A simplified summary of the fracture toughness trend and relationship with dominant fracture morphology is presented in Figure 8-1, for SENB specimens tested in a simulated marine environment. The diagram illustrates that by applying a PWHT, the resistance to crack growth is improved until the point at which M_7C_3 carbide in the planar zone is formed. For the F22-Alloy 625 joint, M_7C_3 forms further into the PWHT cycle, thus loss in mechanical performance occurs far later. Once the continuous planar zone is M_7C_3 abundant,

dominant fracture mode transitions to ‘cleavage-like’. However, in the as-welded condition, interface disbonding was prevalent.

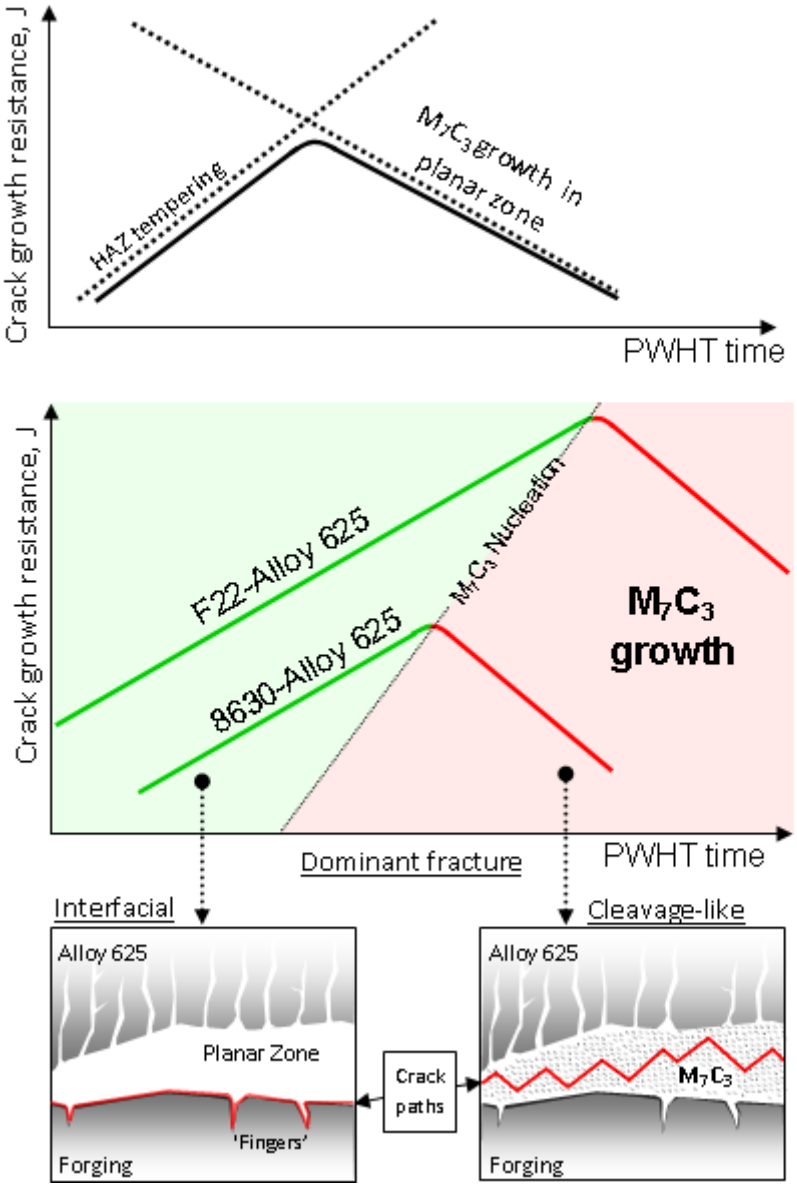

Figure 8-1 - Illustration of the competitive process between crack growth resistance and length of PWHT time for the F22 and 8630-Alloy 625 joint, and its effect on fracture morphology.

With the exception of the retrieved joint, which was found to have a number of subsurface cracks, all fracture surfaces presented in this work were as a consequence of

mechanically driven stress (i.e. SENB testing). The validity of these tests in assessing in-service failures is called into question when considering the nature of the environment in which full-scale specimens perform. For example, the stress state of SENB test coupons is undoubtedly modified by machining practices and initial sample geometry. Moreover, the notch orientation, whilst likened to circumferential crack propagation, is not necessarily representative of the cracking characteristics (such as direction) of full size specimens. In full-scale dissimilar weld specimens, different stress states may be expected between the inner and outer diameters. In fact, residual stresses which are compressive in nature, such as may be found near the internal diameter of the pipe, decrease the crack driving force [202]. However, the effect of residual stress is dependent on the location of the flaw, as well as the stress state arising due to the introduction of the flaw itself. Therefore, residual stress measurement may be useful in determining the degree of flaw acceptance in relation to orientation and placement through the thickness of the weld.

CHAPTER 9. Conclusions and Recommendations

9.1 Conclusions

Arc welding of dissimilar metals creates intricate localised microstructures within the fusion zone, which form as a result of complex weld pool stirring. Broadly, these have been divided into two types based on solidified morphology: continuous and discontinuous partially mixed zones. In the former, and bordering the boundary between ferritic and austenitic materials, thin bands of martensite were found. The weld metal within these continuous PMZ regions solidifies initially in a planar manner, creating the so-called 'planar zone'. In discontinuous PMZ swirls, their composition is such that the formation of untempered martensite may be possible even after post weld heat treatment, resulting in microstructures that are particularly sensitive to hydrogen embrittlement. Partially mixed parent steel that has penetrated into the weld metal results in primary and secondary planar zones, each solidifying from the steel towards the undiluted weld metal.

During PWHT, the heat affected zone is tempered, while residual stresses that have formed in the as-welded condition are redistributed. However, during heat treatment carbon diffuses into the austenitic planar zone, whereupon it reaches a saturation point and forms M_7C_3 carbide. By extending the duration of heating, the extent of diffusion becomes more pronounced: significant HAZ decarburisation is succeeded by carbon pile-up in the weld metal. High carbon concentrations are not limited to the planar zone, but were seen to extend further into the weld metal.

For all applied heat treatments, a considerable increase in resistance to hydrogen embrittlement was achieved over the as-welded condition. However, a competition between tempering and new phase precipitation became apparent in both the F22 and 8630-Alloy 625 combinations. Within the planar zone of the most-optimally performing samples, the HAZ

presented a tempered morphology, yet M_7C_3 carbide had not nucleated. Significant losses in resistance to crack growth were observed in 'over-aged' samples where the carbide was abundant, despite further HAZ tempering. Whilst interspersed with localised regions of many fracture morphologies, the dominant fracture modes were different between the as-welded and 'over-aged' samples. Large swathes of interfacial failure were apparent in the as-welded condition, yet 'cleavage-like' failure (with subsurface M_7C_3) was found after excessive PWHT. These results illustrate the deleterious impact of the carbide on subsea performance. A better balance between forging chemistry, desired mechanical properties, and microstructure after PWHT is fundamental to the improvement of resistance to subsea fracture.

The microanalysis techniques used herein may be used to qualify joints for subsea service, provided a comparison between true in-service failures and those of small scale specimens is made. The recognition of improper heat treatment as the root cause of cracking in post-mortem examination of in-service failures necessitates the correct identification of fracture surfaces. For example, in 'over-aged' specimens, despite manifesting as cleavage, the cleavage-like fracture surfaces have arisen due to a localised plasticity process, which is accelerated in the presence of hydrogen. There may be a local accumulation of hydrogen at carbide-matrix interfaces and within the deformed region ahead of the crack tip, such that in these dissimilar joints the carbide rich planar zone acts as a low energy crack path. Flat, crater-like failure coincides with regions of discontinuous, partial mixing. Therefore, the low energy cleavage-like failure along the carbide-matrix interfaces acts to link together these partially-mixed regions. Fractographically, the presence of crater-like failure at multiple elevations is attributed to the penetration of the swirl into the weld metal, and the emergence of primary and secondary planar zones. Crack linking through the discontinuities happens

abruptly, and serves to link the two planar regions together. The result is an alternating fracture morphology through discontinuous swirls and M_7C_3 rich planar zones.

In the as-welded samples, the dominant fracture morphology was interfacial failure, typically outlined by prior austenite GB protrusions. Through TEM investigation, this failure mode was found to occur because of disbonding at the fusion boundary itself. This failure mode is easily discernible because the fracture surface follows the macroscopic bead profile. Though not dominant, intermixed within the interfacial failure was the crater-like failure through discontinuous PMZ regions with a high proportion of untempered martensite. Characteristic to its hydrogen sensitivity, these martensite regions presented the poorest resistance to CP-induced hydrogen embrittlement.

9.2 Recommendations

The fractographic studies have considered the as-welded and 'over-aged' conditions. Qualitative assessments have been made, in terms of a 'dominant fracture mode'. Significant potential to advance the fractographic technique lies in the quantitative failure mode assessment, and would be facilitated by outlining the entire fracture surface, and by mapping individual fracture modes. This would further aid in determining the correlations between microstructure, mechanical properties and fracture morphology.

Whilst the reduction in mechanical performance has been linked to the formation of M_7C_3 carbide within the planar zone, the tolerance of the joint to these precipitates has not been assessed. To qualify resistance to fracture of the planar zone, environmental performance tests and microstructural evaluations on bulk material, which is representative of the planar zone chemistry and structure, is recommended. In doing so, a quantitative relationship between chemistry, extent of precipitation, and resistance to hydrogen related fracture, may be established. Following this, environmental performance tests are recommended on dissimilar joint coupons with a known amount of discontinuous PMZ. By comparing the

two, the mechanical properties corresponding to each fracture type may be isolated. This would aid the identification of the mechanisms for hydrogen embrittlement.

The findings presented herein should not be applied to in-service failure scenarios before a study encompassing the full-scale stress state and degree of CP is conducted.

References

[1] J. N. DuPont and C. S. Kusko, “Technical Note : Martensite Formation in Austenitic / Ferritic Dissimilar Alloy Welds.”

[2] P. Fjellheim, “Retesting of Asgard Hubs,” 2001 026, 2001.

[3] R. B. Johansen and A. Karlsen, “Asgard B Examination of failed weld connection,” 2001-3042 Rev. 01, 2001.

[4] J. Morlet, H. Johnson, and A. Troiano, “A New Concept of Hydrogen Embrittlement in Steel,” *J. Iron Steel Inst.*, vol. 189, pp. 37–44, 1958.

[5] P. H. M. Hart, “Hydrogen Cracking - Its Causes, Costs and Future Occurrence,” in *International conference on Weld Metal Hydrogen Cracking in Pipeline Girth Welds*, 1999.

[6] A. Turnbull, *Hydrogen transport and cracking in metals*. London: The Institute of Materials, 1994.

[7] J. R. Davis, “Corrosion of Dissimilar Metal Weldments,” in *Corrosion of Weldments*, ASM International, 2006, pp. 169–175.

[8] S. Kou, “Fluid Flow and Solidification in Welding: Three Decades of Fundamental Research at the University of Wisconsin,” *Weld. J.*, no. November, 2012.

[9] K. Poorhaydari, B. Patchett, and D. Ivey, “Estimation of cooling rate in the welding of plates with intermediate thickness,” *Weld. J.*, no. October, pp. 149–155, 2005.

[10] D. Rosenthal, “The Theory of Moving Sources of Heat and Its Application to Metal Treatments,” *Trans. ASME*, vol. 68, pp. 849–866, 1946.

[11] T. Eagar and N. Tsai, “Temperature fields produced by traveling distributed heat sources,” *Weld. J.*, no. December, 1983.

[12] J. N. DuPont, J. C. Lippold, and S. D. Kiser, *Welding Metallurgy and Weldability of Nickel-Base Alloys*. John Wiley and Sons, Inc., 2009.

[13] S. Kou, *Welding Metallurgy*, Second Edi. Hoboken, New Jersey: John Wiley and Sons, Inc., 2003.

[14] J. A. Fenske, “Microstructure and Hydrogen Induced Failure Mechanisms in Iron-Nickel Weldments,” 2010.

[15] K. Easterling, *Introduction to the Physical Metallurgy of Welding*, 1st ed. Butterworths Monographs in Materials, 1983.

[16] M. C. Coleman, “The Structure of Weldments and its Relevance to High Temperature Failure.,” 1978.

[17] R. J. Cristoffel, E. F. Nippes, and H. D. Solomon, “Weldments: Physical Metallurgy and Failure Phenomena,” in *Proceedings of the 5th Bolton Landing Conference*, 1978, p. 409.

[18] G. Almqvist, C. S. Polgary, C. H. Rosendahl, and G. Valland, “Some Basic Factors Controlling the Properties of Weld Metal,” in *Welding Research Relating to Power Plant*, 1972, p. 204.

[19] J. F. Lancaster, *Metallurgy of Welding*. Cambridge, UK, 1999.

[20] K. A. Jackson, *Solidification*. Metals Park, OH: American Society for Metals, 1971, p. 121.

[21] K. A. Jackson, J. D. Hunt, D. R. Uhlmann, and T. P. Sewand, “On origin of equiaxed zone in castings.,” *Metall. Soc. Am. Inst. Mining, Metall. Pet. Eng. - Trans.*, vol. 236, no. 149, 1966.

[22] R. F. Sekerka, “A Stability Function for Explicit Evaluation of the Mullins-Sekerka Interface Stability Criterion,” *J. Appl. Phys.*, vol. 36, no. 1, pp. 264–268, 1965.

[23] W. W. Mullins and R. F. Sekerka, “Stability of a planar interface during solidification of a dilute binary alloy,” *J. Appl. Phys.*, vol. 35, no. 2, pp. 444–451, 1964.

[24] R. F. Sekerka, “Application of the Time-Dependent Theory of Interface Stability to an Isothermal Phase Transformation,” *J. Appl. Phys. Chem. Solids*, vol. 28, no. 6, pp. 983–994, 1967.

[25] J. W. Rutter and B. Chalmers, “A Prismatic Substructure Formed During Solidification of Metals,” *Can. J. Phys.*, vol. 31, no. 1, pp. 15–39, 1953.

[26] W. A. Tiller, K. A. Jackson, J. W. Rutter, and B. Chalmers, “The Redistribution of Solute Atoms During the Solidification of Metals,” *Acta Metall.*, vol. 1, no. 4, pp. 428–437, 1953.

[27] M. C. Flemings, *Solidification Processing*. McGraw-Hill, 1974.

[28] K. A. Jackson and J. D. Hunt, “Transparent Compounds That Freeze Like Metals,” *Acta Metall.*, vol. 13, 1965.

[29] D. Walton, W. A. Tiller, J. W. Rutter, and W. C. Winegard, “Instability of a Smooth Solid-Liquid Interface During Solidification,” *Trans. AIME*, vol. 203, 1955.

[30] G. S. Cole and W. C. Winegard, “The Transition from Plane to Cellular Interface in Solidifying Tin-Lead-Antimony Alloys,” United States, 1963.

[31] M. D. Hunt, J. A. Spittle, and R. W. Smith, “The Solidification of Metals,” *Publication No. 110,*, p. 57, 1968.

[32] T. S. Plaskett and W. C. Winegard, “Cellular Growth in Tin Alloys,” *Can. J. Phys.*, vol. 37, p. 1555, 1959.

[33] W. Bardsley, J. M. Callan, H. A. Chedzey, and D. T. J. Hurle, “Constitutional supercooling during crystal growth from stirred melts,” *Solid State Electron.*, vol. 3, no. 142–154, 1961.

[34] J. O. Coulthard and R. Elliott, “The Solidification of Metals,” *Publication No. 110,*, p. 61, 1968.

[35] H. Nakagawa, H. Kato, F. Matsuda, and T. Senda, “X-ray investigations on Solidification Structures in Weld Metal,” *Trans. Japan Weld. Soc.*, vol. 39, p. 94, 1970.

[36] M. E. Glicksman, “Microsegregation,” in *Principles of Solidification*, New York: Springer, 2011, pp. 345–368.

[37] C. L. Estes and P. W. Turner, “Dilution in multipass welding of AISI 4130 to type 304 stainless steel,” *Weld. J.*, vol. 43, no. 12, p. 541s–550s, 1964.

[38] I. Magnabosco, P. Ferro, F. Bonollo, and L. Arnberg, “An investigation of fusion zone microstructures in electron beam welding of copper–stainless steel,” *Mater. Sci. Eng. A*, vol. 424, no. 1–2, pp. 163–173, May 2006.

[39] Y. Yang and S. Kou, “Fusion-boundary macrosegregation in dissimilar-filler metal Al-Cu welds,” *Weld. J.*, no. November, pp. 331–339, 2007.

[40] Y. K. Yang, “Macrosegregation in Arc Welds Caused by Dissimilar Filler Metals,” University of Wisconsin - Madison, 2008.

[41] Y. K. Yang, “Macrosegregation in Cu–30Ni welds made with dissimilar filler metals,” *Sci. Technol. Weld. Join.*, vol. 13, no. 4, pp. 318–326, 2008.

[42] S. Kou and Y. Yang, “Fusion-boundary macrosegregation in dissimilar-filler welds,” *Weld. J.*, pp. 303–312, 2007.

[43] Y. K. Yang and S. Kou, “Mechanisms of Macrosegregation Formation near Fusion Boundary in Welds Made with Dissimilar Filler Metals,” *Weld. Metall. Fail. Anal.*, vol. 2007, pp. 329–341, 2007.

[44] Y. Yang and S. Kou, “Weld-bottom macrosegregation caused by dissimilar filler metals,” *Weld. J.*, pp. 379–387, 2007.

[45] S. Kou, *Transport Phenomena and Materials Processing*. New York, 1996, pp. 57–60.

[46] W. F. Savage, E. F. Nippes, and E. S. Szekeres, “A Study of Weld Interface Phenomena in a Low Alloy Steel,” *Weld. J.*, vol. 55, no. 1, pp. 260–268, 1976.

[47] W. F. Savage, C. D. Lundin, and A. H. Aronson, “Weld Metal Solidification Mechanics,” *Weld. J.*, vol. 44, p. 175s–181s, 1965.

[48] W. F. Savage and A. H. Aronson, “Preferred Orientation in the Weld Fusion Zone,” *Weld. J.*, vol. 45, p. 85s–89s, 1966.

[49] W. F. Savage and R. H. Hrubec, “Synthesis of Weld Solidification using Crystalline Organic Materials,” *Weld. J.*, vol. 51, p. 260s–271s, 1972.

[50] J. W. Elmer, S. M. Allen, and T. W. Eagar, “Microstructural Development during Solidification of Stainless Steel Alloys,” *Metall. Trans. A*, vol. 20, no. A, 1989.

[51] T. Nelson, J. Lippold, and M. Mills, “Nature and Evolution of the Fusion Boundary in Ferritic-Austenitic Dissimilar Metal Welds—Part 2: On-Cooling Transformations,” *Weld Res Suppl 267s-277s*, no. October, 2000.

[52] T. Nelson, J. Lippold, and M. Mills, “Nature and evolution of the fusion boundary in ferritic-austenitic dissimilar weld metals, Part 1-Nucleation and growth,” *Weld. J.*, no. October, 1999.

[53] R. Ayer, R. R. Mueller, D. P. Leta, and W. J. Sisak, “Phase Transformations at Steel/IN625 Clad Interfaces,” *Metall. Mater. Trans. A*, vol. 20, no. 4, pp. 665–681, 1989.

[54] B. T. Alexandrov, J. C. Lippold, J. W. Sowards, a. T. Hope, and D. R. Saltzmann, “Fusion boundary microstructure evolution associated with embrittlement of Ni–base alloy overlays applied to carbon steel,” *Weld. World*, vol. 57, no. 1, pp. 39–53, Dec. 2012.

[55] J. E. Tomlinson and J. G. Young, *Argon-Arc Welding of Aluminium: Metallurgical Considerations*. 1957, pp. 12–13.

[56] J. N. DuPont and A. R. Marder, “Dilution in Single Pass Arc Welds,” *Metall. Mater. Trans. B*, vol. 27B, pp. 481–489, 1996.

[57] A. L. Schaeffler, “Constitution Diagram For Stainless Steel Weld Metal,” *Met. Prog.*, vol. 56(11), pp. 680–680b, 1956.

[58] M. T. Hutchings, P. J. Withers, T. M. Holden, and T. Lorentzen, *Introduction to the Characterization of Residual Stress by Neutron Diffraction*. CRC Press, 2005.

[59] R. C. Bradt, “The Fractography and Crack Patterns of Broken Glass,” *J. Fail. Anal. Prev.*, vol. 11, no. 2, pp. 79–96, Jan. 2011.

[60] P. J. Withers, “Residual Stress: Definition,” *Encyclopedia of Materials: Science and Technology (Second Edition)*. 2001.

[61] CEGB, “Assessment of the Integrity of Structures Containing Defects R/H/R6,” UK, 2001.

[62] British Standards Institution, “Guide to methods for assessing the acceptability of flaws in metallic structures,” vol. 3, no. 1, 2005.

[63] P. J. Bouchard, “Residual Stresses in Lifing and Structural Integrity Assessment,” in *Encyclopedia of Materials: Science and Technology, IV: Structural Phenomena*, K. H. J. Buschow, Ed. Oxford: Elsevier, 2001, pp. 8134–8142.

[64] K. Masabuchi, “Residual Stresses and Distortion in Welds,” in *Encyclopedia of Materials: Science and Technology*, K. H. . Buschow, Ed. Oxford: Elsevier, 2003, pp. 8121–8126.

[65] S. Spooner, “Neutron Residual Stress Measurement in Welds,” in *Analysis of Residual Stress by Diffraction using Neutron and Synchrotron Radiation*, M. E. Fitzpatrick and A. Lodini, Eds. Taylor and Francis, 2003, pp. 296–297.

[66] N. Bailey, F. R. Coe, T. G. Gooch, P. H. M. Hart, N. Jenkins, and R. J. Pargeter, *Welding Steels Without Hydrogen Cracking*, Second Edi. Abington Publishing, 1993.

[67] H. Granjon, “Cracking and Fracture in Welds,” Tokyo, 1972.

[68] C. Sykes, H. H. Burton, and C. C. Gegg, “Hydrogen in Steel Manufacture,” *J. Iron Steel Inst.*, vol. 156, pp. 155–180, 1947.

[69] Hume-Rothery, *The structure of alloys of iron*. Oxford, UK: Pergamon Press, 1966.

[70] R. P. Gangloff and B. P. Somerday, *Gaseous Hydrogen Embrittlement of Materials in Energy Technologies: Volume 1*. Woodhead Publishing, 2012.

[71] S. Sato, “Dilatometric investigation of A3 and A4 transformations in pure iron,” *Philos. Mag.*, vol. 1, pp. 996–1007, 1926.

[72] H. K. D. H. Bhadeshia and R. Honeycombe, *Steels: Microstructure and Properties*, Third Edit. Elsevier, 2006.

[73] M. Cohen, “The Strengthening of Steel,” *Metall. Soc. TMS AIME*, vol. 224, pp. 638–657, 1962.

[74] B. A. Graville, R. G. Baker, and F. Watkinson, “Effect of Temperature and Strain Rate on Hydrogen Embrittlement of Steel,” *Br. Weld. J.*, vol. 14, no. 11, pp. 603–613, 1967.

[75] M. J. Cheaitani and R. J. Pargeter, “Fracture Mechanics Techniques for Assessing the Effects of Hydrogen on Steel Properties,” in *International Steel and Hydrogen Conference*, 2011.

[76] P. G. Marsh and W. W. Gerberich, *Stress Corrosion Cracking*. Materials Park, OH: ASM International, 1992.

[77] B. D. Craig and G. Krauss, “The structure of tempered martensite and its susceptibility to hydrogen stress cracking,” *Metall. Mater. Trans. A*, vol. 11, no. 11, 1980.

[78] F. Y. Cheng, *Stress Corrosion Cracking of Pipelines*. Wiley, 2013.

[79] B. Lucas, G. Mathers, and D. Abson, “Defects - hydrogen cracks in steels - identification,” *Connect*, 2000. [Online]. Available: http://www.twi-global.com/technical-knowledge/job-knowledge/defects-hydrogen-cracks-in-steels-identification-045/. [Accessed: 10-Feb-2014].

[80] V. Cicek, *Cathodic Protection*. Somerset, NJ: Wiley, 2013.

[81] M. Fontana, *Corrosion Engineering*, Third Edit. New York: McGraw-Hill, 1986.

[82] A. Barnoush, "Hydrogen embrittlement, revisited by in situ electrochemical nanoindentation," 2007.

[83] S. M. Charca, O. N. C. Uwakweh, B. Shafiq, and V. S. Agarwala, "Characterization of Hydrogen Permeation in Armco-Fe during Cathodic Polarization in Aqueous Electrolytic Media," *J. Mater. Eng. Perform.*, vol. 17, no. 1, pp. 127–133, Jun. 2007.

[84] G. P. Tiwari, a. Bose, J. K. Chakravartty, S. L. Wadekar, M. K. Totlani, R. N. Arya, and R. K. Fotedar, "A study of internal hydrogen embrittlement of steels," *Mater. Sci. Eng. A*, vol. 286, no. 2, pp. 269–281, Jul. 2000.

[85] A. Głowacka and W. A. Świątnicki, "Effect of hydrogen charging on the microstructure evolution of duplex stainless steel," *Mater. Chem. Phys.*, vol. 81, no. 2–3, pp. 496–499, Aug. 2003.

[86] J. Kittel, V. Smanio, M. Fregonese, L. Garnier, and X. Lefebvre, "Hydrogen induced cracking (HIC) testing of low alloy steel in sour environment: Impact of time of exposure on the extent of damage," *Corros. Sci.*, vol. 52, no. 4, pp. 1386–1392, Apr. 2010.

[87] A. Pundt and R. Kirchheim, "Hydrogen in metals: Microstructural Aspects," *Annu. Rev. Mater. Res.*, vol. 36, no. 1, pp. 555–608, Aug. 2006.

[88] S. Myers and H. Birnbaum, "Hydrogen interactions with defects in crystalline solids," *Rev. Mod. …*, vol. 64, no. 2, 1992.

[89] Y. Fukai, Y. Ishii, Y. Goto, and K. Watanabe, "Formation of superabundant vacancies in Pd–H alloys," *J. Alloys Compd.*, vol. 313, no. 1–2, pp. 121–132, Dec. 2000.

[90] Y. Fukai, "F ormation of superabundant vacancies in M–H alloys and some of its consequences: a review," vol. 357, pp. 263–269, 2003.

[91] J. Mao and R. B. McLellan, "The thermodynamics of hydrogen–vacancy interactions in aluminum," *J. Phys. Chem. Solids*, vol. 63, no. 11, pp. 2029–2036, Nov. 2002.

[92] G. Lu and E. Kaxiras, "Hydrogen Embrittlement of Aluminum: The Crucial Role of Vacancies," *Phys. Rev. Lett.*, vol. 94, no. 15, p. 155501, Apr. 2005.

[93] T. Boniszewski and G. C. Smith, "The influence of hydrogen on the plastic deformation ductility, and fracture of nickel in tension," *Acta Metall.*, vol. 11, no. 3, pp. 165–178, 1963.

[94] A. Kimura and H. K. Birnbaum, "plastic softening by hydrogen plasma charging in pure iron," *Scr. Metall.*, vol. 21, pp. 53–57, 1987.

[95] H. K. Birnbaum, “Hydrogen effects on deformation - relation between dislocation behaviour and the macroscopic stress-strain behaviour,” *Scr. Metall. Mater.*, vol. 31, no. 2, pp. 149–153, 1994.

[96] P. J. Ferreira, I. M. Robertson, and H. K. Birnbaum, “Hydrogen effects on the interaction between dislocations,” *Acta Mater.*, vol. 46, pp. 1749–1757, 1998.

[97] T. Tsuru and R. M. Latanision, “Grain boundary transport of hydrogen in nickel,” *Scr. Metall.*, vol. 16, no. 575–578, 1982.

[98] A. Brass and A. Chanfreau, “Accelerated diffusion of hydrogen along grain boundaries in nickel,” *Acta Mater.*, vol. 44, no. 9, pp. 3823–3831, 1996.

[99] J. Yao and J. R. Cahoon, “Experimental studies of grain boundary diffusion of hydrogen in metals,” *Acta Metall. Mater.*, vol. 39, no. 1, pp. 119–126, 1991.

[100] A. Oudriss, J. Creus, J. Bouhattate, C. Savall, B. Peraudeau, and X. Feaugas, “The diffusion and trapping of hydrogen along the grain boundaries in polycrystalline nickel,” *Scr. Mater.*, vol. 66, no. 1, pp. 37–40, Jan. 2012.

[101] B. Makenas and H. Birnbaum, “Phase changes in the Niobium-Hydrogen System I - accommodation effects during hydride precipitation,” *Acta Metall.*, vol. 28, pp. 979–988, 1980.

[102] D. Teter, I. M. Robertson, and H. K. Birnbaum, “The effects of hydrogen on the deformation and fracture of B-titanium,” *Acta Mater.*, vol. 49, pp. 4313–4323, 2001.

[103] I. M. Robertson and D. Teter, “Controlled Environment Transmission Electron Microscopy,” *J. Microsc. Res. Tech.*, vol. 42, no. 260, 1998.

[104] A. Troiano, “The Role of Hydrogen and other Interstitials in the Mechanical Behaviour of Metals,” *Trans. ASM*, vol. 52, pp. 54–80, 1960.

[105] M. Whiteman and A. Troiano, “Hydrogen Embrittlement of Austenitic Stainless Steel,” *Corrosion1*, vol. 21, pp. 53–56, 965.

[106] R. A. Oriani and P. H. Josephic, “Hydrogen-enhanced load relaxation in a deformed medium-carbon steel,” *Acta Metall.*, vol. 27, no. 6, pp. 997–1005, 1979.

[107] R. Oriani, “The Diffusion and Trapping of Hydrogen in Steel,” *Acta Metall.*, vol. 18, pp. 147–157, 1970.

[108] H. A. Wriedt and R. A. Oriani, “Effect of Tensile and Compressive Elastic Stress on Equilibrium Hydrogen Solubility in a Solid,” *Acta Metall.*, vol. 18, pp. 753–760, 1970.

[109] R. Oriani, “A Mechanistic Theory of Hydrogen Embrittlement of Steels,” *Berichte der Bunsengesellschaft für Phys. Chemie*, vol. 76, pp. 848–857, 1972.

[110] R. Oriani and P. Josephic, “Equilibrium Aspects of Hydrogen-Induced Cracking of Steels,” *Acta Metall.*, vol. 22, pp. 1065–1074, 1974.

[111] J. Li, R. Oriani, and L. Darken, “The thermodynamics of stressed solids,” *Zeitschrift fur Phys. Chemie Neue Folge*, vol. 49, pp. 271–290, 1966.

[112] G. Pressouyre, “Trap theory of hydrogen embrittlement,” *Acta Metall.*, vol. 28, pp. 895–911, 1980.

[113] R. Oriani, “Hydrogen - the versatile embrittler,” *Corrosion*, vol. 43, pp. 390–397, 1987.

[114] H. Vehoff and K. Klameth, “Hydrogen embrittlement and trapping at crack tips in Ni single crystals,” *Acta Metall.*, vol. 33, pp. 955–962, 1985.

[115] H. Vehoff and W. Rothe, “Gaseous hydrogen embrittlement in FeSi-and Ni-single crystals,” *Acta Metall.*, vol. 31, no. 11, pp. 1781–1793, 1983.

[116] M. Daw and M. Baskes, “Embedded-atom method: derivation and application to impurities, surfaces, and other defects in metals,” *Phys. Rev. B*, vol. 29, pp. 6443–6453, 1984.

[117] M. Daw and M. Baskes, “Semiemprical, quantum mechanical calculation of hydrogen embrittlement in metals,” *Phys. Rev. Lett.*, vol. 50, pp. 1285–1288, 1983.

[118] M. Daw and M. Baskes, “Application of embedded atom method to hydrogen embrittlement,” *Chem. Phys. Fract.*, pp. 196–218, 1987.

[119] T. Matsumoto, J. Eastman, and H. K. Birnbaum, “Direct observations of enhanced dislocation mobility due to hydrogen,” *Scr. Metall.*, vol. 15, pp. 1033–1037, 1981.

[120] I. M. Robertson and H. K. Birnbaum, “An HVEM study of hydrogen effects on the deformation and fracture of nickel,” *Acta Metall.*, vol. 34, no. 3, pp. 353–366, 1986.

[121] H. K. Birnbaum and P. Sofronis, “Hydrogen-enhanced localized plasticity - a mechanism for hydrogen-related fracture,” *Mater. Sci. Eng. A*, vol. A176, pp. 191–202, 1994.

[122] P. J. Ferreira, I. M. Robertson, and H. K. Birnbaum, “Hydrogen effects on the character of dislocations in high-purity aluminium,” *Acta Mater.*, vol. 47, p. 2991, 1999.

[123] I. Robertson, “The effect of hydrogen on dislocation dynamics,” *Eng. Fract. Mech.*, vol. 64, pp. 649–673, 2001.

[124] P. J. Ferreira, I. M. Robertson, and H. K. Birnbaum, “Hydrogen effects on the character of dislocations in high-purity aluminum,” *Acta Mater.*, vol. 47, p. 2991, 1999.

[125] D. P. Abraham and C. J. Altstetter, “Hydrogen-enhanced localization of plasticity in an austenitic stainless steel,” *Metall. Mater. Trans. A*, vol. 26, no. 11, pp. 2859–2871, 1995.

[126] W. McInteer, A. W. Thompson, and I. M. Bernstein, “The effect of hydrogen on the slip character of nickel,” *Acta Metall.*, vol. 28, no. 7, pp. 887–894, 1980.

[127] X. Tang and A. W. Thompson, “Hydrogen effects on slip character and ductility in Ni-Co alloys,” *Mater. Sci. Eng. A*, vol. 186, pp. 113–119, 1994.

[128] C. Beachem, “A new model for hydrogen-assisted cracking (hydrogen ‘embrittlement’),” *Metall. Trans.*, vol. 3, no. 2, pp. 441–455, 1972.

[129] T. Tabata and H. K. Birnbaum, “Direct observations of hydrogen enhanced crack propagation in iron,” *Scr. Metall.*, vol. 18, no. 3, pp. 231–236, 1984.

[130] T. Tabata and H. K. Birnbaum, “Direct observations of the effect of hydrogen on the behavior of dislocations in iron,” *Scr. Metall.*, vol. 17, no. 7, pp. 947–950, 1983.

[131] T. C. Lee, I. M. Robertson, and H. K. Birnbaum, “An HVEM In situ deformation study of nickel doped with sulfur,” *Acta Metall.*, vol. 37, no. 2, pp. 407–415, 1989.

[132] G. M. Bond, I. M. Robertson, and H. K. Birnbaum, “On the mechanisms of hydrogen embrittlement of Ni3Al alloys,” *Acta Metall.*, vol. 37, no. 5, pp. 1407–1413, 1989.

[133] P. Rozenak, I. M. Robertson, and H. K. Birnbaum, “HVEM studies of the effects of hydrogen on the deformation and fracture of AISI type 316 austenitic stainless steel,” *Acta Metall. Mater.*, vol. 38, no. 11, pp. 2031–2040, 1990.

[134] D. S. Shih, I. M. Robertson, and H. K. Birnbaum, “Hydrogen embrittlement of alpha titanium: In situ TEM studies,” *Acta Metall.*, vol. 36, no. 1, pp. 111–124, 1988.

[135] E. Sirois and H. K. Birnbaum, “Effects of hydrogen and carbon on thermally activated deformation in nickel,” Urbana, IL, 1991.

[136] E. Sirois and H. K. Birnbaum, “Effects of hydrogen and carbon on thermally activated deformation in nickel,” *Acta Metall. Mater.*, vol. 40, no. 6, pp. 1377–1385, 1992.

[137] M. S. Yeh and J. H. Huang, “Internal hydrogen-induced subcritical crack growth in Ti-6Al-4V,” *Scr. Mater.*, vol. 36, no. 12, p. 1415, 1997.

[138] H. Kimura and H. Matsui, “Mechanism of hydrogen-induced softening and hardening in iron,” *Scr. Metall.*, vol. 21, no. 3, pp. 319–324, 1987.

[139] S. P. Lynch, “Environmentally assisted cracking: overview of evidence for an adsorption-induced localised-slip process,” *Acta Metall.*, vol. 36, no. 10, 1988.

[140] S. P. Lynch, “Metallographic contributions to understanding mechanisms of environmentally assisted cracking,” *Metallography*, vol. 23, no. 2, pp. 147–171, 1989.

[141] O. Barrera and A. C. F. Cocks, “Computational modelling of hydrogen embrittlement in welded structures,” *Philos. Mag.*, vol. 93, no. 20, pp. 2680–2700, Jul. 2013.

[142] O. Barrera and A. C. F. Cocks, “Computational Modelling of Hydrogen Embrittlement in Weld Joints in Subsea Oil and Gas Components,” in *Proceedings of of the ASME 2013 32nd International Conference on Ocean, Offshore and Arctic Engineering OMAE2013*, 2013.

[143] M. Tong, G. Duggan, J. Liu, Y. Xie, M. Dodge, L. Aucott, H. Dong, R. L. Davidchack, J. Dantzig, O. Barrera, A. C. F. Cocks, H. Kitaguchi, S. Lozano-Perez, C. Zhao, I. Richardson, A. Kidess, C. R. Kleijn, S. Wen, R. Barnett, and D. J. Browne, “Multiscale, Multiphysics Numerical Modeling of Fusion Welding with Experimental Characterization and Validation,” *JOM*, vol. 65, no. 1, pp. 99–106, Nov. 2012.

[144] P. Fjellheim, “New Hub Design,” 065, 2001.

[145] G. Rorvik, “Failure analysis of fracture Inconel 725 buttering weldment,” MAT-2001 019, 2001.

[146] G. Rorvik, “Verification of Carbon Diffusion across the fusion line of Inconel 725 and 625 Buttering Weldments from Asgard Hubs,” MAT-2001 047, 2001.

[147] J. D. Burk, C. L. Ribardo, and B. P. America, “Thunder Horse – Materials , Welding and Corrosion Challenges and Solutions,” in *Offshore Technology Conference*, 2010.

[148] J. A. Fenske, I. M. Robertson, R. Ayer, M. Hukle, D. Lillig, and B. Newbury, “Microstructure and Hydrogen-Induced Failure Mechanisms in Fe and Ni Alloy Weldments,” *Metall. Mater. Trans. A*, vol. 43, no. 9, pp. 3011–3022, Jun. 2012.

[149] J. A. Fenske, M. W. Hukle, B. . Newbury, J. R. Gordon, R. Noecker, and I. M. Robertson, “hydrogen Induced Mechanical Property Behavious of Dissimilar Weld Metal Interfaces,” in *Proceedings of the 30th International Conference on Ocean, Offshore and Arctic Engineering*, 2011, pp. 1–8.

[150] V. C. M. Beaugrand and M. F. Gittos, “Subsea Dissimilar Joints: Failure Mechanisms and Opportunities for Mitigation,” in *NACE*, 2009, no. 09305, pp. 1–12.

[151] V. C. M. Beaugrand, L. S. Smith, and M. F. Gittos, “Hydrogen Embrittlement of 8630M/625 Subsea Dissimilar Joints: Factors that Influence the Performance,” in *Proceedings of the 28th International Conference on Ocean, Offshore and Arctic Engineering*, 2009, pp. 1–10.

[152] V. C. M. Beaugrand and M. F. Gittos, “Design and Use of Dissimilar Joints for Subsea Applications,” Cambridge, 17434/15/10, 2010.

[153] V. Beaugrand and L. Smith, “Subsea Dissimilar Joints : Failure mechanisms and opportunities for Mitigation,” Cambridge, 2009.

[154] M. F. Gittos, “Resistance of Dissimilar Joints Between Steel and Nickel Alloys to Hydrogen-Assisted Cracking,” in *NACE*, 2008, pp. NACE2008–08095.

[155] V. Olden, P. E. Kvaale, P. A. Simensen, S. Aaldstedt, and J. K. Solberg, “The effect of PWHT on the material properties and micro structure in inconel 625 and inconel 725

buttered joints," in *Proceedings of the 22nd International Conference on Ocean, Offshore and Arctic Engineering*, 2003.

[156] P. E. Kvaale and G. Rorvik, "Experience With Qualification And Use of Stainless Steels In Subsea Pipelines," in *Kvaale P and Rorvik G, 23rd International Conference on Offshore Mechanics & Arctic Engineering*, 2004.

[157] M. Mililitsky, M. F. Gittos, S. E. Smith, and V. Marques, "Assessment of dissimilar metal interfaces for sub-sea application under cathodic protection," in *Materials Science and Technology*, 2010.

[158] British Standards Institution, "Fracture mechanics toughness tests. Part 1: Method for determination of KIc, critical CTOD and critical J values of metallic materials," BS 7448-1, 1991.

[159] British Standards Institution, "Fracture mechanics toughness tests. Part 2: Method for determination of KIc, critical CTOD and critical J values of welds in metallic materials," BS 7448-2, 1997.

[160] British Standards Institution, "Fracture mechanics toughness tests. Part 4: Method for determination of fracture resistance curves and initiation values for stable crack extension in metallic materials: Fracture mechanics toughness tests," BS 7448-4, 1997.

[161] M. Mililitsky and M. F. Dodge, "Characterisation of Dissimilar Metal Interfaces and Evaluation of Resistance to Hydrogen Cracking," 19344-1/2012, 2012.

[162] S. Homrossukon, "Hydrogen induced cracking in low strength steels," *Thammasat Int. J. Sci. Technol.*, vol. 9, no. 2, pp. 56–61, 2004.

[163] A. Cottrell, "Mechanical Properties," in *An introduction to metallurgy*, Second., London: The Institute of Materials, 1995, pp. 386–427.

[164] V. Olden, "The effect of PWHT on the material properties and micro structure in inconel 625 and inconel 725 buttered joints," *Int. Conf. Offshore Mech. Arct. Eng.*, vol. 3, pp. 109–115, OMAE2003–37196, 2003.

[165] M. F. Gittos, "Resistance of Dissimilar Joints Between Steel and Nickel Alloys to Hydrogen-Assisted Cracking," in *NACE*, 2008, pp. NACE2008–08095.

[166] S. Lozano-Perez, "A guide on FIB preparation of samples containing stress corrosion crack tips for TEM and atom-probe analysis.," *Micron*, vol. 39, no. 3, pp. 320–8, Jan. 2008.

[167] S. Lozano-Perez, P. Rodrigo, and L. C. Gontard, "Three-dimensional characterization of stress corrosion cracks," *J. Nucl. Mater.*, vol. 408, no. 3, pp. 289–295, Jan. 2011.

[168] L. A. Giannuzzi and F. A. Stevie, "A review of focused ion beam milling techniques for TEM specimen preparation," *Micron*, vol. 30, no. 3, pp. 197–204, Jun. 1999.

[169] A. C. Fischer-Cripps, *Nanoindentation*, Second Edi. Springer, 2004.

[170] J. Fenske, “Microstructure and Hydrogen induced failure mechanisms in Iron-Nickel Weldments,” University of Illinois, 2010.

[171] P. J. Spencer, “A brief history of CALPHAD,” *Calphad*, vol. 32, no. 1, pp. 1–8, Mar. 2008.

[172] J. Ågren, “Calculation of phase diagrams: Calphad,” *Curr. Opin. solid state Mater. Sci.*, 1996.

[173] J-O Andersson, T. Helander, L. Hoglund, P. Shi, and B. Sundman, “THERMO-CALC & DICTRA, Computational Tools For Materials Science,” *Calphad*, vol. 26, no. 2, pp. 273–312, 2002.

[174] Thermo-Calc Software, “Thermo-Calc.” [Online]. Available: http://www.thermocalc.com/products-services/software/thermo-calc/. [Accessed: 22-Jan-2014].

[175] Thermo-Calc Software, “TCFE6 - TCS Steels/Fe-Alloys Database, Version 6.2,” Stockholm, 2010.

[176] Thermotech, “Thermodynamic databases,” *Website*. .

[177] R. Anand, C. Sudha, S. Saroja, and M. Vijayalakshmi, “Experimental and Thermokinetic Simulation Studies on the Formation of Deleterious Zones in Dissimilar Ferritic Steel Weldments,” *Metall. Mater. Trans. A*, vol. 44, no. 5, pp. 2156–2170, Jan. 2013.

[178] Thermo-Calc Software, “Dictra.” [Online]. Available: http://www.thermocalc.com/products-services/software/dictra/. [Accessed: 22-Jan-2014].

[179] A. Borgenstam, L. Höglund, J. Ågren, and A. Engström, “DICTRA, a tool for simulation of diffusional transformations in alloys,” *J. Phase Equilibria*, vol. 21, no. 3, pp. 269–280, May 2000.

[180] H. Larsson and L. Höglund, “Multiphase diffusion simulations in 1D using the DICTRA homogenization model,” *Calphad*, vol. 33, no. 3, pp. 495–501, Sep. 2009.

[181] Thermo-Calc Software, “TCS Alloy Mobility Database ‘MOB2,’” *Website*. .

[182] J. N. DuPont and R. E. Mizia, “Review of Dissimilar Metal Welding for the NGNP Helical-Coil Steam Generator,” no. March, 2010.

[183] K. Laha, K. S. Chandravathi, K. B. S. Rao, and S. L. Mannan, “An Assessment of Creep Deformation and Fracture Behavior of 2.25Cr-1Mo Similar and Dissimilar Weld Joints,” *Metall. Mater. Trans. A*, vol. 32, no. January, pp. 115–124, 2001.

[184] L. P. Karjalainen, “Weld fusion boundary structures in aluminium and Al-Zn-Mg alloy,” *Zeitschrift fur Met.*, 1979.

[185] P. Villars, *Pearson's handbook*. 1997, p. 961.

[186] C. Boudias and D. Monceau, "CaRIne Crystallography," *Webpage*. [Online]. Available: http://carine.crystallography.pagespro-orange.fr/. [Accessed: 01-Feb-2014].

[187] P. Pagliaro, M. B. Prime, H. Swenson, and B. Zuccarello, "Measuring Multiple Residual-Stress Components using the Contour Method and Multiple Cuts," *Exp. Mech.*, vol. 50, no. 2, pp. 187–194, Aug. 2009.

[188] N. S. Rossini, M. Dassisti, K. Y. Benyounis, and a. G. Olabi, "Methods of measuring residual stresses in components," *Mater. Des.*, vol. 35, pp. 572–588, Mar. 2012.

[189] P. J. Withers, "Mapping residual and internal stress in materials by neutron diffraction," *Comptes Rendus Phys.*, vol. 8, no. 7–8, pp. 806–820, Sep. 2007.

[190] B. Chen, A. Skouras, Y. Q. Wang, J. F. Kelleher, S. Y. Zhang, D. J. Smith, P. E. J. Flewitt, and M. J. Pavier, "In situ neutron diffraction measurement of residual stress relaxation in a welded steel pipe during heat treatment," *Mater. Sci. Eng. A*, vol. 590, pp. 374–383, Jan. 2014.

[191] P. J. Withers, M. Preuss, A. Steuwer, and J. W. L. Pang, "Methods for obtaining the strain-free lattice parameter when using diffraction to determine residual stress," *J. Appl. Crystallogr.*, vol. 40, no. 5, pp. 891–904, Sep. 2007.

[192] J. A. James, J. R. Santisteban, L. Edwards, and M. R. Daymond, "A virtual laboratory for neutron and synchrotron strain scanning," *Phys. B Condens. Matter*, vol. 350, no. 1–3, pp. E743–E746, Jul. 2004.

[193] M. R. Daymond, M. A. M. Bourke, R. B. Von Dreele, B. Clausen, and T. Lorentzen, "Use of Rietveld refinement for elastic macrostrain determination and for evaluation of plastic strain history from diffraction spectra," *J. Appl. Phys.*, vol. 82, no. 1554, 1997.

[194] M. W. Johnson and M. R. Daymond, "An optimum design for a time-of-flight neutron diffractometer for measuring engineering stresses," *J. Appl. Crystallogr.*, vol. 35, pp. 49–57, 2002.

[195] A. Skouras, A. Paradowska, M. J. Peel, P. E. J. Flewitt, and M. J. Pavier, "Residual stress measurements in a ferritic steel/In625 superalloy dissimilar metal weldment using neutron diffraction and deep-hole drilling," *Int. J. Press. Vessel. Pip.*, vol. 101, pp. 143–153, Jan. 2013.

[196] M. F. Gittos, "Materials selection for dissimilar joints in subsea hubs," Cambridge, 2006.

[197] K. Nibur, D. Bahr, and B. Somerday, "Hydrogen effects on dislocation activity in austenitic stainless steel," *Acta Mater.*, vol. 54, no. 10, pp. 2677–2684, Jun. 2006.

[198] I. M. Robertson, "The effect of hydrogen on dislocation dynamics," *Eng. Fract. Mech.*, vol. 64, no. 5, pp. 649–673, Nov. 1999.

[199] J. P. Hirth, “Effects of hydrogen on the properties of iron and steel,” *Metall. Trans. A*, vol. 25, no. 6, pp. 125–890, Jun. 1980.

[200] P. Novak, R. Yuan, B. P. Somerday, P. Sofronis, and R. O. Ritchie, “A statistical, physical-based, micro-mechanical model of hydrogen-induced intergranular fracture in steel,” *J. Mech. Phys. Solids*, vol. 58, no. 2, pp. 206–226, Feb. 2010.

[201] O. Barrera, E. Tarleton, and A. C. F. Cocks, “Microstructural model of welded joints . An image-based approach .,” *Philos. Mag.*, 2013.

[202] K. Sotoudeh, S. Y. Zhang, S. E. Eren, S. Kabra, M. Mililitsky, and M. F. Gittos, “Evaluation of Residual Stresses in Steel-to-Nickel Dissimilar Joints,” in *Proceedings of the 32nd International Conference on Ocean, Offshore and Arctic Engineering*, 2013, pp. 1–16.

Appendix A – Welding Procedure Details

Dissimilar joint: F22-309LSi

Manufacturer: Instytut Spawalnictwa, Gliwice

Mode of metal transfer: Globular

Joint type: Overlay

Preparation: Milling and degreasing

Material thickness (mm): 40

Joint design and welding sequence:

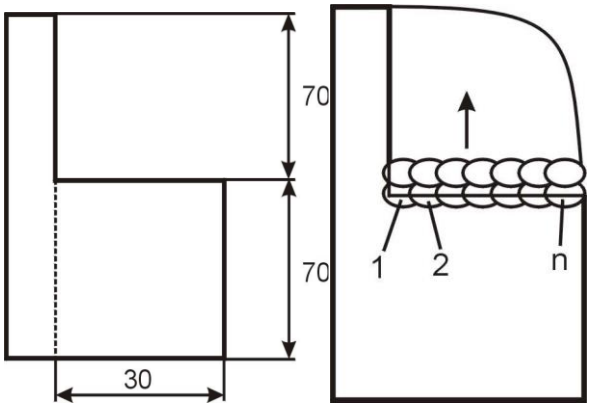

Run	Welding process	Size of filler	Current, A	Voltage, V	Type of current/polarity	Wire feed speed, m/min	Travel speed, cm/min	Heat input, kJ/mm	Metal Transfer
1	135	1.2	205	25.3	DC+ pulse	6.5	35	0.71	globular spray
2-n	135	1.2	315	26.4	DC+ pulse	10	40	0.99	globular spray

Filler material designation and make:

PN-EN ISO 14343-A-G 23 12 L Si, LNM 309 LSi Lincoln Electric

Gas shielding: PN-EN ISO 14175 – M13 – ArO – 2

Gas flow rate, l/min: 15

Preheat temperature, °C: 250

Interpass temperature, °C: 300

Distance, contact tube-workpiece, mm: 13

Welding Device: Lincoln Electric Power Wave 455/STT
Program no.: 22

Dissimilar joint: F22, 8630-Alloy 625

Manufacturer: Frenzak, Mikołow

Joint type: Overlay

Preparation: Cutting, grinding, milling and degreasing

Material thickness (mm): 40

Joint design and welding sequence:

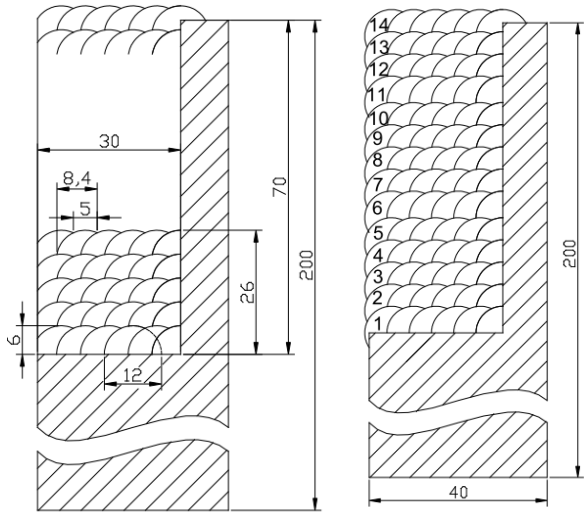

Run	Welding process	Size of filler	Current, A	Voltage, V	Type of current/polarity	Wire feed speed, m/min	Travel speed, cm/min	Heat input, kJ/mm
1	131	1	150±15	22±3	DC+ pulse	3.6	0.32 ± 0.05	0.495
2-n	131	1	170±15	24±3	DC+ pulse	4.2	0.35 ± 0.05	0.56

Filler material designation and make:

EN18274-S Ni 6625 (NiCr22Mo9Nb), Thermanit 625

Gas shielding: EN 14175 – I1 (Argon 99,99% purity)

Gas flow rate, l/min: 12

Preheat temperature, °C: 250 (min)

Interpass temperature, °C: 300 (max)

Distance, contact tube-workpiece, mm: 13

Appendix B – Chemical Analyses

Table 9- Chemical analysis of forgings used for investigation of heat treatment time. Performed using optical emission spectroscopy (UKAS accredited).

		Element, wt%																					
Joint Ref.	Notes	C	Si	Mn	P	S	Cr	Mo	Ni	Al	As	B	Co	Cu	Nb	Pb	Sn	Ti	V	W	Zr	Ca	Ce	Sb
F22- Alloy 625	F22 forging from F22-Alloy 625 joint, used for investigation of PWHT	0.12	0.34	0.5	0.007	0.003	2.09	0.95	0.15	0.038	0.007	0.0006	0.008	0.16	<0.002	<0.005	0.011	0.004	0.006	<0.01	<0.005	0.0004	<0.002	<0.002
F22 - 309LSi	F22 forging from F22-309LSi joint, used for investigation of PWHT	0.11	0.29	0.58	0.009	0.003	2.23	0.94	0.053	0.024	0.004	0.0004	0.007	0.032	<0.002	<0.005	<0.004	0.003	0.006	<0.01	<0.005	0.0015	<0.002	<0.002
8630-Alloy 625	8630 forging from 8630-Alloy 625 joint, used for investigation of PWHT	0.32	0.25	0.81	0.015	0.003	0.87	0.4	0.87	0.011	0.007	0.0003	0.009	0.12	0.038	<0.005	0.009	0.003	0.008	0.01	<0.005	0.0015	<0.002	<0.002

Appendix C – Thermodynamic Calculations

Table 10 – Summary of dilution calculations and Thermo-Calc solidification analysis for the 8630-Alloy 625 joint. The percentages of BCC and FCC were calculated under equilibrium conditions. Liquidus and Solidus temperatures were calculated using the Scheil-Gulliver module (under equilibrium conditions). Percentage δ-ferrite was calculated using the Scheil-Gulliver module under non-equilibrium conditions. Dashed lines indicate lower accuracy simulations.

	Dilution (parent material, %)																		
	8630																		625
	100	98	96	94	92	90	80	70	60	50	40	30	20	10	8	6	4	2	0
Ni (Wt%)	0.55	1.78	3.01	4.25	5.48	6.71	12.87	19.04	25.20	31.36	37.52	43.68	49.85	56.01	57.24	58.47	59.71	60.94	62.17
Cr (Wt%)	0.50	0.92	1.34	1.76	2.18	2.60	4.70	6.80	8.90	11.00	13.10	15.20	17.30	19.40	19.82	20.24	20.66	21.08	21.50
Liquidus, °C	1504	1497	1491	1486	1481	1477	1453	1429	1406	1405	1394	1384	1373	1361	1357	1354	1350	1346	1342
Solidus, °C	1453	1437	1417	1392	1392	1387	1361	1336	1309	1341	1316	1291	1272	1257	1255	1253	1251	1249	1244
Solidification	51.0	60.0	74.0	94.0	89.0	90.0	92.0	93.0	97.0	64.0	78.0	93.0	101.0	104.0	102.0	101.0	99.0	97.0	98.0
Solidification Mode	36% δ-ferrite + Aust	14% δ-ferrite + Aust	Aust.	Aust.	Aust.	Aust.	Aust.	Aust.	Aust.	Aust.	Aust.	Aust.	Aust.	Aust.	Aust.	Aust.	Aust.	Aust.	Aust.
BCC%	96.6	95.7	91.8	88.7	85.9	83.1	80.4	57.1	47.4	0.0	0.0	0.0	0.0	0.0	0.0	0.0	0.0	0.0	0.0
FCC%	0.0	0.0	2.5	5.2	8.3	8.5	11.0	34.4	30.5	91.6	88.4	80.0	79.0	76.7	76.2	76.0	75.7	75.5	59.1
Cr Equivalent	1.0	1.7	2.3	3.0	3.6	4.3	7.5	10.7	13.9	17.2	20.4	23.6	26.8	30.1	30.7	31.4	32.0	32.6	33.3
Ni Equivalent	10.1	11.2	12.3	13.3	14.4	15.5	20.9	26.3	31.7	37.0	42.4	47.8	53.2	58.6	59.7	60.7	61.8	62.9	64.0

Planar Zone

Table 11 – Summary of dilution calculations and Thermo-Calc solidification analysis for the F22-309LSi joint.

	Dilution (parent material, %)																		
	F22																		**309LSi**
	100	**98**	**96**	**94**	**92**	**90**	**80**	**70**	**60**	**50**	**40**	**30**	**20**	**10**	**8**	**6**	**4**	**2**	**0**
Ni (Wt%)	0.25	0.51	0.76	1.02	1.27	1.53	2.80	4.08	5.35	6.63	7.90	9.18	10.45	11.73	11.98	12.24	12.49	12.75	13.00
Cr (Wt%)	2.25	2.69	3.12	3.56	3.99	4.43	6.60	8.78	10.95	13.13	15.30	17.48	19.65	21.83	22.26	22.70	23.13	23.57	24.00
Liquidus, °C	1516	1514	1513	1511	1508	1506	1501	1491	1481	1472	1464	1456	1449	1443	1443	1441	1441	1440	1440
Solidus, °C	1472	1473	1473	1470	1469	1468	1463	1456	1448	1439	1430	1422	1414	1408	1406	1405	1404	1403	1402
Solidification	44.0	41.0	40.0	41.0	39.0	38.0	38.0	35.0	33.0	33.0	34.0	34.0	35.0	35.0	37.0	36.0	37.0	37.0	38.0
Solidification Mode	84% δ-ferrite + Aust	82.5% δ-ferrite + Aust	82.6% δ-ferrite + Aust	82% δ-ferrite + Aust	81% δ-ferrite + Aust	80% δ-ferrite + Aust	75.6% δ-ferrite + Aust	70.4% δ-ferrite + Aust	64.4% δ-ferrite + Aust	59.4% δ-ferrite + Aust	55.7% δ-ferrite + Aust	53% δ-ferrite + Aust	50% δ-ferrite + Aust	50% δ-ferrite + Aust	50% δ-ferrite + Aust	50.6% δ-ferrite + Aust	50.6% δ-ferrite + Aust	50.6% δ-ferrite + Aust	50.6% δ-ferrite + Aust
BCC%	97.0	97.0	97.0	97.0	97.0	96.7	95.0	93.6	91.4	89.1	83.4	78.7	80.1	75.8	75.2	75.0	73.6	73.2	72.0
FCC%	0.0	0.0	0.0	0.0	0.0	0.0	2.4	4.2	6.6	8.8	12.0	15.2	19.1	22.8	23.5	24.2	25.0	25.7	26.6
Cr Equivalent	3.7	4.2	4.6	5.0	5.5	5.9	8.1	10.2	12.4	14.5	16.7	18.9	21.0	23.2	23.6	24.0	24.5	24.9	25.3
Ni Equivalent	3.9	4.1	4.3	4.5	4.8	5.0	6.0	7.0	8.1	9.1	10.2	11.2	12.2	13.3	13.5	13.7	13.9	14.1	14.3

Table 12 - Summary of dilution calculations and Thermo-Calc solidification analysis for the F22-Alloy 625 joint

	Dilution (parent material, %)																		
	F22																		**625**
	100	**98**	**96**	**94**	**92**	**90**	**80**	**70**	**60**	**50**	**40**	**30**	**20**	**10**	**8**	**6**	**4**	**2**	**0**
Ni (Wt%)	0.25	1.49	2.73	3.97	5.20	6.44	12.63	18.83	25.02	31.21	37.40	43.59	49.79	55.98	57.22	58.45	59.69	60.93	62.17
Cr (Wt%)	2.25	2.64	3.02	3.41	3.79	4.18	6.10	8.03	9.95	11.88	13.80	15.73	17.65	19.58	19.96	20.35	20.73	21.12	21.50
Liquidus, °C	1516	1510	1503	1495	1489	1482	1456	1431	1407	1409	1396	1385	1374	1361	1357	1354	1350	1346	1342
Solidus, °C	1472	1466	1456	1441	1424	1406	1304	1318	1278	1316	1292	1274	1262	1244	1244	1251	1249	1244	1244
Solidification	44.0	44.0	47.0	54.0	65.0	76.0	152.0	113.0	129.0	93.0	104.0	111.0	112.0	117.0	113.0	103.0	101.0	102.0	98.0
Solidifcation Mode	84% δ-ferrite + Aust	79% δ-ferrite + Aust	69% δ-ferrite + Aust	54% δ-ferrite + Aust	27% δ-ferrite + Aust	Aust.	Aust.	Aust.	Aust.	Aust.	Aust.	Aust.	Aust.	Aust.	Aust.	Aust.	Aust.	Aust.	Aust.
BCC%	97.0	93.6	94.4	92.7	92.0	87.7	76.6	61.8	48.9	0.0	0.1	0.0	0.0	0.0	0.0	0.0	0.0	0.0	0.0
FCC%	0.0	0.0	2.3	3.4	4.3	5.7	16.8	21.4	29.4	88.8	85.3	80.8	79.2	76.7	76.3	75.9	75.7	75.5	59.1
Cr Equivalent	3.7	4.3	4.9	5.5	6.1	6.7	9.6	12.6	15.6	18.5	21.5	24.4	27.4	30.3	30.9	31.5	32.1	32.7	33.3
Ni Equivalent	3.9	5.1	6.3	7.5	8.7	9.9	15.9	21.9	27.9	34.0	40.0	46.0	52.0	58.0	59.2	60.4	61.6	62.8	64.0

Planar Zone

Appendix D – Thesis Structure

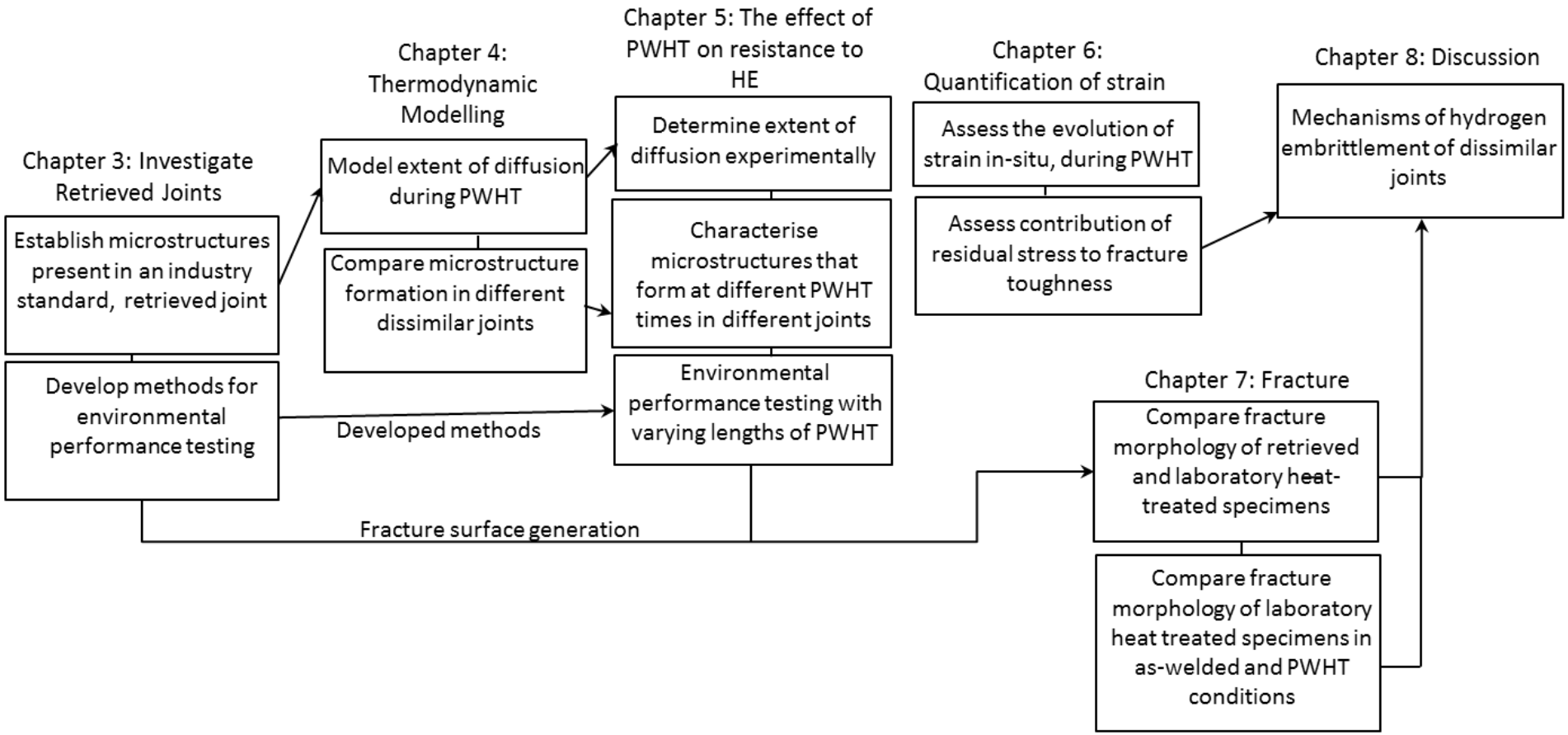

Figure 0-1 - Structure of thesis and knowledge exchange between Chapters